OECD/MCCI-2007-TR06

OECD MCCI Project
2-D Core Concrete Interaction (CCI) Tests:
CCI-4 Final Report

Rev. 1 - FINAL

November, 2010

by:

M. T. Farmer, R. W. Aeschlimann, D. J. Kilsdonk, and, S. Lomperski

Nuclear Engineering Division
Argonne National Laboratory
9700 S. Cass Avenue
Argonne, IL 60439
USA

Table of Contents

1.0 INTRODUCTION.....1
2.0 FACILITY DESCRIPTION.....3
2.1 Test Apparatus.....3
2.2 Water Supply System.....12
2.3 Quench System.....14
2.4 Test Section Pressure Relief System.....15
2.5 Off Gas System.....16
2.6 Cover Gas System.....17
2.7 Power Supply.....18
2.8 Concrete Sidewalls and Basemat.....18
2.9 Corium Composition and Concrete-Metal Inserts.....20
2.10 Instrumentation and Data Acquisition.....23
3.0 TEST PROCEDURES.....30
3.1 Pretest Preparations.....30
3.2 Test Operations.....33
4.0 RESULTS.....39
4.1 Electric Power.....39
4.2 Melt Temperatures.....39
4.3 Concrete Basemat and Sidewall Ablation Rates.....45
4.4 Melt Zone MgO Sidewall Heat Losses.....50
4.5 Crust Lance Data.....52
4.6 Corium Quench Rate.....54
4.7 Posttest Debris Examination and Chemical Analysis Results.....55
5.0 REFERENCES.....65
APPENDIX A: Data Acquisition System Channel Assignments.....66
APPENDIX B: Test Data.....79
APPENDIX C: Chemical Analysis Results.....111

List of Figures

Figure **Page**

2-1 Key Elements of the CCI-4 Test Apparatus 4
2-2 Overview Photograph of CCI Test Facility 4
2-3 Details of the CCI-4 Test Section 5
2-4 Top View of Lower Test Section 5
2-5 Side View of Lower Test Section Showing Inert MgO Sidewall Sections 6
2-6 Side View of Lower Test Section Showing Concrete Sidewall Sections 6
2-7 Photograph Showing Lower Section Sidewall Components after Fabrication 7
2-8 Illustration of the CCI-4 Thermite Powder Loading Scheme 9
2-9 Photograph Showing Electrodes Installed in Clamps 9
2-10 Details of the Top Test Section Showing Water Weirs 10
2-11 Illustration of CCI-4 Crust Lance Assembly Installed in Test Section 11
2-12 Details of Crust Lance Loading Device 11
2-13 Illustration of CCI-4 Test Section Mounted on ZPR-9 Reactor Bed 12
2-14 Illustration of Test Section Clamping Bars 13
2-15 Test Section Water Supply System 13
2-16 CCI-4 Quench and Overflow Tanks 14
2-17 CCI-4 Spray Tank System 15
2-18 CCI-2 Test Section Pressure Relief System 16
2-19 CCI-2 Off Gas System 17
2-20 CCI-4 Cover Gas System 18
2-21 Illustration of Concrete-Metal Inserts over the Concrete Basemat 20
2-22 CCI-4 Basemat with Insert Prior to Placement on Test Stand 21
2-23 Data Acquisition System Setup for CCI-4 24
2-24 Plan View of Basemat Instrumentation Layout (dimensions are in cm) 25
2-25 Elevation View of Basemat Type C Thermocouple Locations 26
2-26 CCI-4 Test Section Sidewall Instrumentation (View from West) 27

List of Figures (Contd.)

Figure **Page**

2-27 Thermocouple Arrays Installed in Basemat Concrete Form 27
2-28 CCI-4 Test Section Sidewall Instrumentation (View from South).....28
2-29 CCI-4 Test Section Pressure Transducer Layout 29
3-1 Illustration of Thermite Sample Train Installed in Test Section 32
3-2 Voltage Reading Across Thermite Igniter Shunt 36
3-3 Bulk Melt Temperature Data over the First 5 Minutes of the Interaction.....36
3-4 Test Section Plenum Gas Temperatures during the Initial Interaction.....37
3-5 Power Supply Current during the Initial Interaction 37
3-6 Pressure in the Test Section Plenum and at the Side of the Basemat.....38
4-1 Power Supply Voltage.....40
4-2 Power Supply Current 40
4-3 DEH Input Power 41
4-4 Melt Temperature Data from Basemat Type C "WCL" Array 41
4-5 Melt Temperature Data from Basemat Type C "WNW" Array. 42
4-6 Melt Temperature Data from Basemat Type C "WNE" Array 42
4-7 Melt Temperature Data from Basemat Type C "WSE" Array.....43
4-8 Melt Temperature Data from Basemat Type C "WSW" Array.....43
4-9 Melt Temperature Data from North Sidewall Type C "WN" Array 44
4-10 Melt Temperature Data from North Sidewall Type C "WS" Array.....44
4-11 Data from all 36 Melt Temperature Thermocouples 45
4-12 Thermal Response of the Concrete Basemat at the Centerline ("A" Array) 46
4-13 North Concrete Sidewall Thermal Response at +0.0 cm ("SWG" Array) 47
4-14 South Concrete Sidewall Thermal Response at +0.0 cm ("SWH" Array) 47
4-15 Basemat Axial Ablation Front Location.....48
4-16 North Sidewall Radial Ablation Front Location.....48
4-17 South Sidewall Radial Ablation Front Location.....49
4-18 Characteristic Axial and Radial Ablation Depths versus Time.....49

List of Figures (Contd.)

Figure **Page**

4-19 Test Section MgO Sidewall Heat Loss Data at -17.5 cm Elevation 50

4-20 Test Section MgO Sidewall Heat Loss Data at -7.5 cm Elevation 51

4-21 Test Section MgO Sidewall Heat Loss Data at +2.5 cm Elevation 51

4-22 Test Section MgO Sidewall Heat Loss Data at +12.5 cm Elevation 52

4-23 Local Heat Fluxes from the Melt to the Test Section Sidewalls 53

4-24 Load Force Exerted on Crust vs. Time 53

4-25 Lance Tip Elevation over Initial Concrete Surface 54

4-26 Quench Tank Water Volume vs. Time 55

4-27 Debris Cooling Heat Flux Based on Steam Formation Rate 56

4-28 Top View of Mantle Crust after Removal of the Top Sidewall Section 56

4-29 Topographical Map Showing Mantle Crust Surface Elevation Profile 57

4-30 (a) Electrode and (b) Nonelectrode Sidewall Views of the Solidified Debris 58

4-31 (a) View Towards North and (b) South Concrete Sidewalls after Removal of Middle 59
Sidewall Section 59

4-32 (a) Top and (b) West Side Views of Cavity After Removal of MgO Sidewalls 60

4-33 Close-up Photo of Northeast Basemat Corner Showing Melt Penetration 61

4-34 Concrete Basemat and Sidewalls after Complete Disassembly (view from the southwest) .. 62

B-1 Compensator Temperature, Channels B1-B50 and B51-B100 80

B-2 Basemat Type C “WCL” Array Data 80

B-3 Basemat Type C “WNW” Array Data 81

B-4 Basemat Type C “WNE” Array Data 81

B-5 Basemat Type C “WSE” Array Data 82

B-6 Basemat Type C “WSW” Array Data 82

B-7 North Sidewall Type C “NW” Array Data 83

B-8 South Sidewall Type C “WS” Array Data 83

B-9 Basemat Type K “A” Array Data 84

List of Figures (Contd.)

Figure **Page**

B-10 Basemat Type K "B" Array Data....84
B-11 Basemat Type K "C" Array Data....85
B-12 Basemat Type K "D" Array Data....85
B-13 Basemat Type K "E" Array Data....86
B-14 North Sidewall Type K "SWA" Array Data....86
B-15 South Sidewall Type K "SWB" Array Data....87
B-16 North Sidewall Type K "SWC" Array Data....87
B-17 South Sidewall Type K "SWD" Array Data....88
B-18 North Sidewall Type K "SWE" Array Data....88
B-19 South Sidewall Type K "SWF" Array Data....89
B-20 North Sidewall Type K "SWG" Array Data....89
B-21 South Sidewall Type K "SWH" Array Data....90
B-22 North Sidewall Type K "SWI" Array Data....90
B-23 South Sidewall Type K "SWJ" Array Data....91
B-24 North Sidewall Type K "SWK" Array Data....91
B-25 South Sidewall Type K "SWL" Array Data....92
B-26 North Sidewall Type K "SWM" Array Data....92
B-27 South Sidewall Type K "SWN" Array Data....93
B-28 Thermocouple Compensator Data for Channels Q1-Q50 and Q51-Q100....93
B-29 Test Section Sidewall Heat Loss Data at -17.5 cm Elevation....94
B-30 Test Section Sidewall Heat Loss Data at -7.5 cm Elevation....94
B-31 Test Section Sidewall Heat Loss Data at +2.5 cm Elevation....95
B-32 Test Section Sidewall Heat Loss Data at +12.5 cm Elevation....95
B-33 Test Section Sidewall Heat Loss Data at +67.5 cm Elevation....96
B-34 Test Section Sidewall Heat Loss Data at +81.6 cm Elevation....96
B-35 Test Section Sidewall Heat Loss Data at +92.2 cm Elevation....97

List of Figures (Contd.)

Figure **Page**

B-36 Test Section Sidewall Heat Loss Data at +122.4 cm Elevation....97
B-37 Test Section Sidewall Heat Loss Data at +148.8 cm Elevation....98
B-38 Test Section Mainline Thermocouple Data....98
B-39 Test Section Plenum and Insertable Water Level Probe Thermocouple Data....99
B-40 Quench Tank Water Volume, Coil Inlet, and Coil Outlet Temperature Data....99
B-41 Miscellaneous Temperatures in Water Supply, Quench, and Off Gas Systems....100
B-42 Crust Lance Load Cell Data....100
B-43 Lance Position Indicator Data....101
B-44 Total Power Supply Power....101
B-45 Power Supply Voltage Data....102
B-46 Total Power Supply Current Data....102
B-47 Power Supply Current Transformer Data....103
B-48 Hall Effect Meter Data....103
B-49 Voltage across Igniter Shunt....104
B-50 Pressure Transducer Power Supply Voltages....104
B-51 Water Supply, Overflow, and Spray Tank Water Volume Data....105
B-52 Quench Tank Water Volume Data....105
B-53 Supply and Quench System Tank Head Data (Backup)....106
B-54 Test Section Water Head Transducer Data....106
B-55 Calculated Water Depth in Test Section....107
B-56 Water Supply Tank Pressure....107
B-57 Test Section Pressure....108
B-58 Quench/Overflow and Spray Tank Plenum Differential Pressures....108
B-59 Water Flow Rates....109
B-60 Test Section Helium Cover Gas Flow Rates....109
B-61 Final Off Gas Flow Rate....110

List of Tables

Table **Page**

1-1 Specifications for CCI-4 2
2-1 Chemical Composition of Castable MgO 7
2-2 Engineering Composition of CCI-4 LCS Concrete Basemat and Sidewalls 19
2-3 Composition of CCI-4 Concrete 19
2-4 Bulk Composition of CCI-4 Melt at Start of Interaction with Inserts 22
2-5 Detailed Pre- and Post-Reaction Compositions for CCI-4 Thermite 22
2-6 Composition of CCI-4 Concrete/Metal Inserts 23
2-7 Bulk Melt Composition at Start of Basemat Ablation 23
2-8 Detailed Melt Composition at the Start of Basemat Ablation 23
3-1 CCI-4 Event Sequence (times relative to onset of ablation of the basemat) 34
4-1 CCI-4 Pre- and Posttest Mass Balances 64
4-2 Bulk Chemical Analysis Results for Samples Collected from CCI-4 Posttest Debris 64
A-1 "Basemat" DAS Channel Assignments for CCI-4 67
A-2 "Power" DAS Channel Assignments for CCI-4 71
A-3 "Quench" DAS Channel Assignments for CCI-4 75
C-1 Raw Data from CCI-4 Sample Analyses 112

1.0 INTRODUCTION

Ex-vessel debris coolability is an important light water reactor (LWR) safety issue. For existing plants, resolution of this issue will confirm the technical basis for severe accident management guidelines (SAMGs). For new reactors, understanding this issue will help confirm the effectiveness of the design and implementation of new accident mitigation features and severe accident management design alternatives (SAMDAs). The first OECD-MCCI program conducted reactor material experiments focused on achieving the following technical objectives: i) provide confirmatory evidence for various cooling mechanisms through separate effect tests and data for severe accident code model development, and ii) provide longer-term two-dimensional core-concrete interaction data for code assessment and improvement.

Debris cooling mechanisms investigated as part of the first MCCI program included: i) water ingression through cracks/fissures in the core debris, ii) melt eruption caused by gas sparging (volcanic-type event), and iii) large-scale crust mechanical failure leading to renewed bulk cooling. The results of this testing and associated analysis provided an envelope (principally determined by melt depth) for debris coolability. However, this envelope does not encompass the full range of melt depths that are calculated for all plant accident sequences. Cooling augmentation by additional means may be needed at the late stage to assure coolability for new reactor designs as well as for various accident sequences for existing reactors. In addition, the results of the CCI tests showed that lateral/axial power split is a function of concrete type. However, the first program produced limited data sets for code assessment. In light of significant differences in ablation behavior for different concrete types, additional data will be useful in reducing uncertainties and gaining confidence in code predictions.

Based on these findings, a workscope was defined for the follow-on MCCI program that can be divided into the following four categories:

1. Combined effect tests to investigate the interplay of different cooling mechanisms, and to provide data for model development and code assessment purposes.

2. Tests to investigate new design features to enhance coolability, applicable particularly to new reactor designs.

3. Tests to generate two-dimensional core-concrete interaction data.

4. Integral tests to validate severe accident codes.

Aside from these various testing categories, an analysis workscope was also defined to develop and validate debris coolability models to form the technical basis for extrapolating the experiment findings to plant conditions.

As one of the steps in satisfying these program objectives, the Management Board (MB) approved the conduct of a fourth longer-term 2-D Core-Concrete Interaction (CCI) experiment designed to provide information in several areas, including: i) lateral vs. axial power split during dry core-concrete interaction, ii) integral debris coolability data following late phase flooding,

and iii) data regarding the nature and extent of the cooling transient following breach of the crust formed at the melt-water interface. The first three tests [1] investigated the interaction of fully oxidized PWR core melt compositions with specially designed concrete test sections that were initially 50 cm x 50 cm in cross-sectional area. Both siliceous and limestone/common sand concrete types were addressed in the test matrix.

The fourth test that is addressed in this report, CCI-4, utilized a similar test apparatus and experiment boundary conditions, including a limestone/common sand concrete test section. However, instead of a fully oxidized PWR melt, CCI-4 utilized a partially oxidized BWR core melt containing ~ 8 wt % structural steel constituents. Thus, this test evaluated the effect of elevated melt metal content on two-dimensional cavity erosion and debris cooling behavior. The experiment was conducted on May 26, 2007, and early experiment results were reported in a quick-look data report. [2] The objective of this final report is to document both the thermalhydraulic and posttest debris examination results for this test. To this end, a summary description of the test apparatus is provided first, followed by descriptions of the test operating procedure and experimental results that include both thermalhydraulic data and the findings from the posttest examinations. Overall specifications for CCI-4 are provided in Table 1-1.

Table 1-1. Specifications for CCI-4.

Parameter	Specification
Initial Corium Composition[a]	78 % oxidized BWR with 7.7 wt % stainless steel constituents and 10.0 wt % limestone/common sand concrete
Concrete type	Limestone/common sand concrete
Initial basemat dimension	50 cm x 40 cm
Initial melt mass (depth[a])	300 kg (25 cm)
Test section sidewall construction	Nonelectrode walls: concrete Electrode walls: MgO protected by UO_2 pellet layer.
Lateral ablation limit	45.0 cm
Axial ablation limit	42.5 cm
System operating pressure	Atmospheric
Melt formation technique (timescale)	Chemical reaction (~30 seconds)
Initial melt temperature (estimate)[a]	1850 ºC
Melt heating technique	Direct Electrical (Joule) Heating
Power supply operation before water addition	Constant power at 95 kW
Criteria for water addition	1) 7.0 hours of operation with DEH input, or 2) ablation reaches 5 cm of maximum permissible
Inlet water temperature	20 ºC
Inlet water flow rate (2 MW/m^2 equivalent quench rate)	2 liters/second
Sustained water depth over melt	50 ± 5 cm
Power supply operation after water addition	Constant voltage
Test termination criteria	1) Melt temperature falls below concrete solidus, 2) concrete ablation is arrested, or 3) maximum ablation limit is reached.

[a]After erosion of concrete/metal inserts and at start of basemat ablation

2.0 FACILITY DESCRIPTION

The overall facility design and test operating procedures for CCI-4 were similar to those used in the previous three CCI tests [1]. However, at the first PRG meeting for MCCI-2, the MB made two specific design requests [3] for this test that are summarized as follows:

1) Increase the metal content of the melt to the highest practical level to more accurately mock up a prototypic BWR core melt composition at the time of vessel failure, and

2) modify the apparatus design to increase the duration of the dry core-concrete interaction phase.

The approach for satisfying the first requirement was to place a metal-bearing concrete insert on top of the concrete basemat that was ablated into the melt prior to onset of basemat ablation, thereby increasing the melt metal content to the target level. This technique was originally developed as part of the Advanced Containment Experiment Molten Core Concrete Interaction (ACE/MCCI) test series [4] that focused on quantifying fission product source term due to core-concrete interaction. The approach for satisfying the second request was to slightly reduce the initial inside dimension of the concrete crucible to provide more concrete for ablation, and also to let the ablation front to proceed to a deeper depth relative to the limits utilized in the original test series [1]. Additional details regarding these modifications are provided in the balance of this section. Specifications for the experiment were shown previously in Table 1-1.

2.1 Test Apparatus

The CCI test facility consisted of a test apparatus, a power supply for Direct Electrical Heating (DEH) of the corium, a water supply system, two steam condensation (quench) tanks, a ventilation system to complete filtration and exhaust the off-gases, and a data acquisition system. A schematic illustration of the facility for CCI-4 is provided in Figure 2-1, while an overview photograph showing key elements of the facility is provided in Figure 2-2. The principal components of the apparatus, shown in Figure 2-3, consisted of a bottom support plate, three sidewall sections, and an upper enclosure lid. The overall structure was 3.4 m tall. The two upper sidewall sections had a square internal cross sectional area of 50 cm x 50 cm. The concrete test section for containment of the core melt was located at the bottom of the apparatus. A top view of this component is shown in Figure 2-4, while cross-sectional views of the electrode and non-electrode sidewalls are provided in Figures 2-5 and 2-6, respectively. The cross-sectional area of the cavity was 50 cm x 40 cm. The distance between the tungsten electrodes was the same as that of previous tests (50 cm), while the distance between the concrete sidewalls was reduced by 10 cm to a width of 40 cm. This increase in sidewall thickness, combined with a 5 cm extension in allowable ablation, provided a total of ten extra centimeters of concrete for lateral ablation per sidewall. The basemat thickness was increased by 2.5 cm to 57.5 cm to accommodate up to 42.5 cm of axial ablation. This design maintained a minimum concrete thickness of 15 cm in both the sidewalls and basemat for final melt containment.

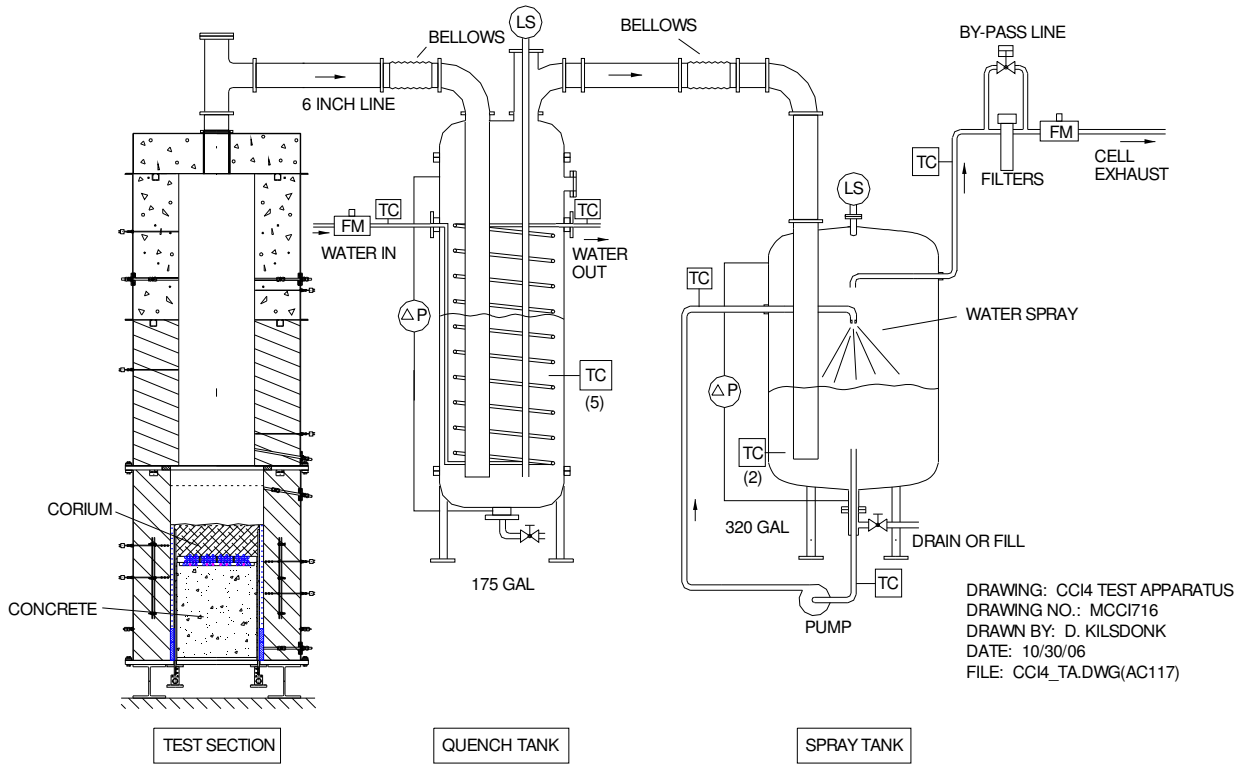

Figure 2-1. Key Elements of the CCI-4 Test Apparatus.

Figure 2-2. Overview Photograph of CCI Test Facility.

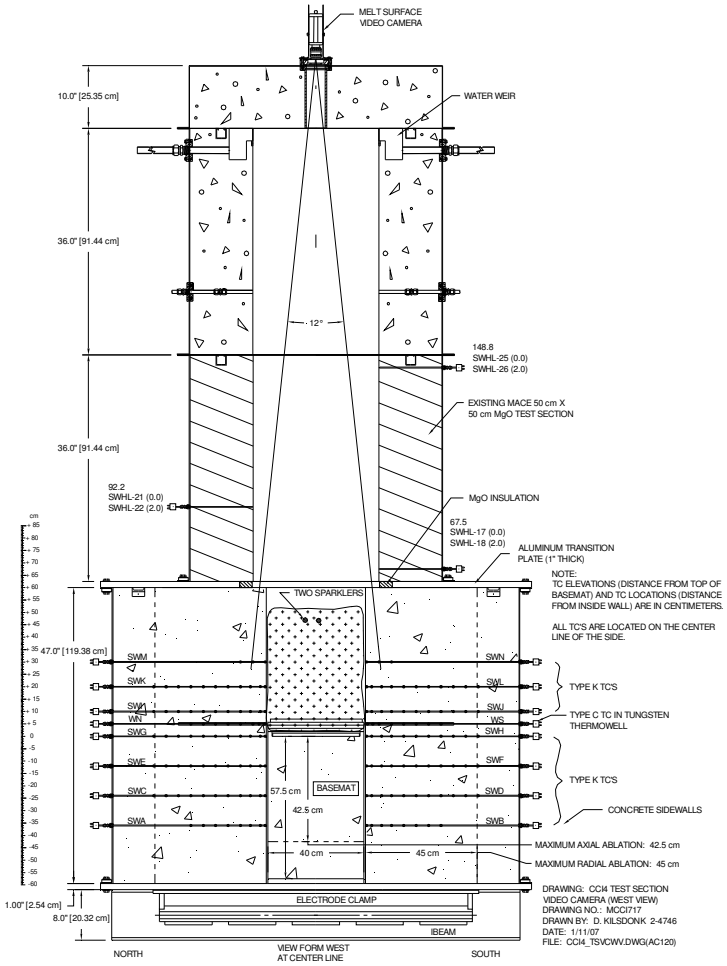

Figure 2-3. Details of the CCI-4 Test Section.

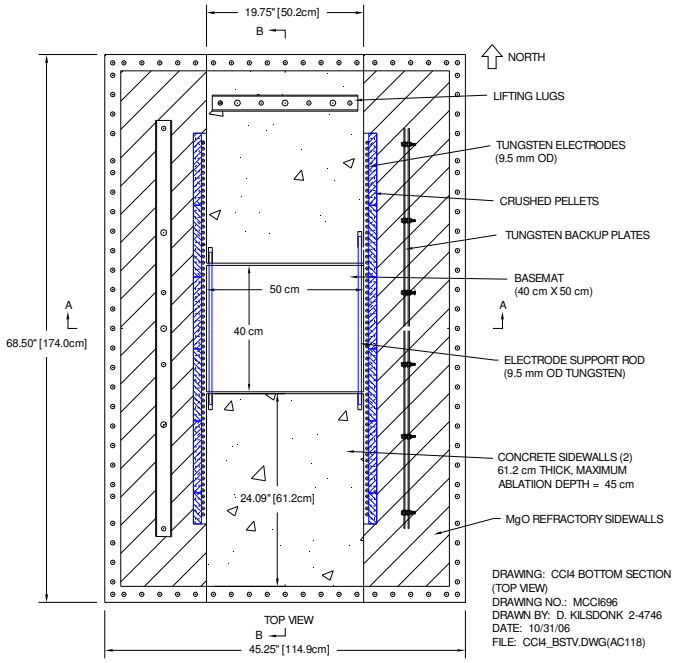

Figure 2-4. Top View of Lower Test Section.

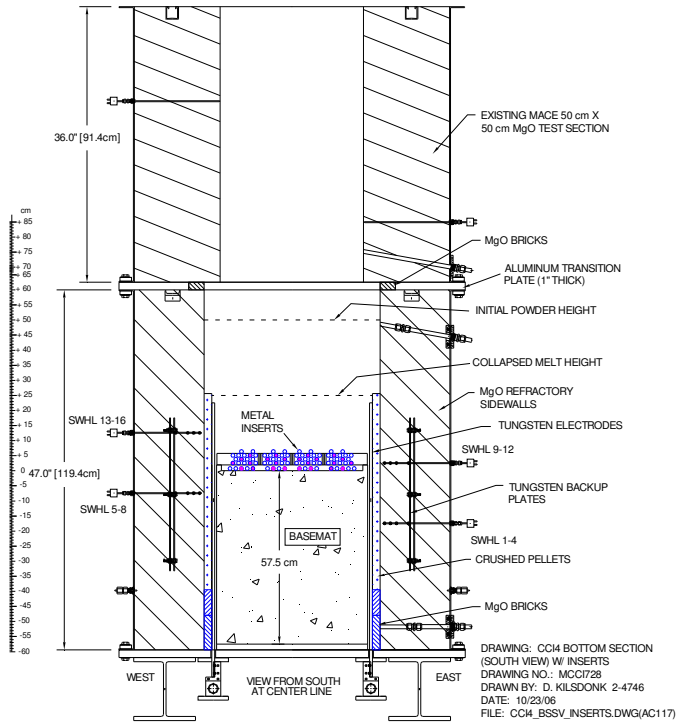

Figure 2-5. Side View of Lower Test Section Showing Inert MgO Sidewall Sections.

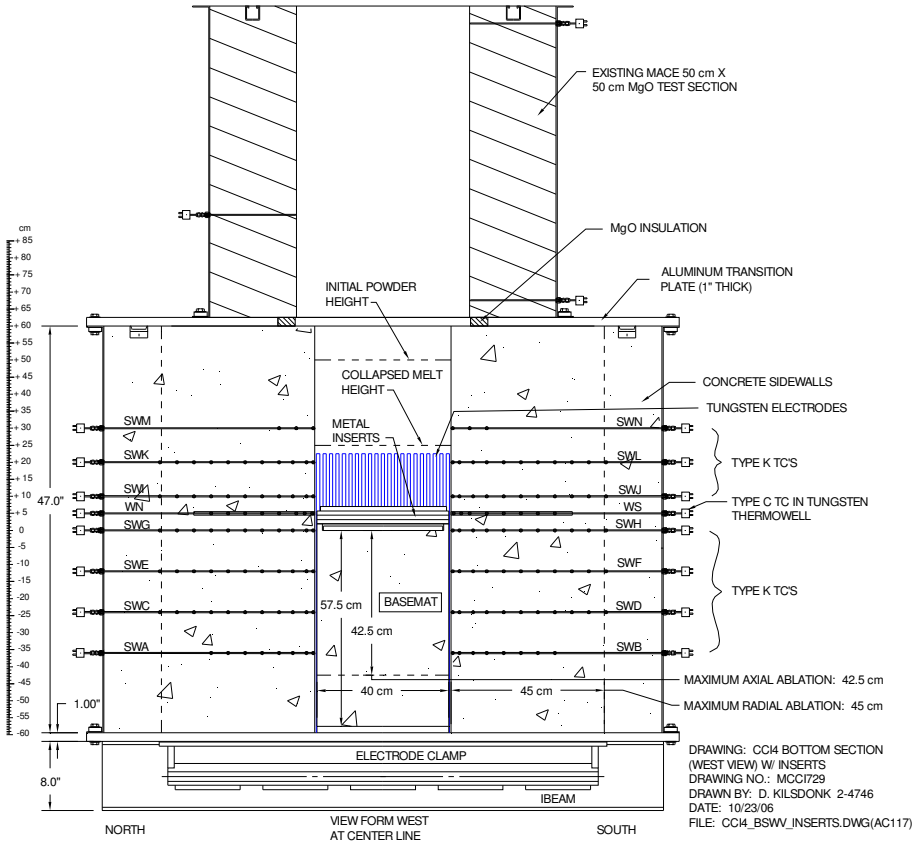

Figure 2-6. Side View of Lower Test Section Showing Concrete Sidewall Sections.

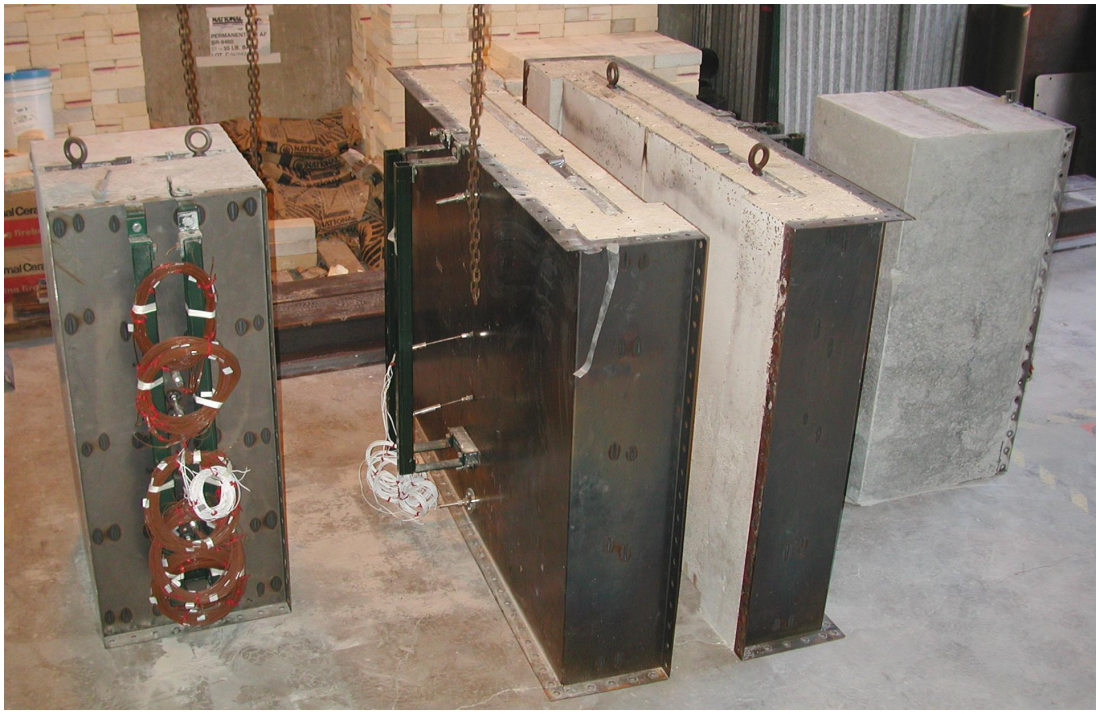

Figure 2-7 Photograph Showing Lower Section Sidewall Components After Fabrication.

Table 2-1. Chemical Composition of Castable MgO.

Element (Oxide Form)	Mass %	
	Element	Oxide
Al (Al_2O_3)	0.24	0.45
B (B_2O_3)	0.12	0.39
Ca (CaO)	0.58	0.81
Fe (Fe_2O_3)	0.14	0.20
Mg (MgO)	58.4	96.8
Mn (MnO)	0.038	0.049
Si (SiO_2)	0.24	0.51
Ti (TiO_2)	0.002	0.003
Zr (ZrO_2)	0.038	0.023
Total		99.24

As shown in Figure 2-4, the electrode sidewalls of the lower section were fabricated from castable MgO[1] refractory, while the non-electrode sidewalls were fabricated from Limestone/Common Sand (LCS) concrete. A photograph showing these components after fabrication is provided in Figure 2-7. The middle sidewall section was fabricated from a high temperature refractory concrete[2], while the upper section and lid were made from locally obtained LCS concrete. The chemical composition of the cast MgO is shown in Table 2-1, while the detailed composition of the LCS concrete basemat and sidewalls is provided later in this section. The concrete and MgO were contained within flanged 11 gauge steel forms that secured

[1]Periclase Permanente 98-AF; from National Refractories and Minerals, Columbiana, OH.
[2]Tufffloor 2500, Matrix Refractories, Columbus, OH.

the lower section to the balance of the existing test section components with an aluminum transition plate. The lower section was fabricated with vertical, flanged casting seams between the MgO and concrete so that the sidewalls could be disassembled to reveal the solidified corium following the test. The MgO sections were intended to be reusable, while the concrete sidewall remnants were disposed of as radioactive waste.

A layer of crushed UO_2 pellets was used to protect the interior surface of the MgO sidewalls against thermo-chemical attack by the corium. In the event that the UO_2 layer did not provide adequate protection, 3.2 mm thick tungsten back-up plates were embedded in these sidewalls as a final barrier to terminate sidewall attack. The plates were instrumented to provide an indication of corium contact with either of these two surfaces during the test. As illustrated in Figure 2-5, multi-junction Type C thermocouple assemblies were also cast within the MgO sidewalls. These thermocouples allowed the time-dependent heat loss from the melt to be estimated from the local temperature gradient and the thermal conductivity of the MgO through standard inverse heat conduction techniques.

Melt pool generation in this test was achieved through an exothermic "thermite" chemical reaction that produced the target initial melt mass over a timescale of ~ 30 seconds. A depiction of the powder loading scheme is provided in Figure 2-8. As is evident from the figure, two iron/alumina sparklers, wrapped with nichrome starter wire, were positioned a few centimeters below the top of the corium charge near the centerline of the test section. One of these sparklers was used to initiate the thermite reaction by heating the neighboring powder to the ignition point. (The thermite composition is described in detail later in this section). The second sparkler was provided as a backup in case the first failed to ignite the material.

After the chemical reaction, DEH was supplied to the melt to simulate decay heat through two banks of tungsten electrodes that lined the interior surfaces of the opposing MgO sidewalls. As illustrated in Figures 2-5 and 2-6, the copper electrode clamps were attached to the 2.5 cm thick aluminum bottom support plate that formed the foundation for the apparatus. A total of sixty three 91 cm long, 0.95 cm diameter tungsten electrodes were attached to each electrode clamp at a pitch of 1.9 cm. A photograph showing the electrodes after a typical installation in the clamps but prior to placement of the lower section sidewalls is provided in Figure 2-9. The clamps were attached with water-cooled buss bars to a 560 kW AC power supply. As shown in Figure 2-4, each electrode bank was vertically restrained by a horizontally mounted, 0.95 cm diameter tungsten rod which was recessed into the concrete sidewalls near the tops of the electrodes. These restraints were provided to prevent slumping of the electrodes away from the sidewalls, as occurred in the MACE Scoping Test. [5]

As illustrated in Figure 2-4, the electrodes spanned a total width of 120 cm on each sidewall of the lower section. At the start of the experiment, the electrical current was drawn through the center 40 cm lateral span of electrodes that were in direct contact with the melt. As the test progressed and the concrete sidewalls eroded, additional electrodes were exposed to the corium. Electrical current was drawn through these newly exposed heating elements, thereby maintaining a uniform heating pattern in the melt over the course of the experiment. Given the overall electrode span of 120 cm, up to 45 cm of radial sidewall ablation could be accommodated in this design while maintaining uniform heat input. As shown in Figure 2-4, the concrete

sidewalls were 61 cm thick, which provided ~ 15 cm of remaining sidewall thickness once the 45 cm radial ablation limit had been reached.

Water was introduced into the test section through weirs located in the upper sidewall section just beneath the lid of the apparatus. The layout for the weirs is shown in Figure 2-10. A total of nine penetrations were cast into the upper lid of the test section. Of these penetrations,

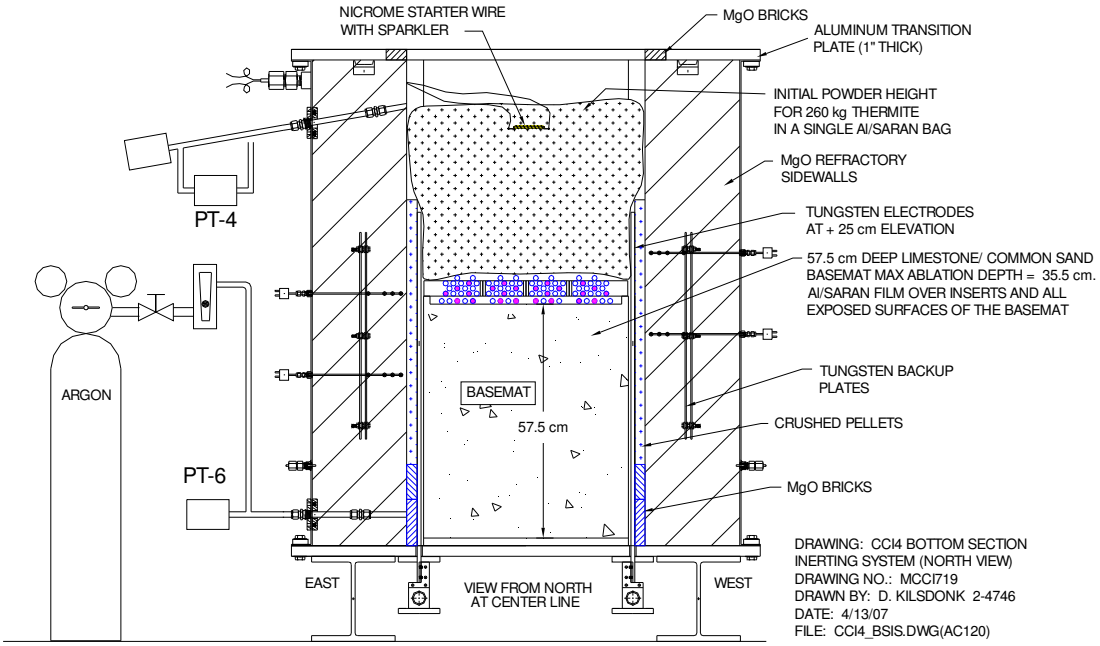

Figure 2-8. Illustration of the CCI-4 Thermite Powder Loading Scheme.

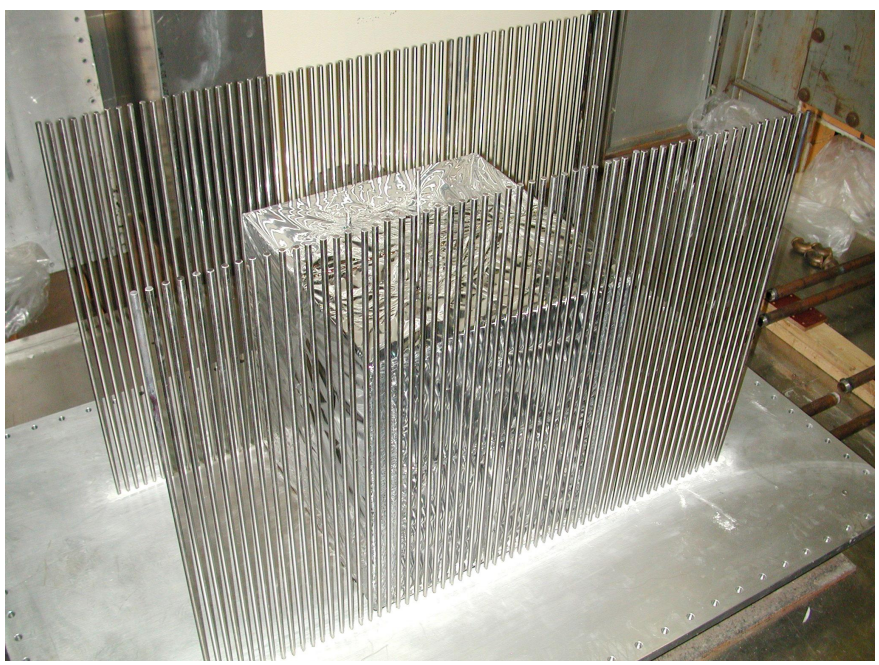

Figure 2-9. Photograph Showing Electrodes Installed in Clamps.

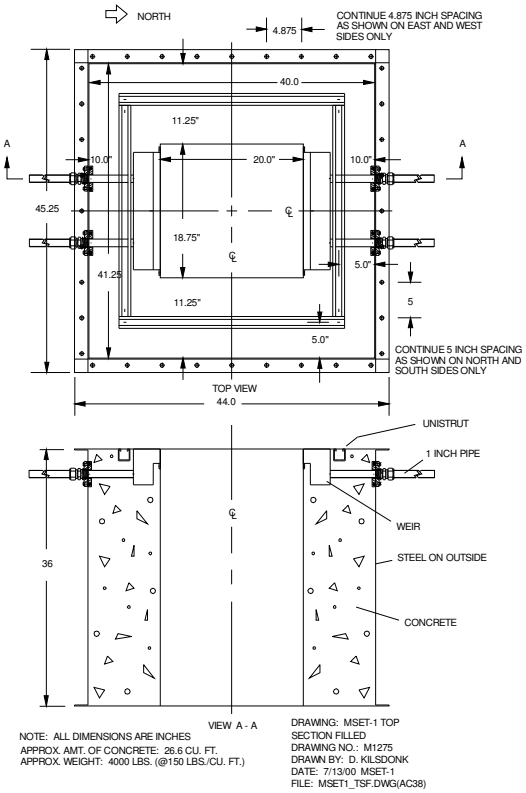

Figure 2-10. Details of the Top Test Section Showing Water Weirs.

six were utilized for Test CCI-4: one stationary lid video camera view port, a port for an insertable water level probe, a 15 cm steam line to the quench system, two light ports, and a port for an insertable crust lance. An illustration of the lid camera installed in the test section is shown in Figure 2-3.

The insertable crust lance was designed to fail the crust formed at the melt/water interface in order to obtain data on the transient crust breach cooling mechanism. An illustration of the lance installed in the test section is shown in Figure 2-11, while details of the lance loading device are provided in Figure 2-12. The lance was made from 2.54 cm diameter, 304 stainless steel rod with a pointed tip. The lance contained an electrical isolation hub so that there was no need to terminate DEH power input during the crust loading procedure. As shown in Figure 2-12, the driving force for the lance was simply a 450 kg dead weight that was remotely lowered with the crane during the test. The lance assembly was equipped with a load cell and displacement transducer to record load vs. position data as the force was applied to the crust.

The test section components were bolted together on the stationary half of the existing ZPR-9 reactor bed. Zirconia felt and silicon gasket material were used to seal the flanges. An illustration is provided in Figure 2-13. Installation and torquing of test section flange bolts was performed according to an approved procedure to ensure uniform preload on the flange surfaces. Additional reinforcement of each test section component was provided by clamping bars installed in both the North-South and East-West directions. A diagram illustrating the complete flange bolt and clamping bar layout is provided in Figure 2-14.

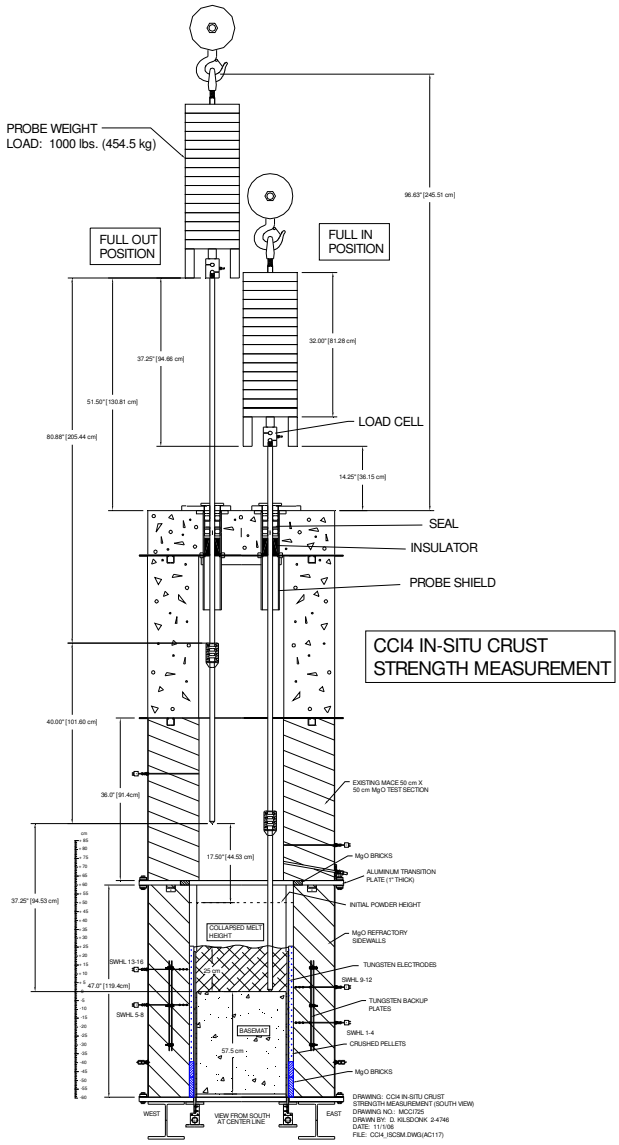

Figure 2-11. Illustration of CCI-4 Crust Lance Assembly Installed in Test Section.

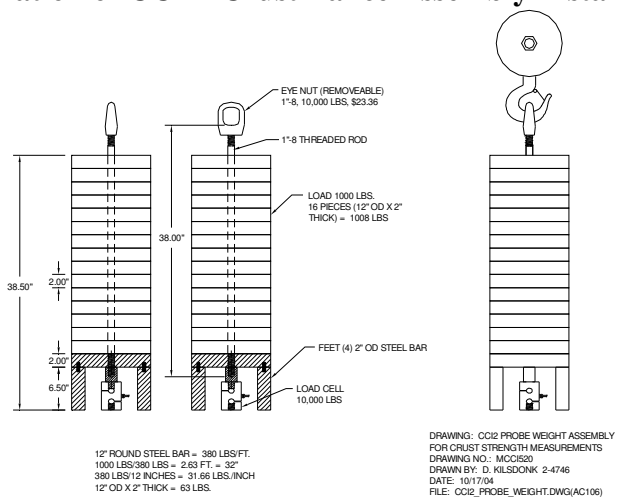

Figure 2-12. Details of Crust Lance Loading Device.

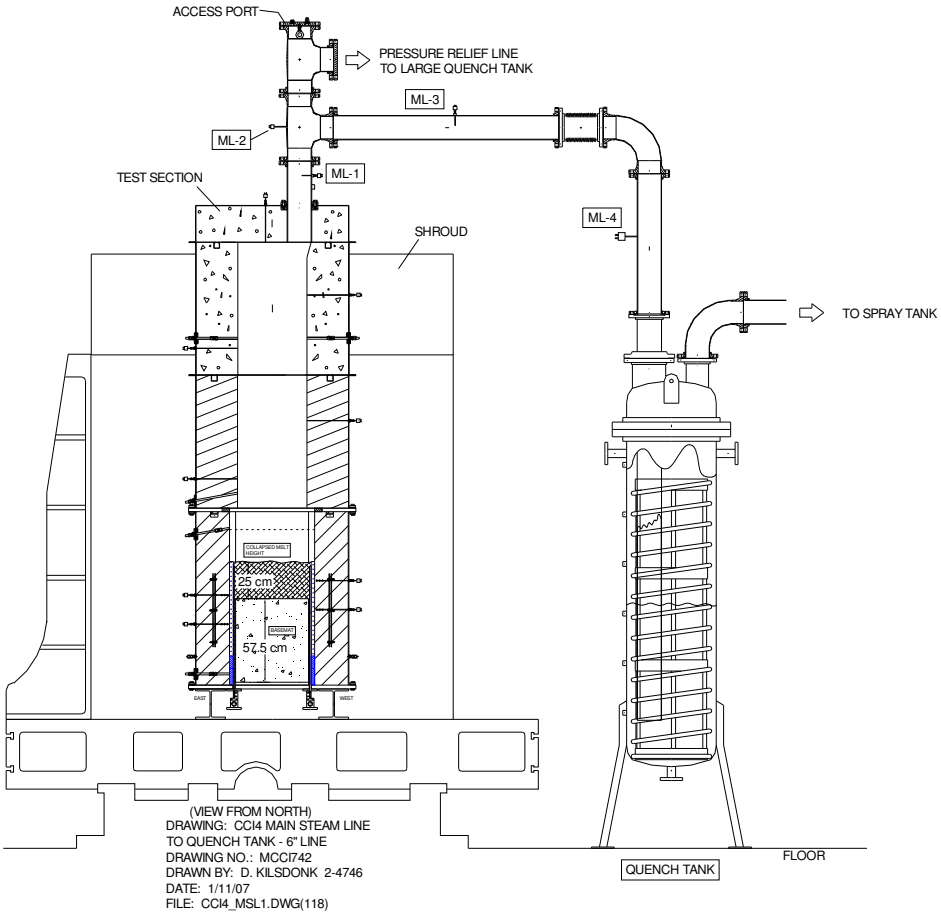

Figure 2-13. Illustration of CCI-4 Test Section Mounted on ZPR-9 Reactor Bed.

2.2 Water Supply System

The water supply system consisted of a 1900 l capacity tank connected to the flooding weirs in the north and south sidewalls of the top test section through a valve-controlled supply line that provided water to the test section at a specified flow rate. A schematic illustration of the supply system is provided in Figure 2-15; details of the flooding weirs are shown in Figure 2-10. The supply system flowmeter, pressure transducer, level sensor, and thermocouple instrumentation locations are also shown in Figure 2-15. Water flow through the system was driven by an 80 kPa differential pressure in the supply tank at a nominal flow rate of 120 lpm (2 l/s). The inlet water flow rate of 120 lpm corresponds to a melt/water heat flux in excess of 20 MW/m^2 based on a specific enthalpy of 2.6 MJ/kg for saturated steam at atmospheric pressure, assuming heat transfer occurs through boiling of the overlying coolant. The inlet water flow rate to the test section was monitored with a paddlewheel flowmeter. Both the initial water inventory (125 l) and makeup were provided through pneumatic ball valve RV-1, which was opened as needed at the control console to maintain the water volume inside the test section constant at 125 ± 13 l (50 ± 5 cm). A redundant supply line, activated by pneumatic ball valve RV-2, was provided in case RV-1 failed to open during the test. A third pneumatic valve, RV-3, was provided in case RV-1 or RV-2 failed in the open position. The test was initiated with valve RV-3 in the open position.

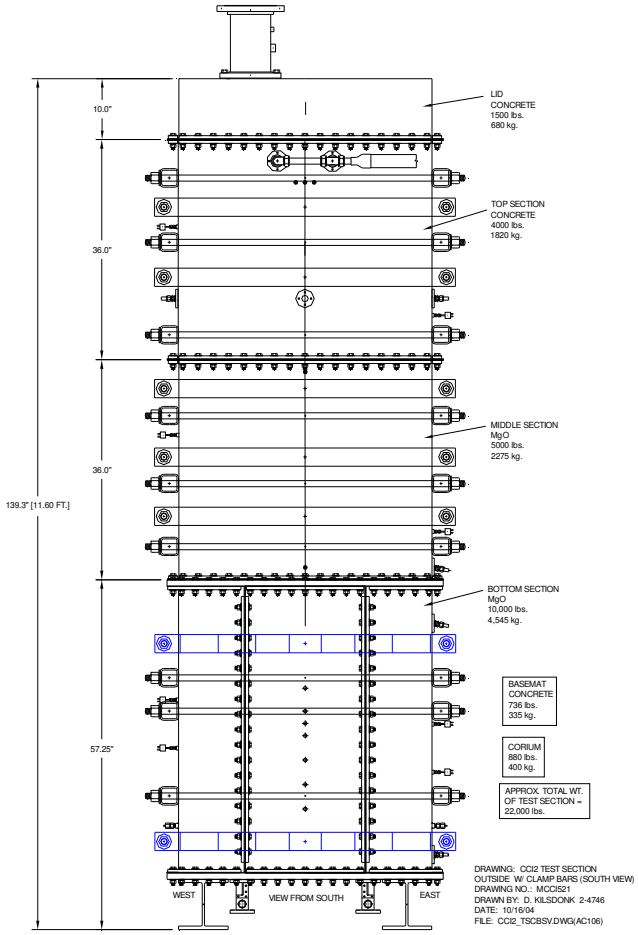

Figure 2-14. Illustration of Test Section Clamping Bars.

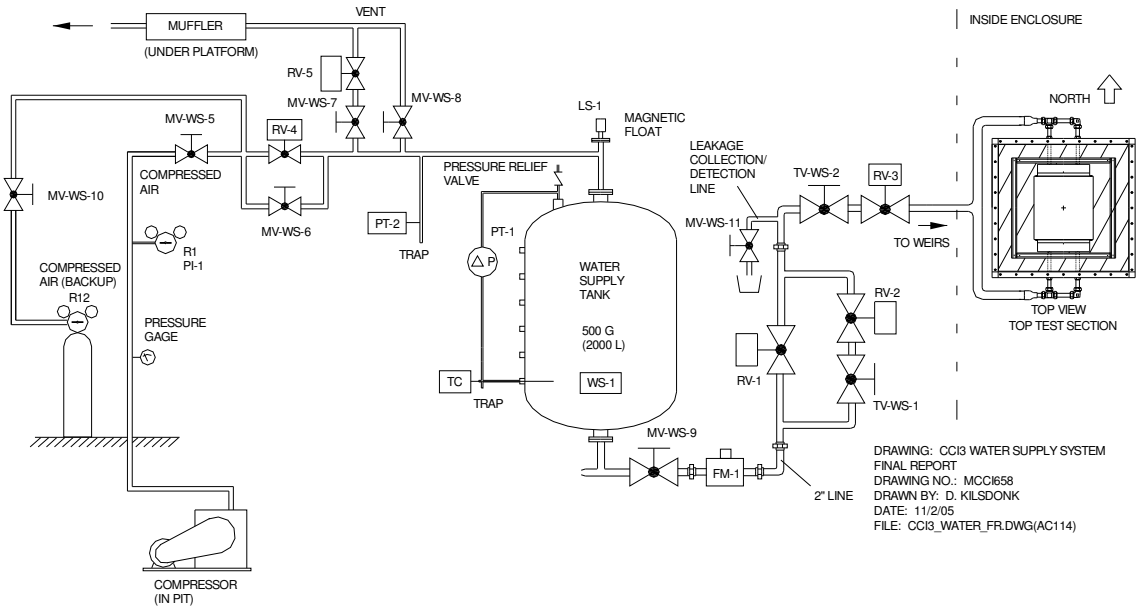

Figure 2-15. Test Section Water Supply System.

Note from Figure 2-15 that the supply line to the test section contains a manual bypass valve downstream of water injection valves RV-1 and RV-2. This valve was vented to a catch pan equipped with an alarmed water detector. During pretest procedures, this valve was left in the open position to divert any water leakage away from the test section. The alarm was intended to notify personnel that a leak was present so that corrective action could be taken. This valve was closed as one of the final steps of pretest operations just prior to evacuation of the cell.

2.3 Quench System

The quench system, shown in Figures 2-16 and 2-17, consisted of a primary quench tank, a secondary spray tank, and a condensate overflow tank. The quench system flowmeter, pressure transducer, level sensor, and thermocouple instrumentation locations are also shown in these two figures. Steam and concrete decomposition gases passed from the test section through a 16.1 cm ID stainless steel pipe into the 680 l capacity, 60 cm ID primary quench tank. This tank contained an initial water inventory of 250 l. With this amount of water, a pool void fraction of ~ 60% could initially be accommodated before the voided water height reached the top of the tank. The quench tank was equipped with a 1.9 cm diameter cooling coil to remove heat from steam condensation, thereby maintaining a subcooled state. The water supply to the cooling coil was drawn from the building supply system. The coil water flow rate was throttled to ~ 30 lpm, which corresponds to a heat removal rate of 170 kW assuming a heat capacity of 4200 J/kg•K for water and a temperature rise of 80 °C across the coil. Should the condensate level in the quench tank rise to a level of 560 l, spillover into the adjacent 930 l overflow tank would occur through a 2.5 cm ID pipe. The quench tank and interconnecting piping between the test section and quench tank were insulated to minimize heat losses.

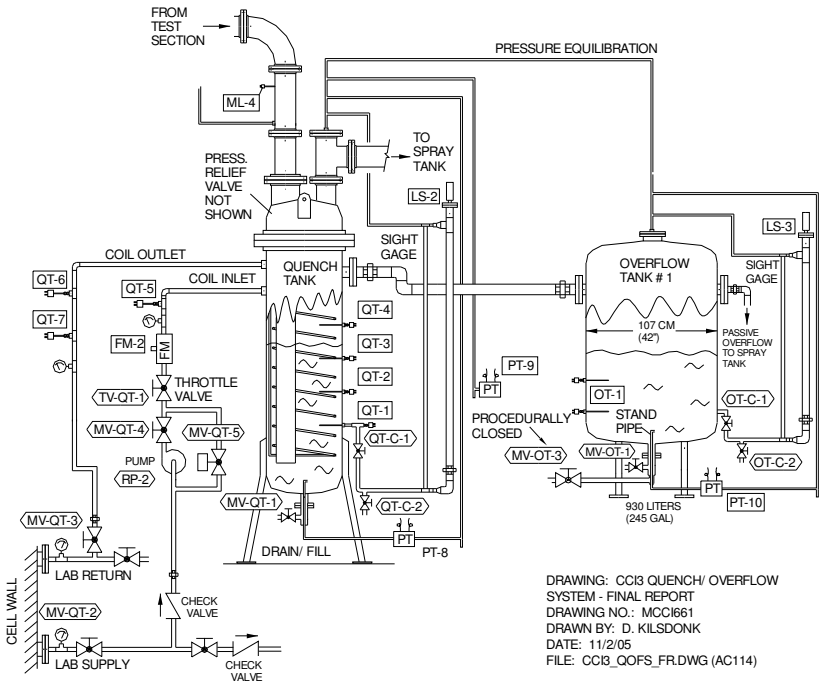

Figure 2-16. CCI-4 Quench and Overflow Tanks.

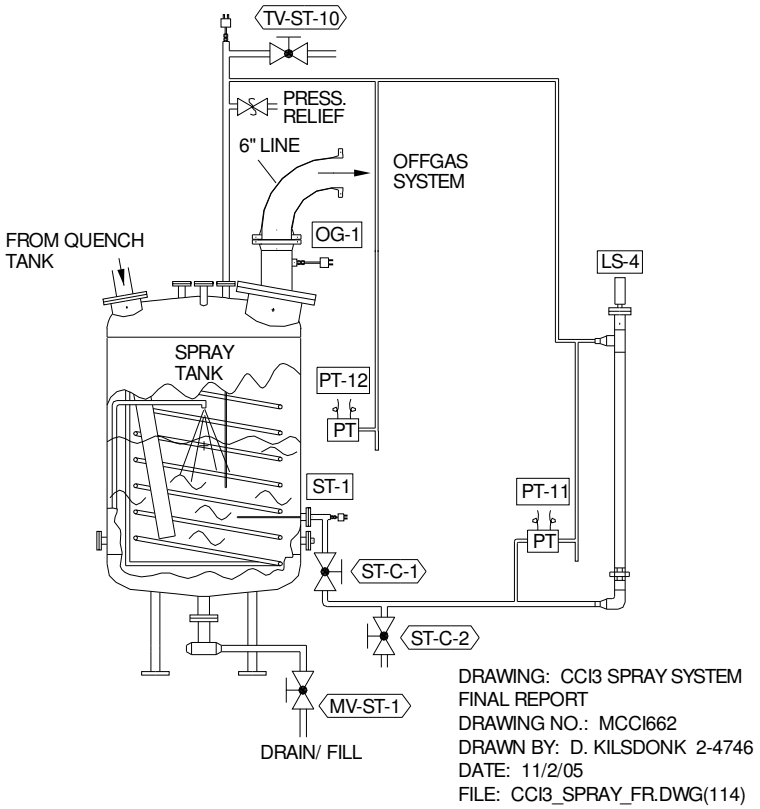

Figure 2-17. CCI-4 Spray Tank System.

The secondary 1230 l capacity spray tank was connected to the quench tank by a 16.1 cm ID stainless steel pipe. In the event that the steam generation rate overwhelmed the primary quench tank, the secondary spray tank served to condense the remaining steam. This tank contained an initial water inventory of 375 l. With this amount of water, a pool void fraction in excess of 60% could be accommodated before the voided water height reached the top of the tank. The spray tank and interconnecting piping between the spray and quench tanks was also insulated to minimize heat losses.

2.4 Test Section Pressure Relief System

A pressure relief system was provided to prevent over-pressurization and possible failure of the test section. A schematic illustration of the system is shown in Figure 2-18. The system consisted of a 16.1 cm vent line from the test section to an auxiliary tank containing a nominal initial water inventory of 400 l. The auxiliary tank had an inside diameter of 1.22 m and a capacity of 4100 l. The tank was open to the atmosphere. The pressure relief line to the tank was equipped with a passive, counter-weighted check valve set to open at a differential pressure of nominally 68 kPa. A rupture diaphragm (68 ± 13.4 kPa differential failure pressure) upstream from the check valve prevented any flow through the line unless the pressure in the test section exceeded the design value of 68 kPa differential. As shown in Figure 2-18, the relief line was also equipped with a 7.5 cm vacuum breaker valve. This valve was provided to prevent water hammer from occurring due to stream condensation should the pressure relief valve open and then reseat after water had been introduced into the test section.

The initial 400 1water inventory in the auxiliary tank was provided to cool gases from the test section and to remove aerosols before any noncondensables present in the gas stream passed into the cell atmosphere. The tank was instrumented with a Type K thermocouple to measure water temperature and a differential pressure transducer to measure water depth. The instrumentation locations are shown in Figure 2-18. Water depth and temperature instruments were provided so that the steam condensation rate could be determined should the pressure relief valve open during the test. In this manner, there would be no loss of data should the pressure relief system activate.

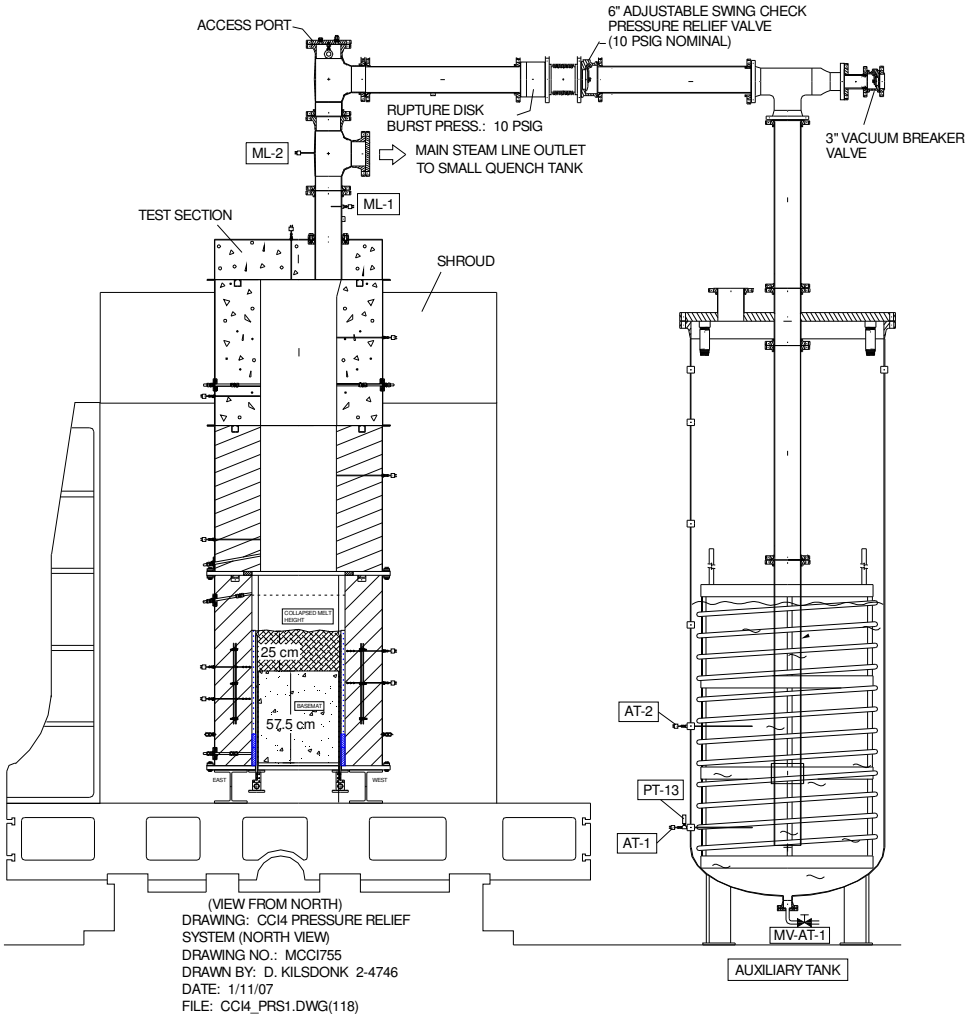

Figure 2-18. CCI-4 Test Section Pressure Relief System.

2.5 Off Gas System

An illustration of the off gas system is provided in Figure 2-19. Thermocouple and flowmeter instrumentation locations are also shown in this figure. This system filtered and vented the noncondensable concrete decomposition gases to the cell exhaust. The decomposition gases (H_2, CO, CO_2 and the cover gas) exited the spray tank and passed through a flow separator. The cleanup efficiency of the separator was 99% of all entrained solid and liquid when the particle size exceeded 10 microns. After passing through the flow separator, the flow could

potentially split into two parallel off gas system lines. One line was constructed from 7.5 cm piping, while the second was made from 10.0 cm piping. The system was designed with the capacity to accommodate large-scale (up to 120 cm x 120 cm) tests. Since CCI-4 used a reduced scale 50 cm x 40 cm test section, the 7.5 cm side of the parallel off gas system was taken out of service using a blank-off plate at the branch point in the system (see Figure 2-19). As a result, all gas flow was diverted through the 10 cm side of the off gas system. Reduction in available flow area was required to achieve a resolvable gas flow rate through the large capacity flowmeter at the end of the off gas system train (the flow meter in the 10 cm line had a capacity of 5,400 sl/min). The final filters in the system (4 individual filters per filter housing, yielding a total of 8 filters for each side of the off gas system) removed any remaining particulate before venting the off gases through the flowmeter to the cell atmosphere. The filters on the side of the off gas system used for CCI-4 (10 cm) were equipped with a passive counter-weighted check valve set to open at a nominal differential pressure of 7 kPa. The bypass valve was provided in the event that the filters become plugged during the experiment.

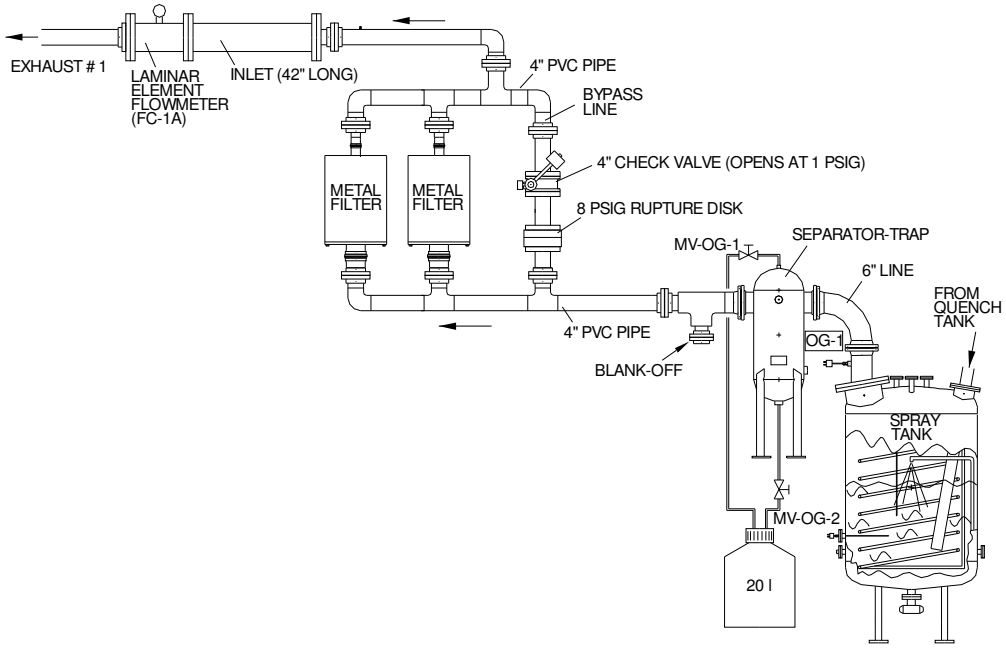

Figure 2-19. CCI-4 Off Gas System.

2.6 Cover Gas System

During the test a uniform flow rate of helium was fed into the test section to suppress burning of combustible concrete decomposition gases (H_2 and CO) and protect test section internals. An illustration of the cover gas system is shown in Figure 2-20. Cover gas flow was modulated by a total of three Hastings Flow Controllers (FC's). One 0-200 slpm FC provided cover gas to the lid camera and light port penetrations, while a second 0-350 slpm FC provided dedicated cover gas flow to the lid camera to prevent aerosol deposition on the camera quartz window through which the melt upper surface was viewed. A third 0-100 slpm FC was used to inert the apparatus on the evening before the test.

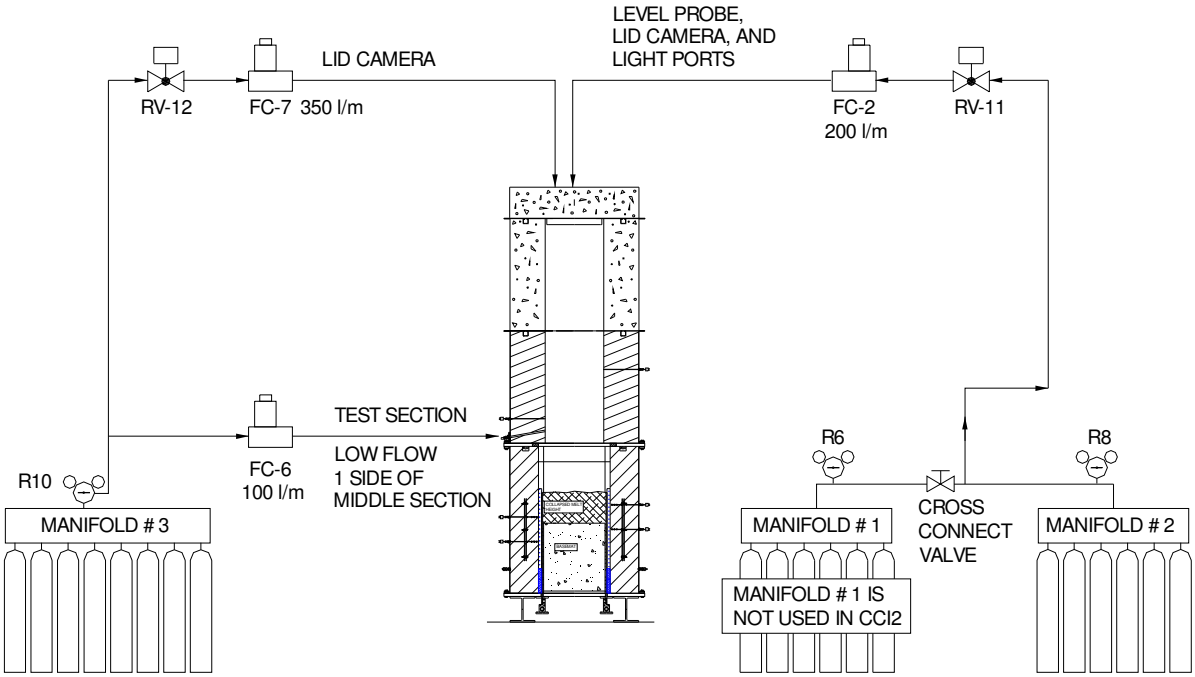

Figure 2-20. CCI-4 Cover Gas System.

2.7 Power Supply

The power for Direct Electrical Heating (DEH) of the corium was provided by a 0.56 MW single phase AC power supply made by NWL Transformers. Output of the power supply was voltage or current controlled. The supply had four voltage/current ranges: 56.4 V/10 kA, 113 V/5 kA, 169 V/3.3 kA, and 226 V/2.5 kA. The power supply was connected to the two arrays of tungsten electrodes in the test section through water cooled copper pipes that passed through a wall of the former reactor fuel loading compartment. The calculated total voltage drop through the water cooled copper pipes and tungsten electrodes at operational temperature and maximum current was less than 0.5 V. The leakage current through the overlying water pool during test operation has been estimated to be less than 1% of the total current.

2.8 Concrete Sidewalls and Basemat

As shown in Table 1-1, the composition of the CCI-4 concrete basemat and sidewalls was specified to be of the Limestone/Common Sand (LCS) type. The engineering composition of the CCI-4 LCS concrete is shown in Table 2-2. Sand and aggregate for the mix were obtained from Meyer Materials (McHenry, IL, U.S.A.). The chemical composition of this concrete is shown in Table 2-3. This composition was determined[3] based on chemical analysis of the archive sample that was produced when the components for this test were poured.

To prevent downward migration and possible escape of concrete decomposition gases during the course of the experiment, the electrode penetrations through the bottom support plate were sealed using O-rings. As described in the next section, the test section was leak checked at

[3]Chemical analysis carried out by the Construction Technologies Laboratories (CTL Group) in Skokie, Illinois.

83 kPa differential pressure as part of pretest operations, and found to have a very low leak rate. On this basis, essentially all concrete decomposition gases migrated upwards through the melt pool during the experiment, as opposed to partial loss through the bottom support plate of the apparatus. Reinforcing rod was eliminated so that it did not mask or delay the attainment of a fully oxidized melt. To prevent thermal shock of the concrete basemat and sidewalls during the initial exothermic chemical reaction, the concrete surfaces were protected by a layer of 3 mm thick ZrO_2 felt insulation (density ~480 kg/m^3; thermal conductivity ~0.14 W/m•K at 1170 °C). After the exothermic reaction was complete, the felt dissolved into the melt.

The density of the LCS concrete was ~2404 kg/m^3, which was calculated on the basis of the measured mass and volume of the CCI-4 concrete archive sample. Instrumentation locations within the concrete sidewalls and basemat are described later in this section.

Table 2-2. Engineering Composition of CCI-4 LCS Concrete Basemat and Sidewalls.

Constituent	wt %
Coarse Aggregate	44.8
Common Sand	32.4
Fly Ash	2.7
Type 1 Cement	14.1
Tap Water[a]	6.0

[a]Contains 1.4 ml/l Airalon 20 Air Entraining Agent (AEA).

Table 2-3. Composition of CCI-4 Concrete.

Oxide	Wt%
SiO_2	25.99
Al_2O_3	2.78
Fe_2O_3	1.40
CaO	27.81
MgO	9.21
SO_3	0.91
Na_2O	0.39
K_20	0.54
TiO_2	0.17
P_2O_5	0.09
Mn_2O_3	0.04
SrO	0.02
CO_2	23.80
H_2O, Free	3.58
H_2O, Bound	3.42
Total	100.15

2.9 Corium Composition and Concrete-Metal Inserts

As discussed earlier, one of the key objectives of this test was to increase the metal content of the melt to the highest practical level to more accurately mock up a prototypic BWR core melt at the time of vessel failure. The target value for the initial metal content was 15 wt % [3]. The overall approach for satisfying this requirement was to place a metal-bearing concrete insert that overlaid the basemat for dissolution into the melt prior to onset of basemat ablation, thereby increasing the melt metal content to the target level. This technique was originally developed as part of the Advanced Containment Experiment Molten Core Concrete Interaction (ACE/MCCI) test series [4] that focused on quantifying fission product source term during core-concrete interaction. The metal content of the inserts, shown in cross-sectional view over the basemat in Figure 2-21, included Zr that represented unoxidized cladding plus iron that, when combined with the Cr metal reaction byproduct from the thermite reaction, produced a mixture that mocked up stainless steel from ablated vessel structures. A photograph showing the inserts in place over the CCI-4 basemat is provided in Figure 2-22.

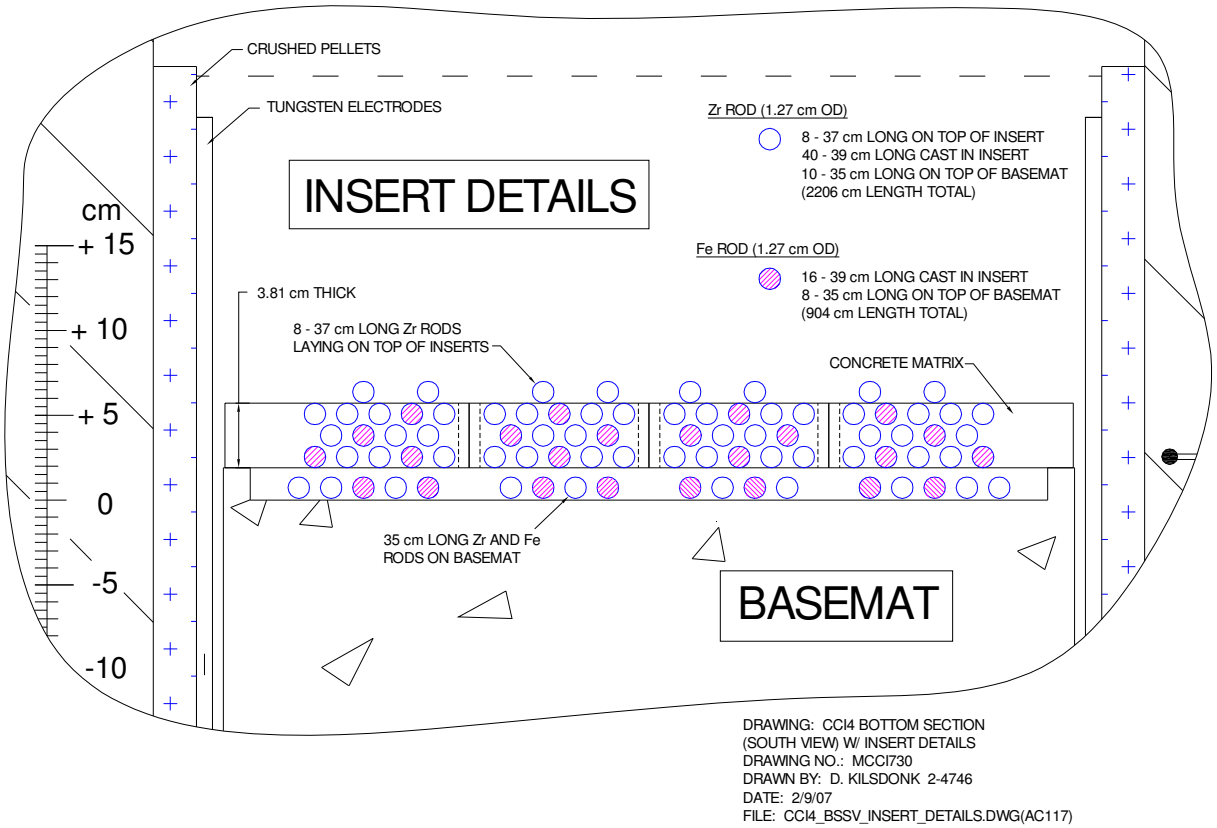

Figure 2-21. Illustration of Concrete-Metal Inserts over the Concrete Basemat.

As part of the test development, it was necessary to design and test a new thermite that, after complete oxidation of metallic cladding, yielded a melt composition with a fuel-to-cladding ratio of ~ 1 (molar basis) that is typical of many BWRs. Initially, a thermite was designed and

tested that included both Fe_2O_3 and CrO_3 as oxidizers, so that a stainless steel-like metal byproduct was produced during the reaction that also added to the melt metal content. However, during mixing of the 1 kg sample for this test, the powders noticeably warmed, which is an indication of thermal instability. On this basis, a second thermite was designed and tested that only used CrO_3 as the oxidizer, since this type of mixture is known to be thermally stable. With this approach, the Fe needed to obtain the stainless steel surrogate in the melt was placed in the inserts along with the Zr metal. Details regarding the thermite developmental tests are provided elsewhere. [6]

Figure 2-22. CCI-4 Basemat with Insert Prior to Placement on Test Stand.

As shown in Table 1-1, the corium composition for CCI-4 was specified to be a 78 % oxidized BWR core melt containing 7.7 wt % stainless steel constituents and ~10.0 wt % limestone/common sand concrete. This was the best estimate melt composition after erosion of the concrete/metal inserts and at the start of basemat ablation, which defines time t = 0 for the experiment (see Section 3). The composition estimate includes additional cladding (both Zr and ZrO_2 from oxidation reactions that occurred during insert erosion), concrete slag, and steel constituents from the inserts. The thermite reaction that produced the initial melt composition over the inserts was of the form:

$$1.22U_3O_8 + 2.80Zr + 0.46Si + 0.46SiO_2 + 0.46Mg + 0.91\ CaO + 0.13Al + 1.58CrO_3 \rightarrow$$
$$3.66UO_2 + 2.80ZrO_2 + 0.92SiO_2 + 0.46MgO + 0.91CaO + 0.065Al_2O_3 + 1.58Cr;$$
$$Q = -192.8\ kJ/mole\ (1.64\ MJ/kg);$$
$$T_{adiabatic} = 2422\ ^\circ C$$
$$T_{actual} \sim 2200\ ^\circ C$$

The bulk composition of the melt produced from this reaction is summarized in Table 2-4, while the detailed pre- and post-reaction compositions are provided in Table 2-5. The reaction temperature of this thermite was measured as ~ 2200 ˚C during developmental tests [6].

Table 2-4. Bulk Composition of CCI-4 Melt at Start of Interaction with Inserts.

Constituent	Wt%
UO_2	63.91
ZrO_2	22.27
Calcined concrete[a]	8.51
Chromium metal	5.31
Total	100.00

[a]Calcined LCS concrete: 42.0/14.1/38.8/5.1 wt% SiO_2/MgO/CaO/Al_2O_3

Table 2-5. Detailed Pre- and Post-Reaction Thermite Compositions for CCI-4.

Constituent	Reactant		Product	
	Wt %	Mass (kg)	Wt %	Mass (kg)
U_3O_8	66.44	176.07	-	-
UO_2	-	-	63.91	169.36
Zr	16.48	43.67	-	
ZrO_2	-	-	22.27	59.02
Si	0.84	2.23	-	
SiO_2	1.79	4.74	3.58	9.48
Al	0.23	0.61	-	
Al_2O_3	-		0.43	1.14
Mg	0.72	1.91	-	
MgO	-	-	1.20	3.18
CaO	3.30	8.74	3.30	8.74
CrO_3	10.20	27.03	-	
Cr	-		5.31	14.08
Total	100.00	265.00	100.00	265.00

As noted earlier, the inserts contained all the Zr and Fe in the corium inventory. As shown in Figure 2-21, they were supported on a lip around the upper surface of the basemat. The composition of the inserts, which were 3.8 cm thick and weighed 36.58 kg, is shown in Table 2-6. The metals were in the form of 1.27 cm diameter rods that were cast into a concrete matrix. The rods ran parallel to the tungsten electrode banks so that an electrical shorting path between the electrode banks was not created. The Zr and Fe rods were intermixed to distribute the metals uniformly across the basemat.

The estimated bulk melt composition after erosion of the inserts and at the start of basemat ablation is shown in Table 2-7, while the detailed composition is provided in Table 2-8. These estimates include the expected oxidation of Zr with H_2O and CO_2 gases that were liberated upon decomposition of the concrete in the inserts (see Section 2.8 for concrete composition). In particular, of the 17.88 kg of Zr rod, 4.06 kg was estimated to be oxidized to ZrO_2, while the balance (13.82 kg) entered the melt in metallic form. As shown in Table 2-7, the corium metal content at the start of basemat ablation was 12.3 wt %, of which 4.6 wt% was unoxidized cladding, and 7.7 wt % was in the form of steel constituents. This metal content can be compared with the 15 wt % target level requested by the MB [3].

Table 2-6. Composition of CCI-4 Concrete/Metal Inserts.

Constituent	Wt%	Mass (kg)
Zr rod	48.88	17.88
Fe rod	24.52	8.97
Limestone/common sand concrete	26.60	9.73
Total	100.00	36.58

Table 2-7. Bulk Melt Composition at Start of Basemat Ablation.

Constituent	Wt%
UO_2	56.52
ZrO_2	21.53
Calcined concrete	9.65
Stainless steel components [a]	7.69
Unoxidized cladding	4.61
Total	100.00

[a]61.1/38.9 wt % Cr/Fe

Table 2-8. Detailed Melt Composition at the Start of Basemat Ablation.

Constituent	Wt %	Mass (kg)
UO_2	56.52	169.36
ZrO_2	21.53	64.51
SiO_2	4.05	12.15
Al_2O_3	0.49	1.47
MgO	1.36	4.08
CaO	3.75	11.23
Zr	4.61	13.82
Cr	4.70	14.08
Fe	2.99	8.97
Total	100.00	299.67

2.10 Instrumentation and Data Acquisition

The CCI-4 facility was instrumented to monitor and guide experiment operation and to log data for subsequent evaluation. Principal parameters that were monitored during the course

of the test included the power supply voltage, current, and gross input power to the melt; melt temperature and temperatures within the concrete basemat and sidewalls; crust lance position and applied load; supply water flow rate; water volume and temperature within the test apparatus, and water volume and temperature within the quench system tanks. Other key data recorded by the DAS included temperatures within test section structural sidewalls, off gas temperature and flow rate, and pressures at various locations within the system.

All data acquisition and process control tasks were managed by a PC executing LabVIEW 6.i under Windows XP. Sensor output terminals were connected inside the test cell to model HP E1345A 16-channel multiplexers that were integrated into a mainframe chassis in groups of eight. An illustration of the DAS setup is provided in Figure 2-23. The multiplexers directed signals to an HP E1326B 5 ½ digit multimeter incorporated into each chassis. Three independent 128 channel systems were used for a total capacity of 384 channels. The detailed channel assignment lists for each of the three systems are provided in Appendix A.

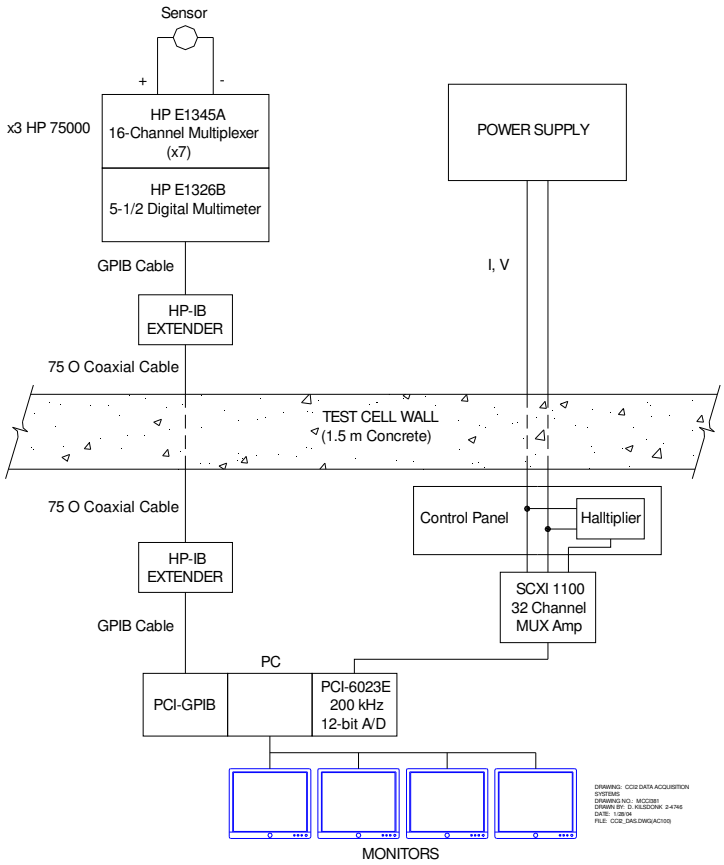

Figure 2-23. Data Acquisition System Setup for CCI-4.

Signal noise was reduced by the digitizer through integration over a single power line cycle (16.7 ms). The digitized sensor readings were routed from the test cell to the PC in the control room via two HP-IB extenders. The extenders allowed the ASCII data from the HP to be sent through the cell wall over a BNC cable. The extender within the control room then communicated with a GPIB card within the PC. This configuration also permitted remote control of the multimeter through LabVIEW.

Integration of the signal over the period of a power line cycle limited the speed with which the multiplexer could scan the channel list. The minimum time for the digitizer to scan the list was ~1.7 s (16.7 ms • 100 channels/chassis for this test). Though the three systems operate independently, implying the ability to update all 300 channels in roughly two seconds, the actual time required for the update was about 5.5 s.

Instrumentation was selected to provide the necessary measurements to determine the time-dependent 2-D concrete ablation profile and the melt temperature distribution. Detailed plan and elevation views of the basemat thermocouple layout are provided in Figures 2-24 and 2-25, respectively, while the concrete sidewall instrumentation locations are shown in Figure 2-26. The thermocouple elevations shown in these figures are all taken with respect to the original height of the basemat surface (Z = 0). Both the concrete sidewalls and basemat were instrumented with multi-junction Type K thermocouple assemblies to determine the 2-D ablation profile as a function of time. In addition, Type C thermocouple assemblies in 9.5 mm diameter long-body tungsten thermowells protruded upwards from the basemat and radially inwards from the concrete sidewalls in several locations. The purpose of these instruments was to provide data on the axial and radial melt temperature distribution as a function of time. Note that the thermocouple junction locations were repositioned to provide melt temperature and ablation front location data over the increased range of lateral and axial concrete ablation that was designed into this experiment. A total of five four-junction (basemat) and two eight-junction (sidewalls) Type C arrays (36 junctions total) in tungsten thermowells were used in the test. A photograph showing the thermocouple assemblies installed in a typical basemat form prior to placement of the concrete is provided in Figure 2-27.

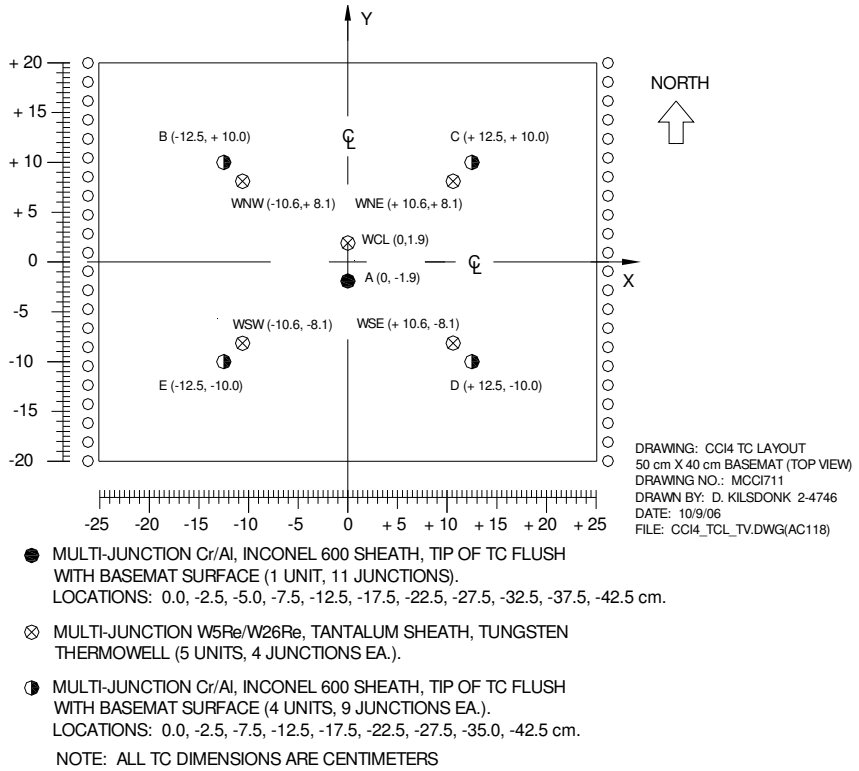

Figure 2-24. Plan View of Basemat Instrumentation Layout (dimensions are in cm).

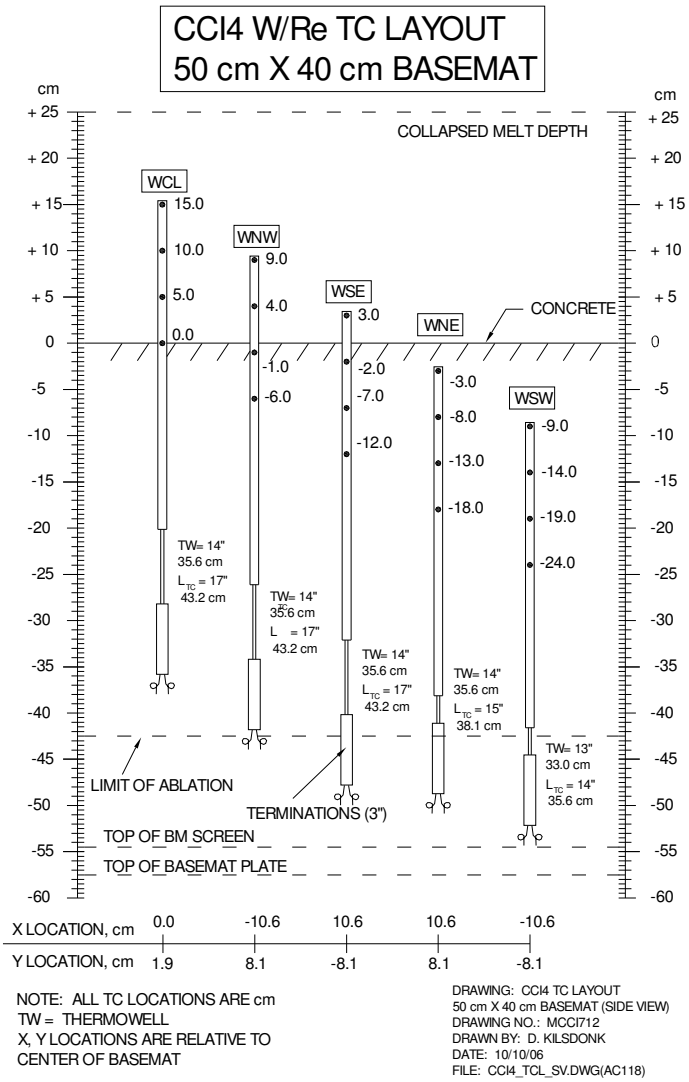

Figure 2-25. Elevation View of Basemat Type C Thermocouple Locations.

The test section sidewalls and upper lid were also instrumented with a total of 32 Type K and Type C thermocouples to measure the sidewall heat up prior to water addition, and also to measure the sidewall cooling rate above the melt surface after water was added. Illustrations of the TC locations in the sidewalls of the test section are provided in Figure 2-26 and 2-28.

One method for monitoring water level in the test section was provided by a differential level probe which was inserted through a sealed penetration in the lid. The probe was maintained in a retracted position during the initial heat up phase until water was added to the test section. After water addition, the probe was inserted to a distance of 50 cm from the initial basemat surface (25 cm from the initial collapsed melt surface). The probe tip was instrumented with two 1.6 mm diameter ungrounded junction Type K TC's which monitored the plenum gas temperature prior to water addition; thereafter, the TC's monitored the water temperature over the melt surface. The probe tip locations after insertion are shown in Figure 2-29.

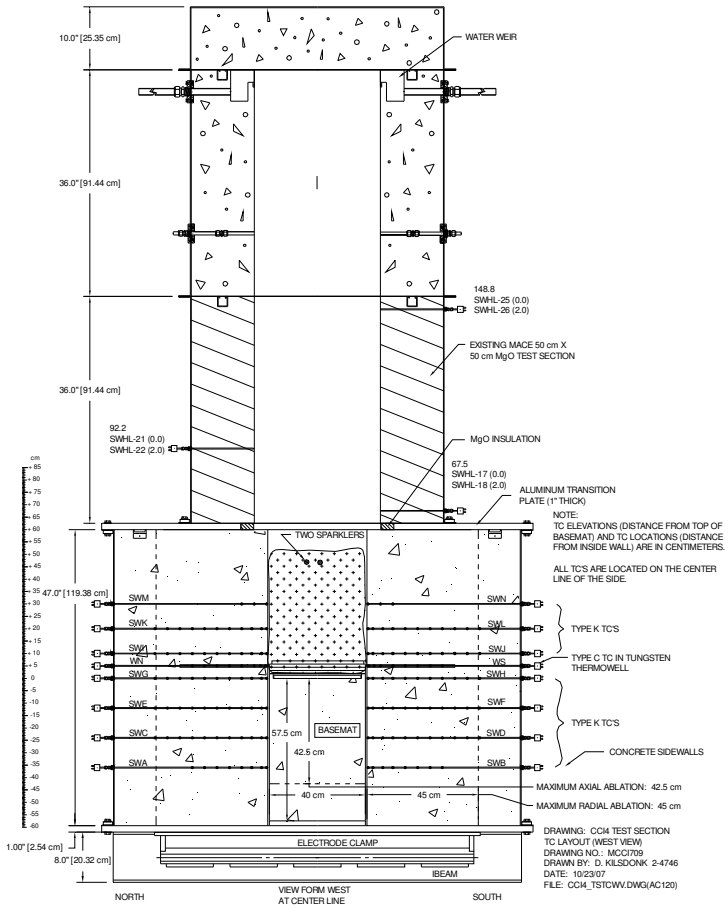

Figure 2-26. CCI-4 Test Section Sidewall Instrumentation (View from West).

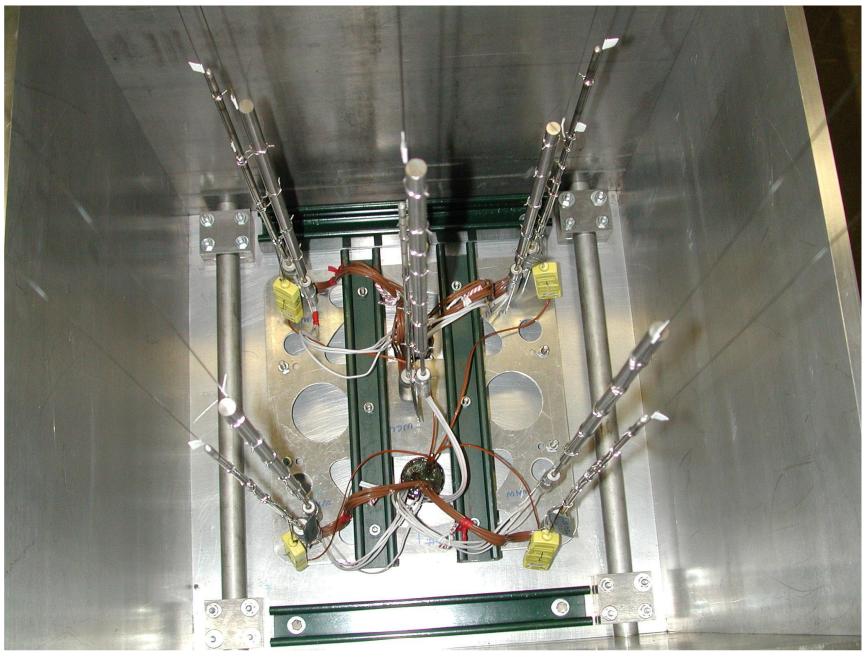

Figure 2-27. Thermocouple Arrays Installed in Basemat Concrete Form.

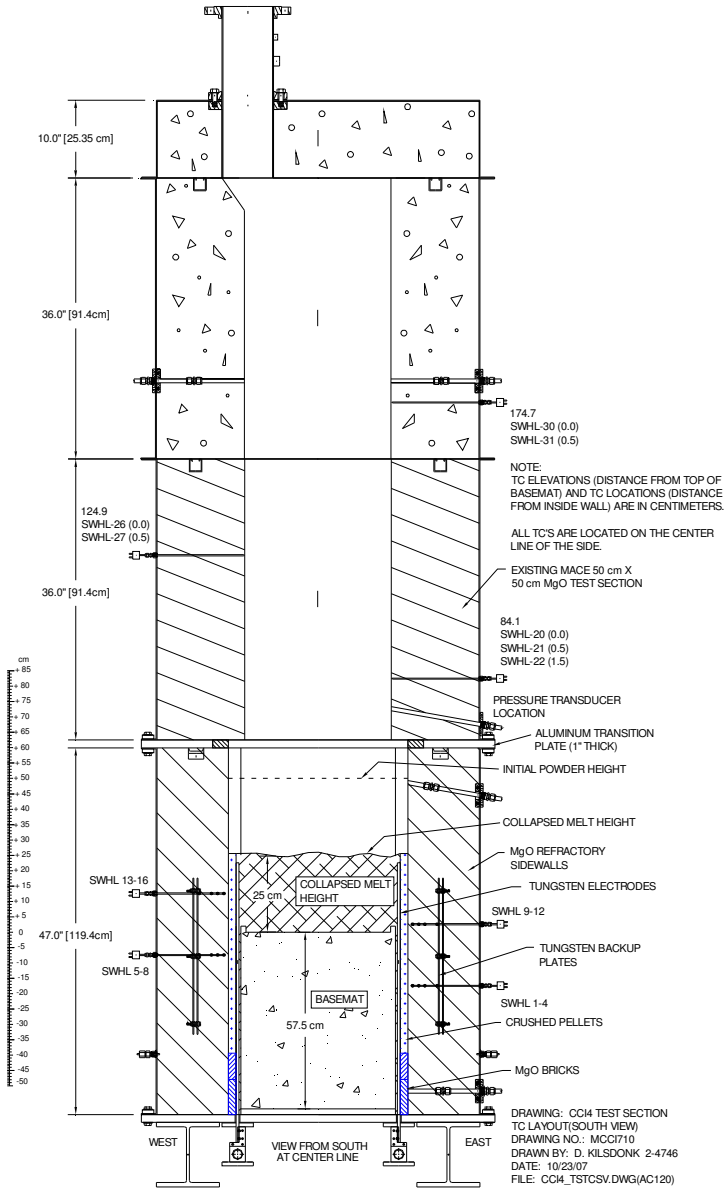

Figure 2-28. CCI-4 Test Section Sidewall Instrumentation (View From South).

Aside from the insertable water level probe, two additional methods were provided to monitor the water volume in the test section. The first was a static water level port located in the North sidewall 55 cm from the initial basemat surface (30 cm from the initial collapsed melt surface). The port location is shown in Figure 2-29. The second method was provided by an on-line calculation of the water volume in the test section based on conservation of mass; i.e., the water volume in the test section at any time was equal to the initial volume in the supply/quench systems minus the volume in the supply/quench systems at the current time.

The water supply tank was equipped with a magnetic float to measure the time-dependent water level. As a redundant level measurement technique, the supply tank was also equipped with a differential PT. Water flow rate to the test section was monitored by a paddlewheel flowmeter. The location of the supply system instrumentation is shown in Figure 2-15.

The quench, overflow, and spray tanks were instrumented to measure the transient energy deposition due to steam generation from corium quenching in the test section. The quench and overflow tank instruments are shown in Figure 2-16, while the spray tank instrumentation is shown in Figure 2-17. Each tank was equipped with a magnetic float and (redundant) differential PT to measure the accumulating water volume due to steam condensation. Transient water temperatures in all tanks were monitored using Type K TC's (two in the quench tank, and one each in the spray tank and overflow tanks). Water flow rate and temperature differential across the quench tank cooling coil were monitored with a paddlewheel flowmeter and Type K TC's, respectively, thus providing a measurement of the time-dependent energy extraction rate from the water mass in the tank. The main steamline between the test section and quench tank was instrumented with Type K TC's to measure the local gas and pipe structure temperatures. The steamline thermocouple locations are shown in Figure 2-13. The outlet noncondensable gas flow rate from the spray tank was monitored by a Hastings mass flow transducer. The location of the off gas system instrumentation is shown in Figure 2-19.

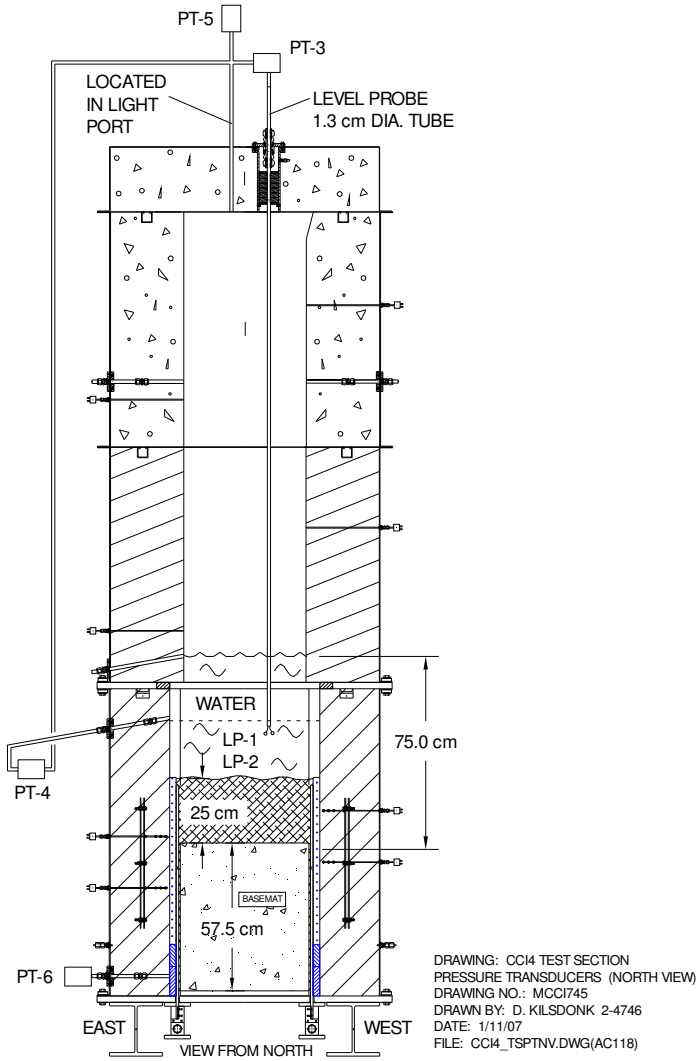

Figure 2-29. CCI-4 Test Section Pressure Transducer Layout.

Key system pressures were monitored with strain-gauge type pressure transducers manufactured by Sensym, Inc. As shown in Figures 2-15 through 2-17 and 2-29, the pressure in all system tanks were monitored, as well as the test section plenum pressure. An Additional PT was located in the lower test section to monitor the pressure beneath the melt upper surface. This transducer was mounted on the east sidewall of the test section at an elevation of 48 cm beneath the initial concrete surface. The gap between the MgO sidewalls and the electrodes was packed with crushed UO_2 pellets during corium loading. Thus, this PT could sense the pressure beneath the melt surface as long as the gap did not plug during the test.

In terms of the power supply operating parameters, voltage drop across the tungsten electrode bank was monitored with the DAS voltmeter, while current input was monitored with two parallel 5000:1 current transformers. Power input to the melt was monitored with two Hall Effect meters.

In addition to the above instrumentation, visual information regarding the core-concrete interaction and melt quenching behavior was provided by a video camera mounted on the upper lid of the apparatus. The camera location and field of view are shown in Figure 2-3. Five area video monitors were also used in the cell to monitor for leaks, and also to record any disruptive events (i.e., steam explosion) should one occur. Finally, the crust lance was equipped with load and displacement transducers to provide data on the crust load vs. time during the crust failure sequence.

3.0 TEST PROCEDURES

3.1 Pretest Operations

Assembly of the apparatus began by installing the tungsten electrodes (126 total; 63 per side) into machined copper electrode clamps. The electrode clamps were then attached to the bottom of the 2.54 cm thick aluminum support plate which served as the foundation for the entire apparatus. With the electrode clamps installed, the support plate was moved into position on the ZPR-9 reactor bed. The concrete basemat and concrete/metal inserts were then placed on top the support plate. The basemat and inserts were then completely covered with a continuous sheet of 1.7 mil aluminized Saran film to prevent moisture contamination of the thermite powders from the basemat once the powders were loaded into the test section. The lower test section concrete and MgO sidewalls were then set in place. The concrete sidewalls were covered with ZrO_2 felt and aluminized Saran before placement to prevent moisture contamination of the thermite from these components once the powders were loaded. The lower section flange bolts and clamping bars were then installed and torqued according to an approved procedure.

In parallel with test section assembly, the thermite powders were mixed in preparation for corium loading. As a precursor for initiating mixing, a gas sample test[a] was conducted to verify

[a]The gas sample test procedure consisted of igniting a representative sample of the thermite in a closed vessel. The amount of noncondensable gas produced was determined from the ideal gas law; the composition of the evolved gases was determined using gas mass spectroscopy.

that the initial level of volatile impurities in a sample prepared from the CCI-4 thermite constituents was sufficiently low to preclude excessive gas release during the burn. The results of this test indicated that moisture and nitrogen contents were within acceptable limits. On this basis, mixing was initiated.

Once the lower section was assembled, preparations for loading of the corium charge began. A single, large 1.7 mil aluminized Saran bag was preinstalled over the basemat. During loading, the 265 kg thermite charge was placed within this bag in order to reduce the amount of bagging material present in the thermite. As the powders were placed in the test section, the basemat melt temperature thermocouples were monitored to detect any localized heating in the corium powders. If heating was observed, the cell was to be evacuated immediately. As the thermite was placed, the gap between the tungsten electrodes and MgO sidewalls was filled with crushed UO_2 pellets. The crushed pellets served as a protective layer against excessive chemical/thermal attack by the corium during the test. Once loading was completed, two sparkler igniters were placed a few centimeters below the top of the powders near the center of the test section, and then the bag was folded and sealed.

Once loading was completed, a removable train containing a 1.0 kg bagged sample of thermite was installed over the powder bed; an illustration is provided in Figure 3-1. The sample train was removed weekly and the sample weighed to monitor the moisture pickup by the thermite during the period between loading and test initiation. Note from Figure 3-1 that the top portion of the train also contained a 4.5 kg canister of desiccant. The desiccant was provided to maintain the plenum gas as dry as possible during pretest operations. As an additional measure to prevent moisture accumulation in the powder bed, the lower test section was continuously purged with argon (2 slpm) from the time loading was completed until the test was initiated.

After installation of the sample train, the remainder of the test apparatus was assembled. This included installation of the transition plate, two upper sidewall sections, and finally the enclosure lid. Peripheral instrumentation was then installed on the lid and sidewalls of the test section. The main steamline run from the test section to the primary quench tank was completed, as well as the pressure relief line from the test section to the auxiliary tank. (The main steamline was closed off from the test section using an insertable blank-off plate throughout pretest operations to preclude moisture migration from the quench tank into the test section).

After assembly was completed, extensive system checkout procedures were performed to ensure that the facility was in proper working order. This included a proof test of the test section at 83 kPad, which is 20 % in excess of the pressure relief system activation pressure of 69 kPad. The pressurization gas for this test was argon. An insertable blind flange was installed upstream of the rupture disk in the pressure relief line to isolate this system. During the test, the apparatus was gradually pressurized to the proof pressure. After a 1 minute hold at this pressure, the system was isolated to determine the leak rate. The leak rate of the CCI-4 test section was found to be 4.2 kPa/min (18 slpm) at a nominal pressure of 55 kPad, which was significantly below the acceptable leak rate of the fully assembled test section (i.e., < 2 % of the expected peak gas/vapor generation rate during the test).

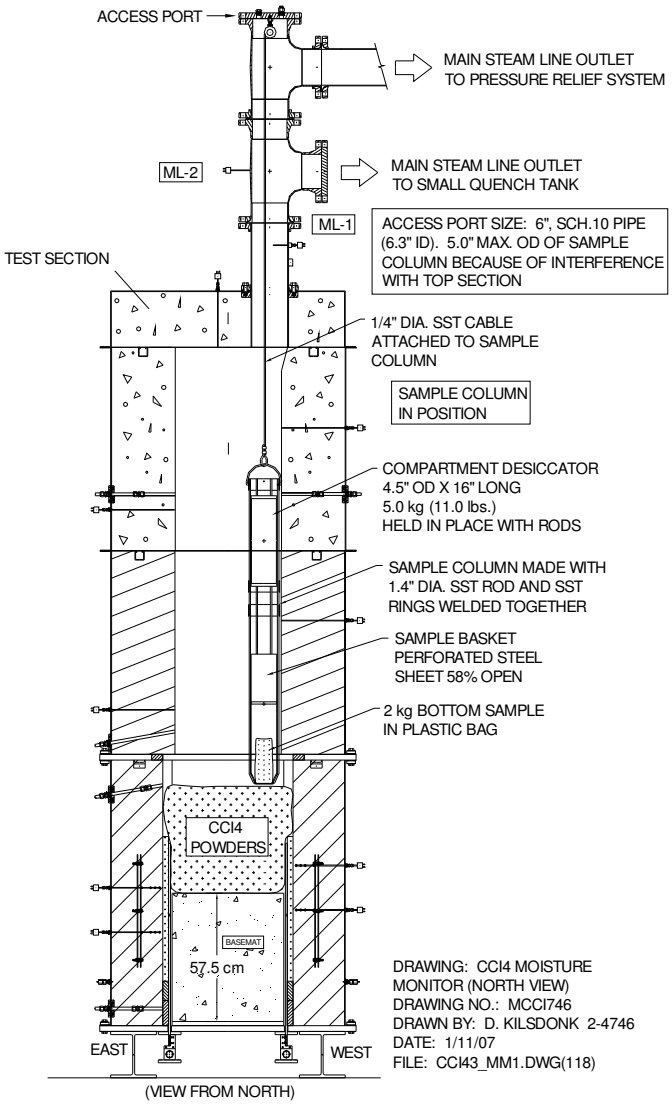

Figure 3-1. Illustration of Thermite Sample Train Installed in Test Section.

Pretest preparations for CCI-4 culminated with a final full system checkout that involved remotely running all equipment with the power supply in operation across a water cooled dummy load. Once the full system check was completed, final system preparations were carried out. These efforts included: (i) hookup of the power supply to the tungsten electrodes through water cooled buss bars, (ii) installation of the final piping connection between the water supply tank and the test section, and (iii) removal of the sample train from within the test section. Following connection of the power supply to the electrode clamps, the key for the power supply lockout located in the cell, as well as the key for the interlock located on the control room console, were assigned to a custodian who kept the keys in their possession until the test was initiated. This step was taken to preclude inadvertent activation of the power supply.

Over the four week time interval spanning pretest operations, the moisture content of the removable sample of bagged thermite increased gradually from 0.18 wt % to 0.28 wt %. The

final moisture content was within the maximum permissible level of 0.3 wt %. On this basis, final approval was granted to proceed with the execution of Test CCI-4.

3.2 Test Operations

The planned test operating procedure is described first, followed by a brief summary of the actual operating procedure.

As shown in Table 1-1, target power for the dry CCI test phase was 95 kW.[b] After melt formation, the input power would be brought up to 95 kW and held there for the balance of dry cavity operations. The initial phase of the interaction would involve ablation of the concrete-metal inserts over the basemat, thereby incorporating the balance of the metals into the melt and producing the initial melt composition shown in Table 2-5. Onset of basemat ablation would define time t = 0 for the experiment. After ablation began, the interaction would be permitted to proceed for 7.0 hours,[c] or until the ablation depth reached 40 cm laterally or 37.5 cm axially. After one of these criteria was met, the cavity would then be flooded. However, if a crust was present at the melt upper surface, the crust lance would be used to fail the crust prior to flooding so that the water would be able to contact the underlying melt. Following water addition, the power supply operation would be switched from constant power at 95 kW to a constant voltage operating mode. (With constant voltage, the input power density would remain relatively constant if a significant quench front developed). Thirty minutes after water addition, or after the debris cooling rate had been reduced to a relatively low level, the crust would be failed with the lance to obtain data on the transient crust breach cooling mechanism. After breach, power supply operations would continue for an additional 30 minutes, yielding a total operating period of 60 minutes with water present in the cavity, or until the ablation limit of 45 cm was reached laterally or 42.5 cm axially. At this point, the input power would be turned off and the test terminated.

CCI-4 was performed on 26 May 2007. On the evening prior to the experiment, the apparatus was inerted with a slow bleed of helium into the test section. On the day of the experiment, the apparatus was brought up to operating conditions, a final walk through inspection was performed by operating personnel, the thermite igniter was hooked up, and finally the power supply was energized before the containment was evacuated and sealed. Data acquisition was initiated at 10:44 am. Coolant and cover gas flows were brought up to design conditions, and the cell ventilation system was closed and sealed per test procedures.

An event sequence for CCI-4 is provided in Table 3-1. In the discussion that follows, time t = 0 corresponds to the onset of basemat ablation. The criterion used to define the onset of concrete ablation at a given location was that the local temperature reached the limestone/common sand concrete liquidus temperature of 1295 °C. [4]

---

[b]The 95 kW power level for CCI-4 is scaled from the 120 kW level used in Tests CCI-2 and CCI-3 [1] based on a surface area scaling that preserves heat flux to the boundaries of the melt at the start of the interaction.
[c]The 7 hour limit on dry cavity ablation for CCI-4 is linearly scaled up from the 5.5 hour limit used in Tests CCI-2 and CCI-3 [1] based on the increase in maximum lateral erosion depth from 30 cm to 40 cm for CCI-4.

Table 3-1. CCI-4 Event Sequence (times relative to onset of ablation of the basemat).

Shifted Time (Minutes)	Event
-48.6	DAS started.
-38.5	Power applied to thermite igniter wire.
-38.2	Thermite burn initiated; view of melt surface occluded by aerosol within 5 seconds.
-37.7	Thermite burn completed (burn time ~ 30 seconds); melt temperature ~1900 °C
-36.6	Target DEH input power of 95 kW reached and maintained until power off.
-10.3	Sharp increase in aerosol production; view of surface eventually blocked. Temperatures in test section gas plenum increase sharply, and power supply operating parameters change (i.e., current decreases and voltage increases), indicating onset of insert ablation.
-6.54 to 4.41	Onset of basemat ablation detected at all five basemat locations; average time for all arrays is 0.0 minutes, which defines time t = 0 for the experiment.
0.0	Onset of basemat ablation based on average time at all five basemat locations. Initial melt temperature ~1850 °C.
20.3	Power supply reached operational limit on Tap 1 (56 V range); switch to Tap 2 (112 V range) initiated.
23.1	DAQ communications failure halts data transmission between the PC and the analog to digital converters in the cell. Recovery efforts initiated.
41.0	DAQ recovery operations completed and data acquisition restarted.
30.6 to 135.2	Aerosols clear to reveal top surface of the interaction. The surface is either devoid of crust, or covered in areas with skin crusts that are not stable. Bubbling pool observed.
135.2 to 172.2	Solid crust platelets form on melt surface, attempting to bond together, as well as the test section sidewalls. Convection within the melt is sufficient to periodically break up these formations.
172.2 to 314.6	Crust becomes fixed and bonded to sidewalls. Two-phase eruption and melt extrusion events occur almost continuously through various vent holes that form, migrate, and close (freeze shut) over the extent of the crust surface.
259.2 to 267.4	Crust lance inserted twice in an attempt to breach the bridge crust. Peak load of 3.33 kN applied, but the crust was not breached. Surface elevation measurements were in the range of 66.5 - 69.8 cm at the point of lance contact.
268.4	Power supply reached operational limit on Tap 2 (112 V range); switch to Tap 3 (168 V range) initiated.
299.6	Power supply reached operational limit on Tap 3 (168 V range); switch to Tap 4 (224 V range) initiated.
314.6	Last eruption through crust occurs, and vent hole freezes shut. Thereafter, pressurization of lower test section occurs due to continued gas production from CCI with partial gas venting through leaks around the electrode clamps.
383.7	Sparks seen from beneath the test section bottom plate; DEH input terminated.
384.9	Water addition to test section initiated.
403.3 to 407.8	Crust lance inserted again in an attempt to breach the bridge crust. Some breakage occurred on initial contact at an elevation of 69.1 cm, but the full depth of the material was not penetrated to reveal the underlying melt. Peak load of 4.70 kN was applied; surface elevation reduced to ~ 60 cm after first breakage.
458.3	Data acquisition terminated.

As shown in Table 3-1, data acquisition began at -48.6 minutes relative to initial melt contact with the basemat. As shown in Figure 3-2, power was applied to the nichrome wire/sparkler located at the top of the powder charge at -38.5 minutes. Based on video camera data from the test section and plenum gas temperature readings inside the test section, thermite ignition was announced and logged in the control room at -38.2 minutes. Based on readings from thermocouples located near the top of the concrete – metal inserts, the burn front reached the bottom of the powder bed in ~ 30 seconds (i.e., at -37.7 minutes), which was within the planning basis for the experiment. The readings from selected melt temperature thermocouples are shown in Figure 3-3 over the first few minutes of the interaction. As is evident from this collection of data, peak melt temperatures near the center of the melt in the first 30 seconds of the interaction were in the range of 1900 to 2070 °C, with the average being close to 1900 °C.

Following the thermite burn, there was a quiescent period during which concrete surfaces were protected by insulating crusts. However, at -10.3 minutes, plenum gas temperatures suddenly increased by several hundred degrees (Figure 3-4), and the power supply operating current dropped at constant power (Figure 3-5), indicating onset of concrete ablation within the test section.[d] The thermocouple data indicates that ablation of the concrete sidewalls was initiated at this time, as well as the concrete-metal inserts. Onset of basemat ablation was detected at the basemat centerline and in the four outer quadrants over the time interval from -6.54 to + 4.41 minutes. The average time for all five arrays was 0.0 minutes, which defines time t = 0 for the experiment. The melt temperature at this time was ~1850 °C. During the first 10 minutes of concrete erosion, several melt temperature thermocouples detected a steady increase in melt temperature from ~1850 °C up to ~2000 °C, which was likely due to exothermic chemical reactions between metallic melt constituents (Zr, Cr, Fe) and concrete decomposition gases.

At completion of the burn, a power supply current ramp up to the target power of 95 kW was initiated. This power level was reached at -36.6 minutes, where it was essentially maintained for the balance of the test involving dry cavity operations.

Near 23 minutes in the operating sequence, an unidentified DAQ communications failure halted transmission between the PC and the Hewlett Packard (HP) analog to digital converters in the cell. The cause is thought to be a transmission error between one of the HP units and one of the two repeaters between each HP and the PC. The error froze traffic along the General Purpose Interface Bus (GPIB) that linked all repeaters with the PC. Diagnostic and recovery operations were initiated, and communications were reestablished at 41 minutes, leaving a 16.9 minute gap in the recorded data. During this time, input power to the melt was maintained at 95 kW based on panel readouts in the control room that were independent of the data acquisition system.

Over the time interval from 30.6 to 135.2 minutes, aerosols in the plenum cleared to reveal the upper surface of the core-concrete interaction. The surface was either completely devoid of crust, or covered in areas with skin crusts that were not stable. Bubbling pool behavior was observed.

---

[d]The decrease in current at constant power is due to the fact that the addition of concrete decomposition products to the melt causes the melt electrical resistance to increase.

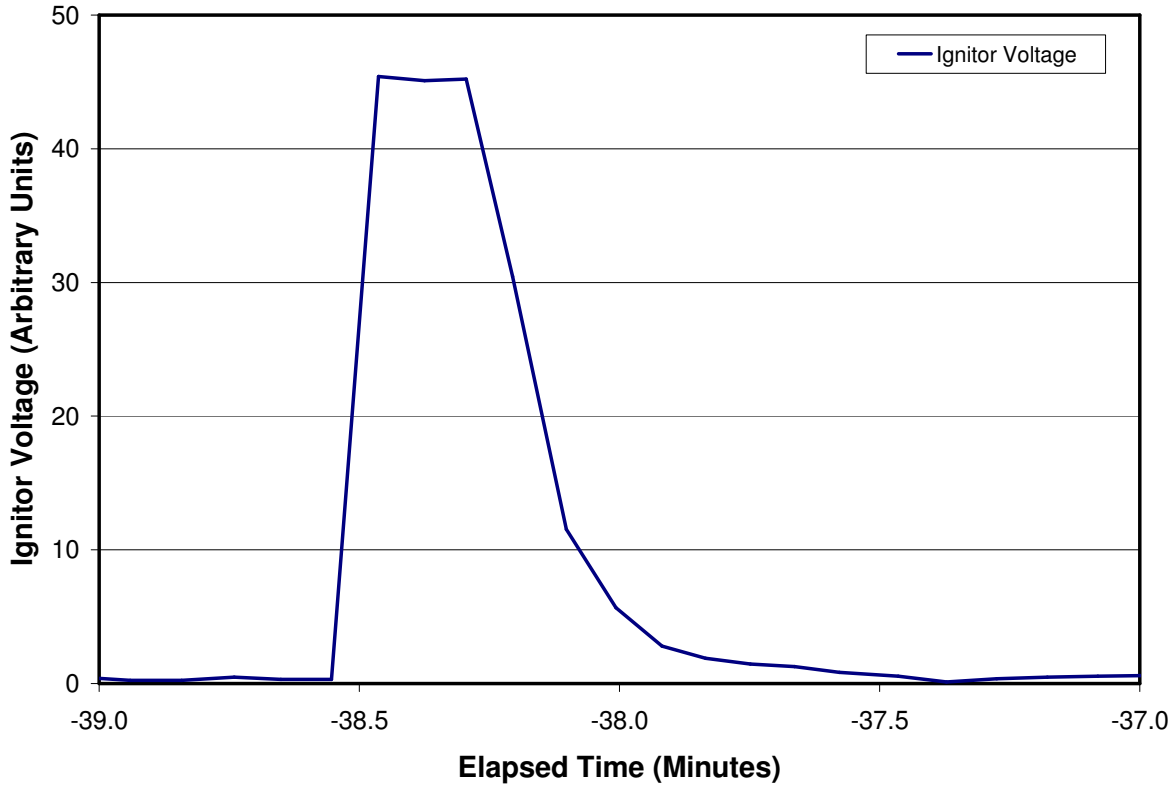

Figure 3-2. Voltage Reading Across Thermite Igniter Shunt.

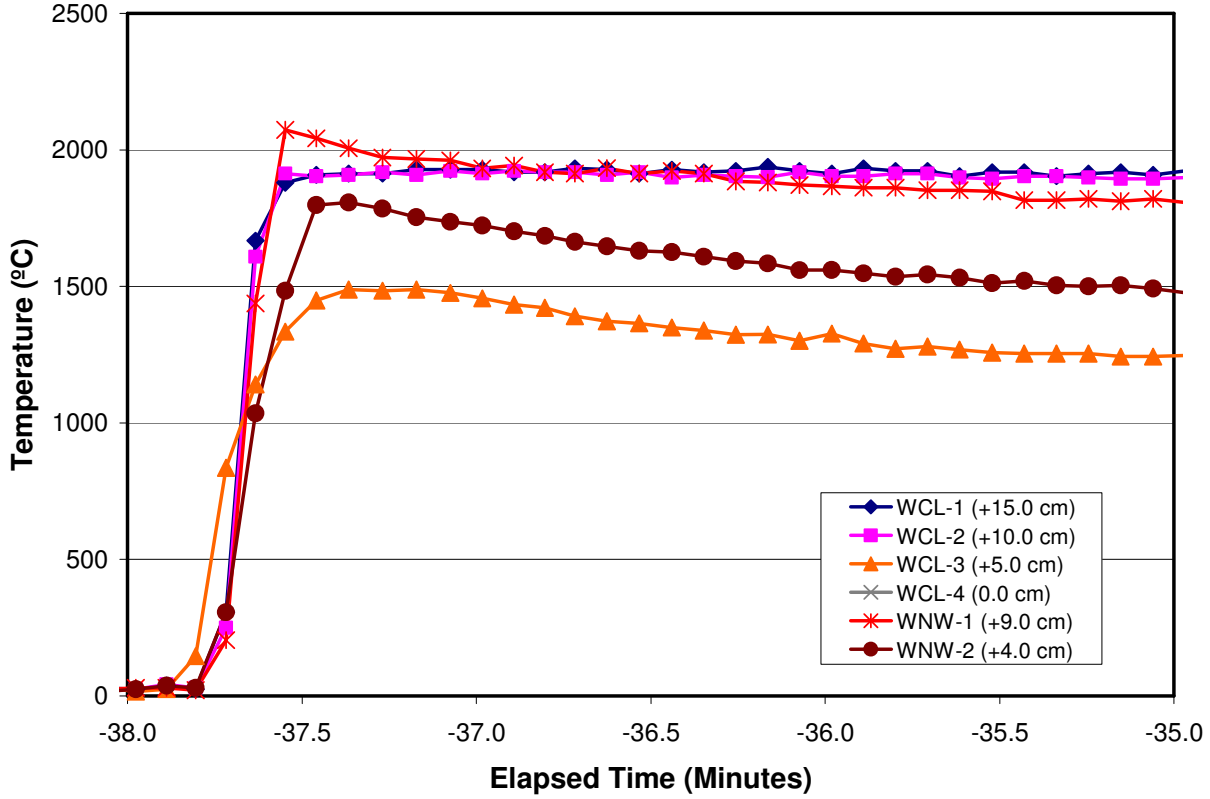

Figure 3-3. Bulk Melt Temperature Data over the First 5 Minutes of the Interaction.

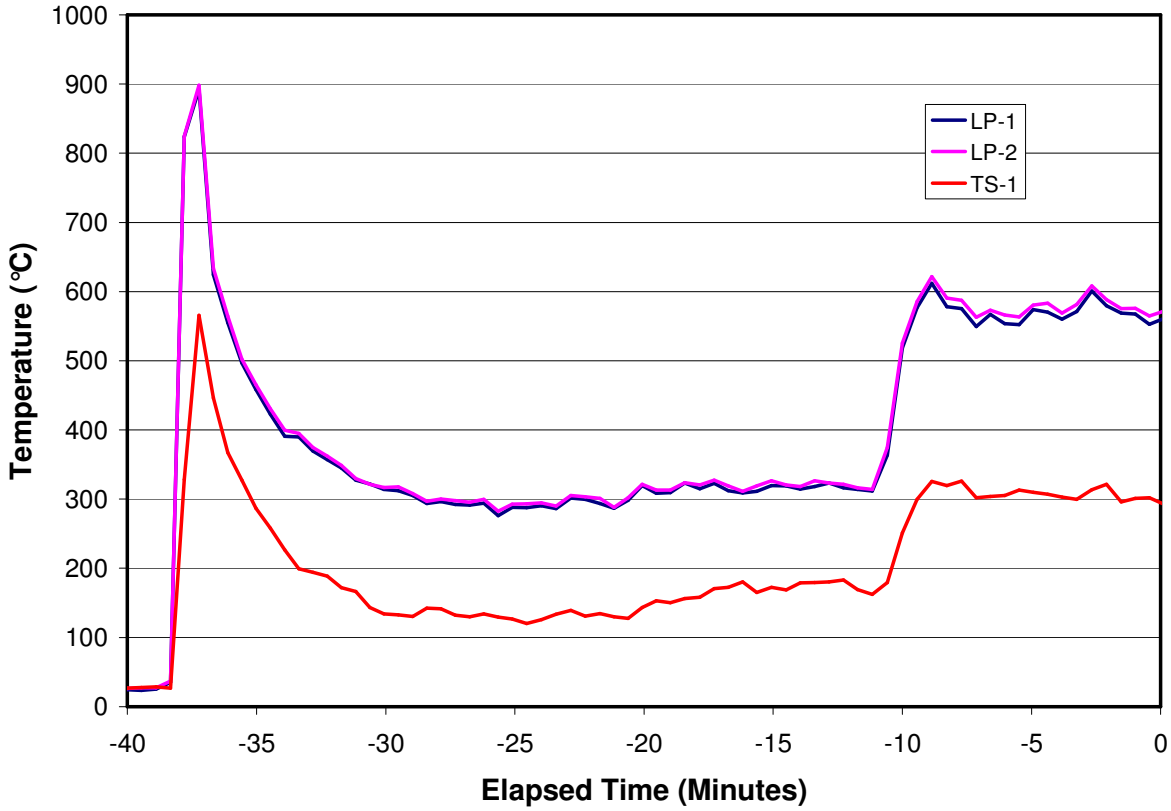

Figure 3-4. Test Section Plenum Gas Temperatures during the Initial Interaction.

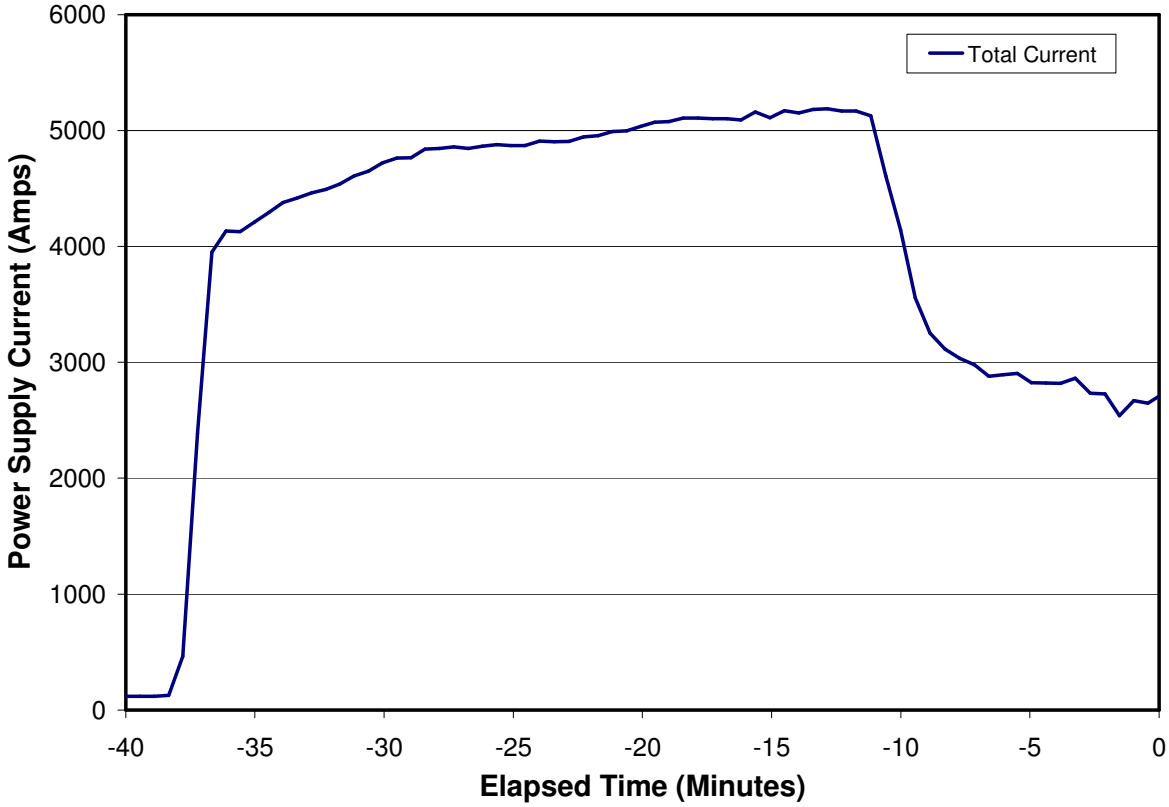

Figure 3-5. Power Supply Current during the Initial Interaction.

Over the time interval from 135.2 to 172.2 minutes, solid crust platelets began to form on the melt surface. These platelets intermittently bonded together, as well as to the test section sidewalls. However, convection within the melt was sufficient to periodically break up these formations, and the process would begin again. At 172.2 minutes, the crust became permanently fixed and bonded to sidewalls. Over the next two hours of the interaction, two-phase eruption and melt extrusion events occurred almost continuously through various vent holes that would form, migrate, and close (freeze shut) over the extent of the crust surface. During this interval (i.e., from 259.2 to 267.4 minutes), the crust lance was inserted twice in an attempt to breach the bridge crust. A peak load of 3.33 kN was applied, but the crust was not breached. Surface elevation measurements were in the range of 66.5 - 69.8 cm at the point of lance contact, which can be compared with the initial collapsed melt pool height of 25 cm.

As shown in Table 3-1, the lid camera view showed that the last melt eruption ended at 314.6 minutes, at which time the final vent hole through the crust was plugged by solidifying melt entrained through the hole. As shown in Figure 3-6, pressurization of the lower test section started at this time due to continued gas production from the core-concrete interaction, while the normal gas flow path up through the system was at least partially blocked by the crust. Posttest examinations further indicated that part of the gas flow was then vented through small leaks at the bottom of the test section where the electrode clamps bolted to the test section bottom support plate. Formation of this significant blockage was not detected by the operators during the conduct of the test.

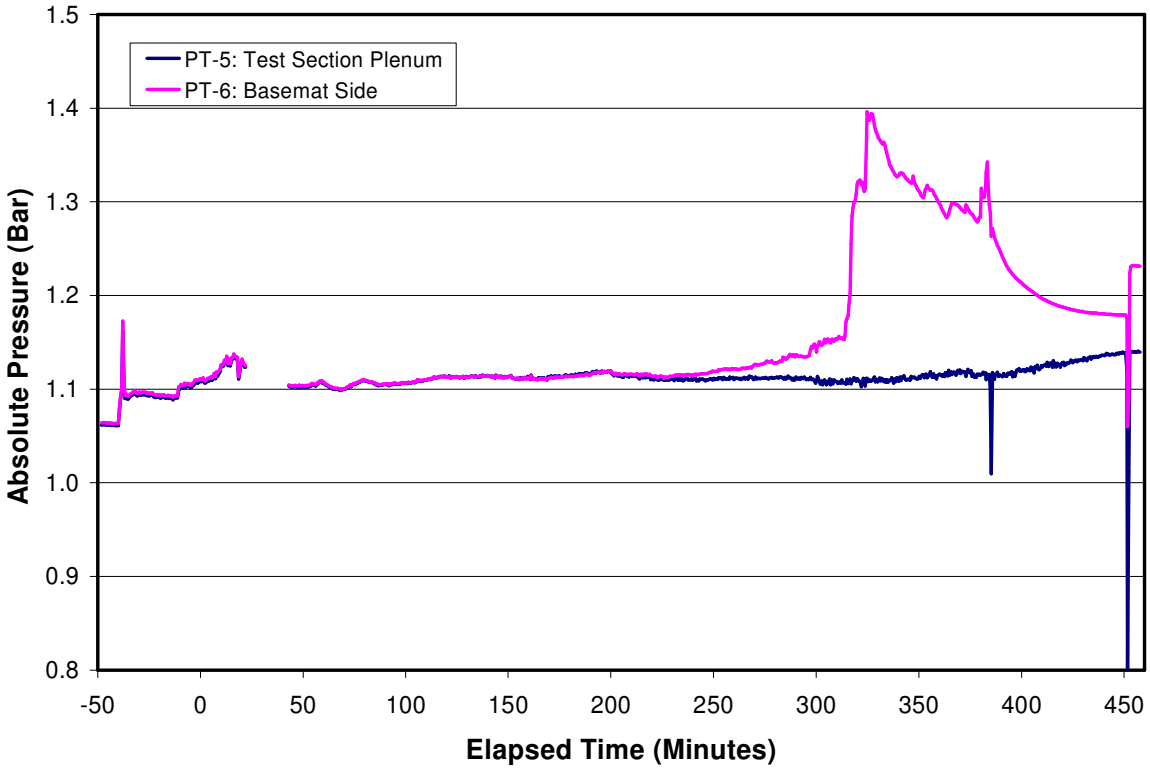

Figure 3-6. Pressure in the Test Section Plenum and at the Side of the Basemat.

During the final stages of test operations, input power was held constant at 95 kW as concrete erosion continued. At 387.7 minutes, sparks were seen emanating from the bottom of the test section, indicating the development of a minor leak. At this time, power input to the melt was terminated. The cavity was flooded soon after (i.e., at 384.9 minutes) to obtain debris cooling data. The crust lance was inserted again over the time interval from 403.3 to 407.8 minutes in an attempt to breach the bridge crust. Some breakage occurred on initial contact at an elevation of 69.1 cm, but the full depth of the material was not penetrated to reveal the underlying melt. The peak load of 4.70 kN was applied; the surface elevation was reduced to ~ 60 cm after first breakage.

Data logging continued until 458.3 minutes. At this point, the system was shutdown following the normal termination procedures. The DAQ was restarted to record the long-term cool down data. The experiment was left unattended to cool down overnight.

4.0 RESULTS

A summary of the principal thermalhydraulic results from CCI-4 is provided in this section. A complete list of instruments used in the test is provided in Appendix A, while plots of all data logged from these instruments are provided in Appendix B.

4.1 Electric Power

The DEH power supply voltage, current, and total input power for CCI-4 are shown in Figures 4-1 through 4-3, respectively. At completion of the thermite burn, the power supply voltage was steadily increased until the input power reached the target level of 95 kW at -36.6 minutes. Thereafter, input power was held constant in the range of 95 ± 5 kW over the balance of dry cavity operations. Voltage tap changes were made at 20.3, 268.1, and 299.6 minutes in order to maintain constant power as the load resistance presented by the melt increased over the course of the test. Power input was terminated at 383.7 minutes when sparks were observed emanating from the bottom of the test section, indicating development of a minor leak.

4.2 Melt Temperatures

A total of thirty six W5%Re/W26%Re (Type C) thermocouple junctions were used to monitor melt temperatures at various axial and radial locations in CCI-4. The junction locations for these thermocouples are shown in Figures 2-6, 2-24, and 2-25. The thermocouples were configured within five four-junction and two eight-junction thermocouple arrays. The five four-junction units were all located in the concrete basemat; each of these arrays was protected by a 0.95 cm diameter tungsten thermowell. The two eight-junction arrays were radially configured in the two concrete sidewalls; each of these units was protected by a 1.27 cm tungsten thermowell. Data from the five Type C arrays in the basemat are provided in Figures 4-4 through 4-8, while data from the two sidewall arrays are provided in Figures 4-9 and 4-10. To provide an indication of the overall melt temperature behavior during the test, a graph showing data from all 36 thermocouples is provided in Figure 4-11. To improve readability, two steps have been taken: i) the data have been averaged over ~30 second (i.e., 6 point) intervals, and ii) only data preceding the first off-scale reading by the thermocouples are shown.

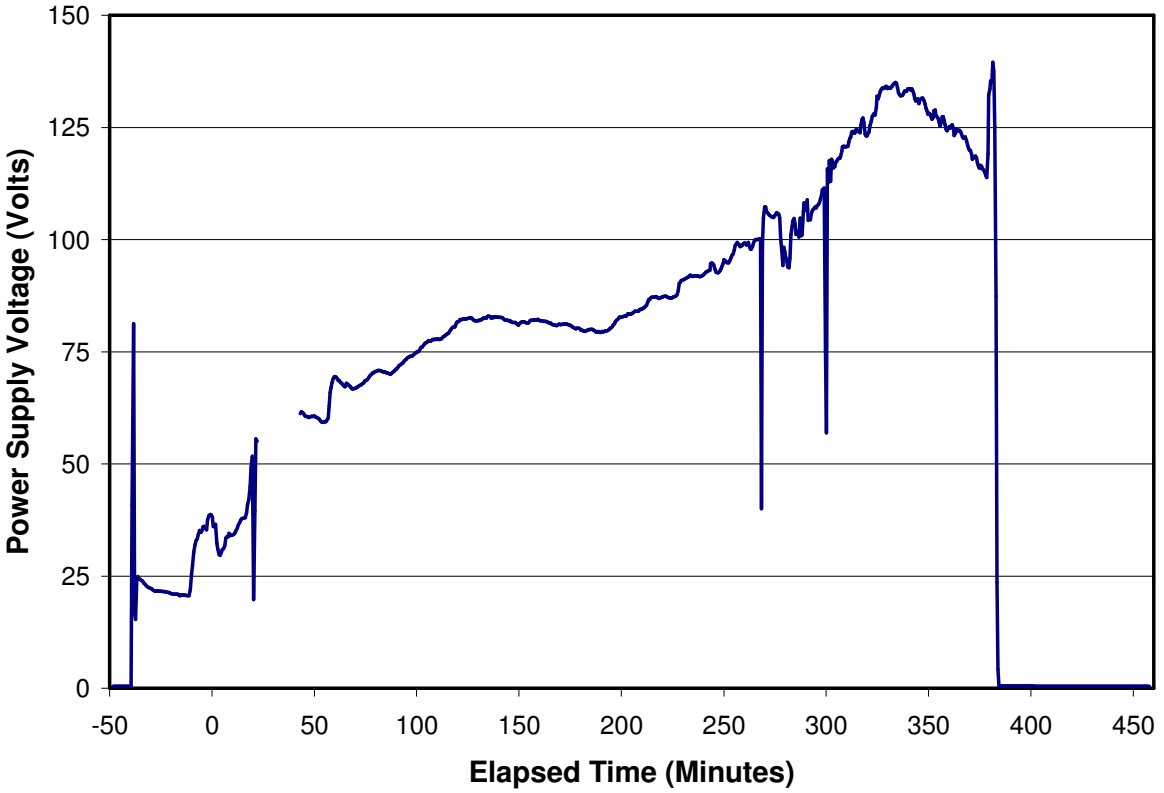

Figure 4-1. Power Supply Voltage.

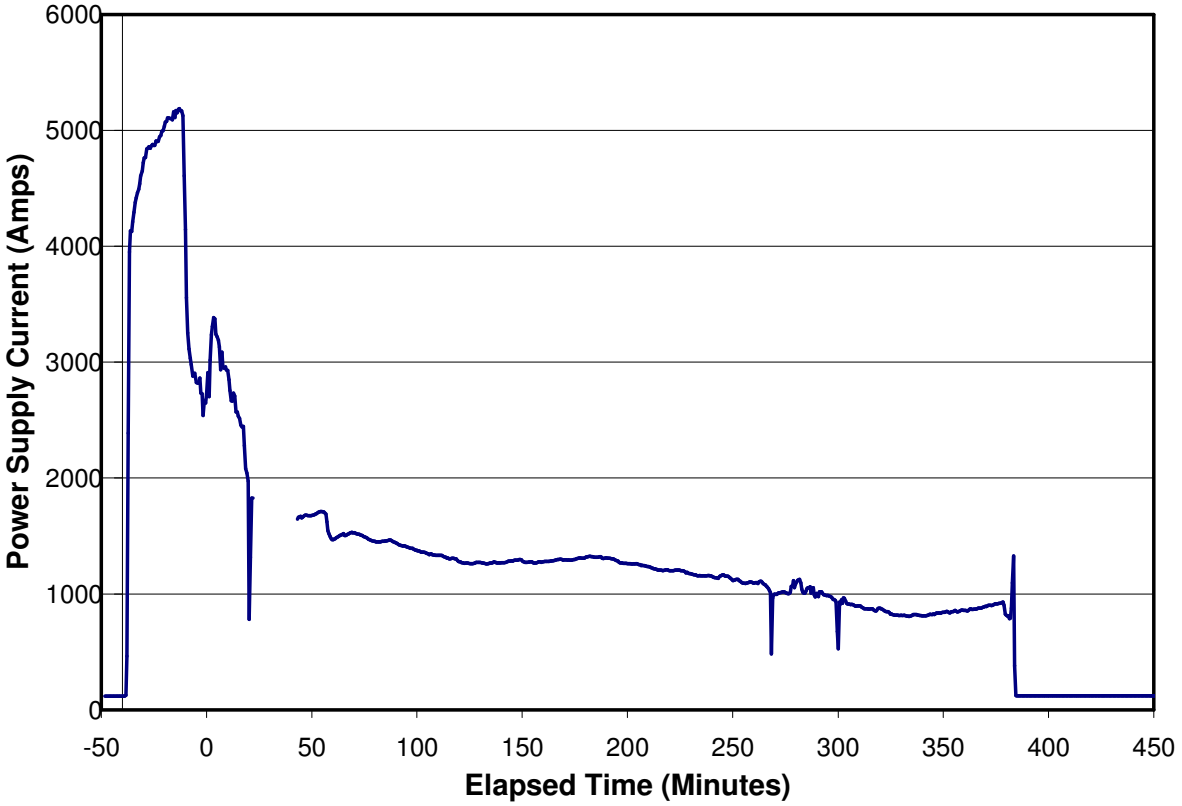

Figure 4-2. Power Supply Current.

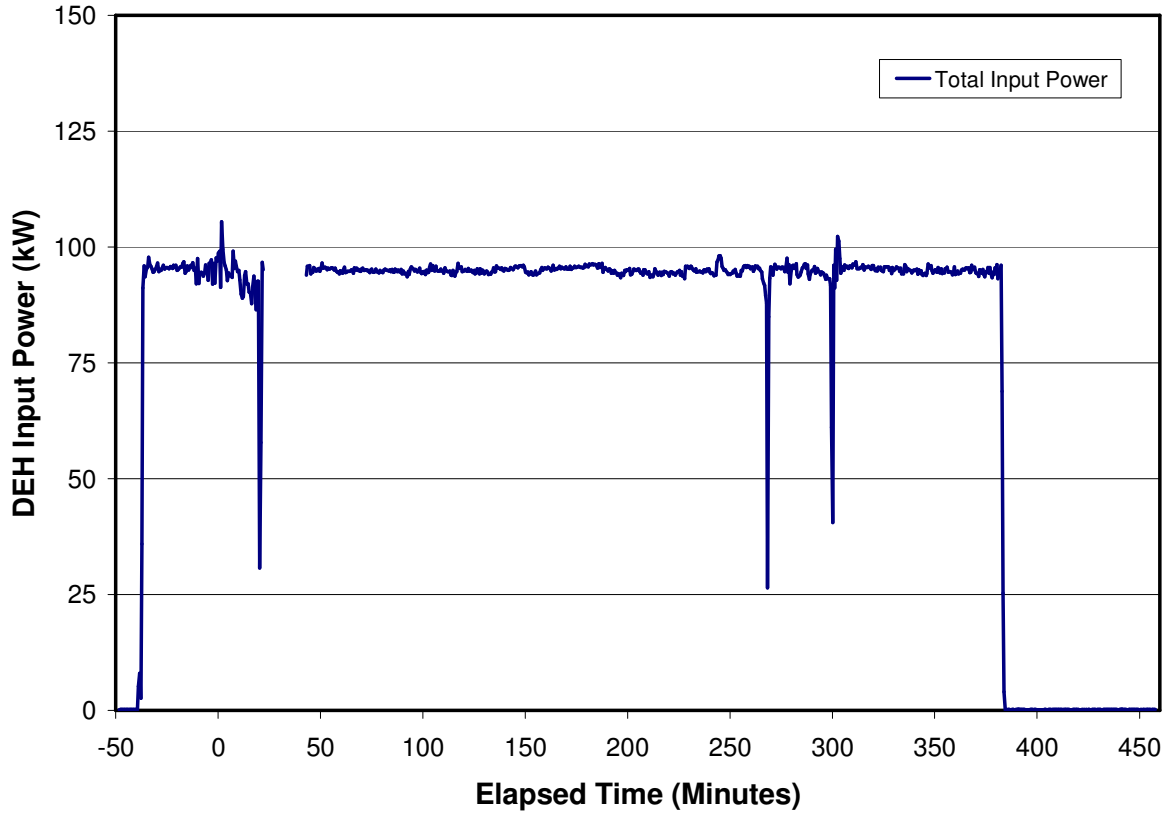

Figure 4-3. Total DEH Input Power.

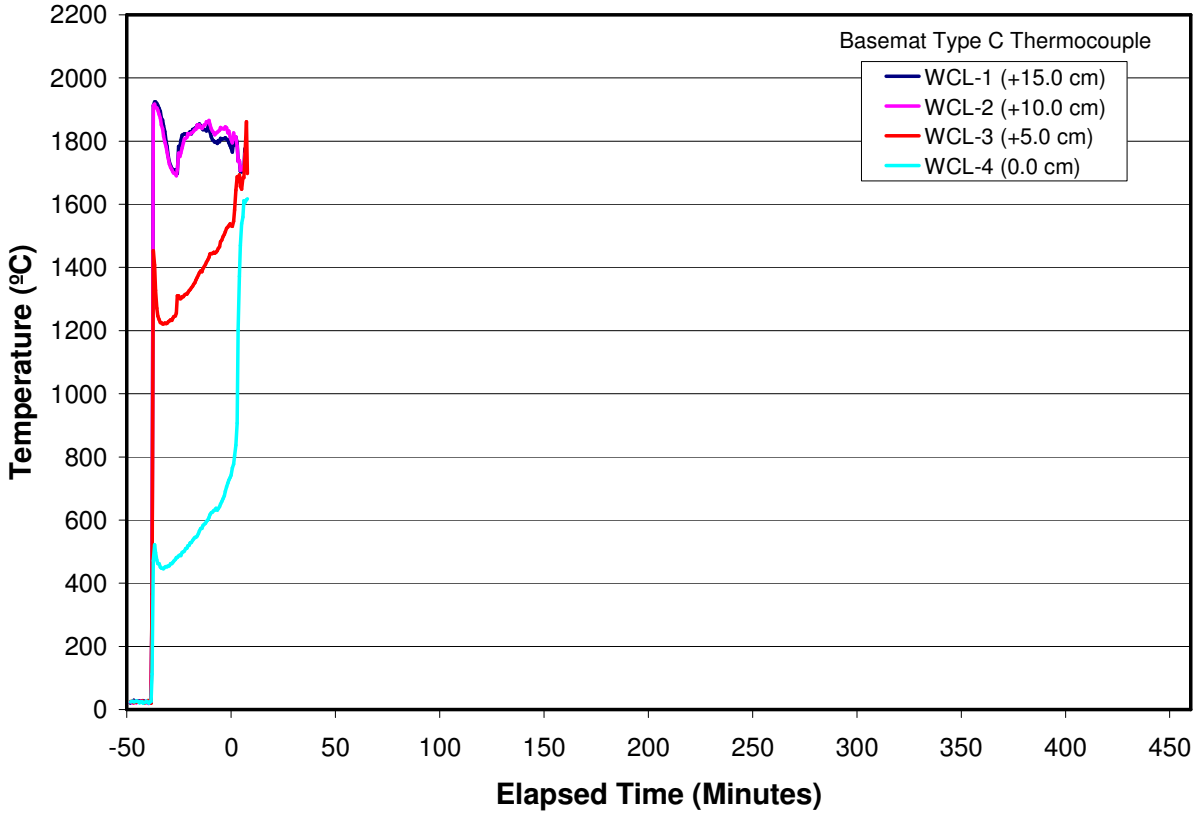

Figure 4-4. Melt Temperature Data from Basemat Type C "WCL" Array.

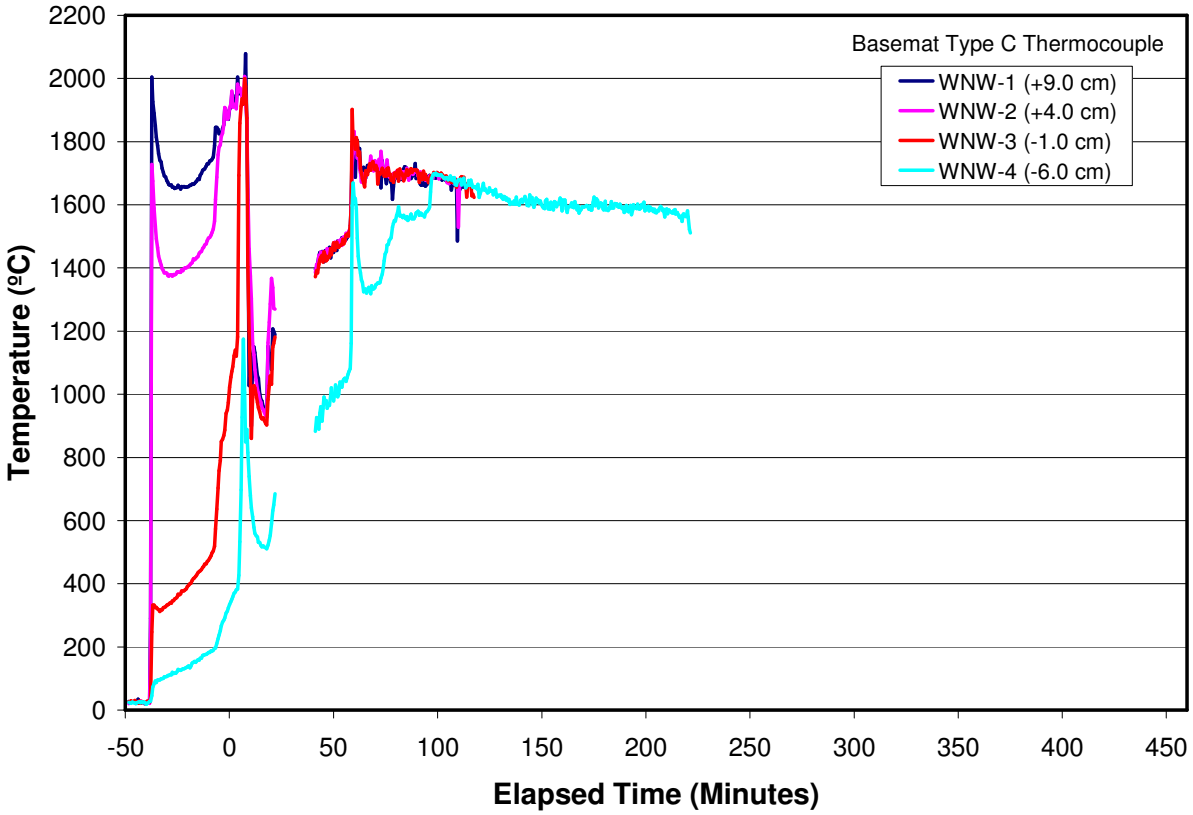

Figure 4-5. Melt Temperature Data from Basemat Type C "WNW" Array.

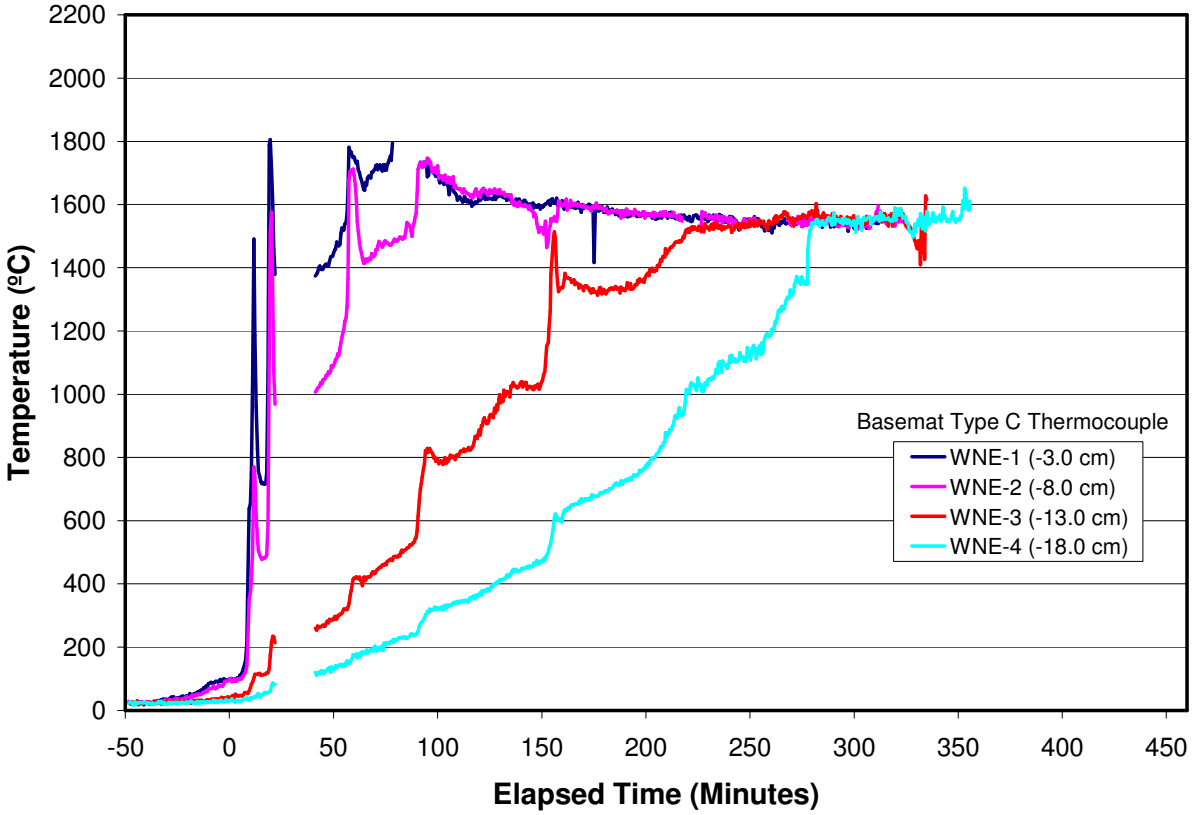

Figure 4-6. Melt Temperature Data from Basemat Type C "WNE" Array.

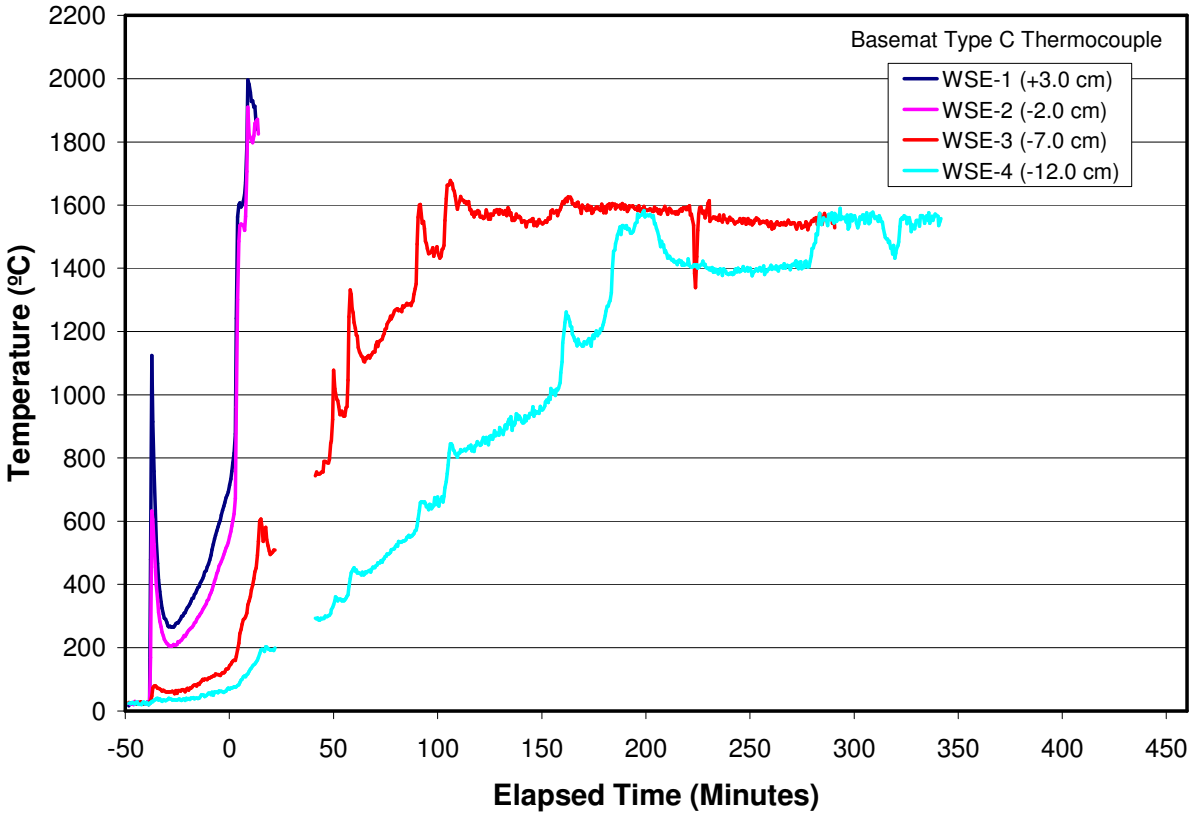

Figure 4-7. Melt Temperature Data from Basemat Type C "WSE" Array.

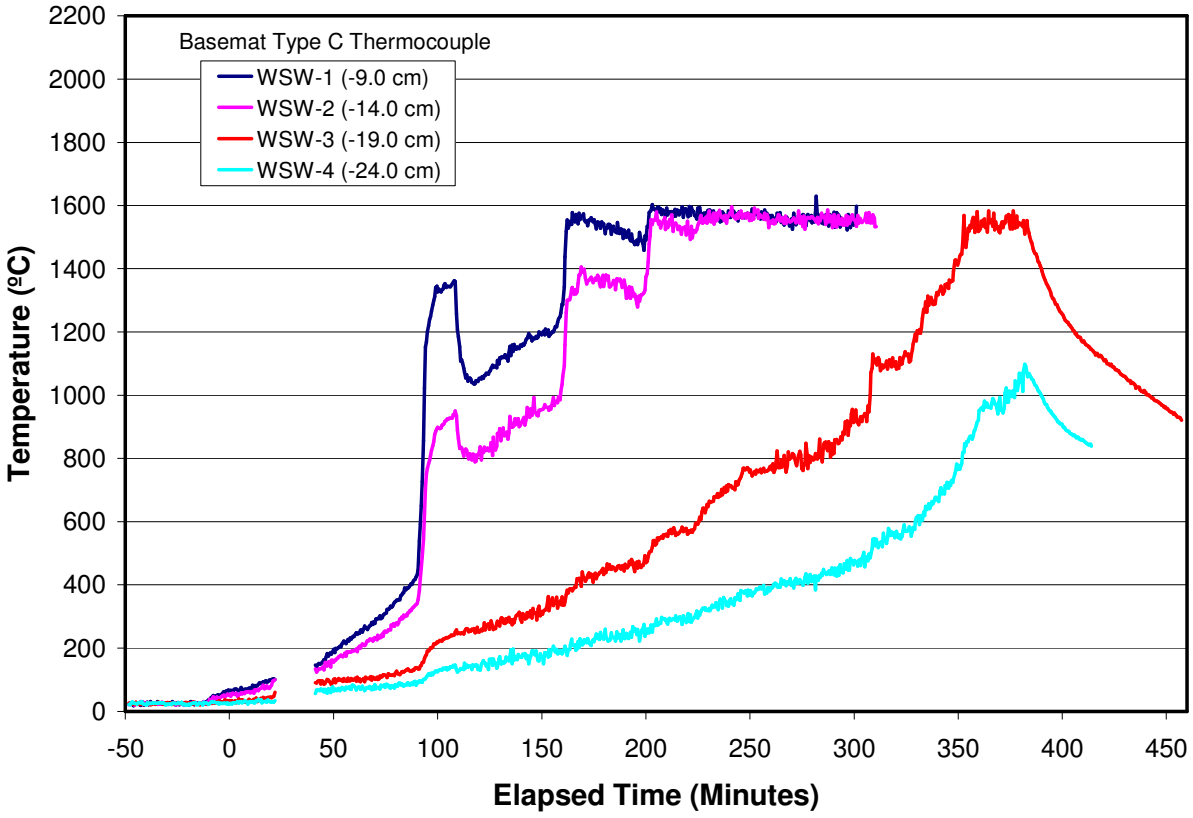

Figure 4-8. Melt Temperature Data from Basemat Type C "WSW" Array.

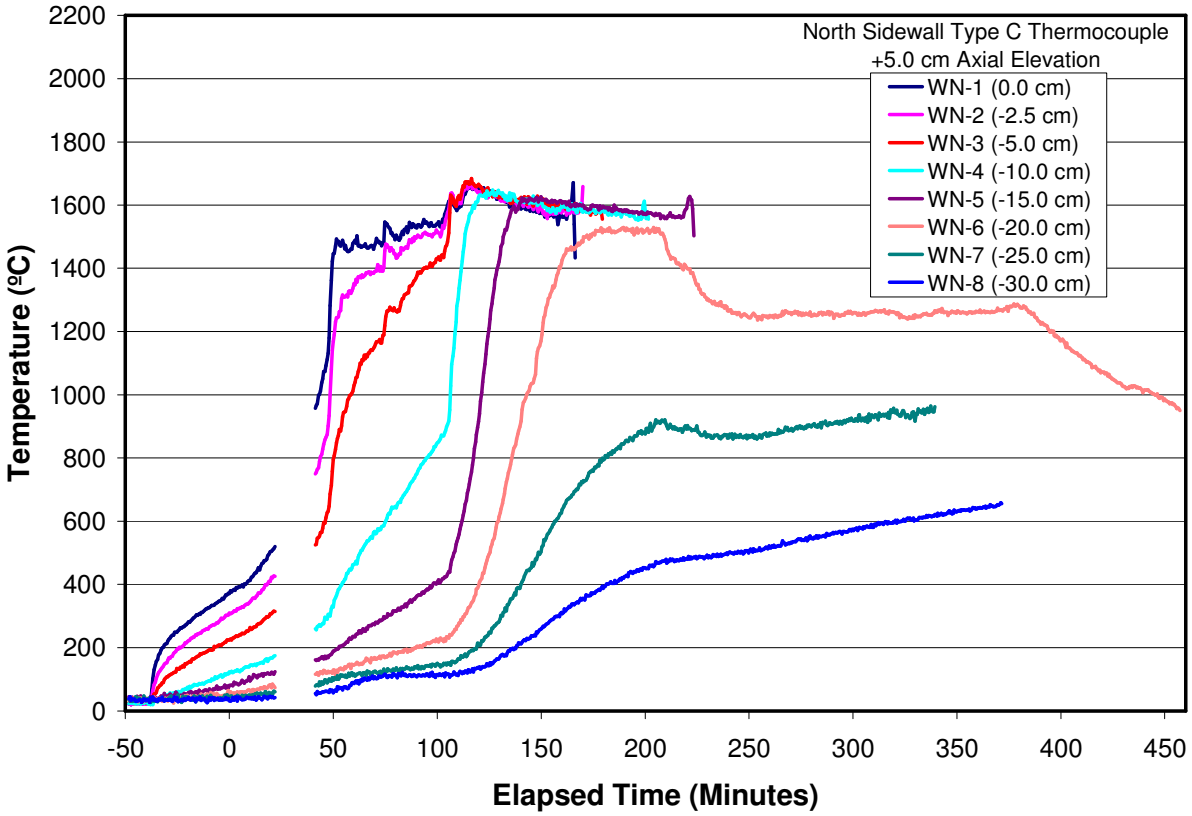

Figure 4-9. Melt Temperature Data from North Sidewall Type C "WN" Array.

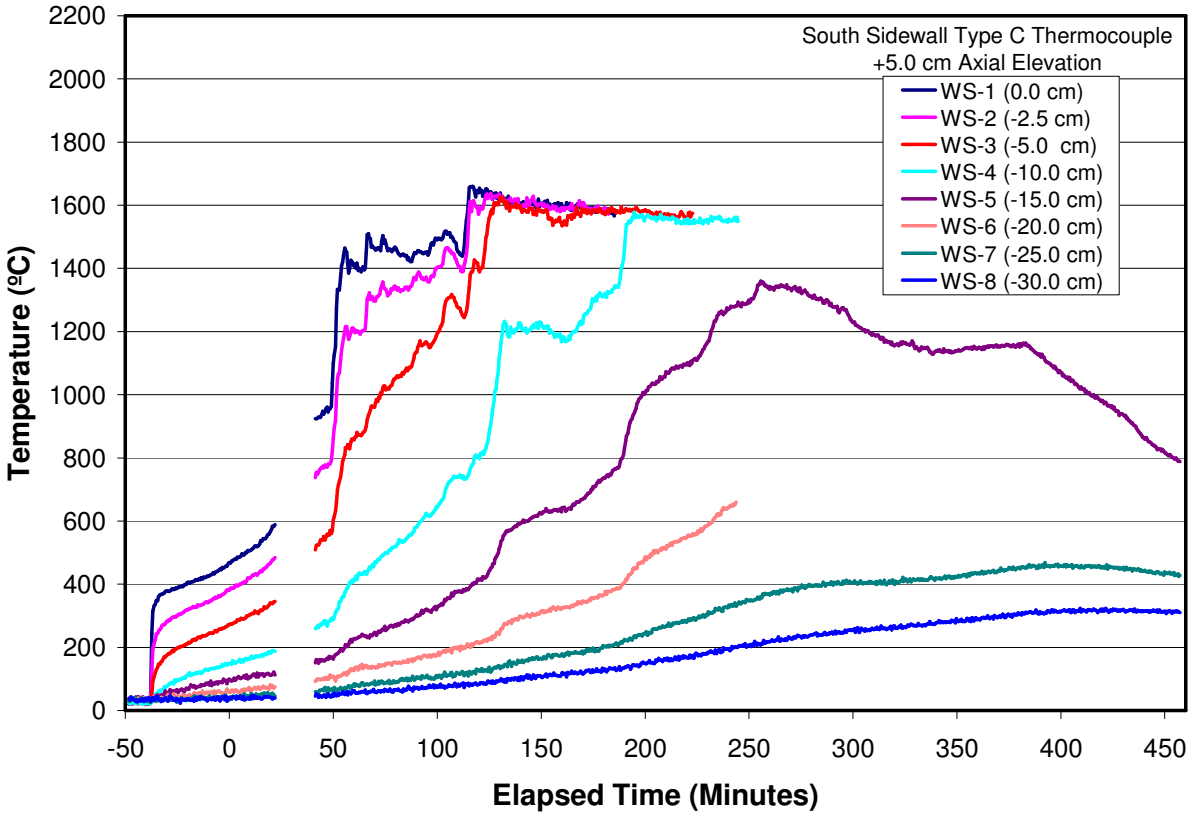

Figure 4-10. Melt Temperature Data from North Sidewall Type C "WS" Array.

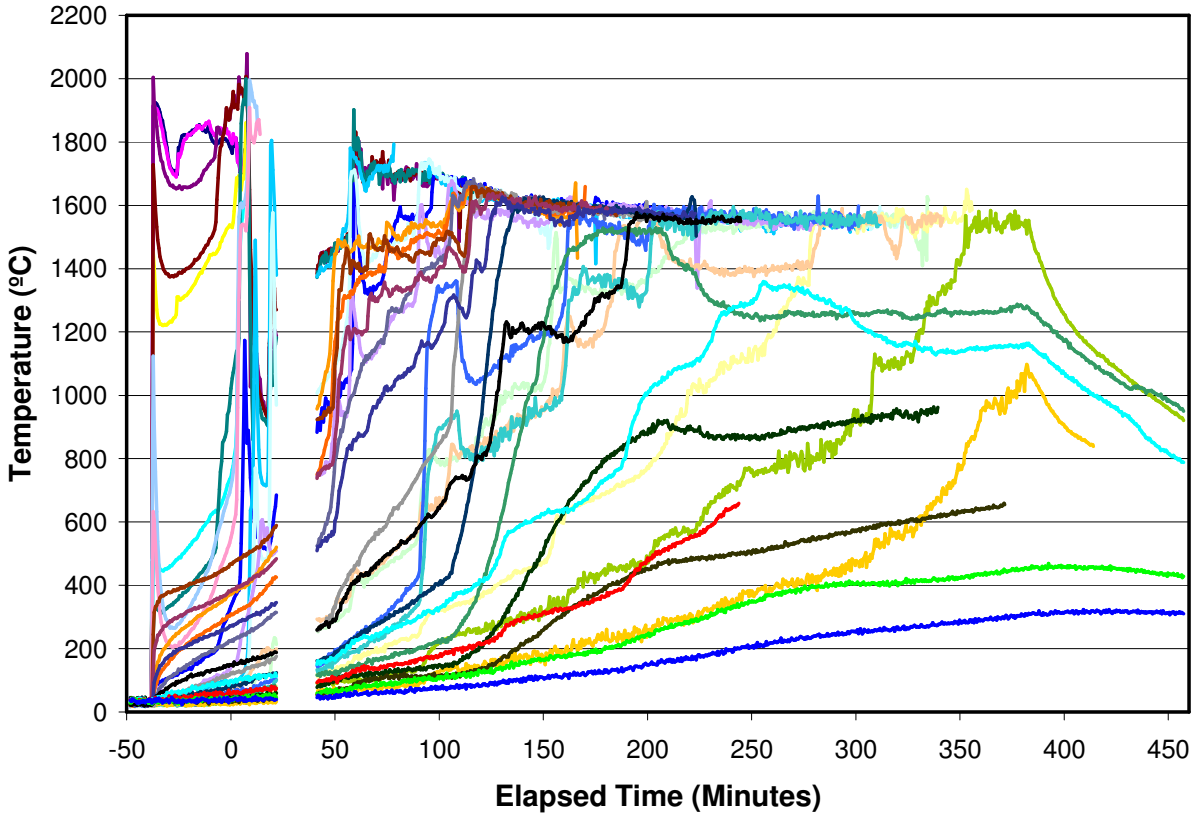

Figure 4-11. Data from all 36 Melt Temperature Thermocouples.

Examination of Figure 4-11 indicates that the average melt temperature declined from ~1900 ˚C at initial melt formation to ~1850 °C at onset of basemat erosion (t = 0). During the first 10 minutes of erosion, several melt temperature thermocouples detected a steady increase in melt temperature from ~1850 °C up to ~2000 °C, which was likely due to exothermic chemical reactions between metallic melt constituents (Zr, Cr, Fe) and concrete decomposition gases. After this initial transient stage, the average melt temperature gradually declined to ~ 1550 ˚C at the time input power was terminated and the cavity was flooded. The temperatures were fairly uniform across the extent of the interaction, generally clustering within a band of approximately ± 50 ˚C of the average at any given time.

4.3 Concrete Basemat and Sidewall Ablation Rates

The basemat was instrumented with five multi-junction Type K thermocouple arrays to monitor the axial progression of the ablation front, while each concrete sidewall was instrumented with seven arrays to monitor the radial ablation front progression at seven different elevations. The location and identification of these thermocouple assemblies are shown in Figures 2-6, 2-24, and 2-25. The first junction of each array was mounted flush with the concrete surface. When a thermocouple reached the LCS concrete liquidus temperature of 1295 ºC [4], the melt was considered to be in contact with the thermocouple at the junction location.

The sequential rise in signals from the basemat centerline array as the test progressed is shown in Figure 4-12. As noted earlier, only data preceding the first off-scale reading by the thermocouples are shown. The analogous plots showing the thermal response in the North and South concrete sidewalls at the +0.0 cm elevation location are provided in Figures 4-13 and 4-14, respectively. Plots of the thermal response at all basemat and sidewall array locations are provided in Appendix B.

Figure 4-15 provides the axial ablation depth versus time based on the signal responses from the Type K basemat arrays, while Figures 4-16 and 4-17 provide the analogous plots of the radial ablation depth in the North and South sidewalls, respectively. Finally, Figure 4-18 provides a comparison of the ablation depths versus time recorded on all three concrete surfaces during the test. Examination of these figures indicates: i) no substantial incoherence between the lateral ablation rates on the North and South sidewalls, and ii) the radial and axial ablation rates are similar. These findings are consistent with the results of test CCI-2, which was also conducted with limestone/common sand concrete [1]. Additional examination of Figure 4-15 indicates that basemat erosion proceeded rapidly in northeast corner of the test section relative to the other basemat locations after the bridge crust sealed at 314 minutes (see Table 3-1). The posttest examinations (see Section 4.7) indicated that the subsequent gas venting out of bottom of test section lead to melt entrainment downward into the gap between the basemat and north concrete sidewall, eventually leading to breach of the test section bottom near this location. The accelerated erosion in the basemat northeast quadrant is thus attributable to a test anomaly, as opposed to a natural phenomenological occurrence.

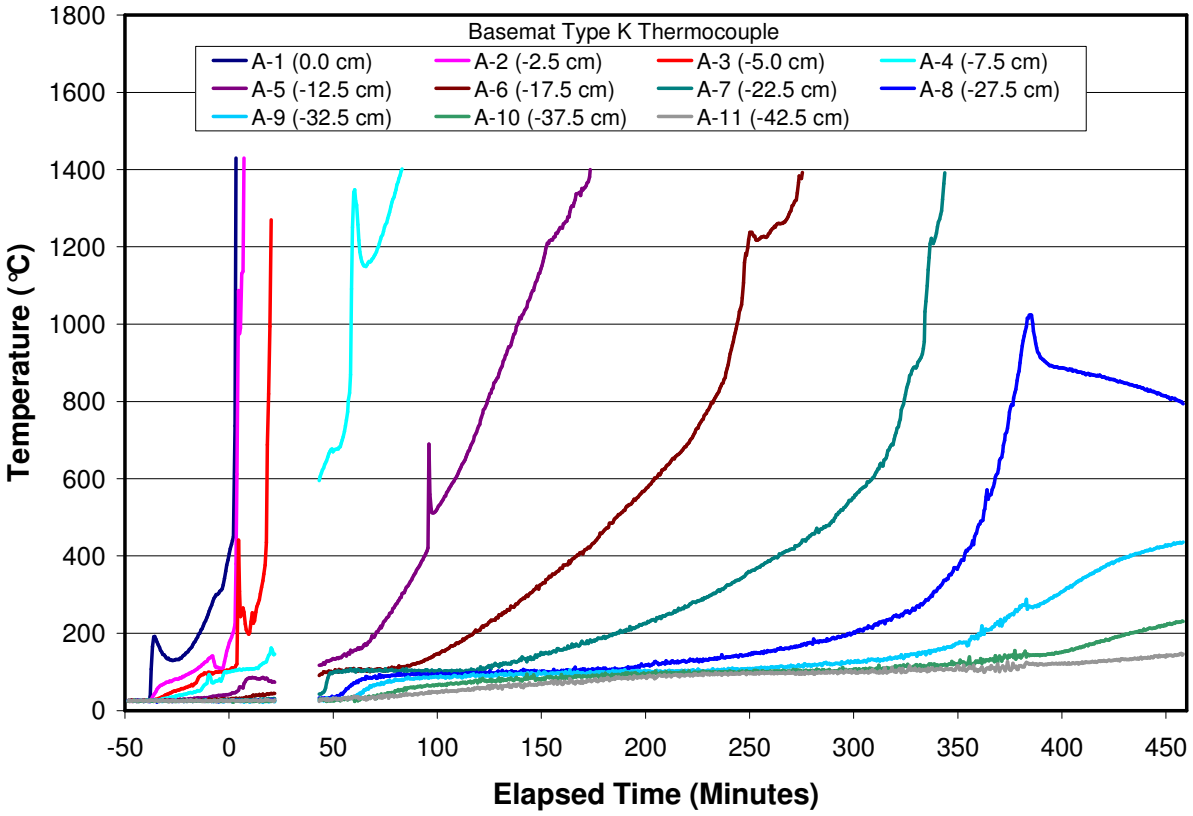

Figure 4-12. Thermal Response of the Concrete Basemat at the Centerline ("A" Array).

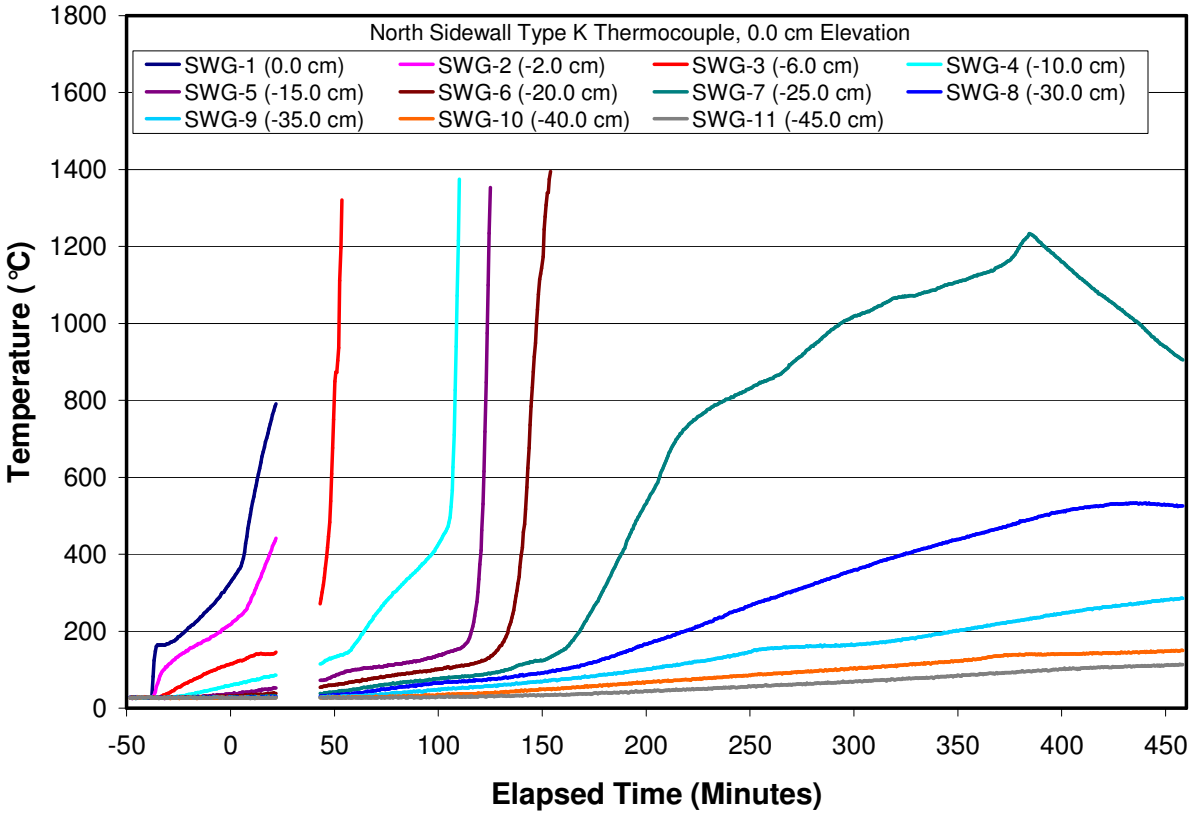

Figure 4-13. North Concrete Sidewall Thermal Response at +0.0 cm ("SWG" Array).

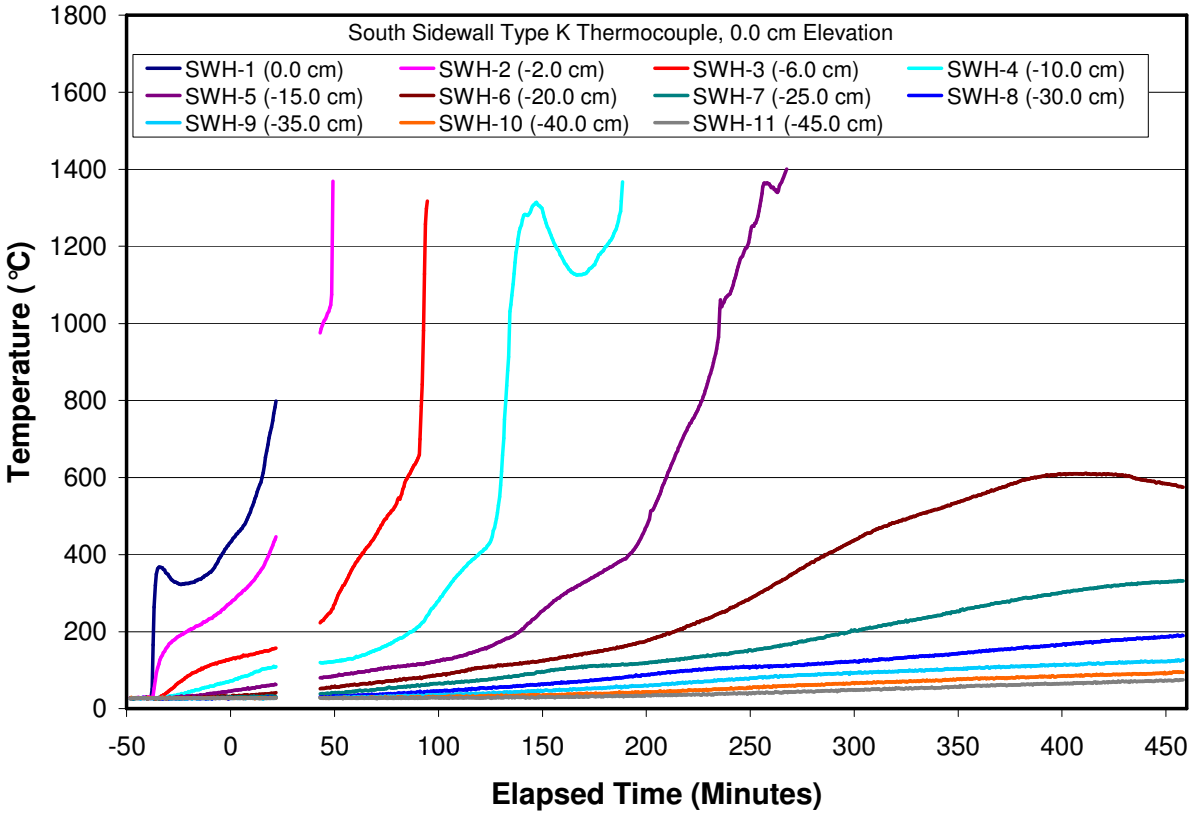

Figure 4-14. South Concrete Sidewall Thermal Response at +0.0 cm ("SWH" Array).

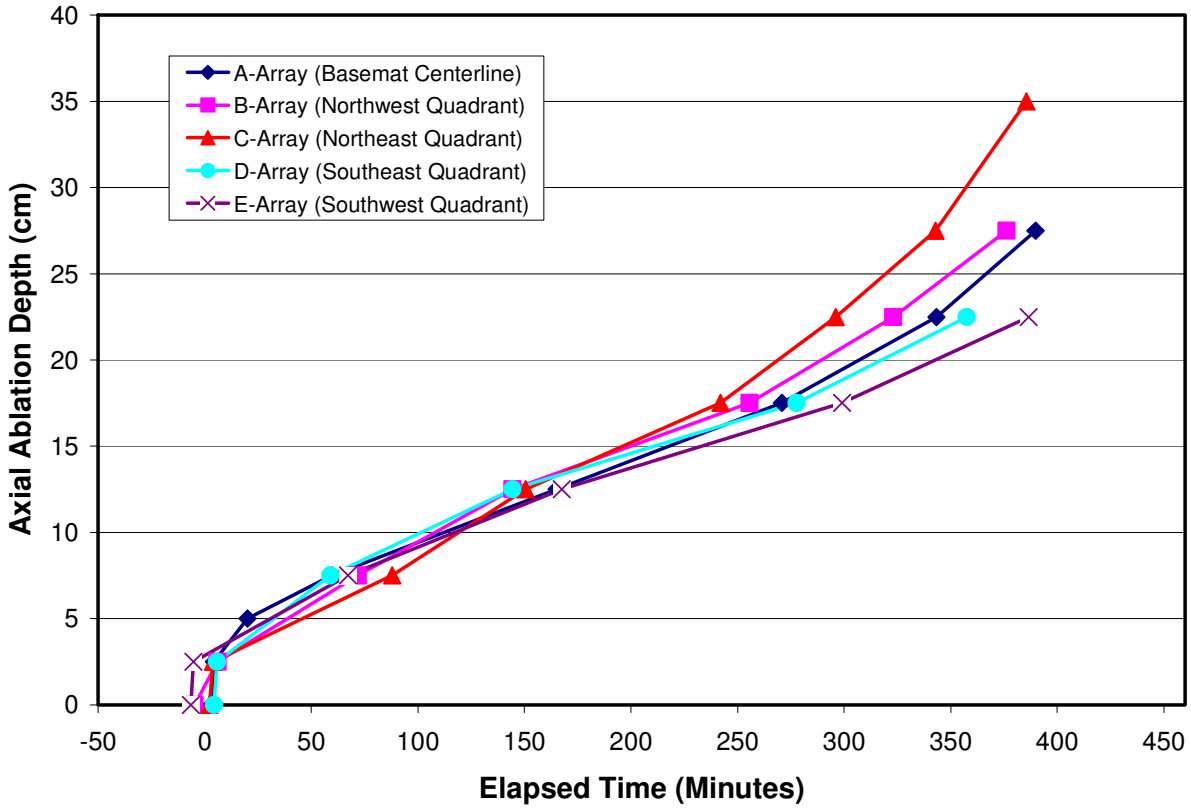

Figure 4-15. Basemat Axial Ablation Front Location.

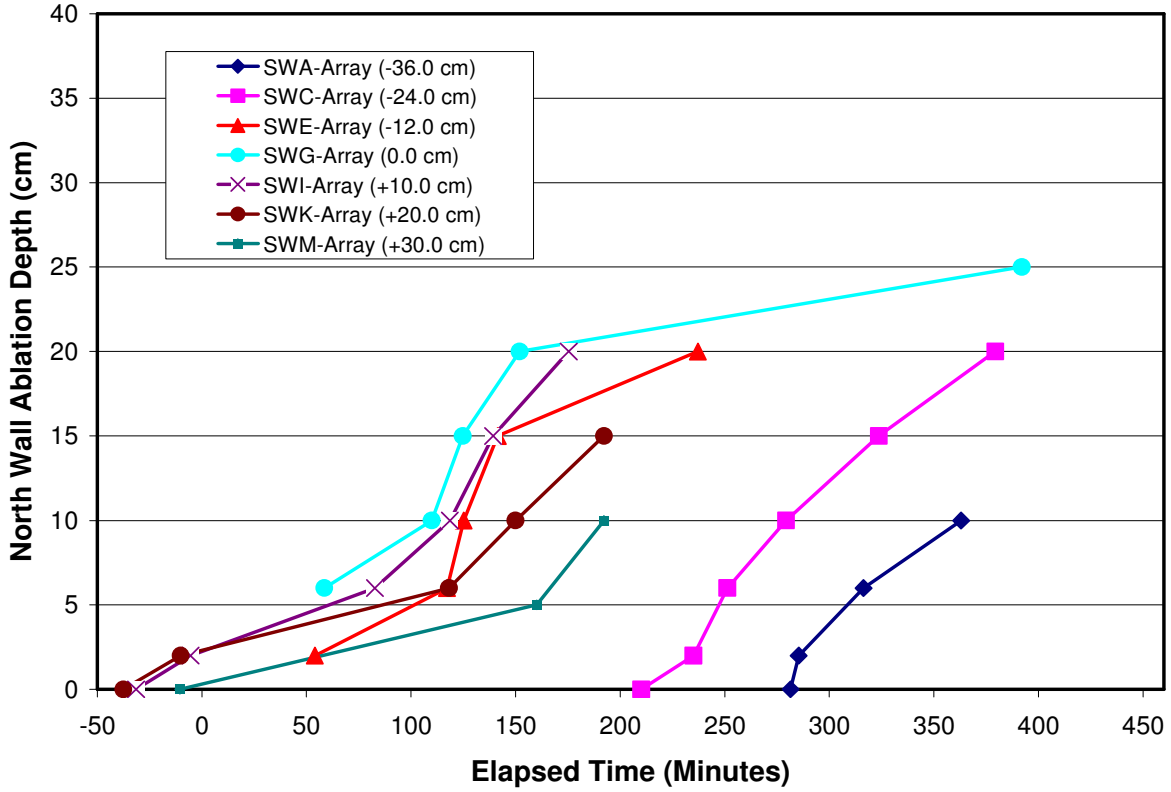

Figure 4-16. North Sidewall Radial Ablation Front Location.

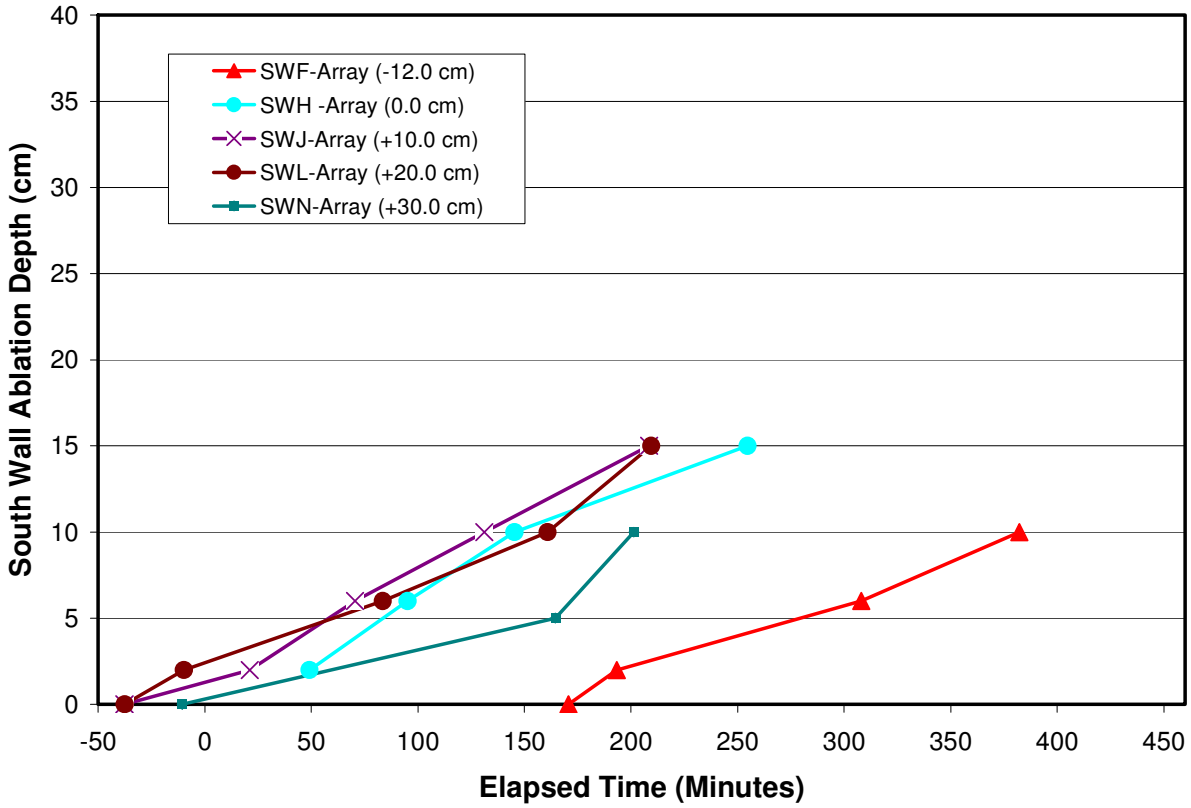

Figure 4-17. South Sidewall Radial Ablation Front Location.

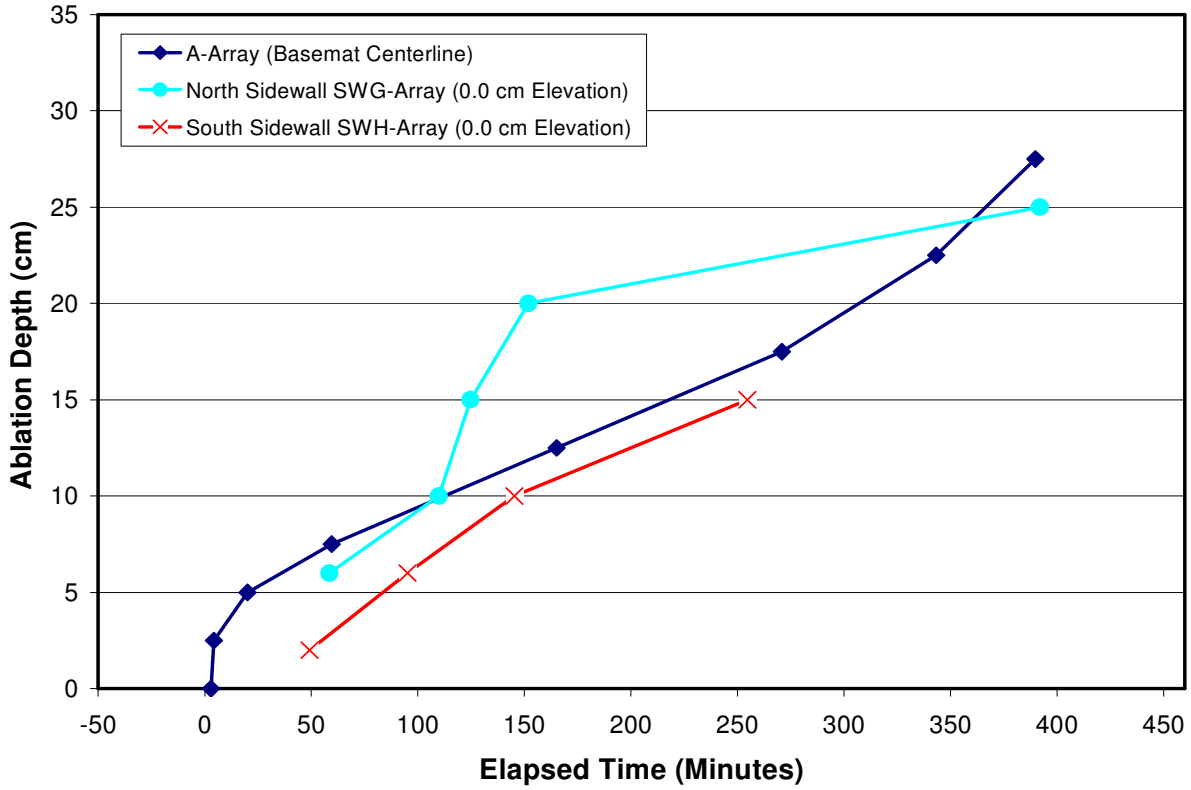

Figure 4-18. Characteristic Axial and Radial Ablation Depths versus Time.

4.4 Melt Zone MgO Sidewall Heat Losses

The MgO sidewalls of the lower test section were instrumented with Type C thermocouple arrays to evaluate heat losses form the melt zone to the sidewalls (see Figure 2-5). The temperature responses recorded in these two walls are provided in Figures 4-19 through 4-22. The local heat flux at each array location was evaluated from the following expression:

$$q'' = -k_{sw} \left. \frac{dT}{dx} \right|_{x=0} \tag{4-1}$$

In this expression, *dT/dx* is the temperature gradient in the sidewall evaluated at the inner MgO surface and k_{sw} is the MgO thermal conductivity evaluated at the surface temperature. The thermal conductivity of castable MgO was evaluated from a parabolic curve fit to the data of Copus et al. [7]:

$$k_{sw} = \begin{cases} 8.18 - 8.08 \cdot 10^{-3} T + 2.98 \cdot 10^{-6} T^2; & 273 \le T \le 1473\ K, \\ 2.74; \quad T > 1473\ K \end{cases} \tag{4-2}$$

where k_{sw} is in units of W/m-K. The temperature gradient in Eq. 4-1 was evaluated based on the measured temperature difference between the two thermocouple junctions closest to the inner surface of the MgO, as well as the known distance between these two junctions. The MgO thermal conductivity was evaluated from Eq. 4-2 using the temperature measured by the innermost thermocouple.

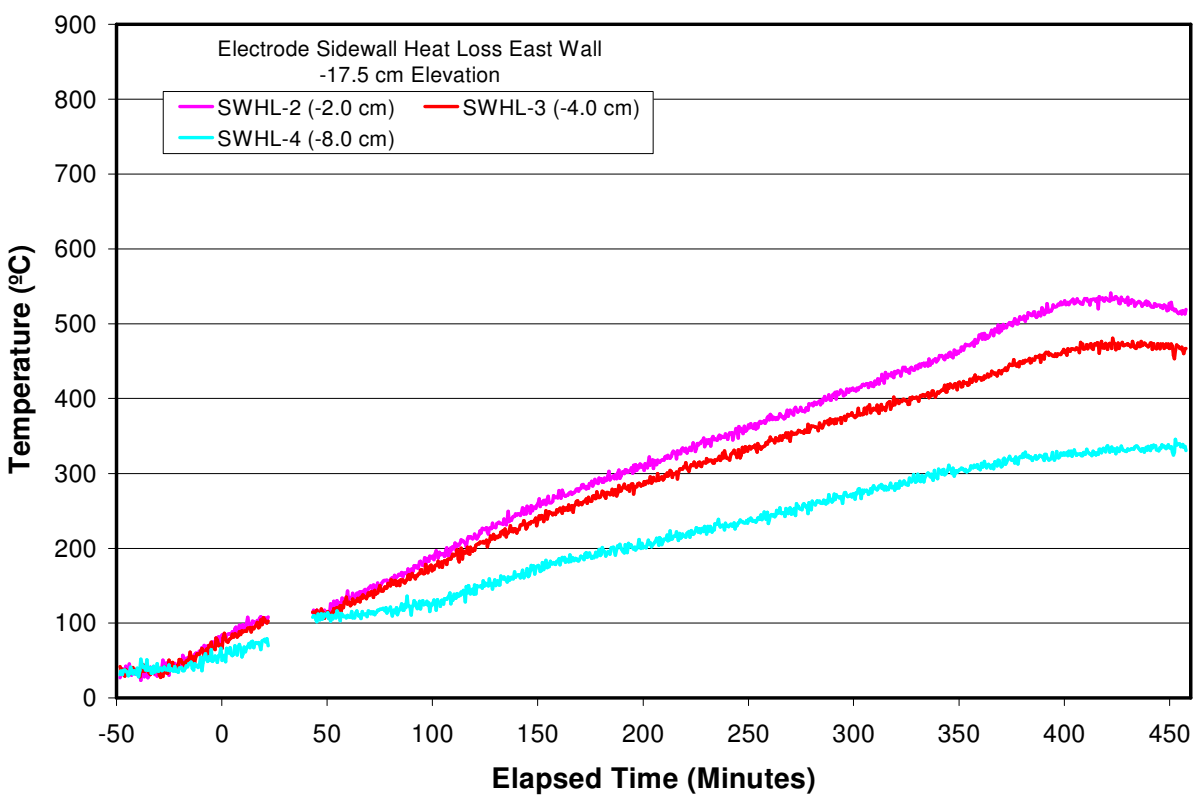

Figure 4-19. Test Section MgO Sidewall Heat Loss Data at -17.5 cm Elevation.

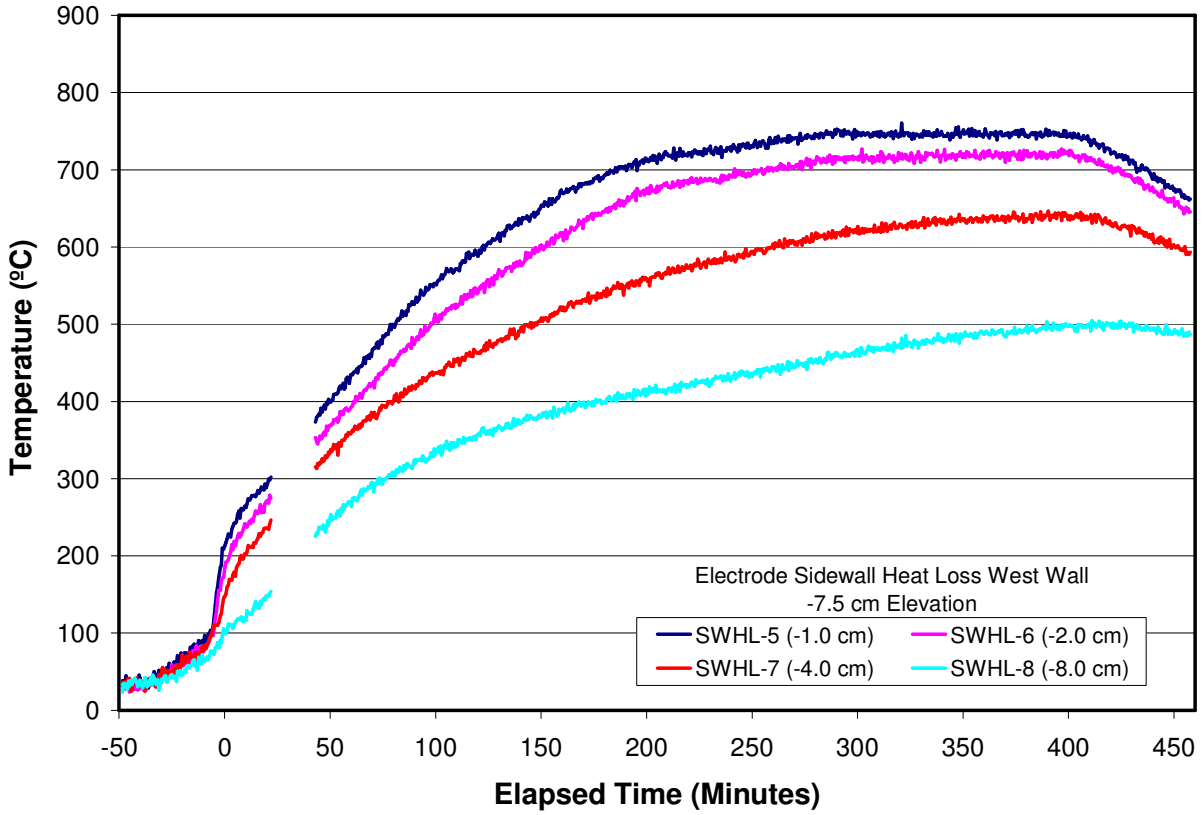

Figure 4-20. Test Section MgO Sidewall Heat Loss Data at -7.5 cm Elevation.

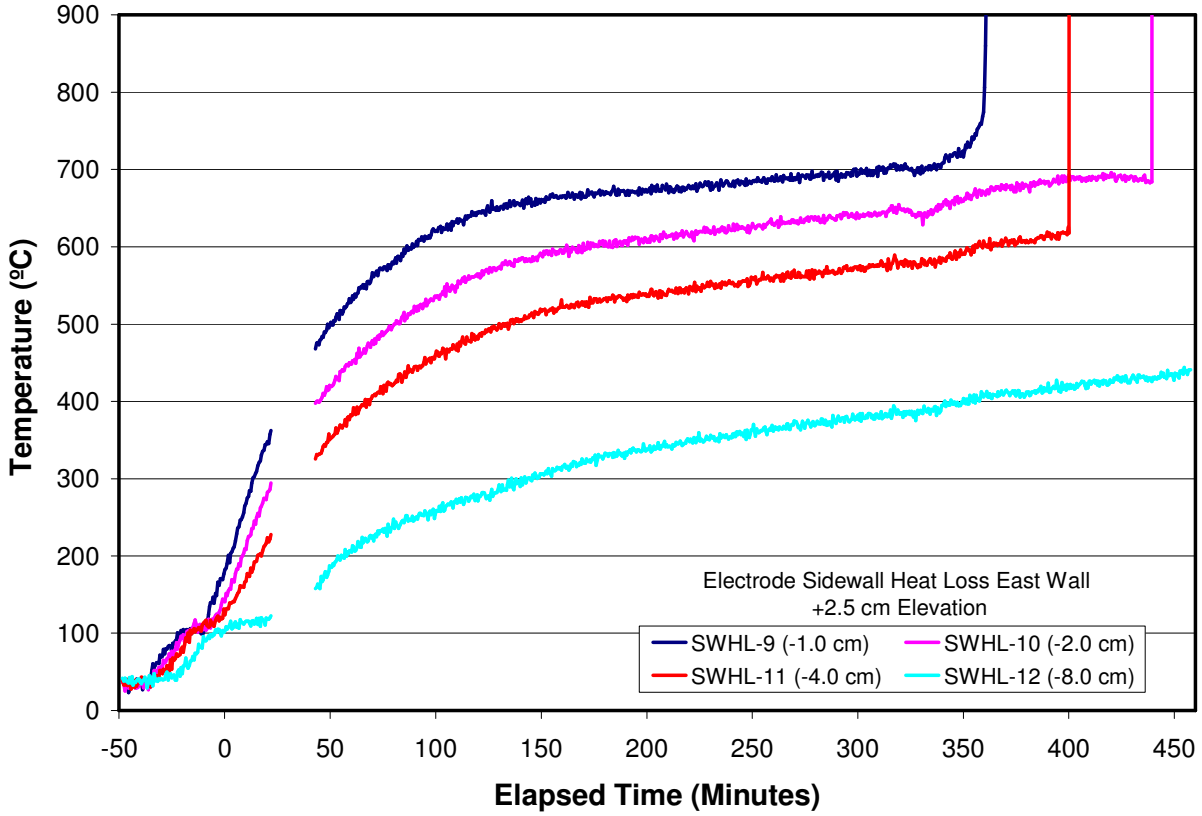

Figure 4-21. Test Section MgO Sidewall Heat Loss Data at +2.5 cm Elevation.

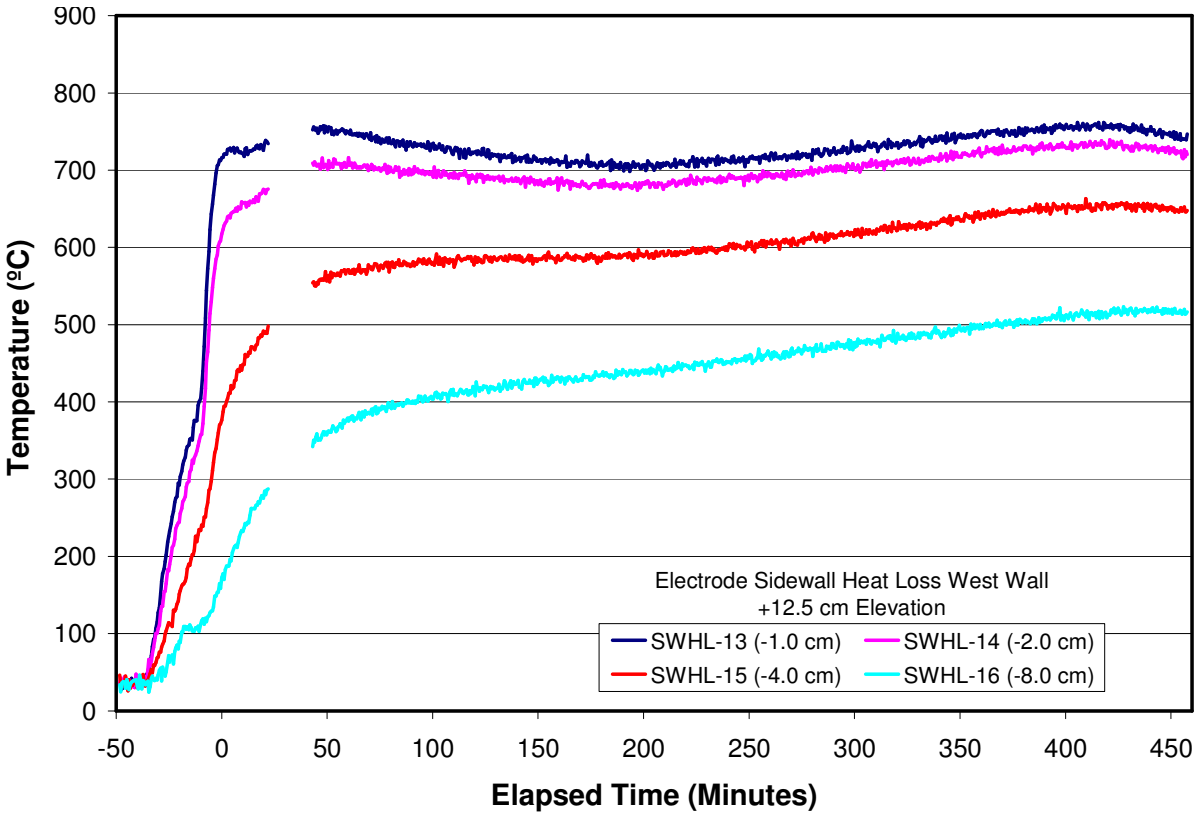

Figure 4-22. Test Section MgO Sidewall Heat Loss Data at +12.5 cm Elevation.

The local melt zone sidewall heat fluxes evaluated using the above methodology at the four array locations are shown collectively in Figure 4-23. The data vary, but generally the fluxes were $\leq$ 20 kW/m^2 over the majority of the test. Given the initial melt depth of 25 cm and MgO exposed sidewall width of 40 cm, then the initial heat losses to the MgO were ~ 2(0.25 m)•(0.40 m) •20 kW/m^2~ 4 kW, which is ~ 4% of the initial input power of 95 kW. However, as the posttest examinations revealed (see Section 4.7), the melt sidewall contact area may have been as high as 1.68 m^2 during the high voiding stages of the experiment (see Table 3-1), and thus heat losses during this stage may have been as high (1.68 m^2)•(20 kW/m^2) = 34 kW, which amounts to ~ 35 % of the total input power.

4.5 Crust Lance Data

Two key test objectives for CCI-4 were to: i) obtain in-situ crust strength data to supplement the room temperature strength database being assembled as part of the SSWICS program, and ii) provide information on the nature and the extent of the debris cooling that occurs after the crust fails. This subsection provides the results of the crust strength measurement, while the debris cooling data is provided in the next subsection.

As shown in Table 3-1, the lance was inserted in an attempt to fail the crust both prior to and after the cavity was flooded. The output from the lance force transducer is shown in Figure

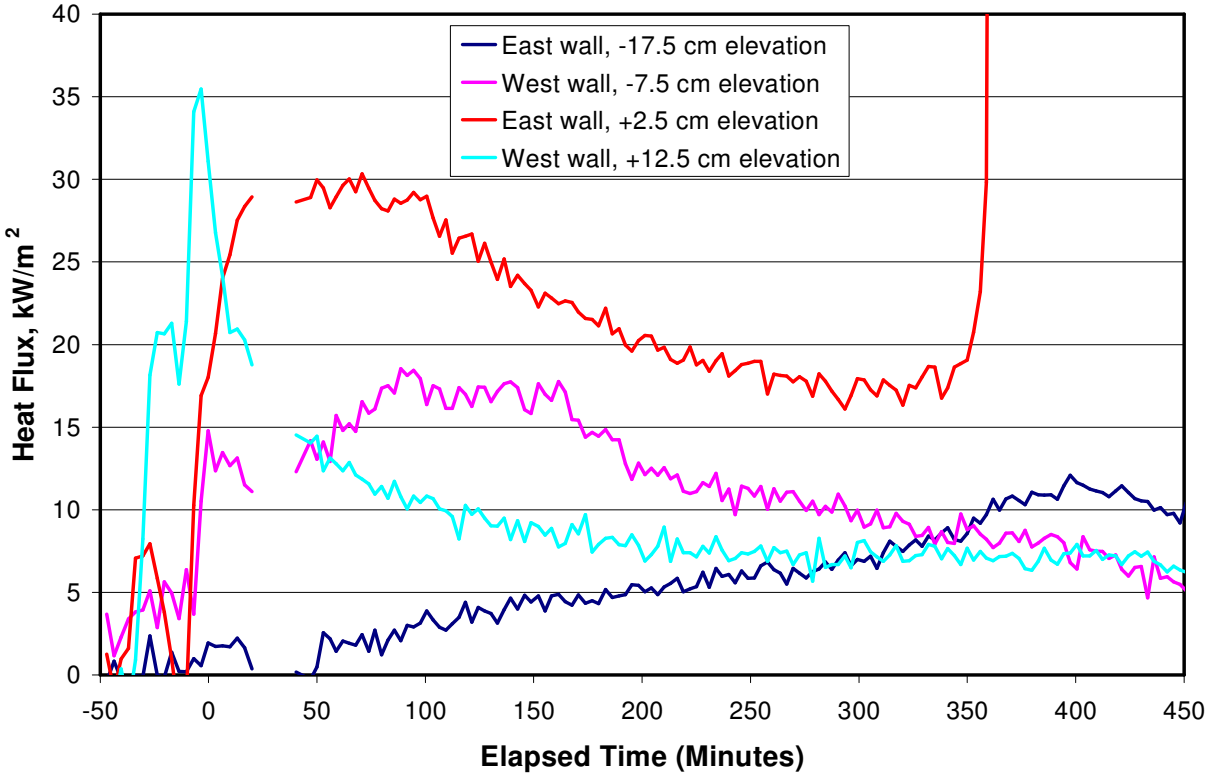

Figure 4-23. Local Heat Fluxes from the Melt to the Test Section Sidewalls.

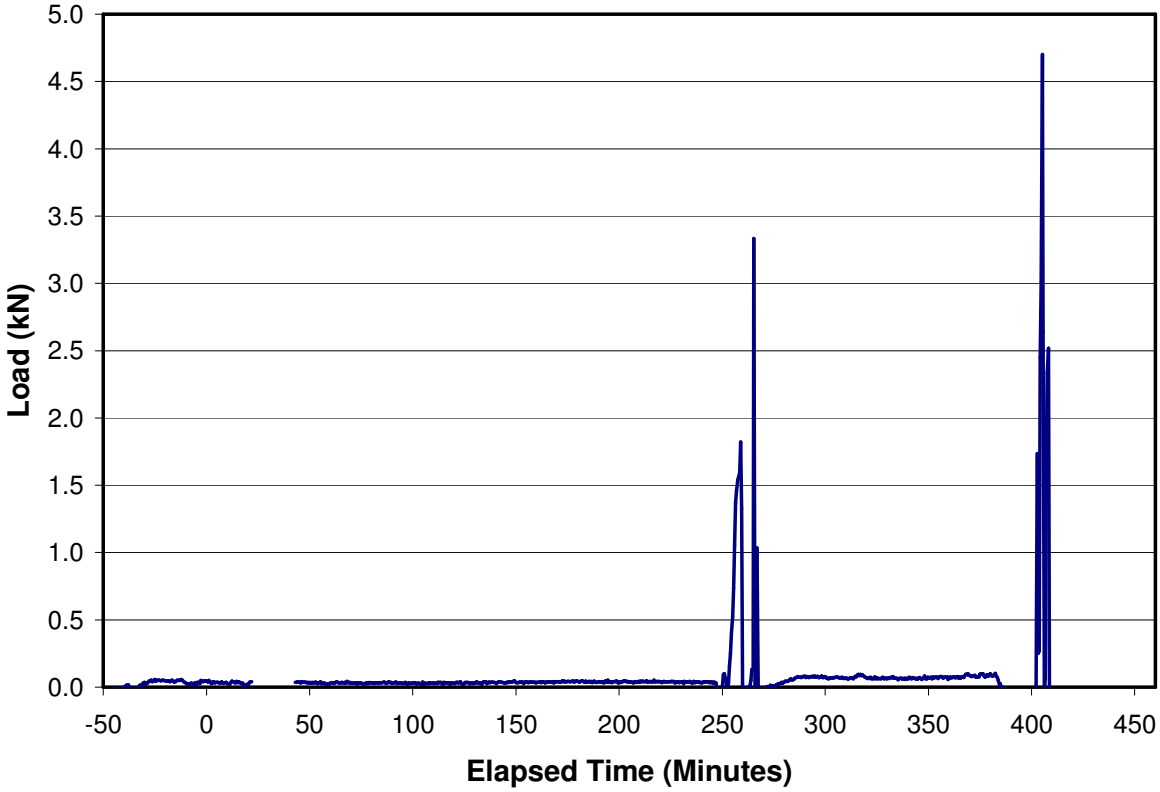

Figure 4-24. Load Force Exerted on Crust vs. Time.

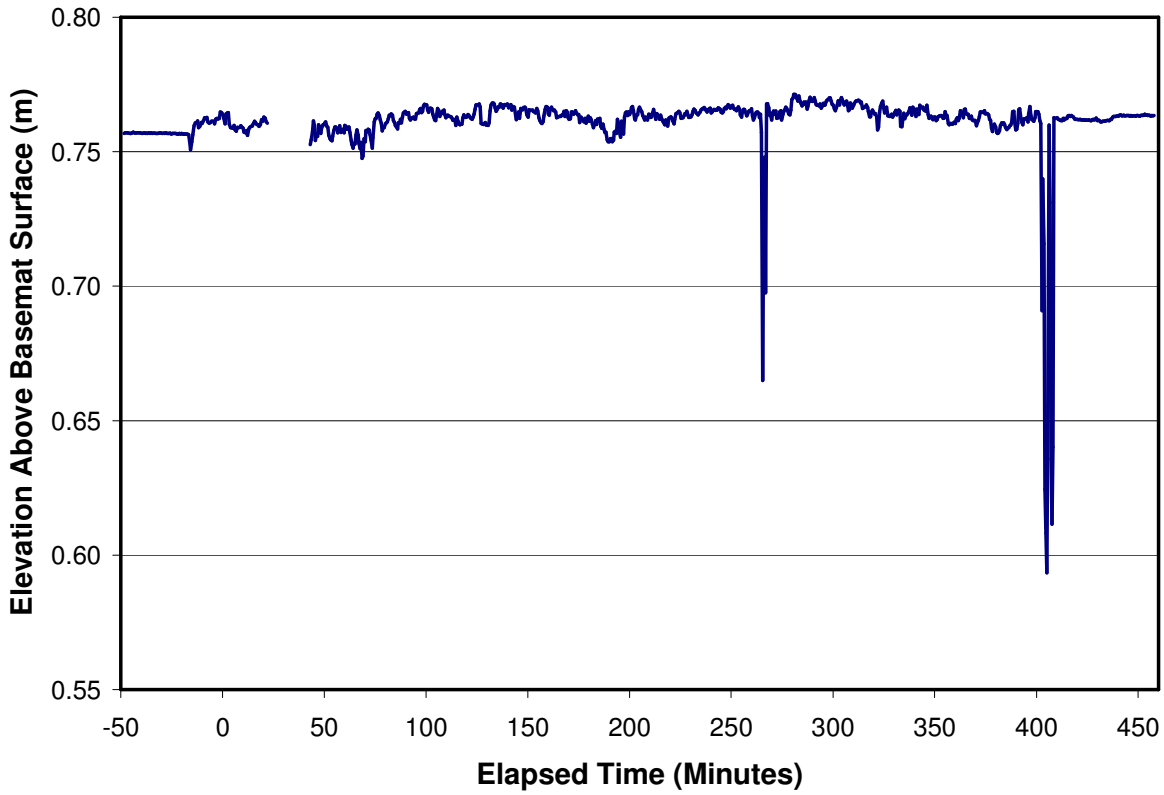

Figure 4-25. Lance Tip Elevation over Initial Concrete Surface.

4-24, while the displacement transducer output is shown in Figure 4-25. During the initial insertion sequence when the cavity was dry (i.e., from 259.2 to 267.4 minutes), a peak load of 3.33 kN was applied, but the crust was not breached. Surface elevation measurements were in the range of 66.5 - 69.8 cm at contact, which are significantly above the initial collapsed melt depth of 25 cm at the start of the test.

After cavity flooding at 384.9 minutes, the lance was inserted a second time from 403.3 to 407.8 minutes. Some breakage occurred on initial contact at an elevation of 69.1 cm, but the full material depth of the material was not penetrated to reveal the underlying melt. The peak load of 4.70 kN was applied; the surface elevation was reduced to ~ 60 cm after first breakage. The high crust surface elevations detected both before and after water addition are consistent with the mantle crust surface elevations determined as part of the posttest examinations (see Section 4.7). Since the applied loads were insufficient to completely puncture or dislodge the mantle, no crust strength or crust breach cooling data were obtained for CCI-4.

4.6 Corium Quench Rate

Another key test objective was to obtain data on the nature and extent of the corium quench process when flooding occurs late in the sequence. To first order, the debris cooling rate can be estimated based on the steaming rate from the test section; i.e.

$$q'' = \frac{h_{lv} \bullet \dot{m}_s}{A} \tag{4-3}$$

where h_{lv} is the water latent heat of vaporization at atmospheric pressure (2.256 MJ/kg), $\dot{m}_s$ is the steam mass flow rate, and A is the surface area of the debris in contact with the coolant. The steam flow rate was calculated by first performing a 6-point (~30 second) running average on the cumulative water level data in the primary quench tank (see Figure 4-26), and then calculating the derivative of the resultant dataset using a central differencing scheme. The corium cooling rate calculated using this approach is shown in Figure 4-6, assuming a test section cross-sectional area of 0.20 m^2. The flux calculated based on this assumed area varied from 2.4 MW/m^2 immediately after flooding, down to ~ 200 kW/m^2 at the time the test was terminated. However, note that posttest examination results indicated that the large mantle crust over the top of the debris prevented water from flooding beneath to cool the underlying melt. Thus, the heat flux shown in Figure 4-27 is indicative of the cooling rate of the mantle crust, and not of the underlying melt. As discussed in Section 4.5, the attempts to dislodge this material with the lance probe both prior to and after cavity flooding were unsuccessful.

4.7 Posttest Debris Examination and Chemical Analysis Results

Following the experiment, the apparatus was carefully disassembled to document the posttest debris configuration. Figure 4-28 provides a picture of the top surface of the mantle crust after removal of the top sidewall section, while Figure 4-29 provides a sketch of the surface showing key elevations and features. These initial views of the debris confirmed the presence of the large mantle crust at very high elevations relative to the initial collapsed melt depth, as

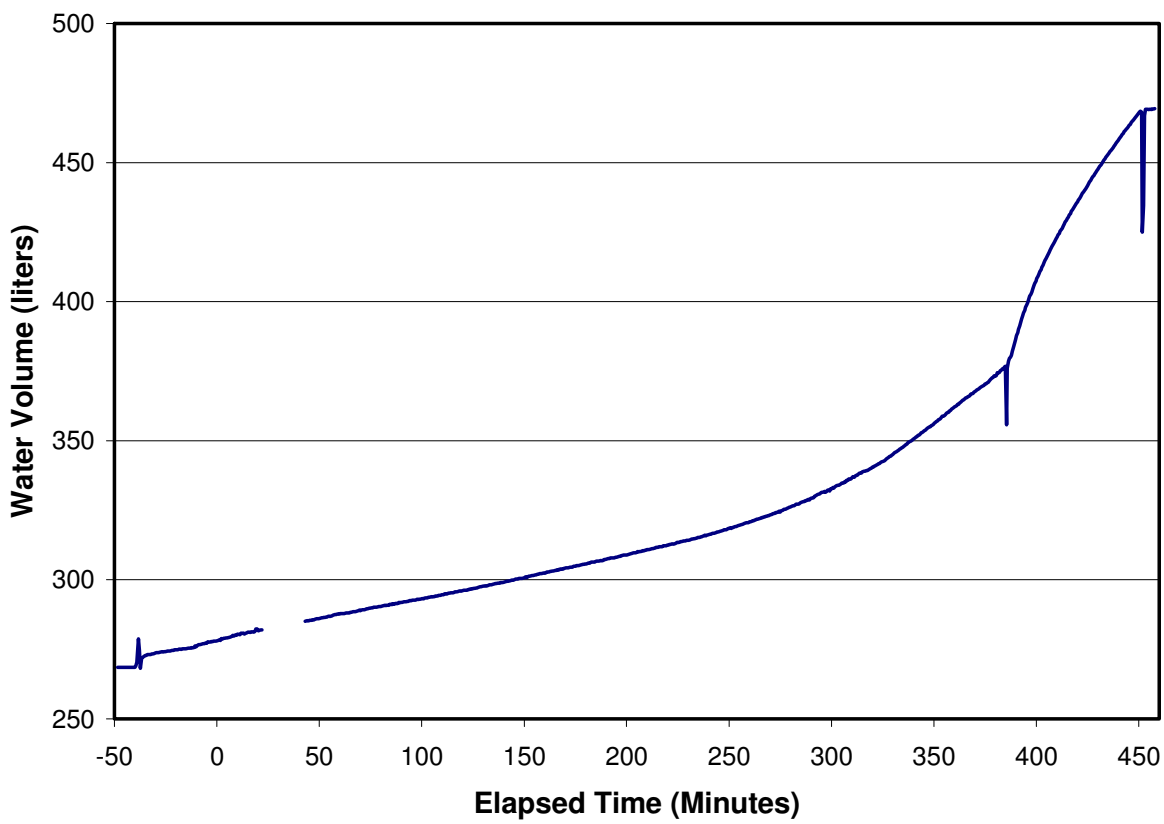

Figure 4-26. Quench Tank Water Volume vs. Time.

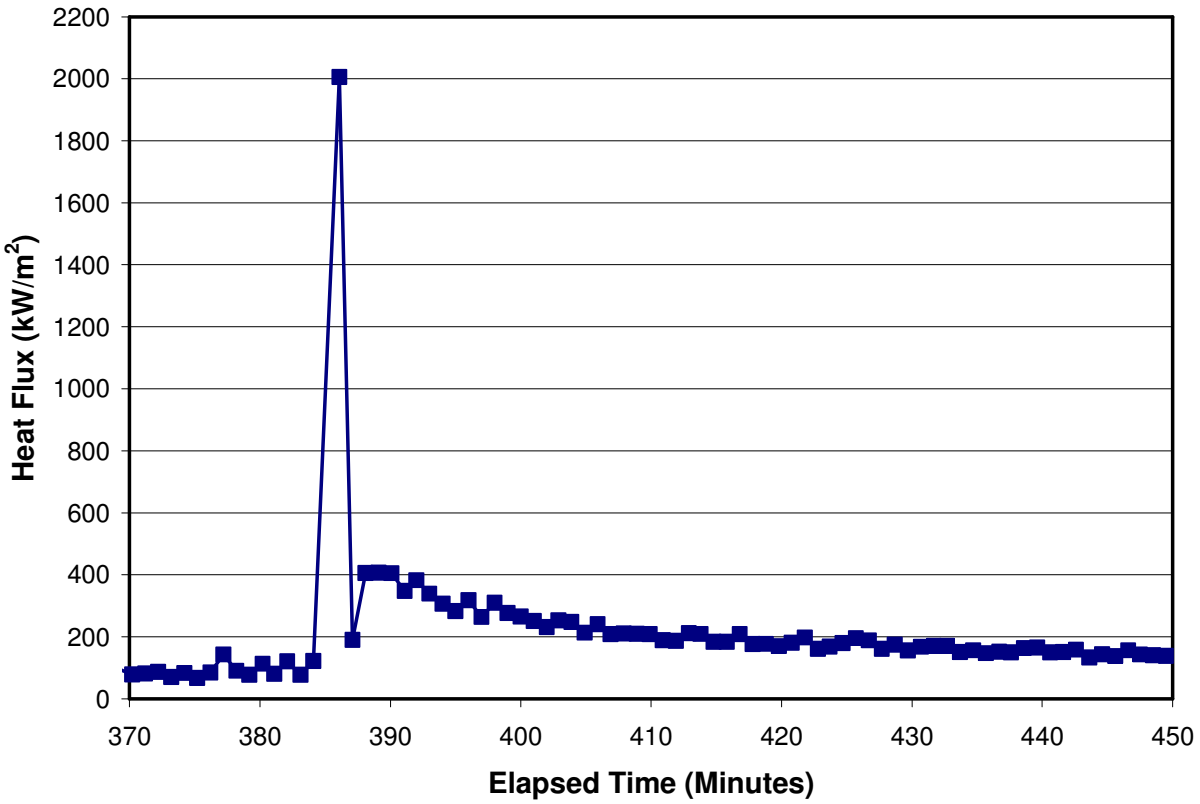

Figure 4-27. Debris Cooling Heat Flux Based on Steam Formation Rate.

Figure 4-28. Top View of Mantle Crust after Removal of the Top Sidewall Section.

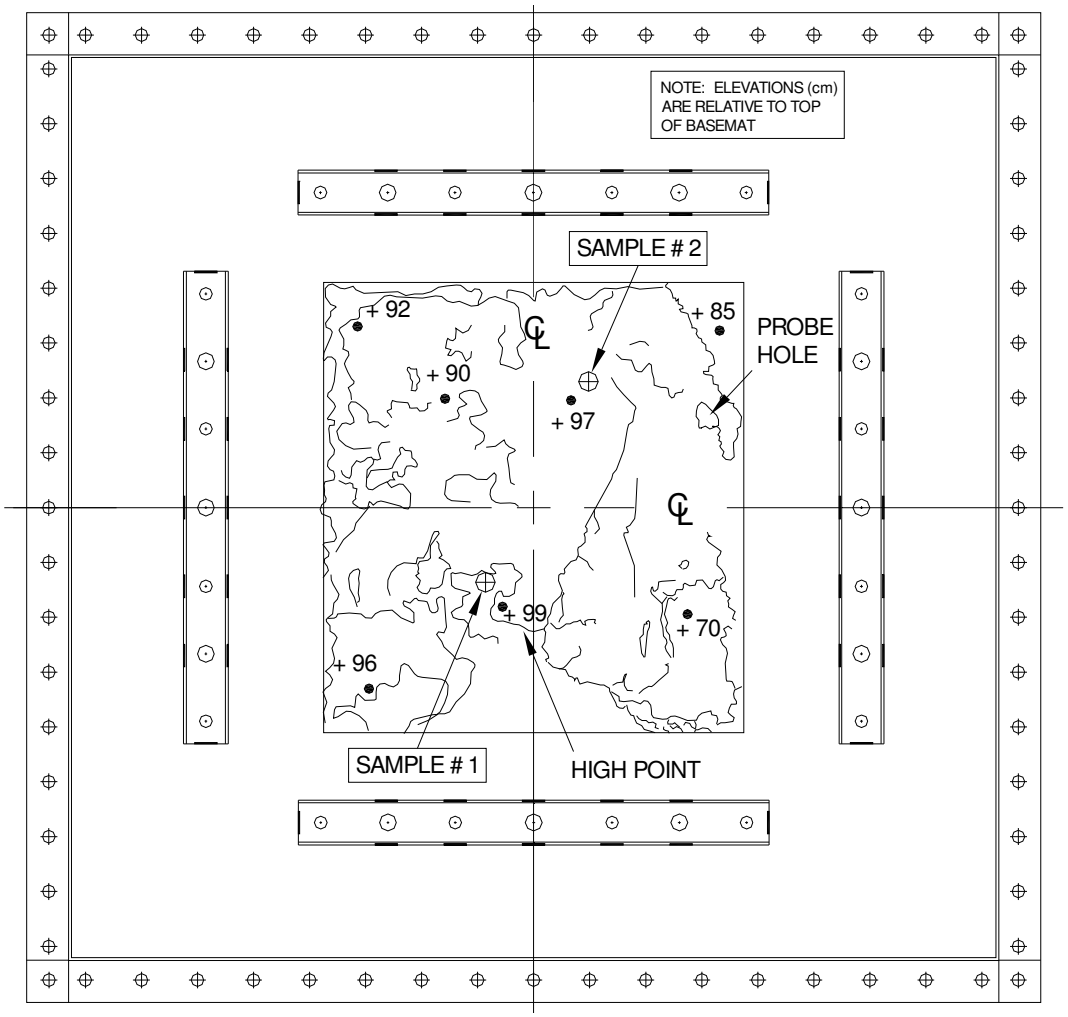

Figure 4-29. Topographical Map Showing Mantle Crust Surface Elevation Profile.

initially surmised from the crust lance elevation measurements made during the test (see Section 4.5). The axial distributions of this mantle are better illustrated in Figure 4-30, which provides renderings of the posttest debris configuration as viewed from the west (non-electrode) and south (electrode) sides of the test section. As indicated in Figure 4-29, the peak height of the mantle was at ~ 1 m elevation relative to the initial concrete surface. Based on the initial collapsed melt depth of 25 cm, then a melt void fraction of ~ 75% would have been required in order for the mantle to form at this elevation. Unlike test CCI-2, there were no discernable openings through this crust that would have allowed intimate melt-water contact to have occurred at the time of cavity flooding.

After key features of the crust were documented, this material was removed to gain access to the lower test section cavity. As shown in Figures 4-30, initial examinations indicated that the remaining corium was essentially in the form of a continuous layer that was distributed fairly uniformly over both the concrete and electrode sidewalls, as well as the concrete basemat. Photographs of the cavity after removal of the crust mantle and middle sidewall section are provided in Figure 4-31.

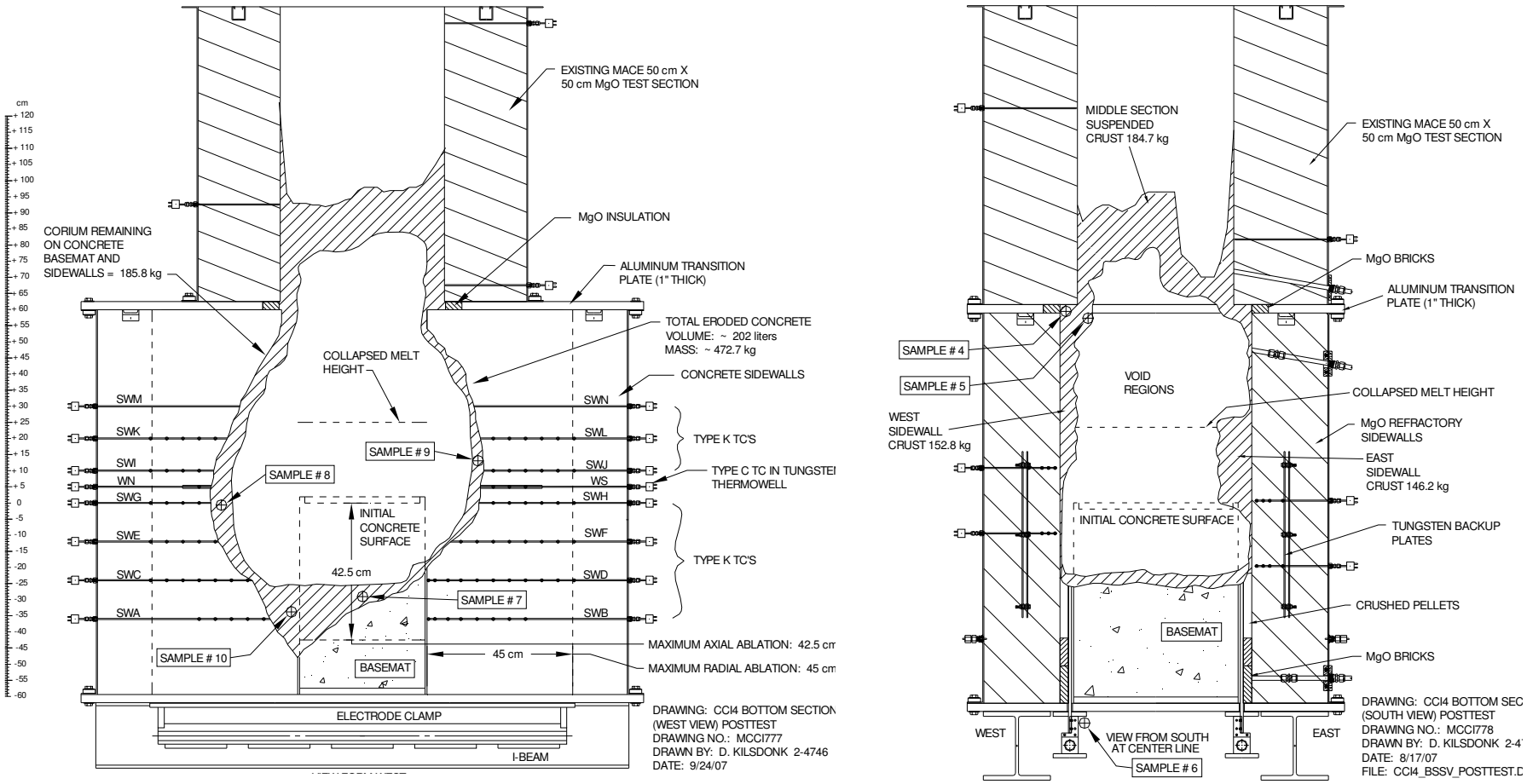

(a) **(b)**

Figure 4-30. (a) Electrode and (b) Nonelectrode Sidewall Views of the Solidified Debris.

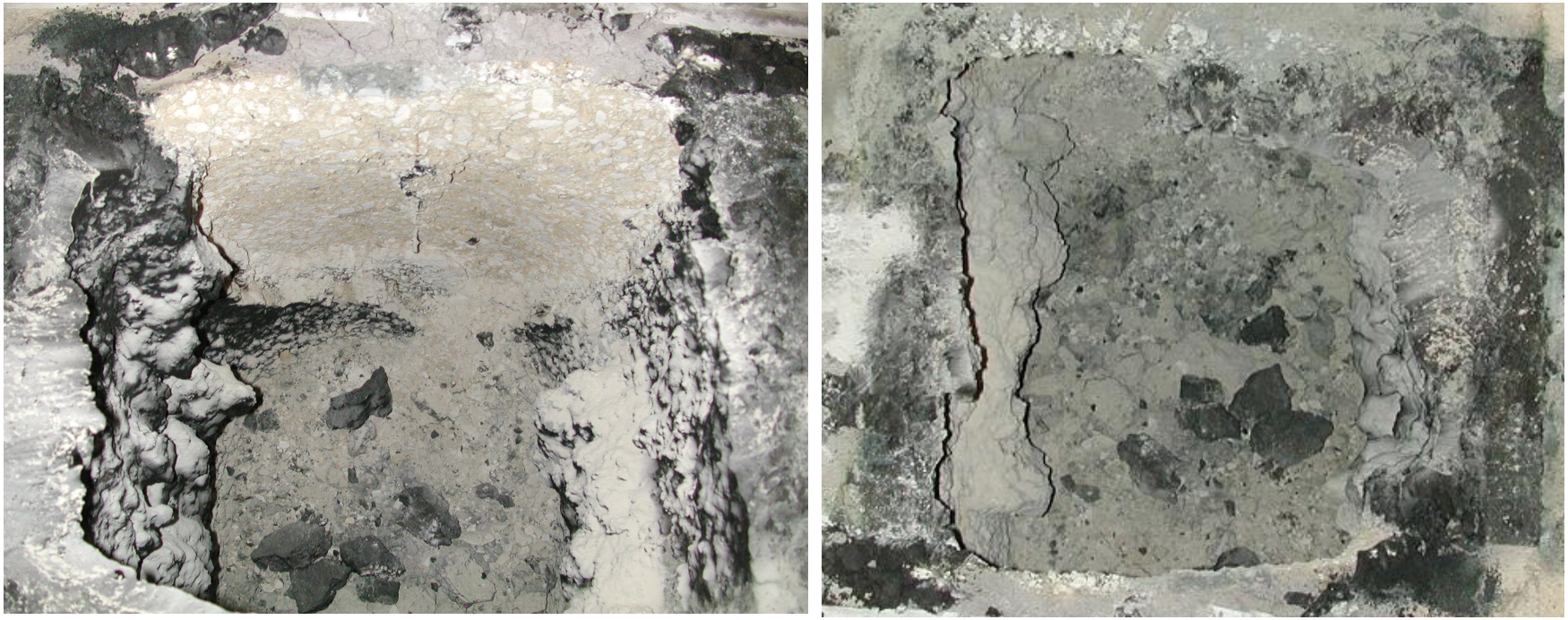

(a) **(b)**

Figure 4-31. (a) View Towards North and (b) South Concrete Sidewalls after Removal of Middle Sidewall Section.

(a) **(b)**

Figure 4-32. (a) Top and (b) West Side Views of Cavity After Removal of MgO Sidewalls.

With these steps completed, the inert MgO sidewalls were removed to gain additional information regarding the shape of the cavity erosion profile. Top and (west) side photographs taken after the sidewalls were removed are provided in Figure 4-32. As is evident from these pictures, cavity erosion was fairly symmetrical, and erosion in the upper region of the test section above the initial collapsed pool height was extensive. Erosion at the higher elevations was probably driven by radiation heat transfer from the melt surface during periods in which the melt pool was collapsed, and also by convective heat transfer directly from the melt pool itself when the pool was undergoing extensive voiding. Additional examinations during this stage indicated that melt had been extruded down into the ~ 3 mm wide gap between the concrete basemat and sidewalls on both the north and south sides of the test section from the top of the remaining basemat surface. On the north side of the test section, the melt was extruded all the way down to the test section bottom plate, eventually leading to plate breach and loss of melt confinement at 383.7 minutes (see Table 3-1). This extrusion behavior had not been observed in prior CCI tests. As discussed in Section 3, concrete decomposition gas venting out of bottom of test section due to sealing of the suspended mantle crust is believed to have been a key driver in this process. A close up photograph taken near the northeast corner of the basemat that shows the melt penetration in this corner is provided in Figure 4-33.

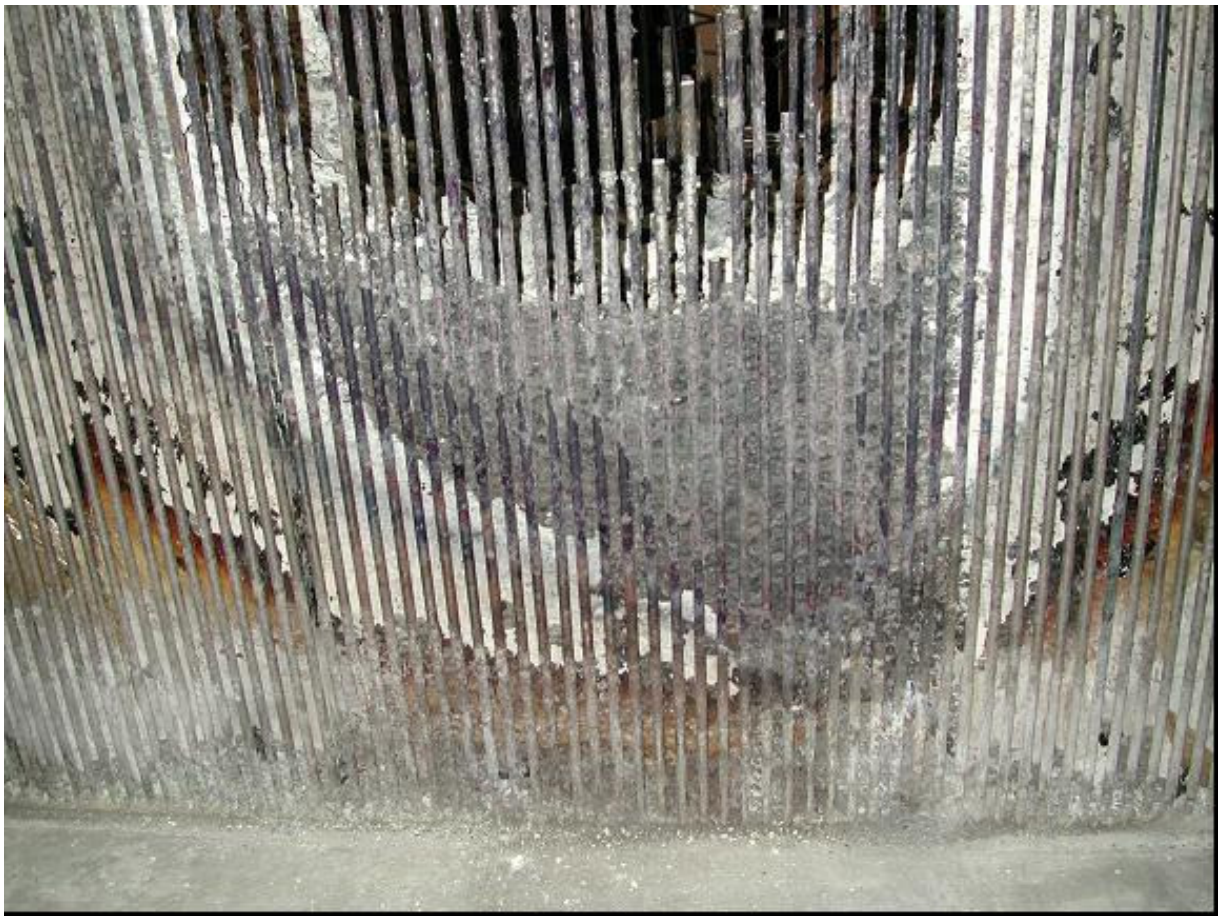

Figure 4-33. Close-up Photo of Northeast Basemat Corner Showing Melt Penetration

Following these examinations, the corium remaining over the basemat and sidewalls was removed and the balance of the test section completely disassembled to fully reveal the final

cavity erosion profile. A photograph showing the concrete components after removal is provided in Figure 4-34. The cavity erosion profile shown in Figure 4-30 (a) is based on contour measurements taken at the centerline of these specimens. Both sidewalls showed slightly concave ablation patterns azimuthally. Thus, the erosion pattern shown in Figure 4-30 is bounding with respect to lateral ablation; erosion near the edges was generally within 3 cm of that at the centerline at all axial elevations. In contrast, the basemat was tapered with the minimum erosion occurring in the southwest quadrant, and the maximum ablation occurring in the northeast quadrant. This is in contrast to previous CCI tests where the basemat ablation profile was fairly uniform. As discussed earlier, the odd erosion pattern for CCI-4 is felt to be due to gas venting out of the bottom of the test section late in the experiment sequence, as opposed to a naturally occurring phenomenological effect.

Figure 4-34. Concrete Basemat and Sidewalls after Complete Disassembly (view from the southwest).

During disassembly, the various debris regions were carefully segregated and weighed to better document the debris distribution. The pre- and posttest mass distributions are summarized in Table 4-1. Test CCI-4 was unique in that all corium was recovered and placed into buckets that could be weighed after the experiment. On this basis, a mass balance could be performed. As shown in Table 4-1, of the nearly 1000 kg of material involved in the experiment, all was recovered except for 20.8 kg, which amounts to ~ 2.1 wt% of the entire material mass.

As the corium remnants were collected, they were examined to determine if there was any trace of the metals present at the start of the interaction (see Table 2-8). These examinations did not reveal the presence of any discrete metal regions, or any small metal inclusions dispersed within the oxide phase. However, this should come as no surprise since more than enough concrete decomposition gas was generated during the test to fully oxidize all metals present at the start of the interaction.

As the debris was removed, samples were collected for chemical analysis by Inductively Coupled Plasma Atomic Emission Spectroscopy (ICP/AES). Sample locations are shown in Figures 4-29 and 4-30. Key results from the analysis of seven of these samples are provided in Table 4-2. The compositions shown in the table have been simplified in the form of core, structural, and concrete oxides; the complete set of raw data is provided in Appendix C. Also provided in the table is an estimate of the end-of-test average melt composition that was formulated by taking the melt composition at the start of the test (see Table 2-8), oxidizing all the metals, and then incorporating the slag from the decomposition of 472.7 of concrete that was eroded during the test (see Figure 4-30). All samples contained elevated concrete content except for Sample No. 4 that was obtained near the MgO in the upper region of the test section. This sample was probably deposited during, or soon after, the thermite burn and therefore the composition is representative of the initial melt (see Table 2-7). Note that the elevated concrete levels in both samples obtained from the mantle crust (i.e., Nos. 1 and 5) are consistent with mantle formation and growth late in the experiment sequence, which is consistent with visual data obtained from the lid video camera (see Table 3-1). This confirms that the mantle was not formed by some test artifact; e.g., a remnant of the thermite burn. Finally, the four samples taken from the interior of the corium cavity below the mantle crust reveal that concrete erosion continued after sealing off of the mantle crust (as evidenced by the comparatively high concrete content of Sample Nos. 7-9 compared to 1 and 4), and that the bulk material in the north-east corner of the test section (Sample No. 10) had higher fuel content relative to the balance of the samples. It is not known whether this situation was present during the experiment, or developed after the test was terminated due to density-driven stratification.

Table 4-1. CCI-4 Pre- and Posttest Mass Balances.

Test Conduct		Posttest	
Constituent	**Mass (kg)**	**Debris Region**	**Mass (kg)**
Thermite Reaction Products (see Table 2-5)	+265.0	Mantle Crust (Figure 4-31)	184.7
Inserts (see Table 2-6).	+36.6	West Electrode Sidewall Crust (Figure 4-31)	152.8
Total Eroded Concrete from Cavity (Figure 4-30)	+472.7	East Electrode Sidewall Crust (Figure 4-31)	146.2
H_2O and CO_2 lost from Concrete Decomposition[a]	-145.6	Concrete Basemat and Sidewalls (Figure 4-30)	185.8
Oxygen Uptake from Metals Oxidation[b]	+15.4	Recovered UO_2 pellet liner	290.9
Installed UO_2 pellet liner	+368.3		
Total	981.2	Total	960.4

[a]Includes that lost from cavity erosion and concrete in inserts assuming a mass loss of 30.80 wt % upon decomposition; see Table 2-3.
[b]Zr and Fe from Inserts (Table 2-6); Cr from thermite reaction (Table 2-5). Assumed oxidation products are ZrO_2, FeO, and Cr_2O_3.

Table 4-2. Bulk Chemical Analysis Results for Samples Collected from CCI-4 Posttest Debris.

Oxide	1 Upper surface bridge crust	4 Near bottom of bridge crust close to MgO	5 Near bottom of bridge crust close to cavity interior	7 Bulk material over basemat	8 Bulk material from north concrete wall	9 Bulk material from south concrete wall	10 Bulk material from pit in NE corner of basemat	Estimated End-of-Test Composition
UO_2	16.80	68.91	19.47	12.88	13.00	14.09	36.34	26.31
ZrO_2	10.79	19.73	12.47	7.73	8.01	8.30	8.24	12.93
Cr_2O_3	0.37	0.36	0.43	0.31	0.34	0.41	0.41	2.01
Fe_2O_3	3.53	0.05	2.82	3.75	3.54	3.32	1.63	3.19
concrete	68.50	10.95	64.81	75.32	75.10	73.89	53.39	55.56
Total	100.00	100.00	100.00	100.00	100.00	100.00	100.00	100.00

5.0 REFERENCES

1. M. T. Farmer, S. Lomperski, D. J. Kilsdonk, and R. W. Aeschlimann, "OECD MCCI Project 2-D Core Concrete Interaction (CCI) Tests: Final Report," OECD/MCCI-2005-TR05, January 2, 2006.

2. M. T. Farmer, R. W. Aeschlimann, D. J. Kilsdonk, and, S. Lomperski, "2-D Core Concrete Interaction (CCI) Tests: CCI-4 Quick Look Data Report," OECD/MCCI-2007-TR04, June 2007.

3. Summary Record of the First Meeting of the Management Board of the OECD MCCI-2 Project, NEA Headquarters, Paris France 4-5 April 2006.

4. D. H. Thompson, M. T. Farmer, J. K. Fink, D. R. Armstrong, and B. W. Spencer, "ACE Phase C Final Report: Volume I-MCCI Thermalhydraulic Results," EPRI/ACE-TR-C42, September, 1997.

5. B. W. Spencer, et al., "MACE Scoping Test Data Report," ACE-TR-D03, June, 1991.

6. M. T. Farmer, D. J. Kilsdonk, S. Lomperski, and R. W. Aeschlimann, "2-D Core Concrete Interaction (CCI) Tests: CCI-4 Test Plan," OECD/MCCI-2007-TR03, Rev. 0, February, 2007.

7. E. R. Copus, et al., "Core-Concrete Interactions Using Molten Steel with Zirconium on a Basaltic Basemat: The SURC-4 Experiment," NUREG/CR-4994, April, 1989.

APPENDIX A
Data Acquisition System Channel Assignments

This Appendix provides the channel assignments for the three independent DAS systems that were used to record the data for CCI-4. For convenience, these three 128 channel systems were referred to the "Basemat", "Power," and "Quench" systems by operating personnel. The channel assignment lists for each of these three systems are provided in Tables A-1 through A-3. The data recorded on each of these channels is provided in Appendix B.

Table A-1. "Basemat" DAS Channel Assignments for CCI-4.

Channel	Variable	Sensor	Location	Level	Range/Limit	Accuracy	Notes
00	T	Diode Sensor	TC compensation Chs. B01-B49		130 C		
01	T	TC Type C	Basemat 0.0 cm, +1.9 cm WCL-1	+15.0 cm	2320 C	± 1%	
02	T	TC Type C	Basemat 0.0 cm, +1.9 cm WCL-2	+10.0 cm	2320 C	± 1%	
03	T	TC Type C	Basemat 0.0 cm, +1.9 cm WCL-3	+5.0 cm	2320 C	± 1%	
04	T	TC Type C	Basemat 0.0 cm, +1.9 cm WCL-4	0.0 cm	2320 C	± 1%	
05	T	TC Type C	Basemat -10.6 cm, +8.1 cm WNW-1	+9.0 cm	2320 C	± 1%	
06	T	TC Type C	Basemat -10.6 cm, +8.1 cm WNW-2	+4.0 cm	2320 C	± 1%	
07	T	TC Type C	Basemat -10.6 cm, +8.1 cm WNW-3	-1.0 cm	2320 C	± 1%	
08	T	TC Type C	Basemat -10.6 cm, +8.1 cm WNW-4	-6.0 cm	2320 C	± 1%	
09	T	TC Type C	Basemat +10.6 cm, +8.1 cm WNE-1	-3.0 cm	2320 C	± 1%	
10	T	TC Type C	Basemat +10.6 cm, +8.1 cm WNE-2	-8.0 cm	2320 C	± 1%	
11	T	TC Type C	Basemat +10.6 cm, +8.1 cm WNE-3	-13.0 cm	2320 C	± 1%	
12	T	TC Type C	Basemat +10.6 cm, +8.1 cm WNE-4	-18.0 cm	2320 C	± 1%	
13	T	TC Type C	Basemat +10.6 cm, -8.1 cm WSE-1	+3.0 cm	2320 C	± 1%	
14	T	TC Type C	Basemat +10.6 cm, -8.1 cm WSE-2	-2.0 cm	2320 C	± 1%	
15	T	TC Type C	Basemat +10.6 cm, -8.1 cm WSE-3	-7.0 cm	2320 C	± 1%	
16	T	TC Type C	Basemat +10.6 cm, -8.1 cm WSE-4	-12.0 cm	2320 C	± 1%	
17	T	TC Type C	Basemat -10.6 cm, -8.1 cm WSW-1	-9.0 cm	2320 C	± 1%	
18	T	TC Type C	Basemat -10.6 cm, -8.1 cm WSW-2	-14.0 cm	2320 C	± 1%	
19	T	TC Type C	Basemat -10.6 cm, -8.1 cm WSW-3	-19.0 cm	2320 C	± 1%	
20	T	TC Type C	Basemat -10.6 cm, -8.1 cm WSW-4	-24.0 cm	2320 C	± 1%	
21	T	TC Type C	N Sidewall, 0.0 cm deep, WN-1	+5.0 cm	2320 C	± 1%	
22	T	TC Type C	N Sidewall, 2.5 cm deep, WN-2	+5.0 cm	2320 C	± 1%	
23	T	TC Type C	N Sidewall, 5.0 cm deep, WN-3	+5.0 cm	2320 C	± 1%	
24	T	TC Type C	N Sidewall, 10.0 cm deep, WN-4	+5.0 cm	2320 C	± 1%	
25	T	TC Type C	S Sidewall, 0.0 cm deep, WS-1	+5.0 cm	2320 C	± 1%	
26	T	TC Type C	S Sidewall, 2.5 cm deep, WS-2	+5.0 cm	2320 C	± 1%	

27	T	TC Type C	S Sidewall, 5.0 cm deep, WS-3	+5.0 cm	2320 C	± 1%	
28	T	TC Type C	S Sidewall, 10.0 cm deep, WS-4	+5.0 cm	2320 C	± 1%	
29	T	TC Type K	Basemat 0.0 cm, -1.9 cm A-1	0.0 cm	1400 C	± 0.75%	
30	T	TC Type K	Basemat 0.0 cm, -1.9 cm A-2	-2.5 cm	1400 C	± 0.75%	
31	T	TC Type K	Basemat 0.0 cm, -1.9 cm A-3	-5.0 cm	1400 C	± 0.75%	
32	T	TC Type K	Basemat 0.0 cm, -1.9 cm A-4	-7.5 cm	1400 C	± 0.75%	
33	T	TC Type K	Basemat 0.0 cm, -1.9 cm A-5	-12.5 cm	1400 C	± 0.75%	
34	T	TC Type K	Basemat 0.0 cm, -1.9 cm A-6	-17.5 cm	1400 C	± 0.75%	
35	T	TC Type K	Basemat 0.0 cm, -1.9 cm A-7	-22.5 cm	1400 C	± 0.75%	
36	T	TC Type K	Basemat 0.0 cm, -1.9 cm A-8	-27.5 cm	1400 C	± 0.75%	
37	T	TC Type K	Basemat 0.0 cm, -1.9 cm A-9	-32.5 cm	1400 C	± 0.75%	
38	T	TC Type K	Basemat 0.0 cm, -1.9 cm A-10	-37.5 cm	1400 C	± 0.75%	
39	T	TC Type K	Basemat 0.0 cm, -1.9 cm A-11	-42.5 cm	1400 C	± 0.75%	
40	T	TC Type K	Basemat –12.5 cm, +10.0 cm B-1	0.0 cm	1400 C	± 0.75%	
41	T	TC Type K	Basemat –12.5 cm, +10.0 cm B-2	-2.5 cm	1400 C	± 0.75%	
42	T	TC Type K	Basemat –12.5 cm, +10.0 cm B-3	-7.5 cm	1400 C	± 0.75%	
43	T	TC Type K	Basemat –12.5 cm, +10.0 cm B-4	-12.5 cm	1400 C	± 0.75%	
44	T	TC Type K	Basemat –12.5 cm, +10.0 cm B-5	-17.5 cm	1400 C	± 0.75%	
45	T	TC Type K	Basemat –12.5 cm, +10.0 cm B-6	-22.5 cm	1400 C	± 0.75%	
46	T	TC Type K	Basemat –12.5 cm, +10.0 cm B-7	-27.5 cm	1400 C	± 0.75%	
47	T	TC Type K	Basemat –12.5 cm, +10.0 cm B-8	-35.0 cm	1400 C	± 0.75%	
48	T	TC Type K	Basemat –12.5 cm, +10.0 cm B-9	-42.5 cm	1400 C	± 0.75%	
49	T	TC Type K	N Sidewall 35.0 cm deep SWK-9	+20.0 cm	1400 C	± 0.75%	
50	T	Diode Sensor	TC compensation Chs. B51-B99		130 C		
51	T	TC Type K	Basemat +12.5 cm, +10.0 cm C-1	0.0 cm	1400 C	± 0.75%	
52	T	TC Type K	Basemat +12.5 cm, +10.0 cm C-2	-2.5 cm	1400 C	± 0.75%	
53	T	TC Type K	Basemat +12.5 cm, +10.0 cm C-3	-7.5 cm	1400 C	± 0.75%	
54	T	TC Type K	Basemat +12.5 cm, +10.0 cm C-4	-12.5 cm	1400 C	± 0.75%	
55	T	TC Type K	Basemat +12.5 cm, +10.0 cm C-5	-17.5 cm	1400 C	± 0.75%	

56	T	TC Type K	Basemat +12.5 cm, +10.0 cm C-6	-22.5 cm	1400 C	± 0.75%	
57	T	TC Type K	Basemat +12.5 cm, +10.0 cm C-7	-27.5 cm	1400 C	± 0.75%	
58	T	TC Type K	Basemat +12.5 cm, +10.0 cm C-8	-35.0 cm	1400 C	± 0.75%	
59	T	TC Type K	Basemat +12.5 cm, +10.0 cm C-9	-42.5 cm	1400 C	± 0.75%	
60	T	TC Type K	N Sidewall 40.0 cm deep SWK-10	+20.0 cm	1400 C	± 0.75%	
61	T	TC Type K	Basemat +12.5 cm, -10.0 cm D-1	0.0 cm	1400 C	± 0.75%	
62	T	TC Type K	Basemat +12.5 cm, -10.0 cm D-2	-2.5 cm	1400 C	± 0.75%	
63	T	TC Type K	Basemat +12.5 cm, -10.0 cm D-3	-7.5 cm	1400 C	± 0.75%	
64	T	TC Type K	Basemat +12.5 cm, -10.0 cm D-4	-12.5 cm	1400 C	± 0.75%	
65	T	TC Type K	Basemat +12.5 cm, -10.0 cm D-5	-17.5 cm	1400 C	± 0.75%	
66	T	TC Type K	Basemat +12.5 cm, -10.0 cm D-6	-22.5 cm	1400 C	± 0.75%	
67	T	TC Type K	Basemat +12.5 cm, -10.0 cm D-7	-27.5 cm	1400 C	± 0.75%	
68	T	TC Type K	Basemat +12.5 cm, -10.0 cm D-8	-35.0 cm	1400 C	± 0.75%	
69	T	TC Type K	Basemat +12.5 cm, -10.0 cm D-9	-42.5 cm	1400 C	± 0.75%	
70	T	TC Type K	N Sidewall 45.0 cm deep SWK-11	+20.0 cm	1400 C	± 0.75%	
71	T	TC Type K	Basemat -12.5 cm, -10.0 cm E-1	0.0 cm	1400 C	± 0.75%	
72	T	TC Type K	Basemat -12.5 cm, -10.0 cm E-2	-2.5 cm	1400 C	± 0.75%	
73	T	TC Type K	Basemat -12.5 cm, -10.0 cm E-3	-7.5 cm	1400 C	± 0.75%	
74	T	TC Type K	Basemat -12.5 cm, -10.0 cm E-4	-12.5 cm	1400 C	± 0.75%	
75	T	TC Type K	Basemat -12.5 cm, -10.0 cm E-5	-17.5 cm	1400 C	± 0.75%	
76	T	TC Type K	Basemat -12.5 cm, -10.0 cm E-6	-22.5 cm	1400 C	± 0.75%	
77	T	TC Type K	Basemat -12.5 cm, -10.0 cm E-7	-27.5 cm	1400 C	± 0.75%	
78	T	TC Type K	Basemat -12.5 cm, -10.0 cm E-8	-35.0 cm	1400 C	± 0.75%	
79	T	TC Type K	Basemat -12.5 cm, -10.0 cm E-9	-42.5 cm	1400 C	± 0.75%	
80	T	TC Type K	S Sidewall 35.0 cm deep SWL-9	+20.0 cm	1400 C	± 0.75%	
81	T	TC Type K	N Sidewall 0.0 cm deep SWA-1	-36.0 cm	1400 C	± 0.75%	
82	T	TC Type K	N Sidewall 2.0 cm deep SWA-2	-36.0 cm	1400 C	± 0.75%	
83	T	TC Type K	N Sidewall 6.0 cm deep SWA-3	-36.0 cm	1400 C	± 0.75%	
84	T	TC Type K	N Sidewall 10.0 cm deep SWA-4	-36.0 cm	1400 C	± 0.75%	

85	T	TC Type K	N Sidewall 15.0 cm deep SWA-5	-36.0 cm	1400 C	± 0.75%	
86	T	TC Type K	N Sidewall 20.0 cm deep SWA-6	-36.0 cm	1400 C	± 0.75%	
87	T	TC Type K	N Sidewall 25.0 cm deep SWA-7	-36.0 cm	1400 C	± 0.75%	
88	T	TC Type K	N Sidewall 30.0 cm deep SWA-8	-36.0 cm	1400 C	± 0.75%	
89	T	TC Type K	S Sidewall 0.0 cm deep SWB-1	-36.0 cm	1400 C	± 0.75%	
90	T	TC Type K	S Sidewall 2.0 cm deep SWB-2	-36.0 cm	1400 C	± 0.75%	
91	T	TC Type K	S Sidewall 6.0 cm deep SWB-3	-36.0 cm	1400 C	± 0.75%	
92	T	TC Type K	S Sidewall 10.0 cm deep SWB-4	-36.0 cm	1400 C	± 0.75%	
93	T	TC Type K	S Sidewall 15.0 cm deep SWB-5	-36.0 cm	1400 C	± 0.75%	
94	T	TC Type K	S Sidewall 20.0 cm deep SWB-6	-36.0 cm	1400 C	± 0.75%	
95	T	TC Type K	S Sidewall 25.0 cm deep SWB-7	-36.0 cm	1400 C	± 0.75%	
96	T	TC Type K	S Sidewall 30.0 cm deep SWB-8	-36.0 cm	1400 C	± 0.75%	
97	T	TC Type K	N Sidewall 0.0 cm deep SWC-1	-24.0 cm	1400 C	± 0.75%	
98	T	TC Type K	N Sidewall 2.0 cm deep SWC-2	-24.0 cm	1400 C	± 0.75%	
99	T	TC Type K	N Sidewall 6.0 cm deep SWC-3	-24.0 cm	1400 C	± 0.75%	

Explanation of Variable Notations
T = temperature

Table A-2. "Power" DAS Channel Assignments for CCI-4.

Channel	Variable	Sensor	Location	Level	Range/Limit	Accuracy	Notes
00	T	TC Type K	S Sidewall 40.0 cm deep SWL-10	+20.0 cm	1400 C	± 0.75%	
01	T	TC Type K	N Sidewall 10.0 cm deep SWC-4	-24.0 cm	1400 C	± 0.75%	
02	T	TC Type K	N Sidewall 15.0 cm deep SWC-5	-24.0 cm	1400 C	± 0.75%	
03	T	TC Type K	N Sidewall 20.0 cm deep SWC-6	-24.0 cm	1400 C	± 0.75%	
04	T	TC Type K	N Sidewall 25.0 cm deep SWC-7	-24.0 cm	1400 C	± 0.75%	
05	T	TC Type K	N Sidewall 30.0 cm deep SWC-8	-24.0 cm	1400 C	± 0.75%	
06	T	TC Type K	N Sidewall 35.0 cm deep SWC-9	-24.0 cm	1400 C	± 0.75%	
07	T	TC Type K	N Sidewall 40.0 cm deep SWC-10	-24.0 cm	1400 C	± 0.75%	
08	T	TC Type K	N Sidewall 45.0 cm deep SWC-11	-24.0 cm	1400 C	± 0.75%	
09	T	TC Type K	S Sidewall 0.0 cm deep SWD-1	-24.0 cm	1400 C	± 0.75%	
10	T	TC Type K	S Sidewall 2.0 cm deep SWD-2	-24.0 cm	1400 C	± 0.75%	
11	T	TC Type K	S Sidewall 6.0 cm deep SWD-3	-24.0 cm	1400 C	± 0.75%	
12	T	TC Type K	S Sidewall 10.0 cm deep SWD-4	-24.0 cm	1400 C	± 0.75%	
13	T	TC Type K	S Sidewall 15.0 cm deep SWD-5	-24.0 cm	1400 C	± 0.75%	
14	T	TC Type K	S Sidewall 20.0 cm deep SWD-6	-24.0 cm	1400 C	± 0.75%	
15	T	TC Type K	S Sidewall 25.0 cm deep SWD-7	-24.0 cm	1400 C	± 0.75%	
16	T	TC Type K	S Sidewall 30.0 cm deep SWD-8	-24.0 cm	1400 C	± 0.75%	
17	T	TC Type K	S Sidewall 35.0 cm deep SWD-9	-24.0 cm	1400 C	± 0.75%	
18	T	TC Type K	S Sidewall 40.0 cm deep SWD-10	-24.0 cm	1400 C	± 0.75%	
19	T	TC Type K	S Sidewall 45.0 cm deep SWD-11	-24.0 cm	1400 C	± 0.75%	
20	T	TC Type K	N Sidewall 0.0 cm deep SWE-1	-12.0 cm	1400 C	± 0.75%	
21	T	TC Type K	N Sidewall 2.0 cm deep SWE-2	-12.0 cm	1400 C	± 0.75%	
22	T	TC Type K	N Sidewall 6.0 cm deep SWE-3	-12.0 cm	1400 C	± 0.75%	
23	T	TC Type K	N Sidewall 10.0 cm deep SWE-4	-12.0 cm	1400 C	± 0.75%	
24	T	TC Type K	N Sidewall 15.0 cm deep SWE-5	-12.0 cm	1400 C	± 0.75%	
25	T	TC Type K	N Sidewall 20.0 cm deep SWE-6	-12.0 cm	1400 C	± 0.75%	
26	T	TC Type K	N Sidewall 25.0 cm deep SWE-7	-12.0 cm	1400 C	± 0.75%	

27	T	TC Type K	N Sidewall 30.0 cm deep SWE-8	-12.0 cm	1400 C	± 0.75%	
28	T	TC Type K	N Sidewall 35.0 cm deep SWE-9	-12.0 cm	1400 C	± 0.75%	
29	T	TC Type K	N Sidewall 40.0 cm deep SWE-10	-12.0 cm	1400 C	± 0.75%	
30	T	TC Type K	N Sidewall 45.0 cm deep SWE-11	-12.0 cm	1400 C	± 0.75%	
31	T	TC Type K	S Sidewall 0.0 cm deep SWF-1	-12.0 cm	1400 C	± 0.75%	
32	T	TC Type K	S Sidewall 2.0 cm deep SWF-2	-12.0 cm	1400 C	± 0.75%	
33	T	TC Type K	S Sidewall 6.0 cm deep SWF-3	-12.0 cm	1400 C	± 0.75%	
34	T	TC Type K	S Sidewall 10.0 cm deep SWF-4	-12.0 cm	1400 C	± 0.75%	
35	T	TC Type K	S Sidewall 15.0 cm deep SWF-5	-12.0 cm	1400 C	± 0.75%	
36	T	TC Type K	S Sidewall 20.0 cm deep SWF-6	-12.0 cm	1400 C	± 0.75%	
37	T	TC Type K	S Sidewall 25.0 cm deep SWF-7	-12.0 cm	1400 C	± 0.75%	
38	T	TC Type K	S Sidewall 30.0 cm deep SWF-8	-12.0 cm	1400 C	± 0.75%	
39	T	TC Type K	S Sidewall 35.0 cm deep SWF-9	-12.0 cm	1400 C	± 0.75%	
40	T	TC Type K	S Sidewall 40.0 cm deep SWF-10	-12.0 cm	1400 C	± 0.75%	
41	T	TC Type K	S Sidewall 45.0 cm deep SWF-11	-12.0 cm	1400 C	± 0.75%	
42	T	TC Type K	N Sidewall 0.0 cm deep SWG-1	0.0 cm	1400 C	± 0.75%	
43	T	TC Type K	N Sidewall 2.0 cm deep SWG-2	0.0 cm	1400 C	± 0.75%	
44	T	TC Type K	N Sidewall 6.0 cm deep SWG-3	0.0 cm	1400 C	± 0.75%	
45	T	TC Type K	N Sidewall 10.0 cm deep SWG-4	0.0 cm	1400 C	± 0.75%	
46	T	TC Type K	N Sidewall 15.0 cm deep SWG-5	0.0 cm	1400 C	± 0.75%	
47	T	TC Type K	N Sidewall 20.0 cm deep SWG-6	0.0 cm	1400 C	± 0.75%	
48	T	TC Type K	N Sidewall 25.0 cm deep SWG-7	0.0 cm	1400 C	± 0.75%	
49	T	TC Type K	N Sidewall 30.0 cm deep SWG-8	0.0 cm	1400 C	± 0.75%	
50	T	TC Type K	S Sidewall 45.0 cm deep SWL-11	+20.0 cm	1400 C	± 0.75%	
51	T	TC Type K	N Sidewall 35.0 cm deep SWG-9	0.0 cm	1400 C	± 0.75%	
52	T	TC Type K	N Sidewall 40.0 cm deep SWG-10	0.0 cm	1400 C	± 0.75%	
53	T	TC Type K	N Sidewall 45.0 cm deep SWG-11	0.0 cm	1400 C	± 0.75%	
54	T	TC Type K	S Sidewall 0.0 cm deep SWH-1	0.0 cm	1400 C	± 0.75%	
55	T	TC Type K	S Sidewall 2.0 cm deep SWH-2	0.0 cm	1400 C	± 0.75%	

56	T	TC Type K	S Sidewall 6.0 cm deep SWH-3	0.0 cm	1400 C	± 0.75%	
57	T	TC Type K	S Sidewall 10.0 cm deep SWH-4	0.0 cm	1400 C	± 0.75%	
58	T	TC Type K	S Sidewall 15.0 cm deep SWH-5	0.0 cm	1400 C	± 0.75%	
59	T	TC Type K	S Sidewall 20.0 cm deep SWH-6	0.0 cm	1400 C	± 0.75%	
60	T	TC Type K	S Sidewall 25.0 cm deep SWH-7	0.0 cm	1400 C	± 0.75%	
61	T	TC Type K	S Sidewall 30.0 cm deep SWH-8	0.0 cm	1400 C	± 0.75%	
62	T	TC Type K	S Sidewall 35.0 cm deep SWH-9	0.0 cm	1400 C	± 0.75%	
63	T	TC Type K	S Sidewall 40.0 cm deep SWH-10	0.0 cm	1400 C	± 0.75%	
64	T	TC Type K	S Sidewall 45.0 cm deep SWH-11	0.0 cm	1400 C	± 0.75%	
65	T	TC Type K	N Sidewall 0.0 cm deep SWI-1	+10.0 cm	1400 C	± 0.75%	
66	T	TC Type K	N Sidewall 2.0 cm deep SWI-2	+10.0 cm	1400 C	± 0.75%	
67	T	TC Type K	N Sidewall 6.0 cm deep SWI-3	+10.0 cm	1400 C	± 0.75%	
68	T	TC Type K	N Sidewall 10.0 cm deep SWI-4	+10.0 cm	1400 C	± 0.75%	
69	T	TC Type K	N Sidewall 15.0 cm deep SWI-5	+10.0 cm	1400 C	± 0.75%	
70	T	TC Type K	N Sidewall 20.0 cm deep SWI-6	+10.0 cm	1400 C	± 0.75%	
71	T	TC Type K	N Sidewall 25.0 cm deep SWI-7	+10.0 cm	1400 C	± 0.75%	
72	T	TC Type K	N Sidewall 30.0 cm deep SWI-8	+10.0 cm	1400 C	± 0.75%	
73	T	TC Type K	N Sidewall 35.0 cm deep SWI-9	+10.0 cm	1400 C	± 0.75%	
74	T	TC Type K	N Sidewall 40.0 cm deep SWI-10	+10.0 cm	1400 C	± 0.75%	
75	T	TC Type K	N Sidewall 45.0 cm deep SWI-11	+10.0 cm	1400 C	± 0.75%	
76	T	TC Type K	S Sidewall 0.0 cm deep SWJ-1	+10.0 cm	1400 C	± 0.75%	
77	T	TC Type K	S Sidewall 2.0 cm deep SWJ-2	+10.0 cm	1400 C	± 0.75%	
78	T	TC Type K	S Sidewall 6.0 cm deep SWJ-3	+10.0 cm	1400 C	± 0.75%	
79	T	TC Type K	S Sidewall 10.0 cm deep SWJ-4	+10.0 cm	1400 C	± 0.75%	
80	T	TC Type K	S Sidewall 15.0 cm deep SWJ-5	+10.0 cm	1400 C	± 0.75%	
81	T	TC Type K	S Sidewall 20.0 cm deep SWJ-6	+10.0 cm	1400 C	± 0.75%	
82	T	TC Type K	S Sidewall 25.0 cm deep SWJ-7	+10.0 cm	1400 C	± 0.75%	
83	T	TC Type K	S Sidewall 30.0 cm deep SWJ-8	+10.0 cm	1400 C	± 0.75%	
84	T	TC Type K	S Sidewall 35.0 cm deep SWJ-9	+10.0 cm	1400 C	± 0.75%	

85	T	TC Type K	S Sidewall 40.0 cm deep SWJ-10	+10.0 cm	1400 C	± 0.75%	
86	T	TC Type K	S Sidewall 45.0 cm deep SWJ-11	+10.0 cm	1400 C	± 0.75%	
87	T	TC Type K	N Sidewall 0.0 cm deep SWK-1	+20.0 cm	1400 C	± 0.75%	
88	T	TC Type K	N Sidewall 2.0 cm deep SWK-2	+20.0 cm	1400 C	± 0.75%	
89	T	TC Type K	N Sidewall 6.0 cm deep SWK-3	+20.0 cm	1400 C	± 0.75%	
90	T	TC Type K	N Sidewall 10.0 cm deep SWK-4	+20.0 cm	1400 C	± 0.75%	
91	T	TC Type K	N Sidewall 15.0 cm deep SWK-5	+20.0 cm	1400 C	± 0.75%	
92	T	TC Type K	N Sidewall 20.0 cm deep SWK-6	+20.0 cm	1400 C	± 0.75%	
93	T	TC Type K	N Sidewall 25.0 cm deep SWK-7	+20.0 cm	1400 C	± 0.75%	
94	T	TC Type K	N Sidewall 30.0 cm deep SWK-8	+20.0 cm	1400 C	± 0.75%	
95	T	TC Type K	S Sidewall 0.0 cm deep SWL-1	+20.0 cm	1400 C	± 0.75%	
96	T	TC Type K	S Sidewall 2.0 cm deep SWL-2	+20.0 cm	1400 C	± 0.75%	
97	T	TC Type K	S Sidewall 6.0 cm deep SWL-3	+20.0 cm	1400 C	± 0.75%	
98	T	TC Type K	S Sidewall 10.0 cm deep SWL-4	+20.0 cm	1400 C	± 0.75%	
99	T	TC Type K	S Sidewall 15.0 cm deep SWL-5	+20.0 cm	1400 C	± 0.75%	

Explanation of Variable Notations
T = temperature

Table A-3. "Quench" DAS Channel Assignments for CCI-4.

Channel	Variable	Sensor	Location	Level	Range/Limit	Accuracy	Notes
00	T	Diode Sensor	TC Compensation CH Q00-Q49		130 C		
01	T	TC Type K	S Sidewall 20.0 cm deep SWL-6	+20.0 cm	1400 C	± 0.75%	
02	T	TC Type K	S Sidewall 25.0 cm deep SWL-7	+20.0 cm	1400 C	± 0.75%	
03	T	TC Type K	S Sidewall 30.0 cm deep SWL-8	+20.0 cm	1400 C	± 0.75%	
04	T	TC Type C	E Sidewall 1.0 cm deep SWHL-1	-17.5 cm	2320 C	± 1.0%	
05	T	TC Type C	E Sidewall 2.0 cm deep SWHL-2	-17.5 cm	2320 C	± 1.0%	
06	T	TC Type C	E Sidewall 4.0 cm deep SWHL-3	-17.5 cm	2320 C	± 1.0%	
07	T	TC Type C	E Sidewall 8.0 cm deep SWHL-4	-17.5 cm	2320 C	± 1.0%	
08	T	TC Type C	W Sidewall 1.0 cm deep SWHL-5	-7.5 cm	2320 C	± 1.0%	
09	T	TC Type C	W Sidewall 2.0 cm deep SWHL-6	-7.5 cm	2320 C	± 1.0%	
10	T	TC Type C	W Sidewall 4.0 cm deep SWHL-7	-7.5 cm	2320 C	± 1.0%	
11	T	TC Type C	W Sidewall 8.0 cm deep SWHL-8	-7.5 cm	2320 C	± 1.0%	
12	T	TC Type C	E Sidewall 1.0 cm deep SWHL-9	+2.5 cm	2320 C	± 1.0%	
13	T	TC Type C	E Sidewall 2.0 cm deep SWHL-10	+2.5 cm	2320 C	± 1.0%	
14	T	TC Type C	E Sidewall 4.0 cm deep SWHL-11	+2.5 cm	2320 C	± 1.0%	
15	T	TC Type C	E Sidewall 8.0 cm deep SWHL-12	+2.5 cm	2320 C	± 1.0%	
16	T	TC Type C	W Sidewall 1.0 cm deep SWHL-13	+12.5 cm	2320 C	± 1.0%	
17	T	TC Type C	W Sidewall 2.0 cm deep SWHL-14	+12.5 cm	2320 C	± 1.0%	
18	T	TC Type C	W Sidewall 4.0 cm deep SWHL-15	+12.5 cm	2320 C	± 1.0%	
19	T	TC Type C	W Sidewall 8.0 cm deep SWHL-16	+12.5 cm	2320 C	± 1.0%	
20	L	Potentiometer	Lance Position Indicator		0-125 cm		
21	T	TC Type K	Steamline internal vertical run from vessel ML-1		1400 C	± 0.75%	
22	T	TC Type K	Steamline external vertical run from vessel ML-2		1400 C	± 0.75%	
23	T	TC Type K	Steamline external lateral run from vessel ML-3		1400 C	± 0.75%	
24	T	TC Type K	Steamline external vertical run to quench tank ML-4		1400 C	± 0.75%	
25	T	TC Type K	S Sidewall 0.0 cm deep SWHL-17	+67.5 cm	1400 C	± 0.75%	
26	T	TC Type K	S Sidewall 2.0 cm deep SWHL-18	+67.5 cm	1400 C	± 0.75%	

27	T	TC Type K	E Sidewall 0.0 cm deepSWHL -19	+81.6 cm	1400 C	± 0.75%	
28	FOR	Strain	Crust Force Load		0-44.6 kN		
29	T	TC Type K	Quench tank internal QT-1	21 cm	1400 C	± 0.75%	
30	T	TC Type K	Quench tank internal QT-2	55 cm	1400 C	± 0.75%	
31	T	TC Type C	N Sidewall, 15.0 cm deep, WN-5	+5.0 cm	2320 C	± 0.75%	
32	T	TC Type C	N Sidewall, 20.0 cm deep, WN-6	+5.0 cm	2320 C	± 0.75%	
33	T	TC Type K	N Sidewall 0.0 cm deep SWM-1	+30.0 cm	1400 C	± 0.75%	
34	T	TC Type K	N Sidewall 5.0 cm deep SWM-2	+30.0 cm	1400 C	± 0.75%	
35	T	TC Type K	Quench tank coil inlet QT-5		1400 C	± 0.75%	
36	T	TC Type K	Quench tank coil outlet QT-6		1400 C	± 0.75%	
37	T	TC Type K	Quench tank coil outlet QT-7		1400 C	± 0.75%	
38	T	TC Type K	Overflow tank internal OT-1	16 cm	1400 C	± 0.75%	
39	T	Voltage	Igniter Current		100 mV		
40	T	TC Type K	Spray tank internal ST-1	10 cm	1400 C	± 0.75%	
41	T	TC Type C	N Sidewall, 25.0 cm deep, WN-7	+5.0 cm	2320 C	± 1%	
42	T	TC Type K	E Sidewall 2.0 cm deep SWHL-20	+81.6 cm	1400 C	± 0.75%	
43	T	TC Type K	N Sidewall 0.0 cm deep SWHL-21	+92.2 cm	1400 C	± 0.75%	
44	T	TC Type K	N Sidewall 2.0 cm deep SWHL-22	+92.2 cm	1400 C	± 0.75%	
45	T	TC Type K	W Sidewall 0.0 cm deep SWHL-23	+122.4 cm	1400 C	± 0.75%	
46	T	TC Type K	W Sidewall 2.0 cm deep SWHL-24	+122.4 cm	1400 C	± 0.75%	
47	T	TC Type K	S Sidewall 0.0 cm deep SWHL-25	+148.8 cm	1400 C	± 0.75%	
48	T	TC Type K	S Sidewall 2.0 cm deep SWHL-26	+148.8 cm	1400 C	± 0.75%	
49	T	TC Type K	N Sidewall 10.0 cm deep SWM-3	+30.0 cm	1400 C	± 0.75%	
50	T	Diode Sensor	TC Compensation CH Q50-Q99		130 C		
51	T	TC Type K	S Sidewall 0.0 cm deep SWN-1	+30.0 cm	1400 C	± 0.75%	
52	T	TC Type K	S Sidewall 5.0 cm deep SWN-2	+30.0 cm	1400 C	± 0.75%	
53	T	TC Type C	N Sidewall, 30.0 cm deep, WN-8	+5.0 cm	2320 C	± 1%	
54	T	TC Type K	Internal, exhaust line OG-1		1400 C	± 0.75%	

55	T	TC Type K	Water supply tank internal WS-1	45 cm	1400 C	± 0.75%	
56	T	TC Type K	S Sidewall 10.0 cm deep SWN-3	+30.0 cm	1400 C	± 0.75%	
57	T	TC Type K	Water level probe LP-1	167/48 cm	1400 C	± 0.75%	
58	T	TC Type K	Water level probe LP-2	167/48 cm	1400 C	± 0.75%	
59	T	TC Type K	Test vessel plenum gas TS-1	223.0 cm	1400 C	± 0.75%	
60	L	Strain	Supply tank head PT-1		350-2000 l		D-6
61	P	Strain	Supply tank pressure PT-2		0-204 kPa		A-17
62	L	Strain	Test vessel head, insertion probe PT-3		63-150 l		D-3
63	L	Strain	Test vessel head, static probe PT-4		32-150 l		D-1
64	P	Strain	Test vessel plenum pressure PT-5		0-204 kPa		A-1
65	P	Strain	Basemat side pressure PT-6		0-204 kPa		A-3
66	Unused						
67	L	Strain	Quench tank head PT-8		80-590 l		D-9
68	P	Strain	Quench/overflow tank pressure PT-9		0-35 kPad		D-2
69	L	Strain	Overflow tank head PT-10		200-900 l		D-8
70	L	Strain	Spray tank head PT-11		240-1290 l		D-5
71	P	Strain	Spray tank pressure PT-12		0-35 kPad		D-4
72	L	Magnetic Float	Supply tank volume LS-1		350-2000 l		
73	L	Magnetic Float	Quench tank volume LS-2		80-590 l		
74	L	Magnetic Float	Overflow tank volume LS-3		200-900 l		
75	L	Magnetic Float	Spray tank volume LS-4		240-1290 l		
76	F	Paddlewheel	Water supply flow rate FM-1		680 lpm		
77	F	Paddlewheel	Quench tank coil flow rate FM-2		190 lpm		
78	Unused						
79	T	TC Type C	S Sidewall, 15.0 cm deep, WS-5	+5.0 cm	2320 C	± 1%	
80	T	TC Type C	S Sidewall, 20.0 cm deep, WS-6	+5.0 cm	2320 C	± 1%	
81	FC	Flow controller	Final Off gas Flow rate FC1a		0-5,600 lpm		
82		-	Calculated Water Volume in Test Section		0-150 l		

83	FC	Flow controller	Lid lights & camera cover gas flow rate FC-2		0-200 lpm		
84	Unused						
85		-	Calculated Total Current (Q92+Q93)		0 -10,000 A		
86	Unused	-	Calculated Total Power (Q94+Q95)		0-500 kW		
87	FC	Flow controller	Test vessel cover gas flow rate FC-6		0-100 lpm		
88	FC	Flow controller	Lid camera cover gas flow rate FC-7		0-350 lpm		
89	V		Pressure transducer power supply #1 voltage		0-30 V		
90	V		Pressure transducer power supply #2 voltage		0-30 V		
91	V	Voltmeter	Power supply voltage		0-200 V		
92	A	Transformer	Power supply current #2		5000 A		
93	A	Transformer	Power supply current #1		5000 A		
94	W	Hall Meter	Power supply power #2		1100 kW		
95	W	Hall Meter	Power supply power #1		1100 kW		
96	L	Strain	Auxiliary Tank Head PT-13		366-4080		D-10
97	T	TC Type K	Auxiliary Tank Internal AT-1	43 cm	1400 C	± 0.75%	
98	T	TC Type C	S Sidewall, 25.0 cm deep, WS-7	+5.0 cm	2320 C	± 1%	
99	T	TC Type C	S Sidewall, 30.0 cm deep, WS-8	+5.0 cm	2320 C	± 1%	

Explanation of variable notations

T = temperature P = Pressure FOR=Force L = Level V = Voltage F = Flow rate A = Current W = Power FC = Flow Controller

APPENDIX B
Test Data

This Appendix provides plots of all data recorded during Test CCI-4. The complete channel assignment list is provided in Appendix A. Time t = 0 in all plots is referenced to the time at which axial ablation of the concrete basemat was nominally initiated. This corresponds to 48.6 minutes after onset of data acquisition; see Table 3-1. All data was logged at ~ 5.5 second time intervals during the test. Selected channels have been averaged over 30 second time intervals to improve readability.

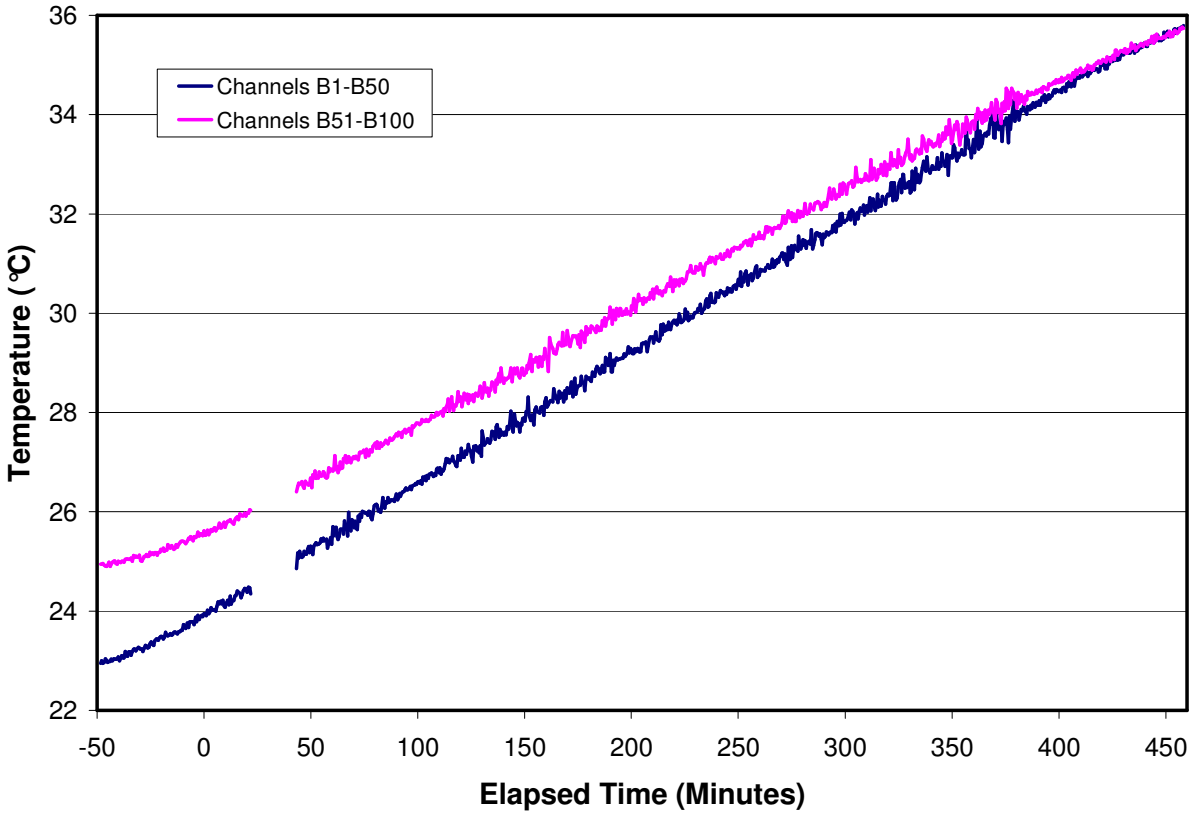

Figure B-1. Compensator Temperature, Channels B1-B50 and B51-B100.

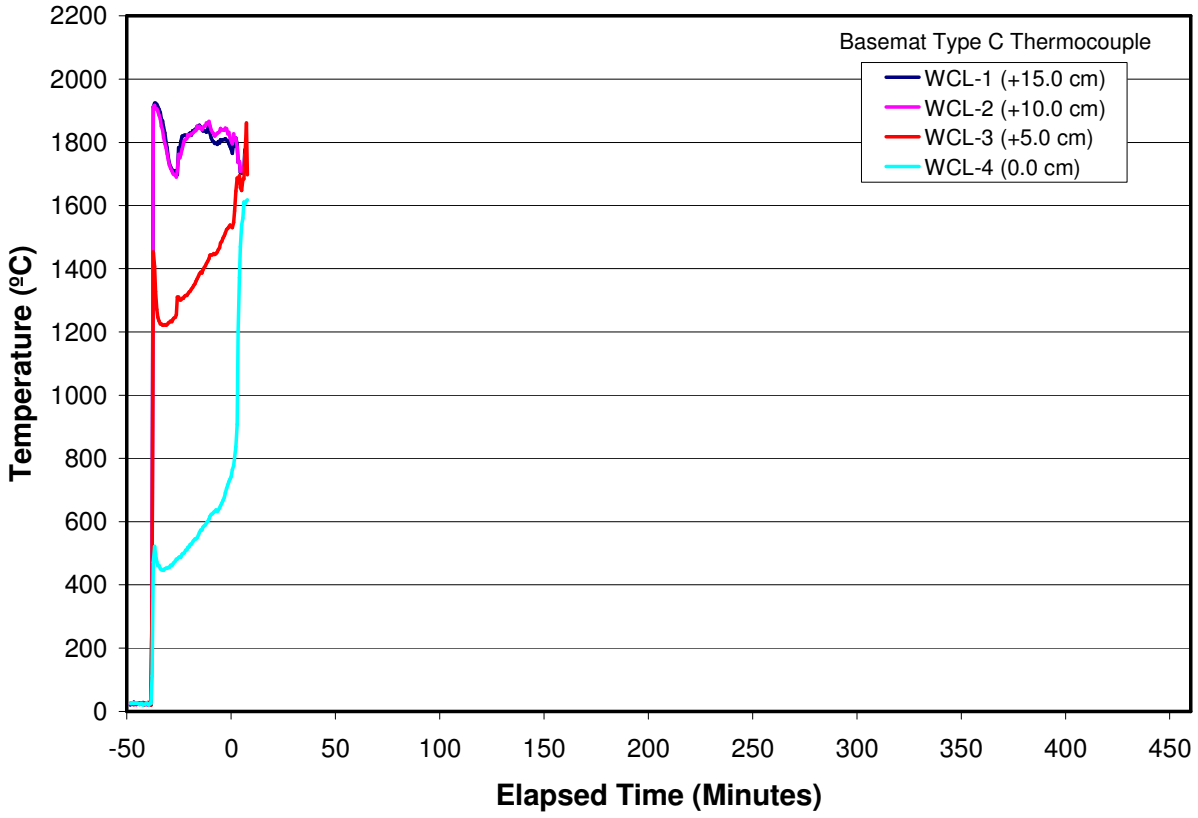

Figure B-2. Basemat Type C "WCL" Array Data.

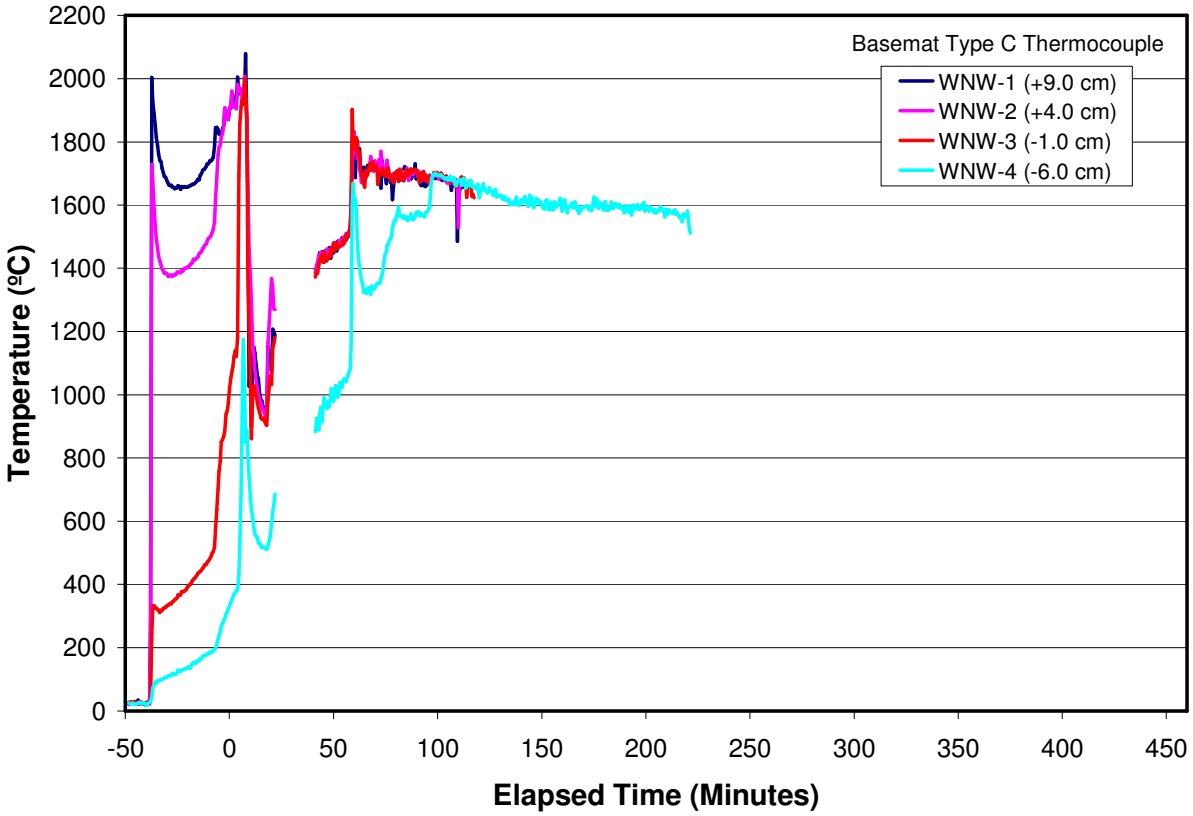

Figure B-3. Basemat Type C "WNW" Array Data.

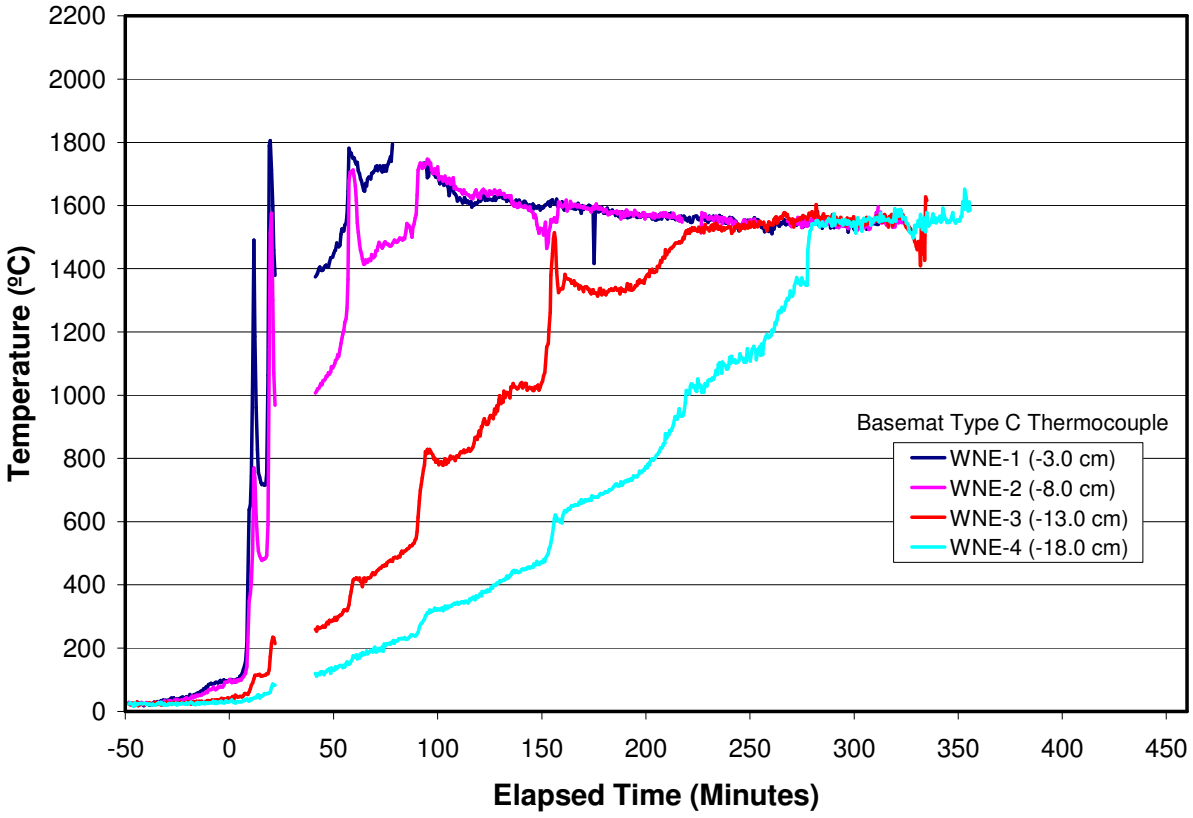

Figure B-4. Basemat Type C "WNE" Array Data.

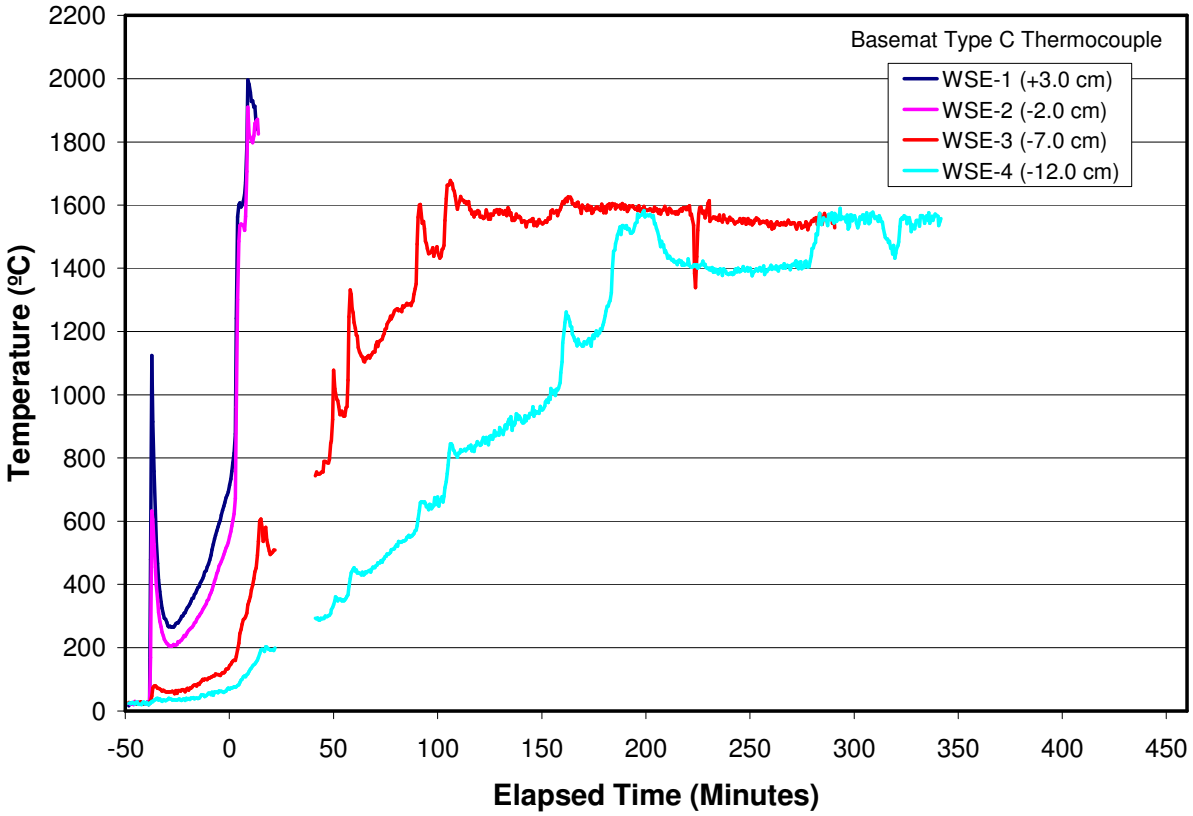

Figure B-5. Basemat Type C "WSE" Array Data.

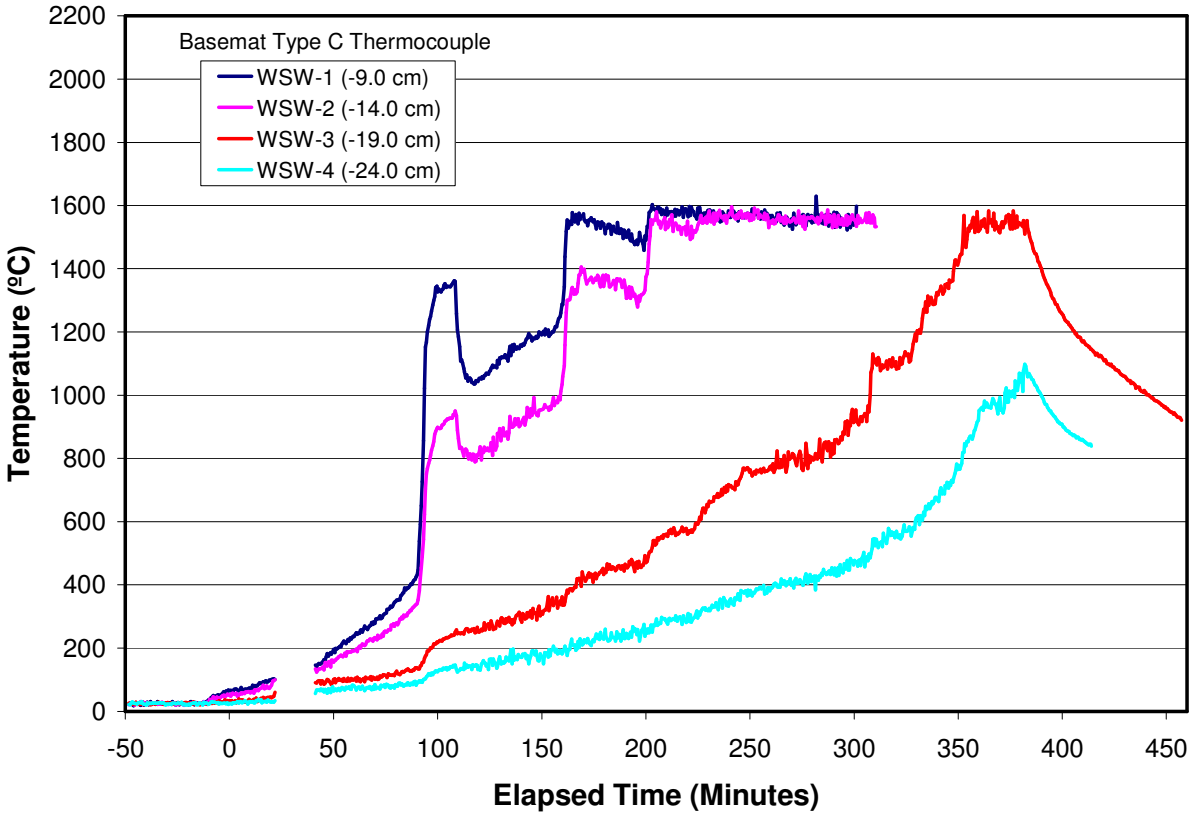

Figure B-6. Basemat Type C "WSW" Array Data.

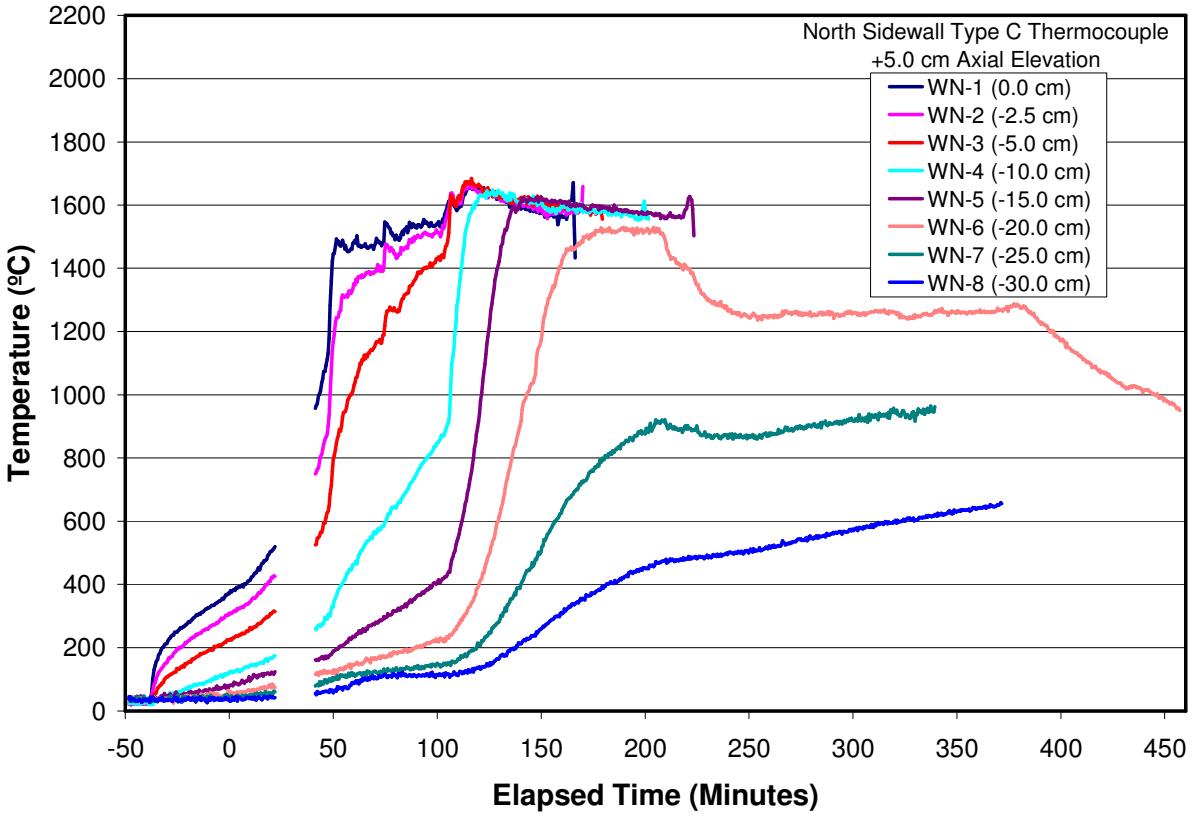

Figure B-7. North Sidewall Type C "WN" Array Data.

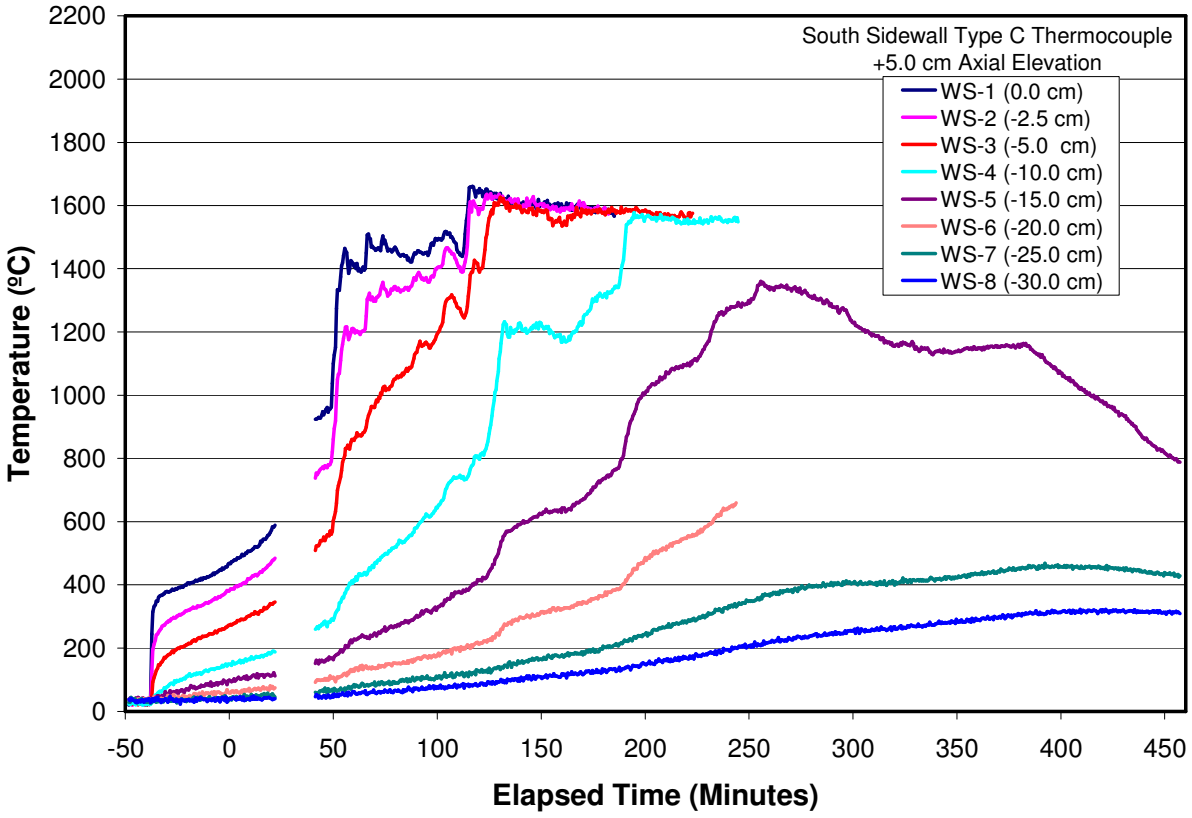

Figure B-8. South Sidewall Type C "WS" Array Data.

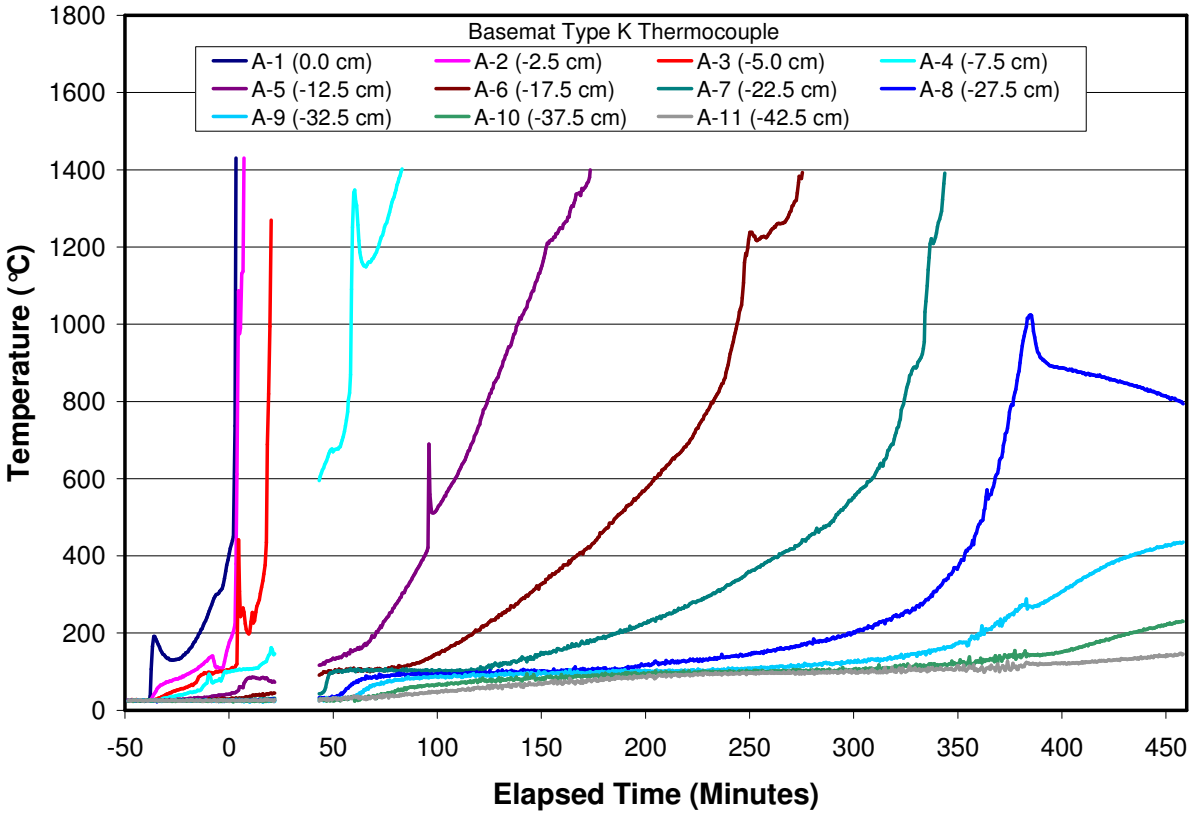

Figure B-9. Basemat Type K "A" Array Data.

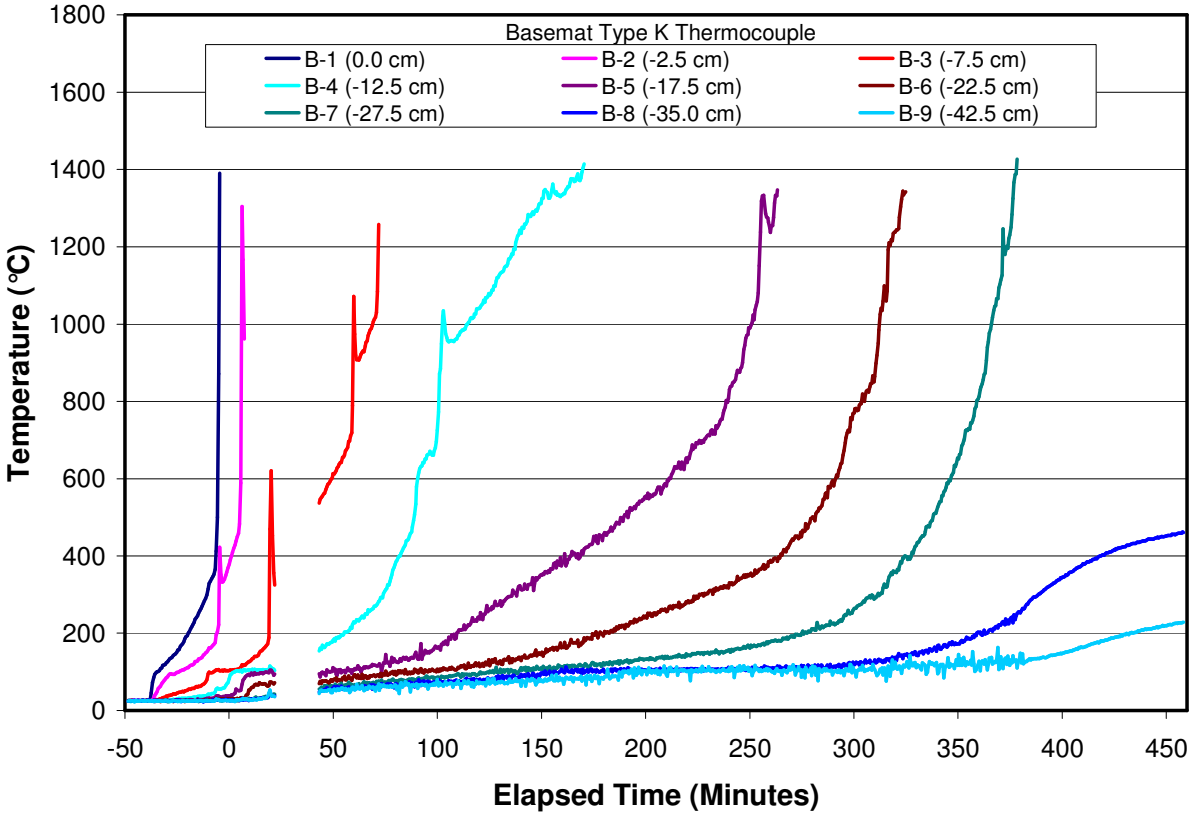

Figure B-10. Basemat Type K "B" Array Data.

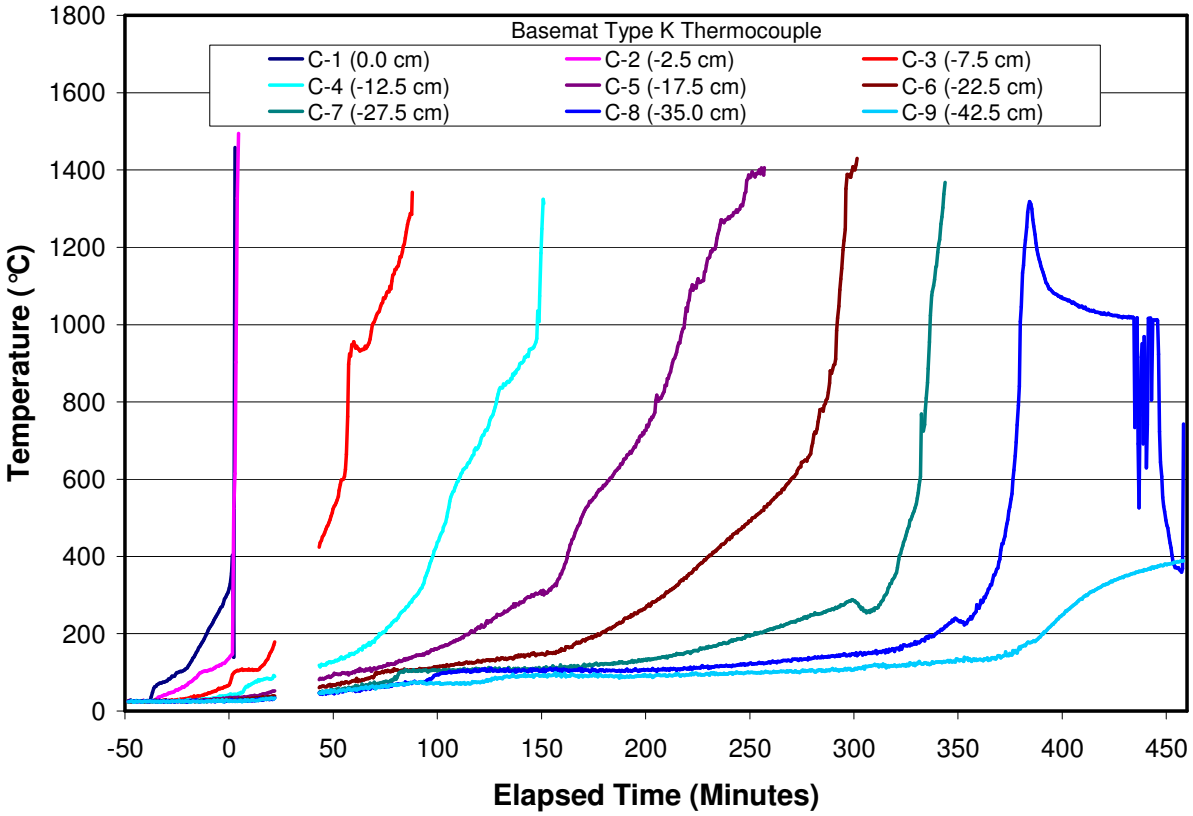

Figure B-11. Basemat Type K "C" Array Data.

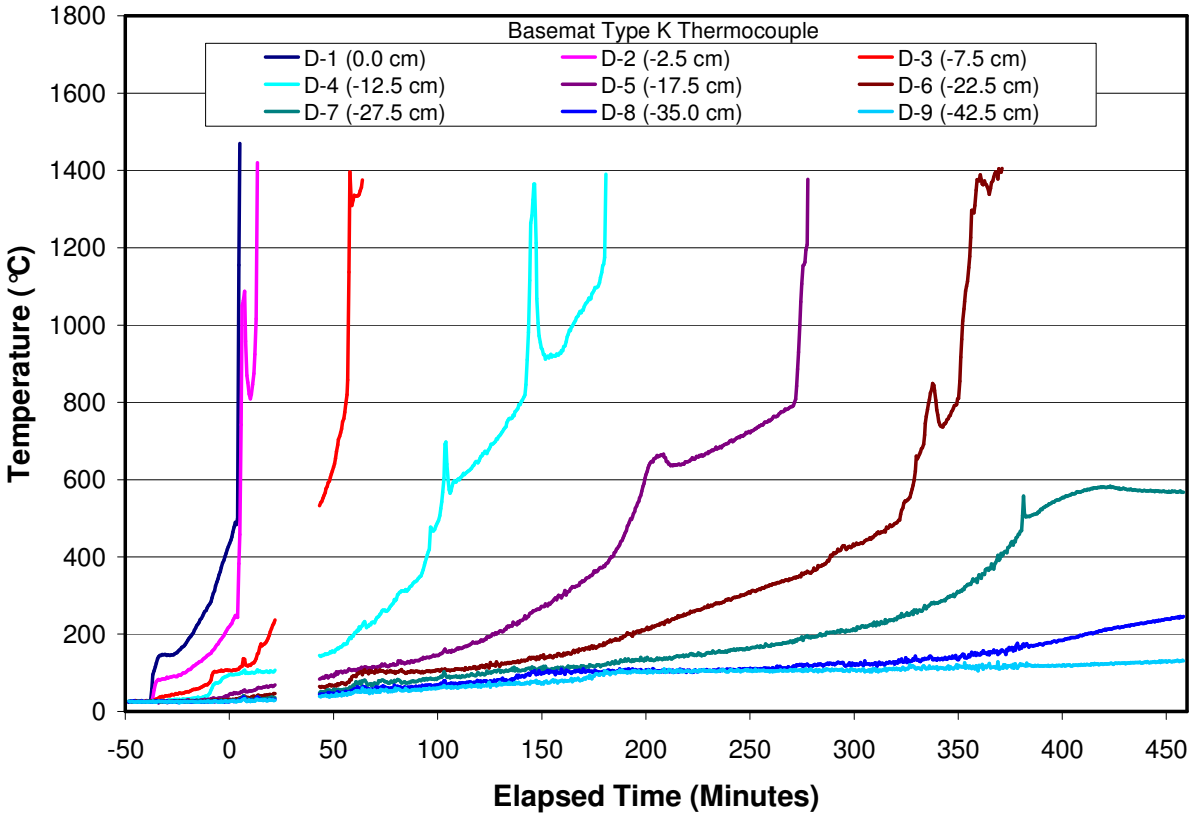

Figure B-12. Basemat Type K "D" Array Data.

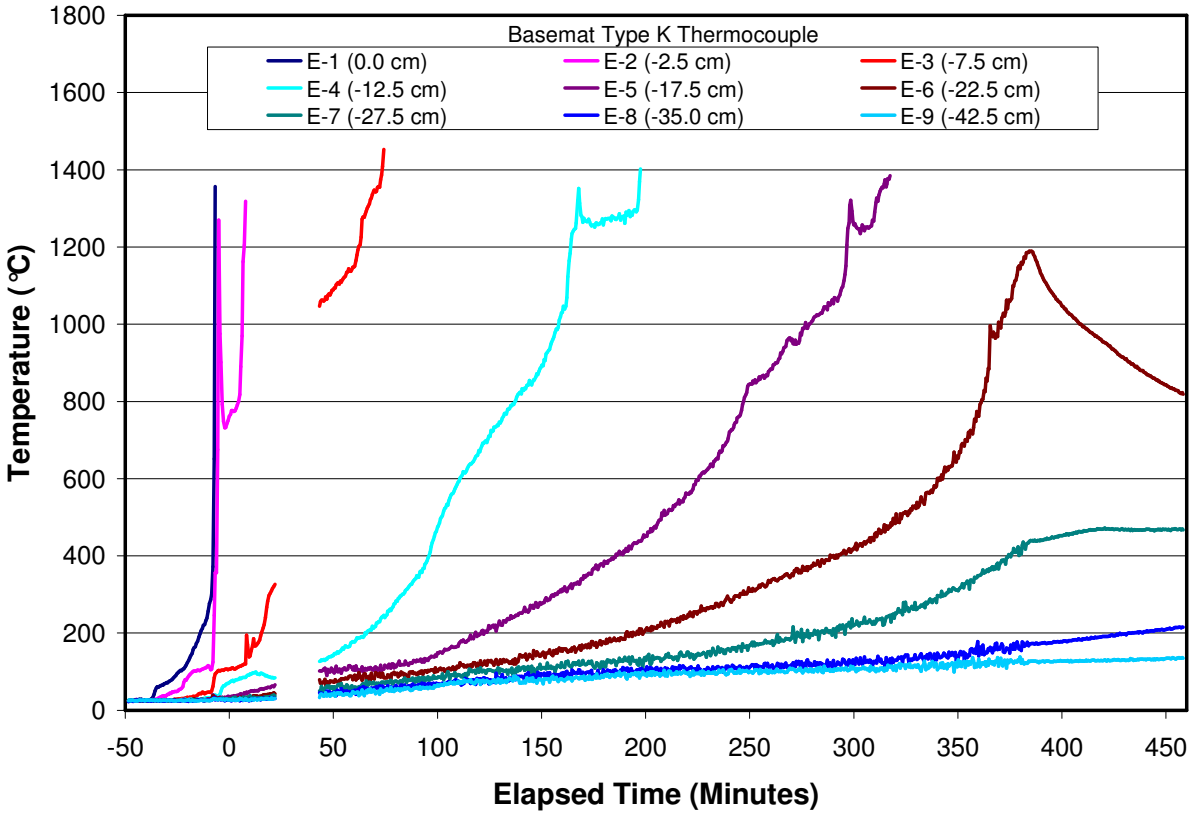

Figure B-13. Basemat Type K "E" Array Data.

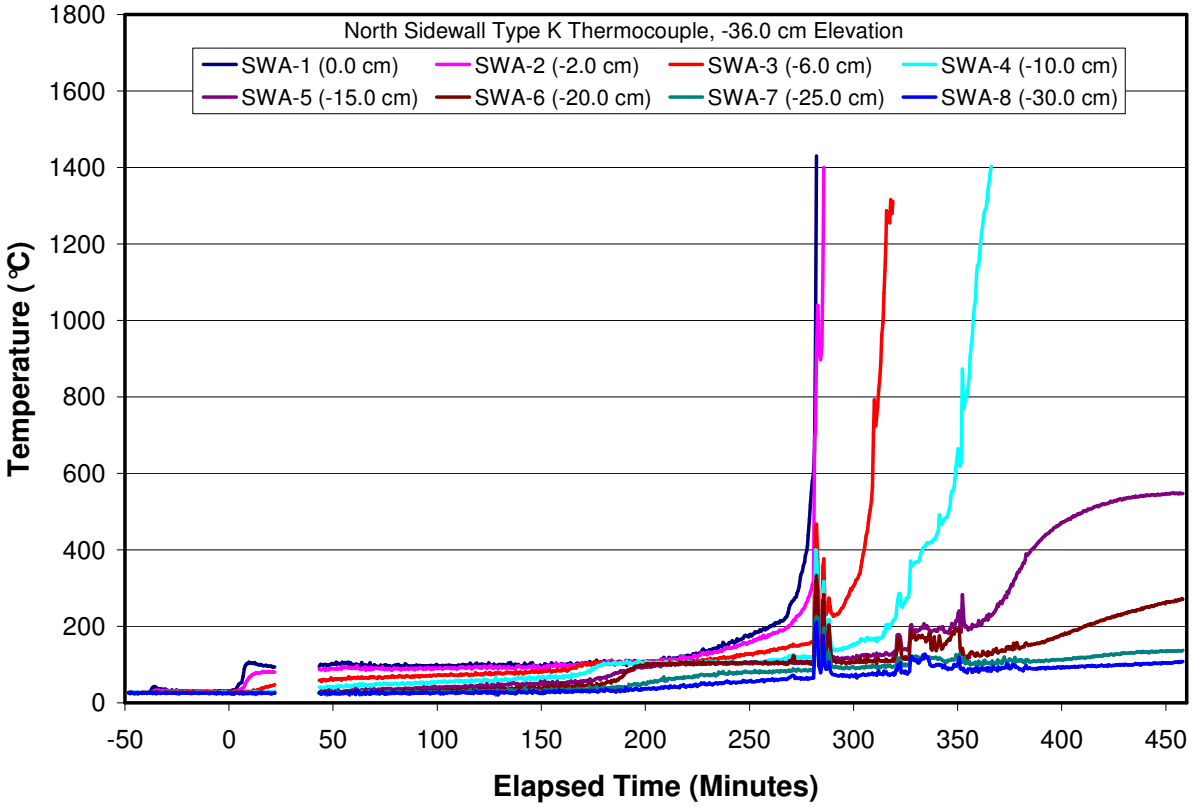

Figure B-14. North Sidewall Type K "SWA" Array Data.

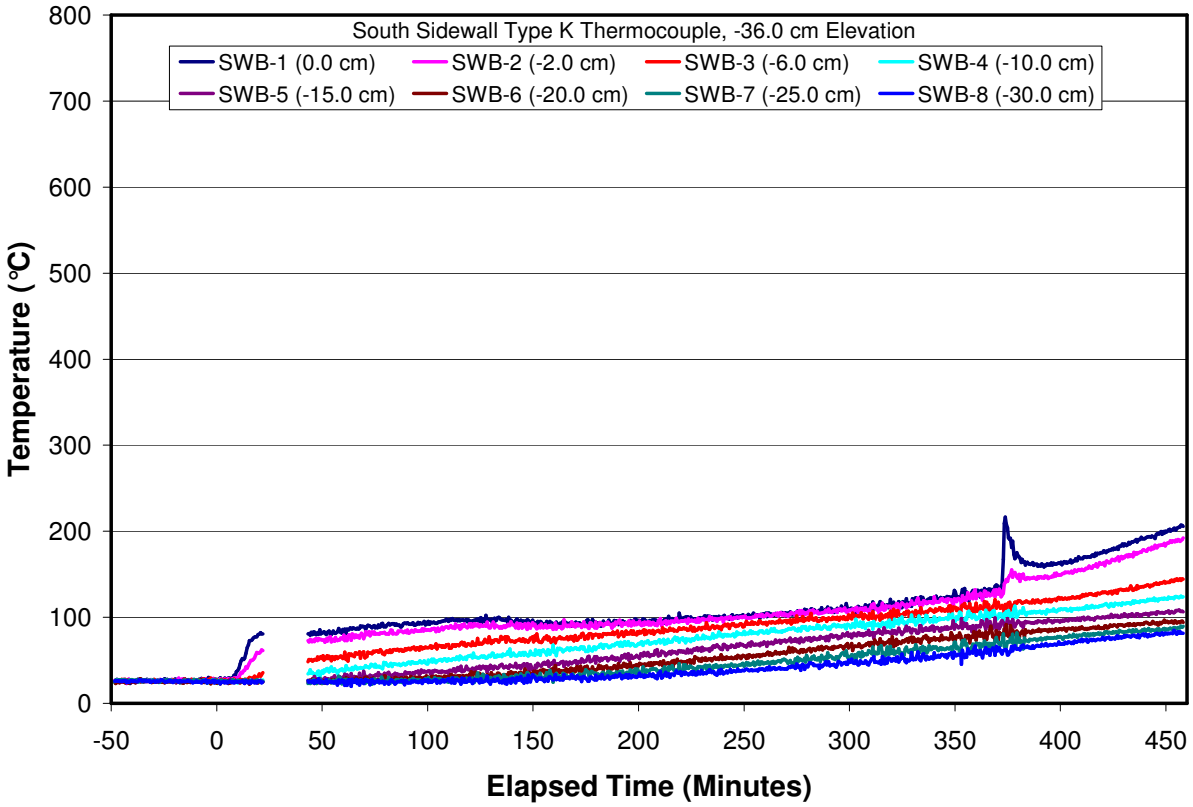

Figure B-15. South Sidewall Type K "SWB" Array Data.

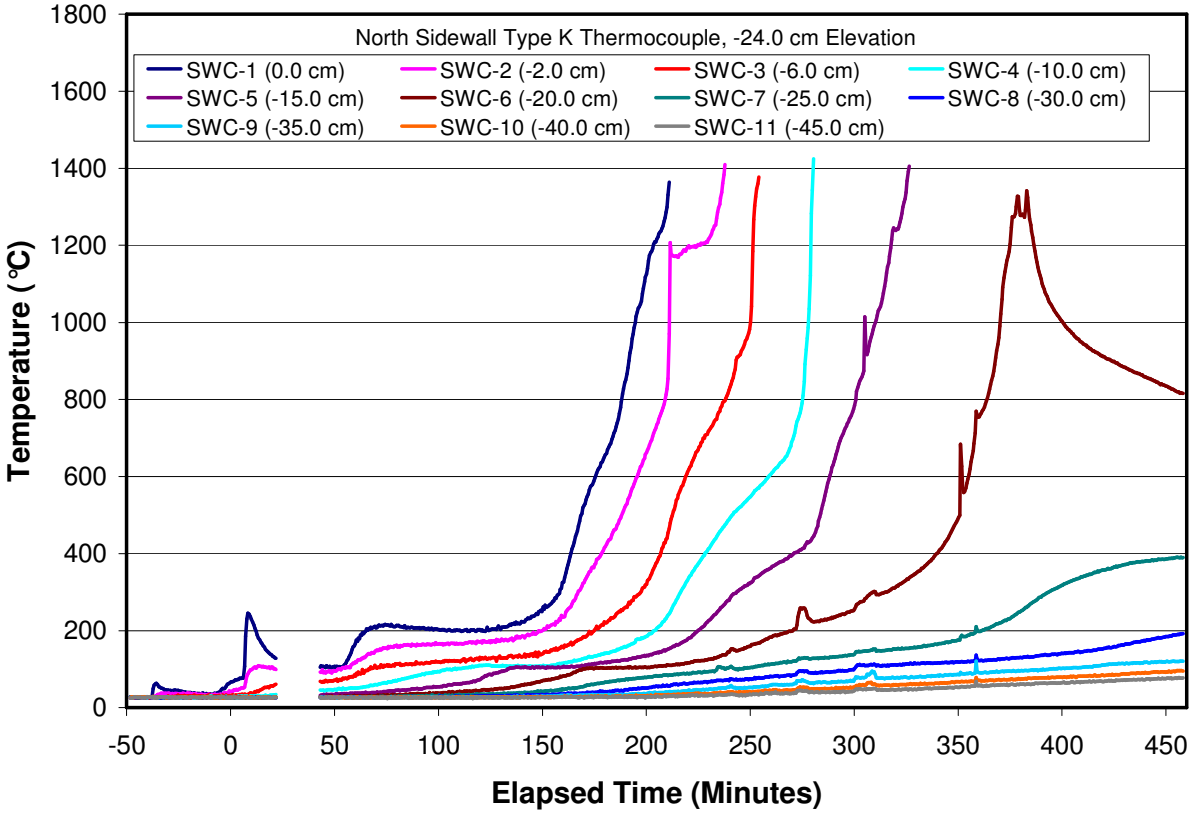

Figure B-16. North Sidewall Type K "SWC" Array Data.

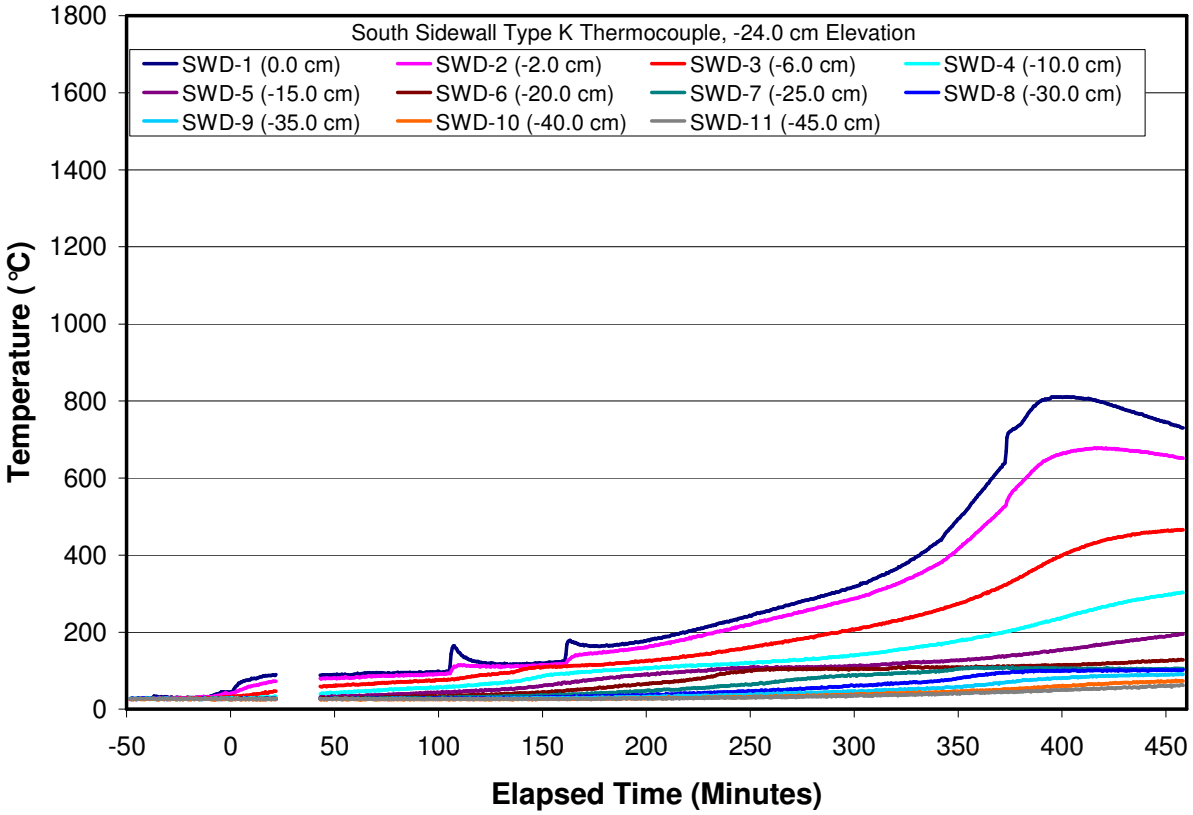

Figure B-17. South Sidewall Type K "SWD" Array Data.

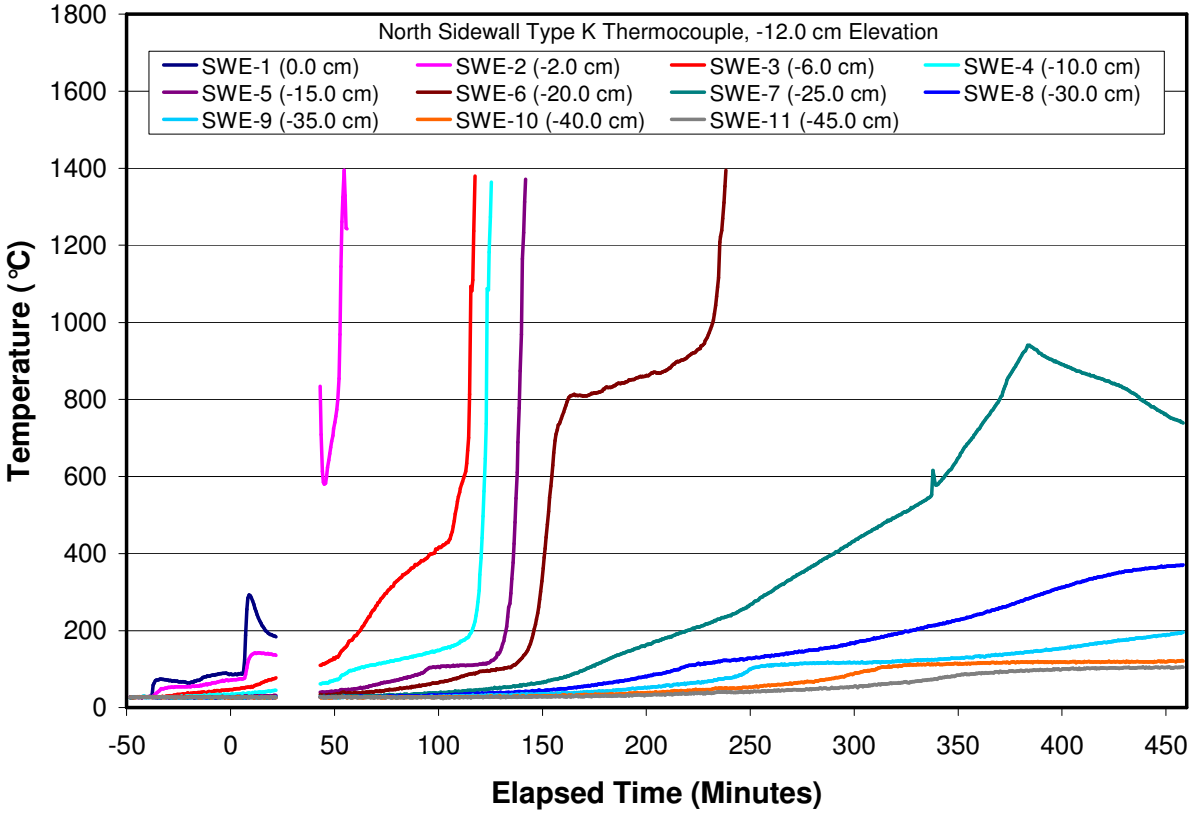

Figure B-18. North Sidewall Type K "SWE" Array Data.

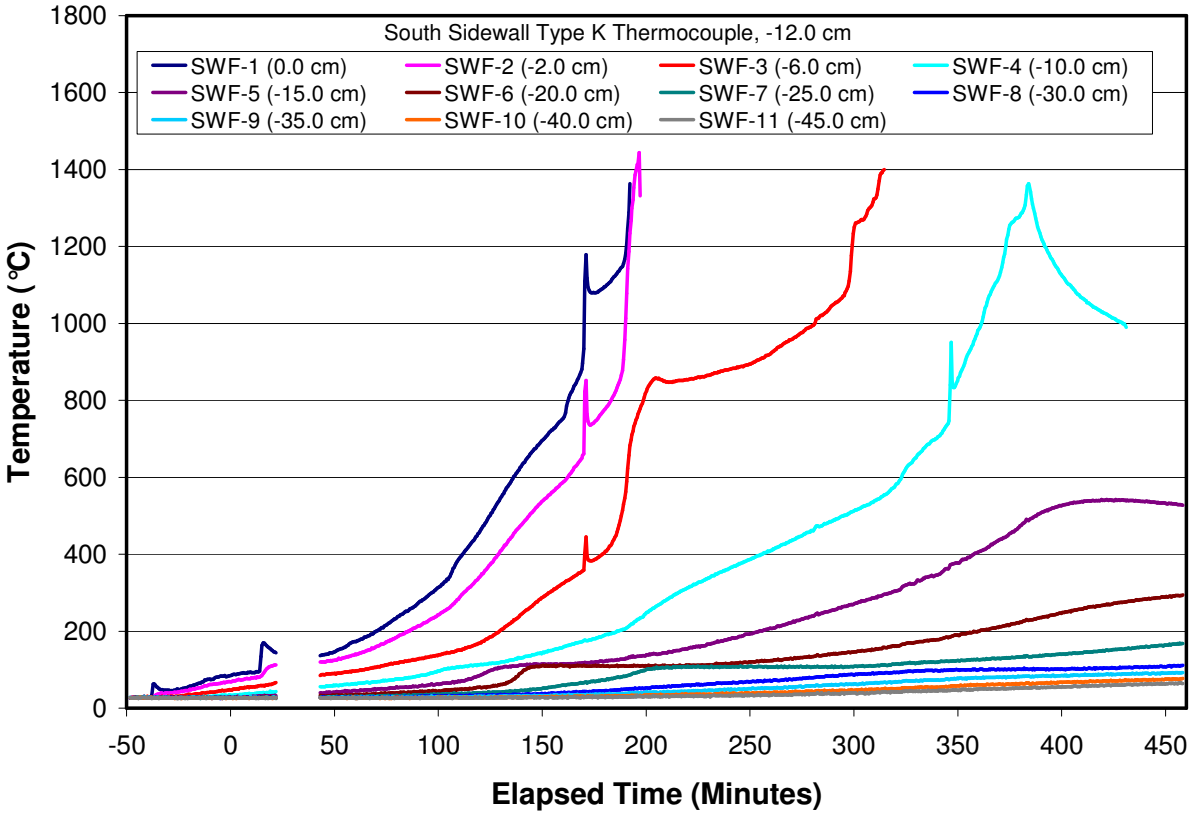

Figure B-19. South Sidewall Type K "SWF" Array Data.

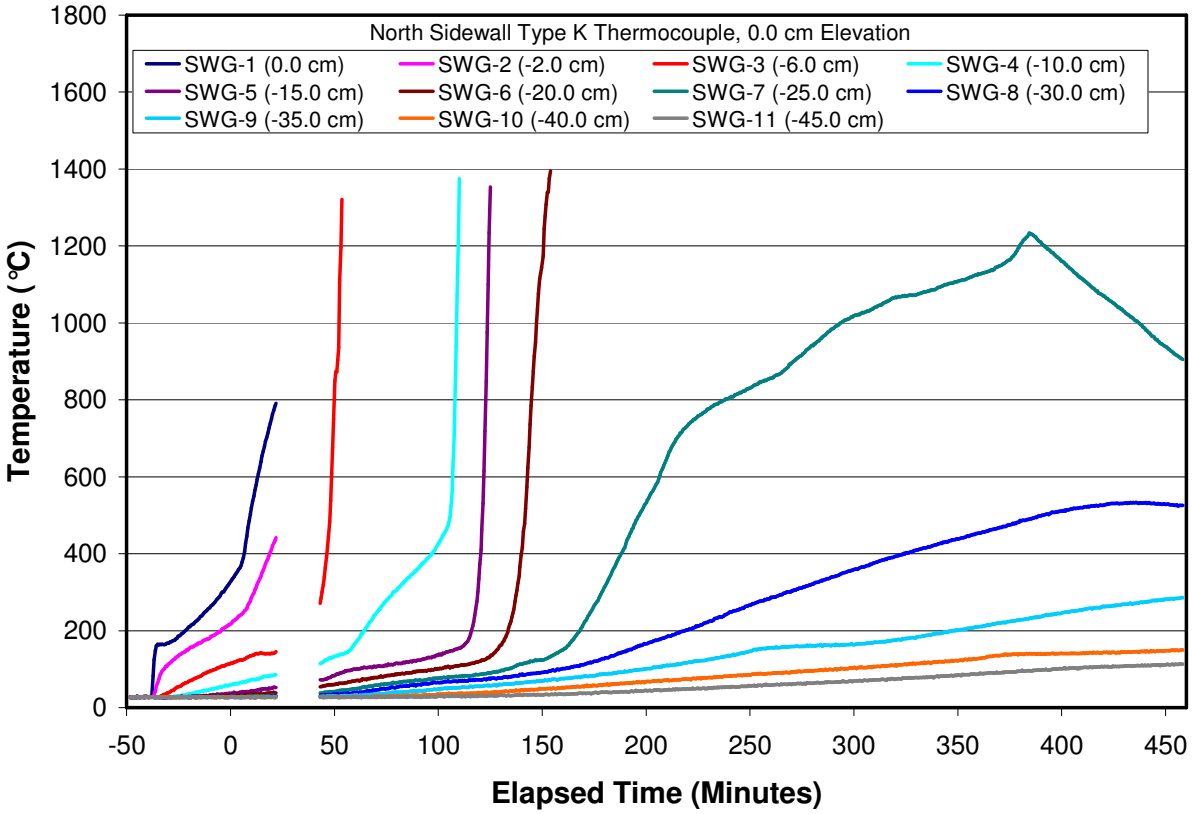

Figure B-20. North Sidewall Type K "SWG" Array Data.

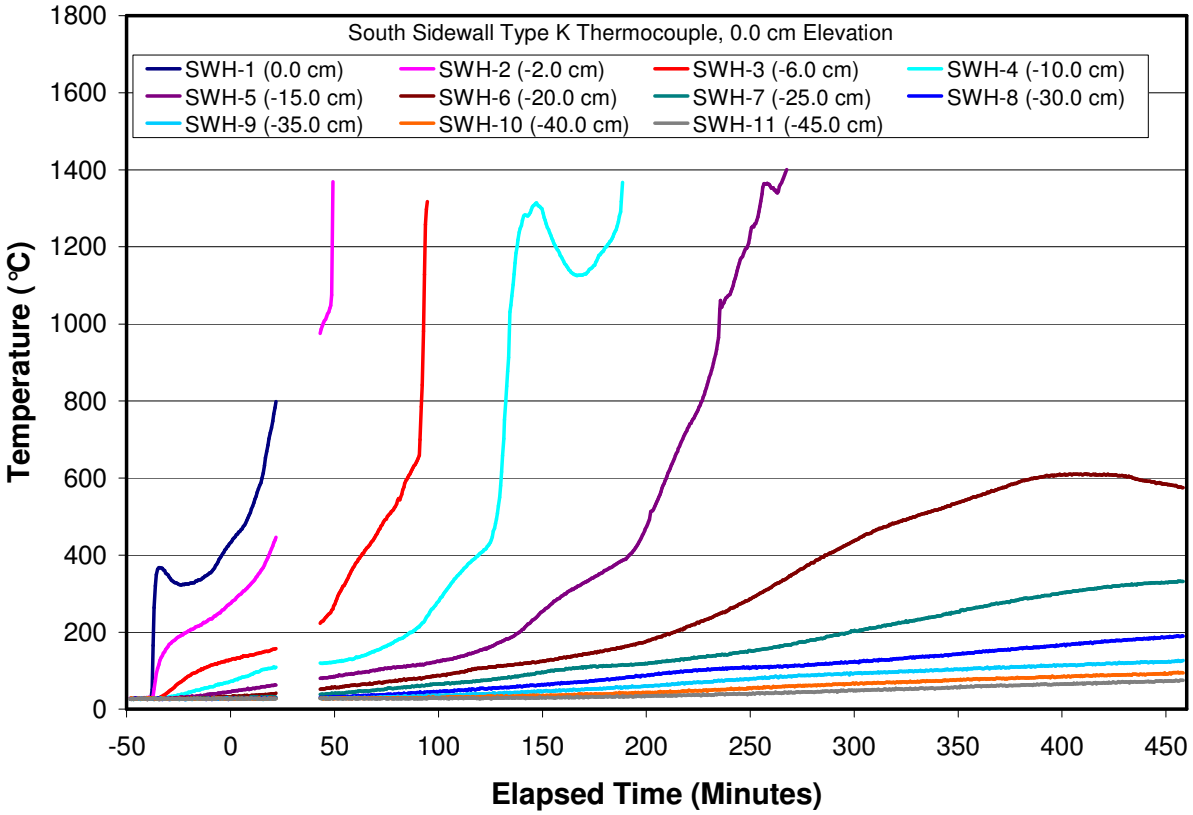

Figure B-21. South Sidewall Type K "SWH" Array Data.

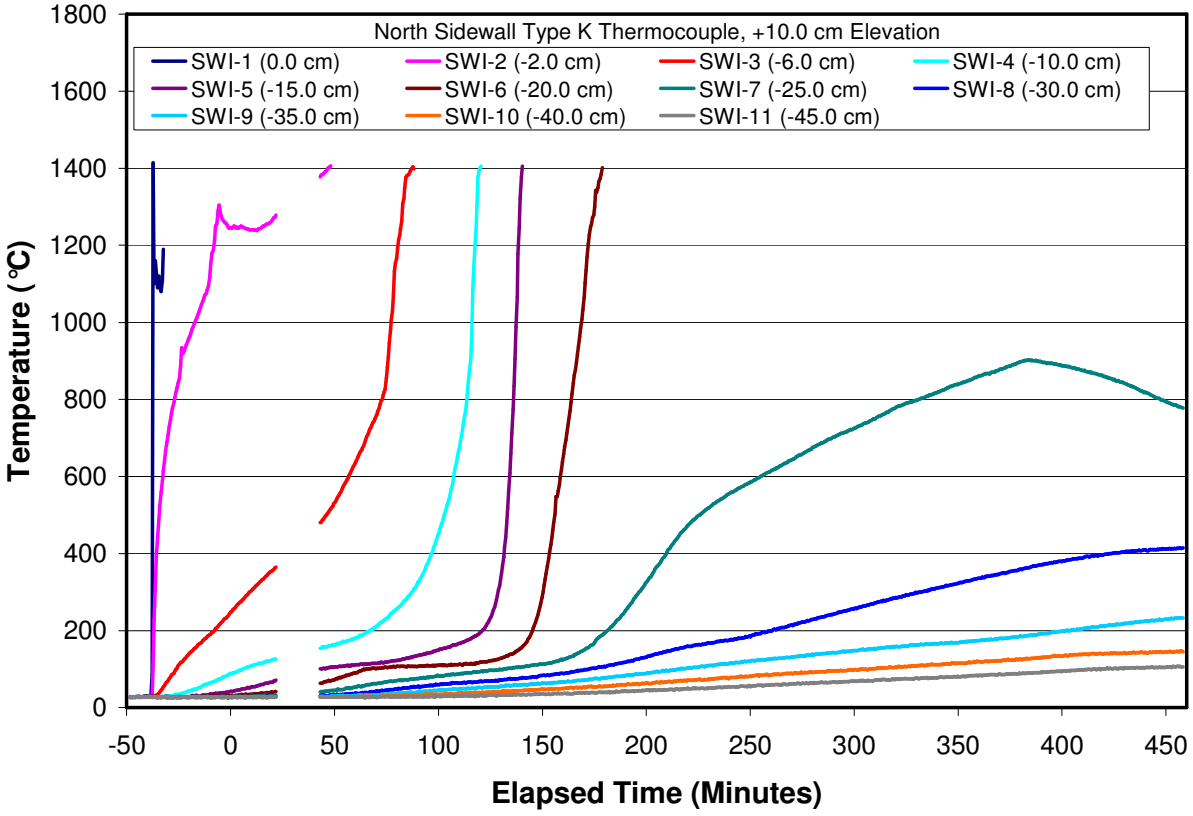

Figure B-22. North Sidewall Type K "SWI" Array Data.

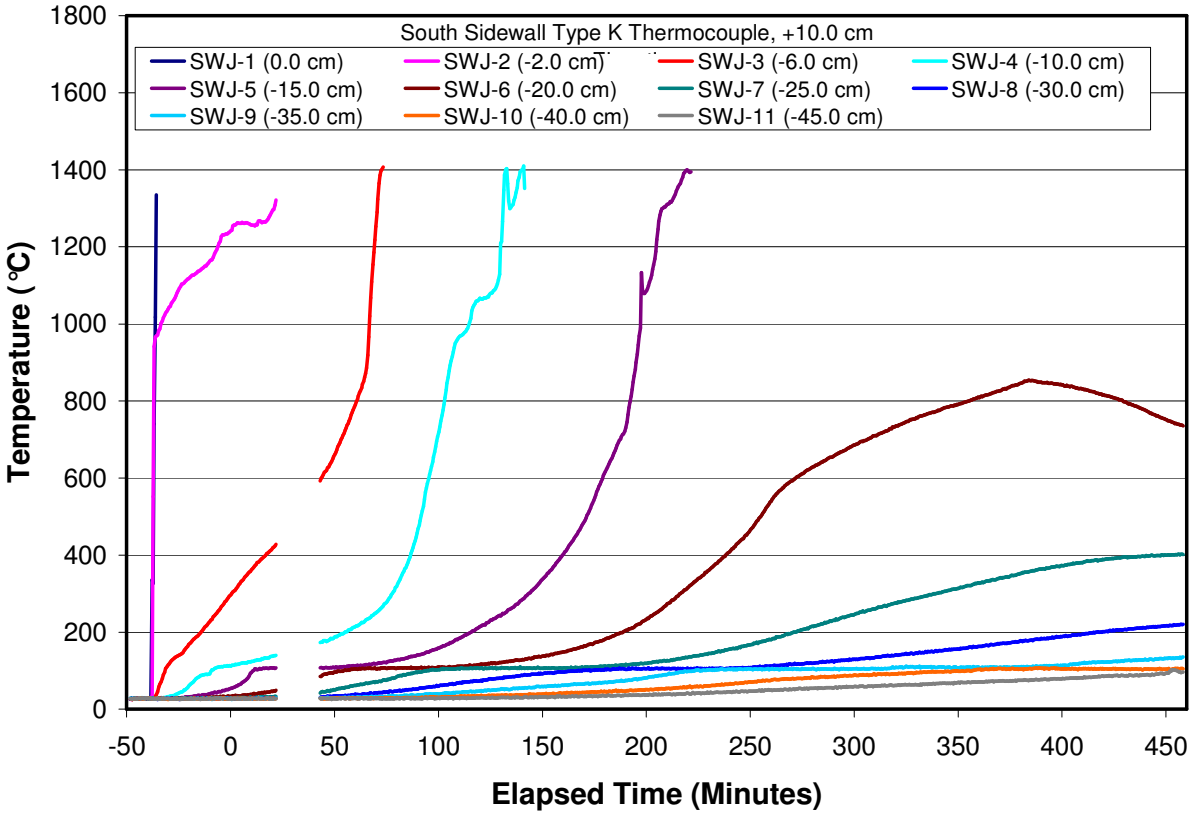

Figure B-23. South Sidewall Type K "SWJ" Array Data.

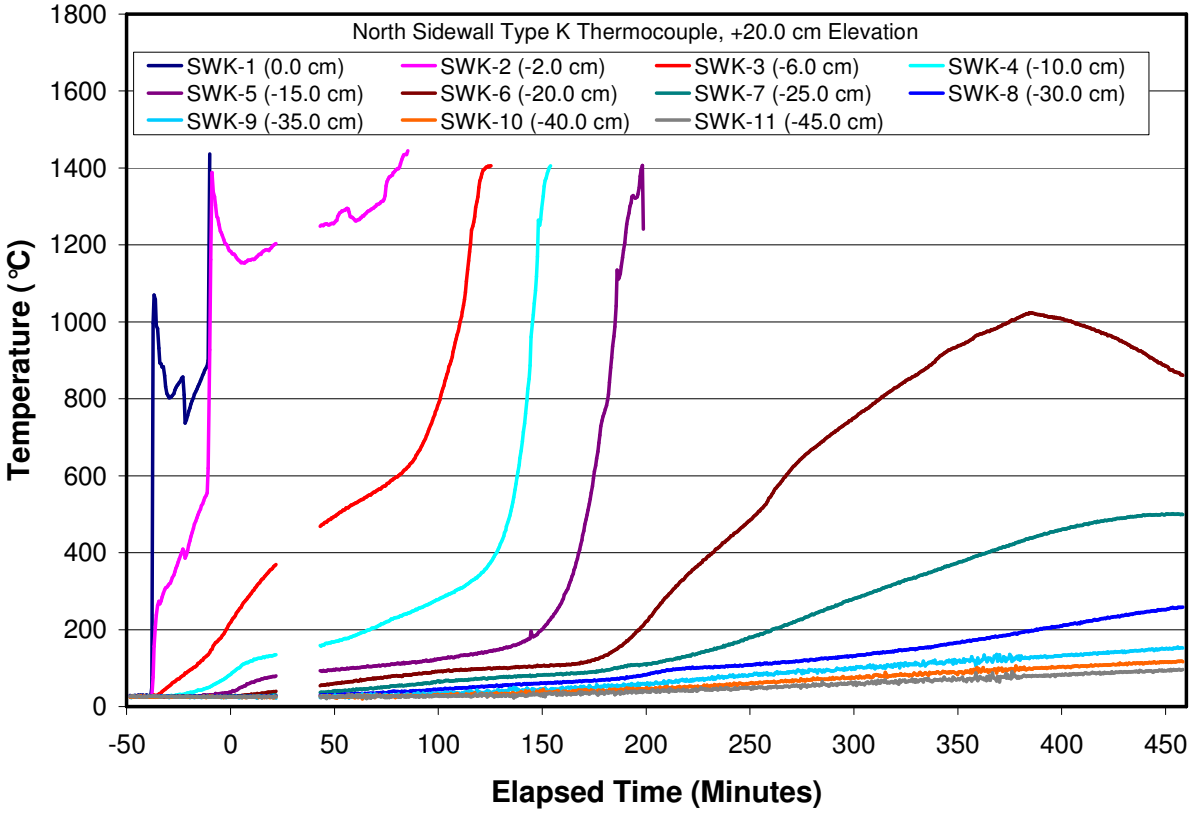

Figure B-24. North Sidewall Type K "SWK" Array Data.

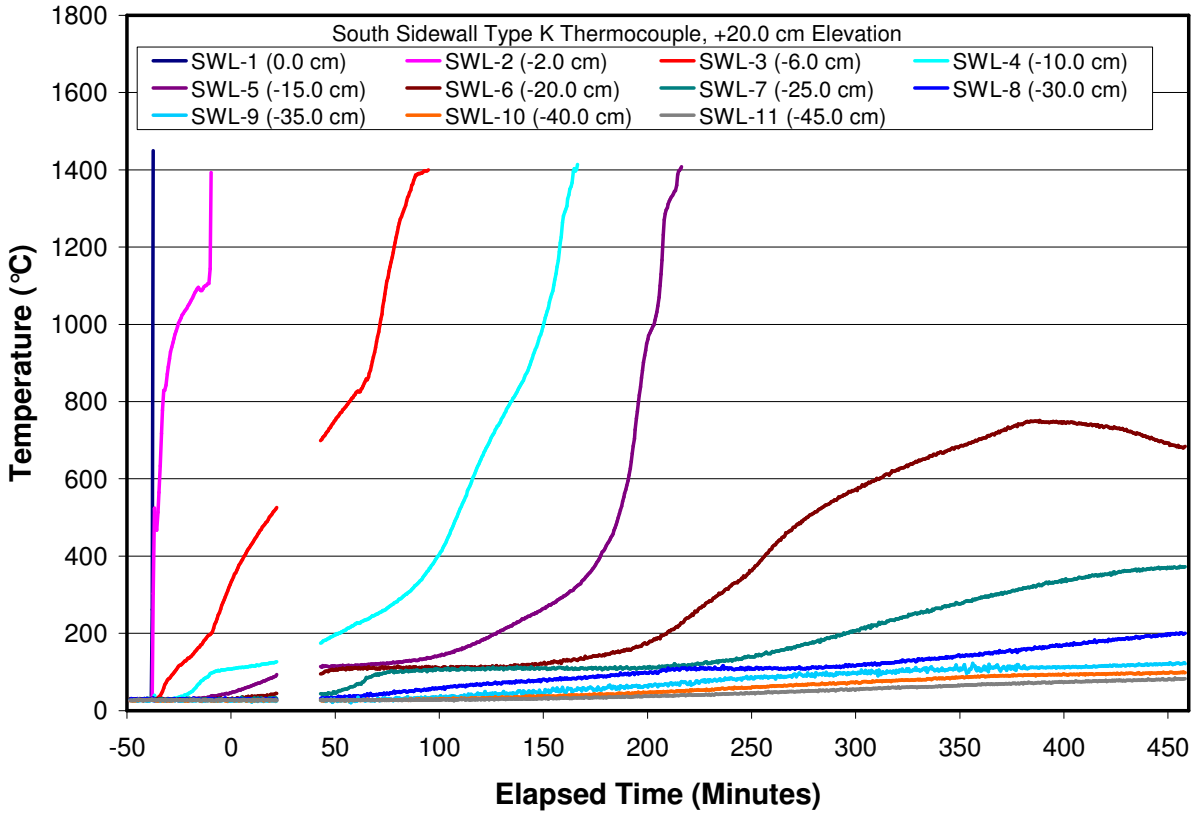

Figure B-25. South Sidewall Type K "SWL" Array Data.

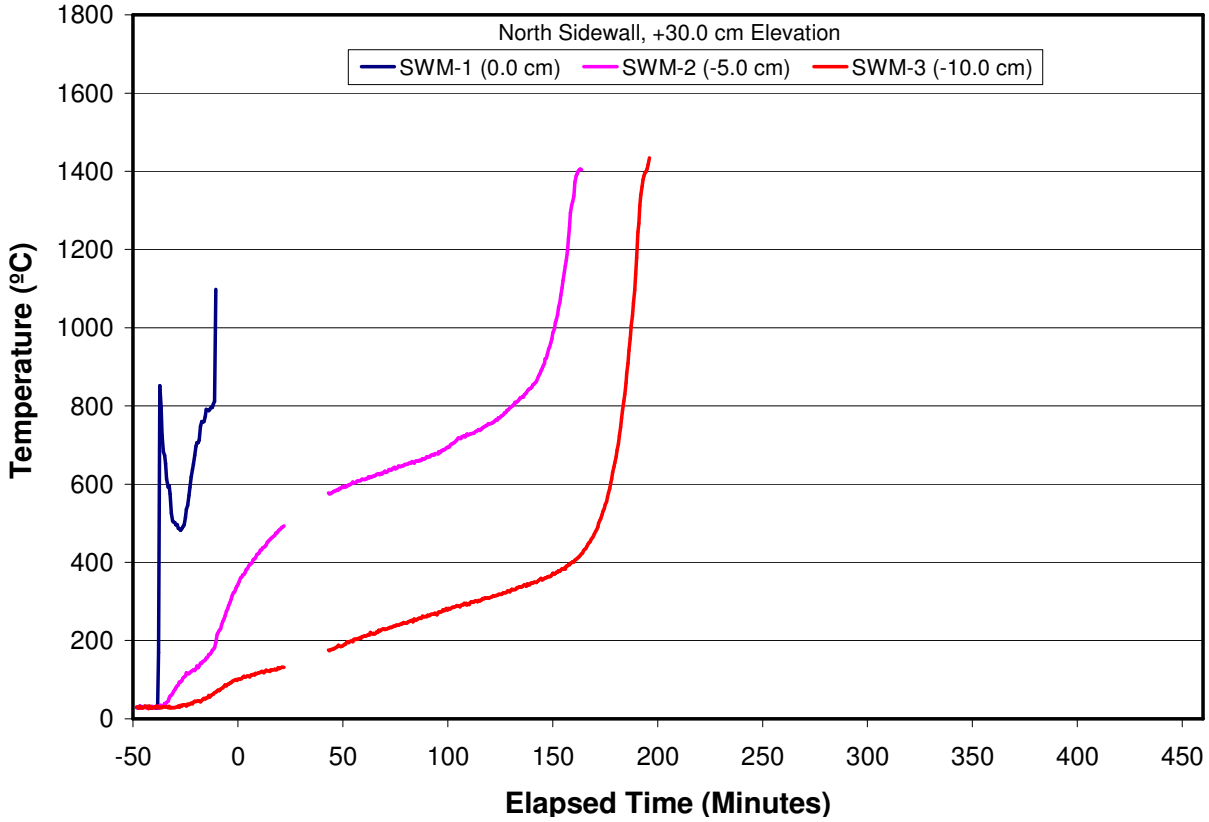

Figure B-26. North Sidewall Type K "SWM" Array Data.

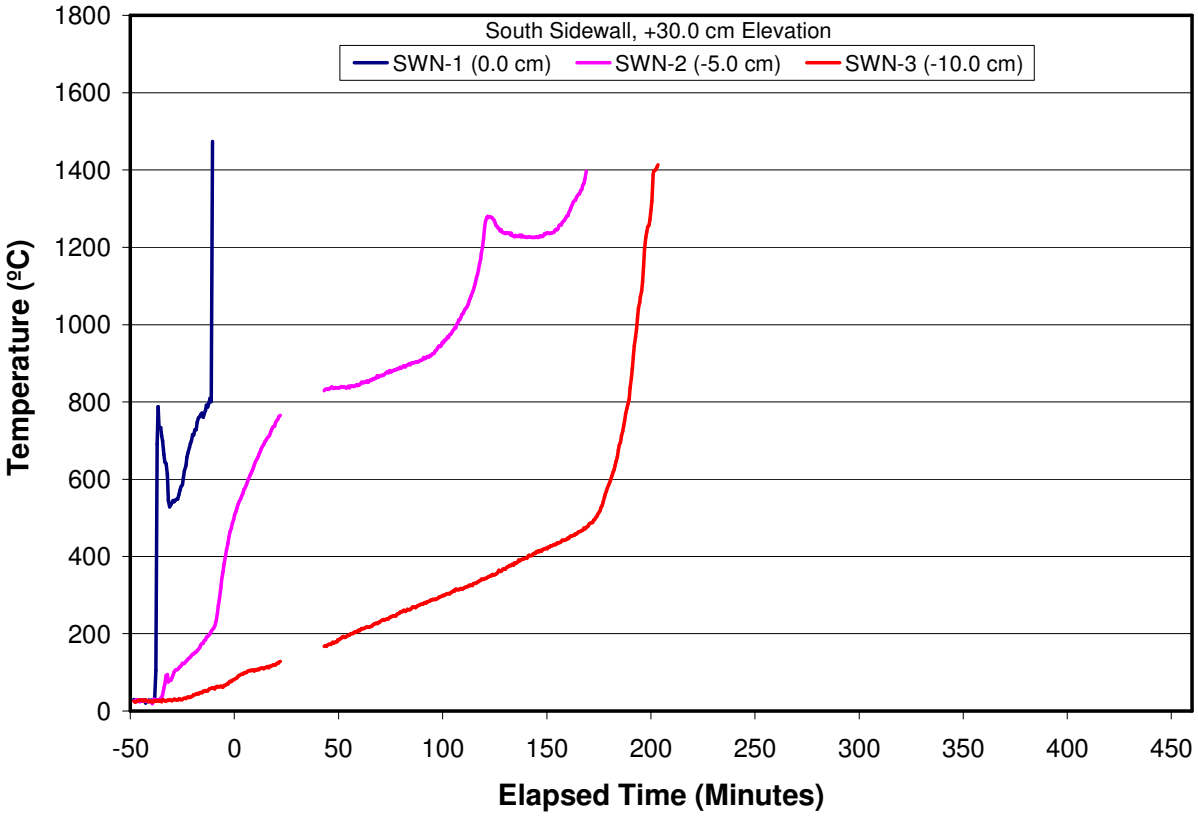

Figure B-27. South Sidewall Type K "SWN" Array Data.

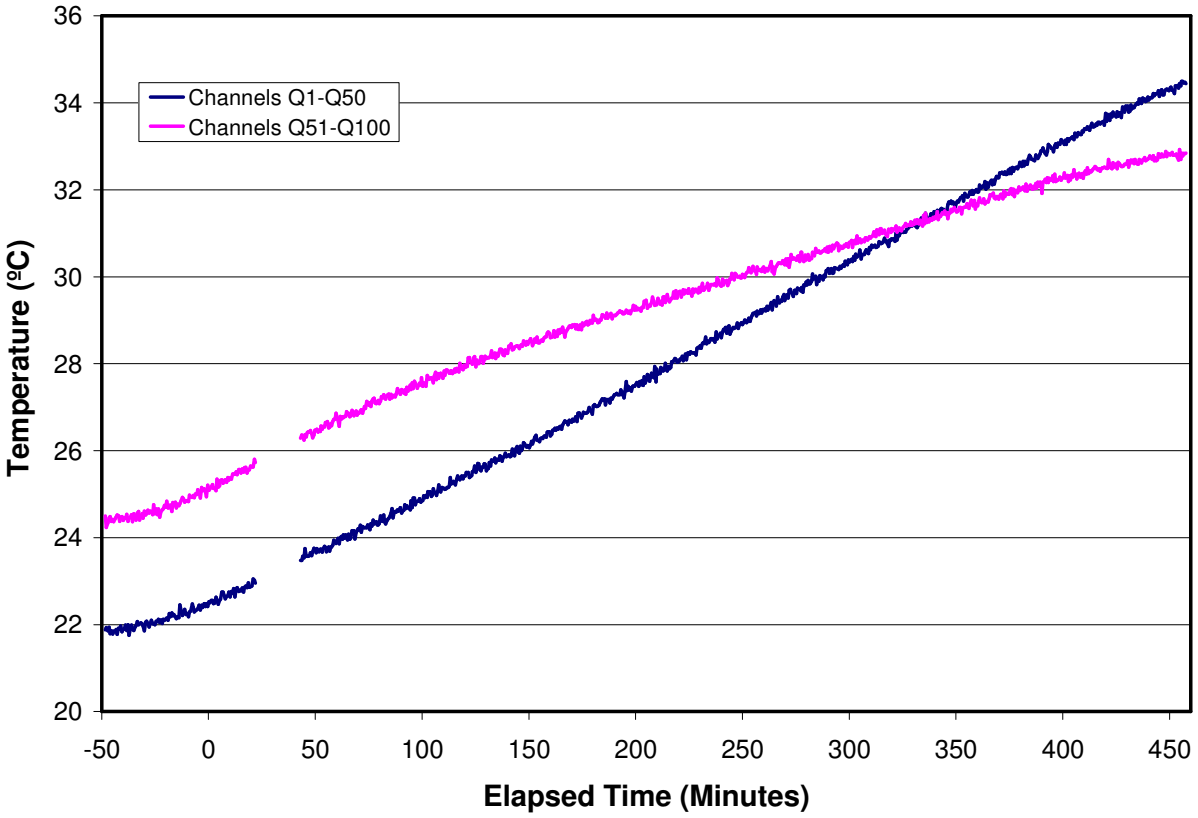

Figure B-28. Thermocouple Compensator Data for Channels Q1-Q50 and Q51-Q100.

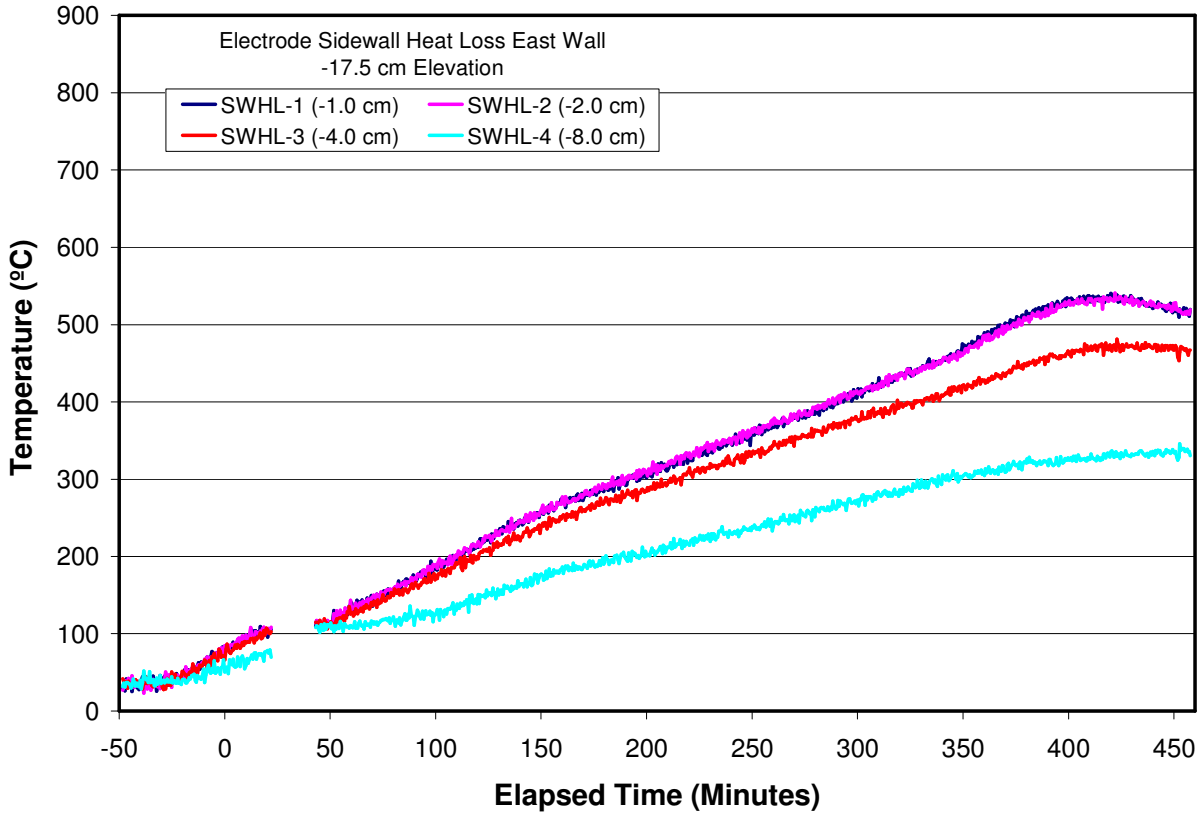

Figure B-29. Test Section Sidewall Heat Loss Data at -17.5 cm Elevation.

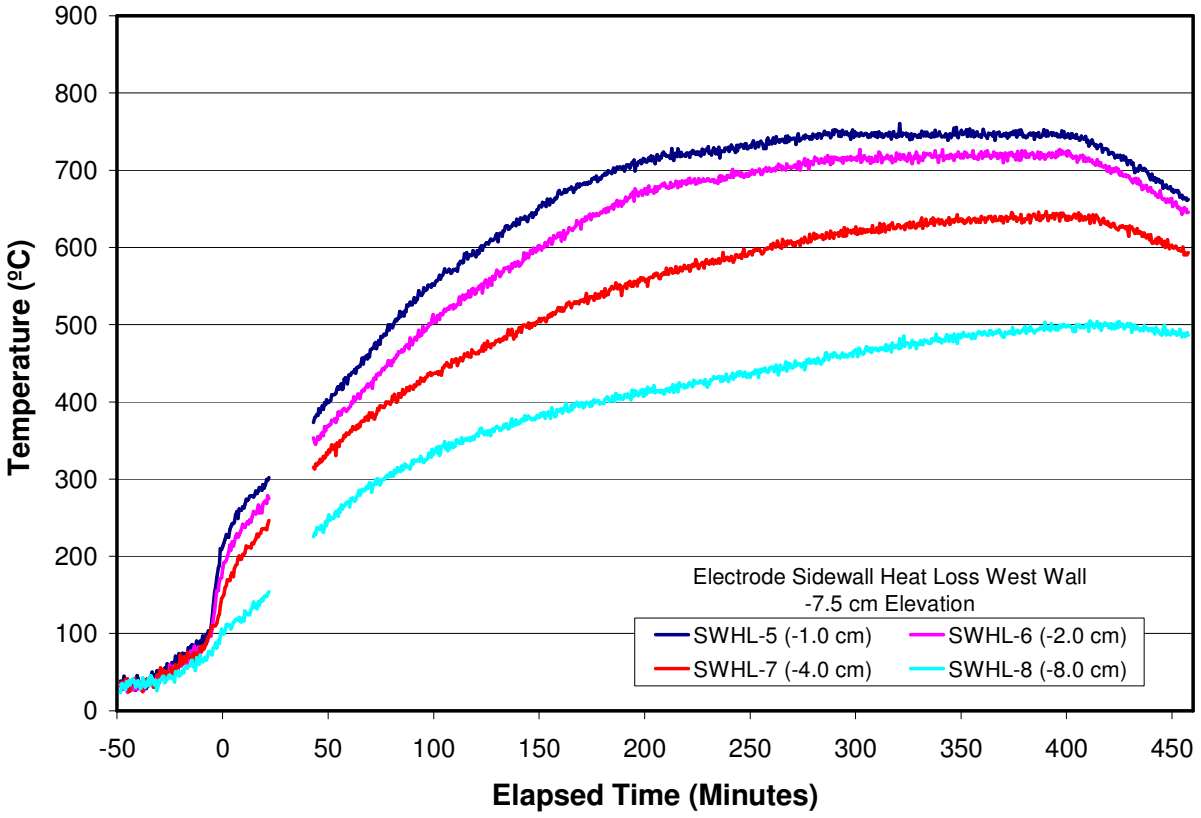

Figure B-30. Test Section Sidewall Heat Loss Data at -7.5 cm Elevation.

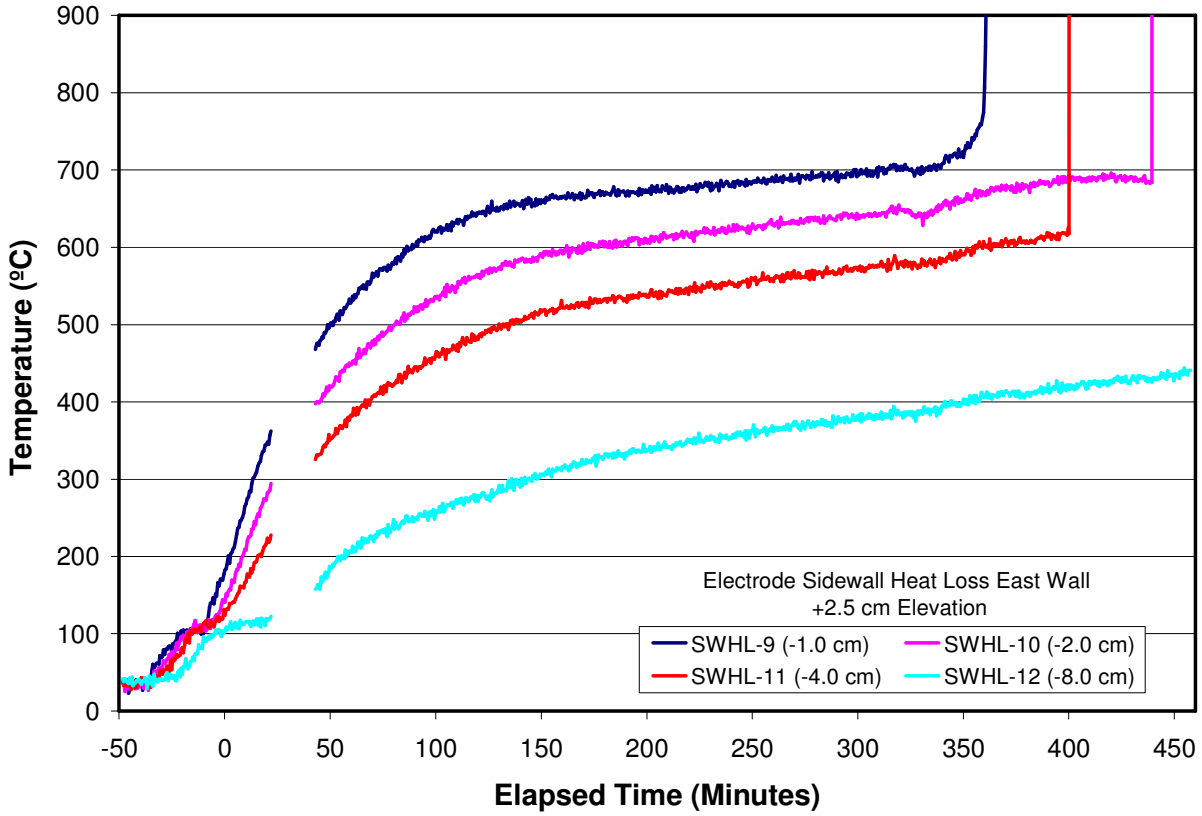

Figure B-31. Test Section Sidewall Heat Loss Data at +2.5 cm Elevation.

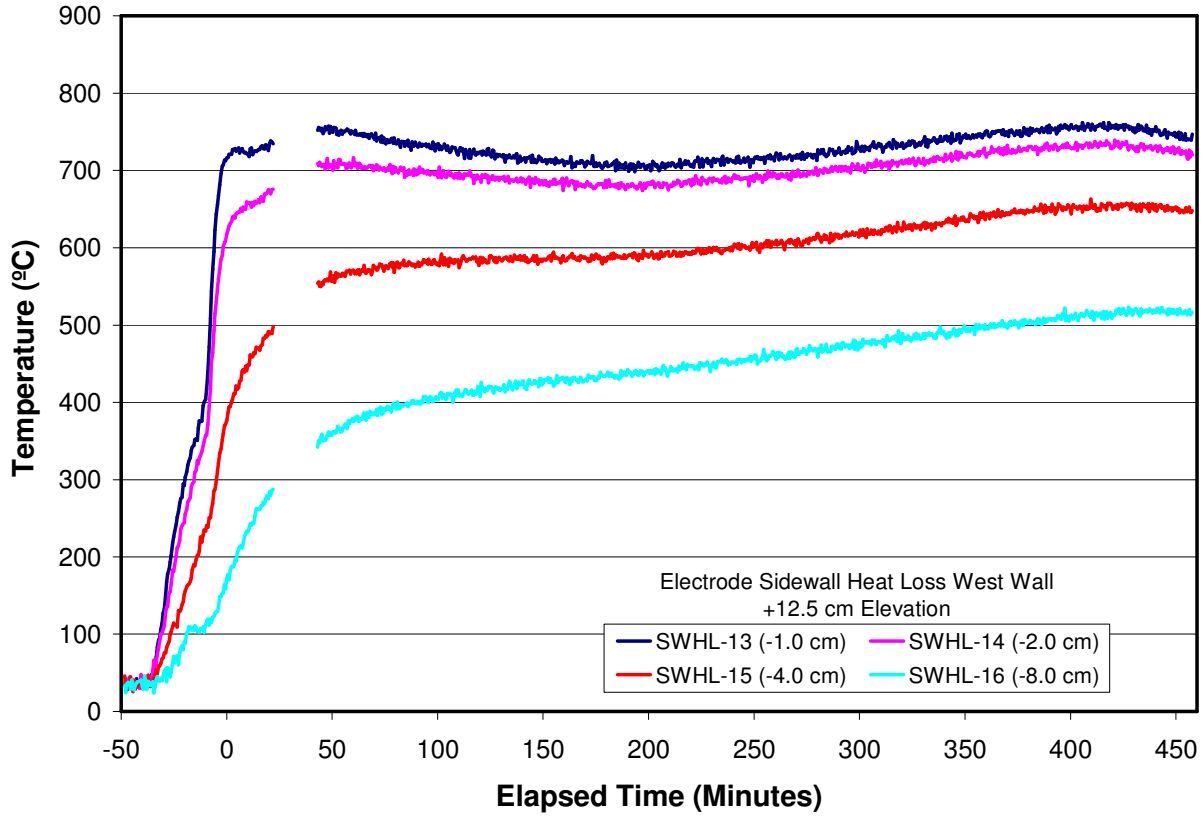

Figure B-32. Test Section Sidewall Heat Loss Data at +12.5 cm Elevation.

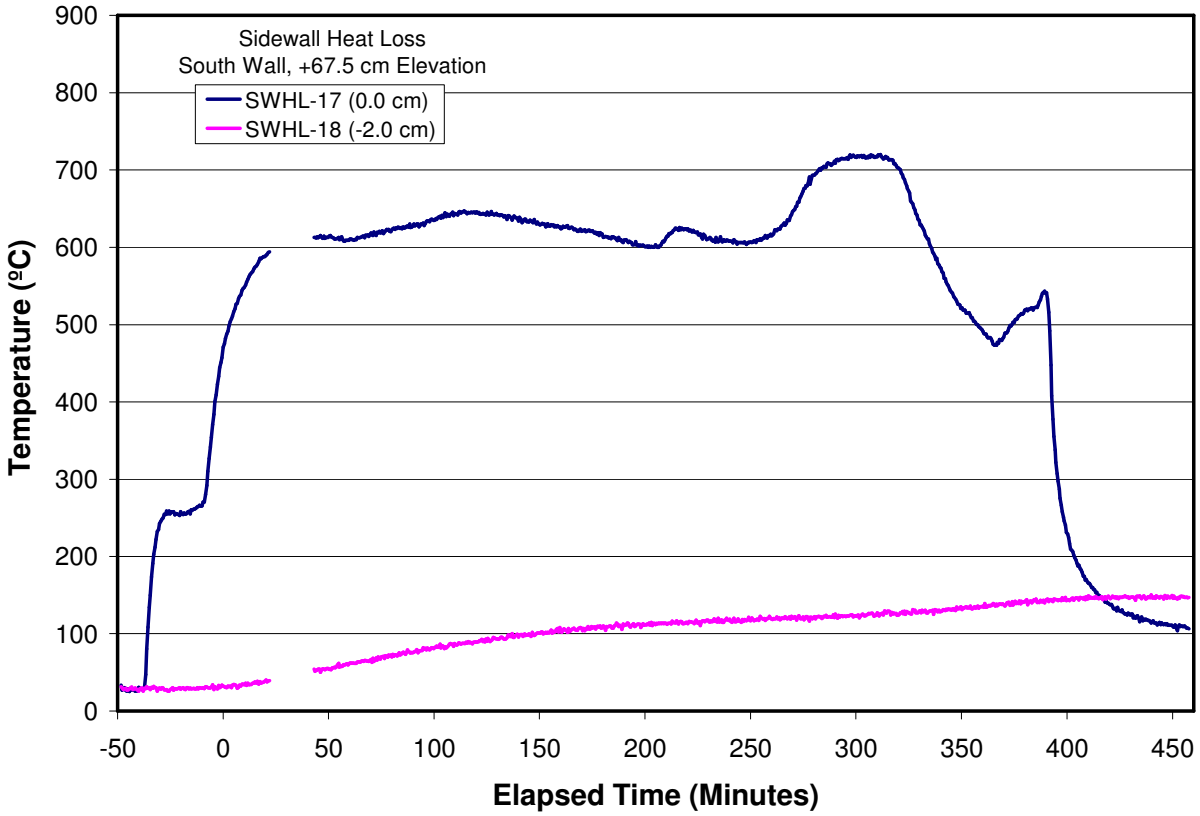

Figure B-33. Test Section Sidewall Heat Loss Data at the +67.5 cm Elevation.

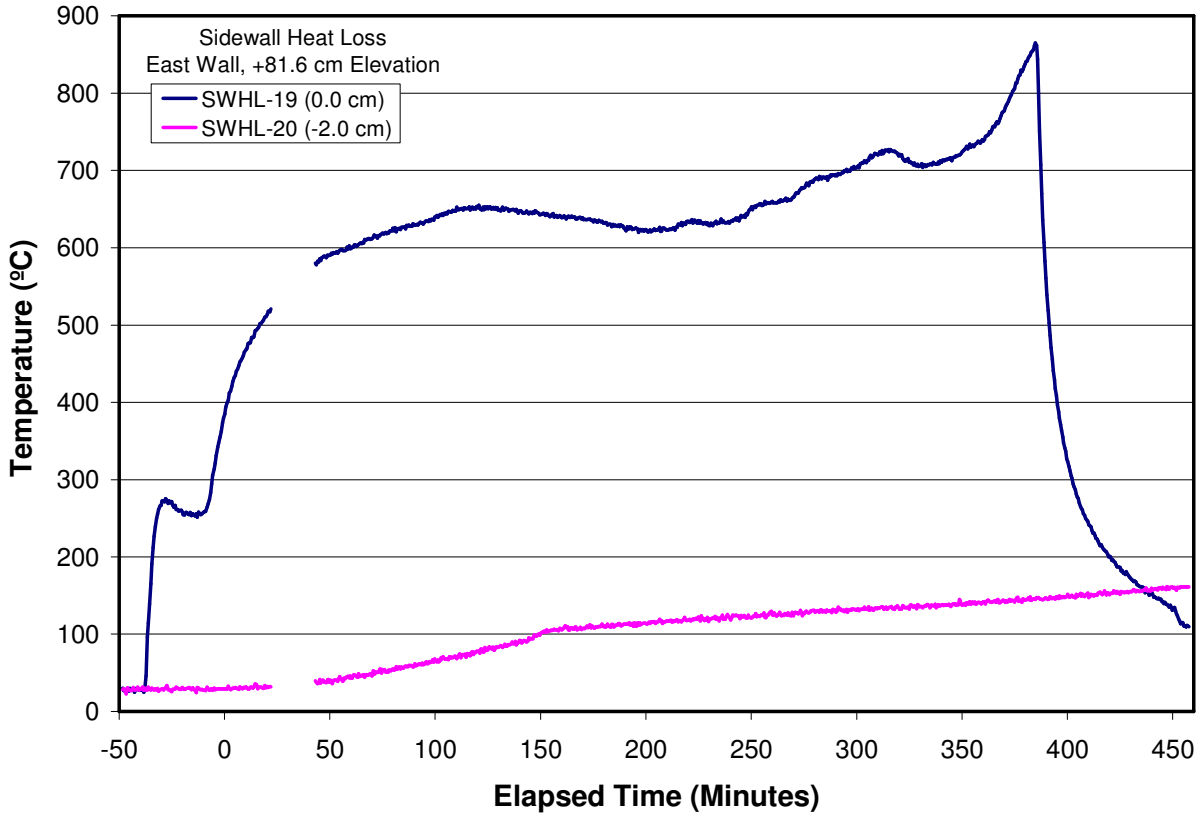

Figure B-34. Test Section Sidewall Heat Loss Data at the +81.6 cm Elevation.

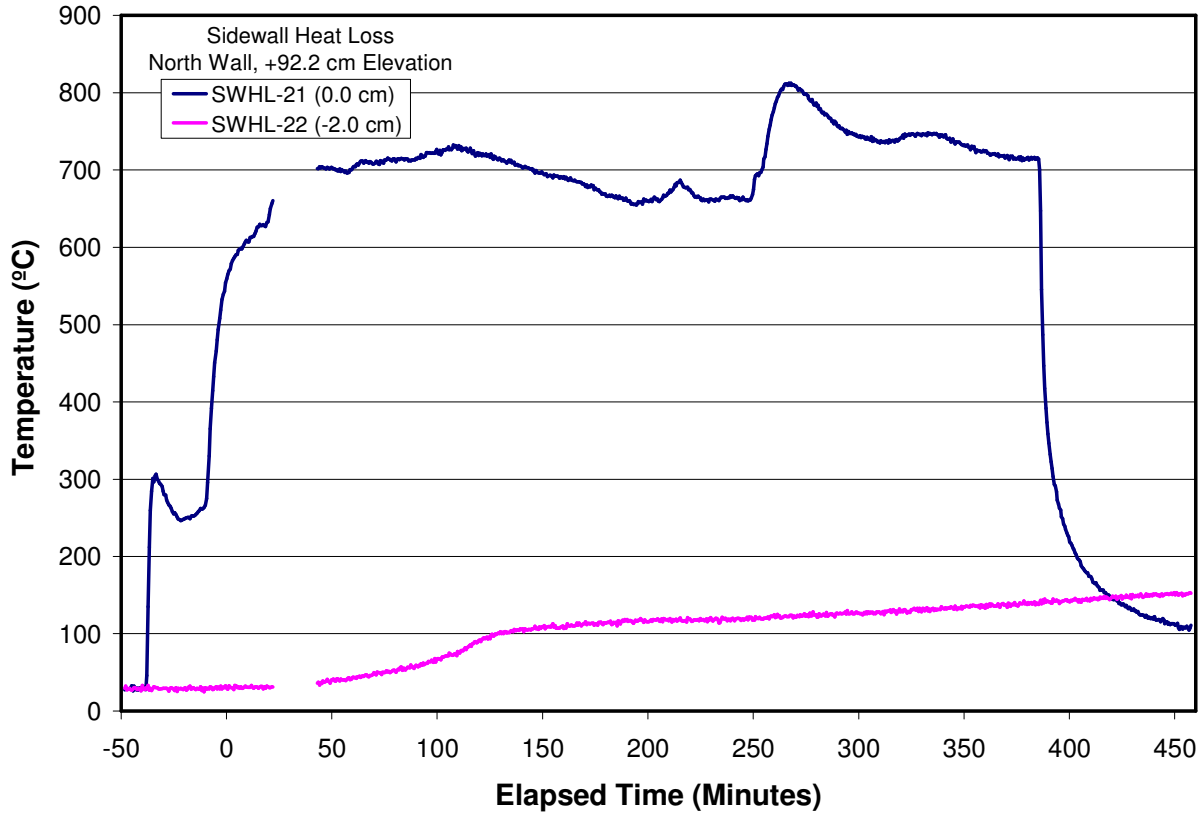

Figure B-35. Test Section Sidewall Heat Loss Data at the + 92.2 cm Elevation.

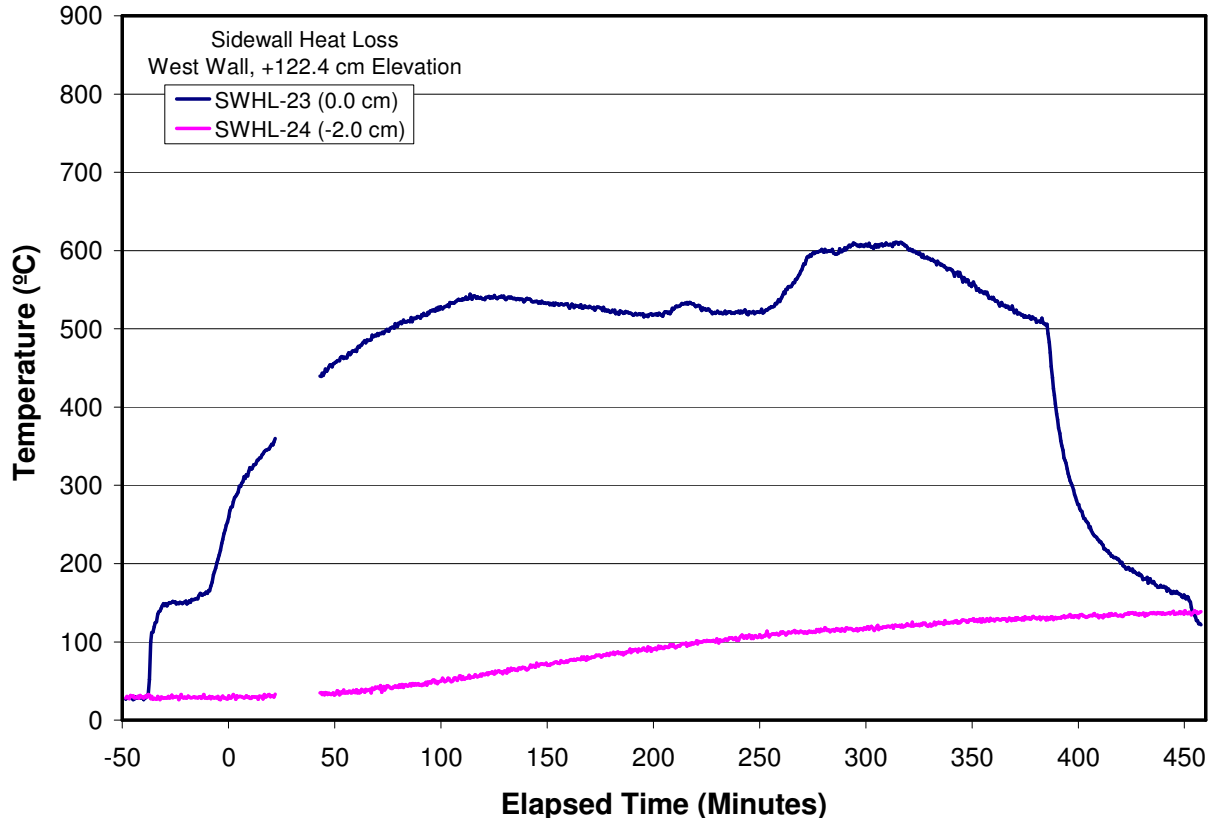

Figure B-36. Test Section Sidewall Heat Loss Data at the + 122.4 cm Elevation.

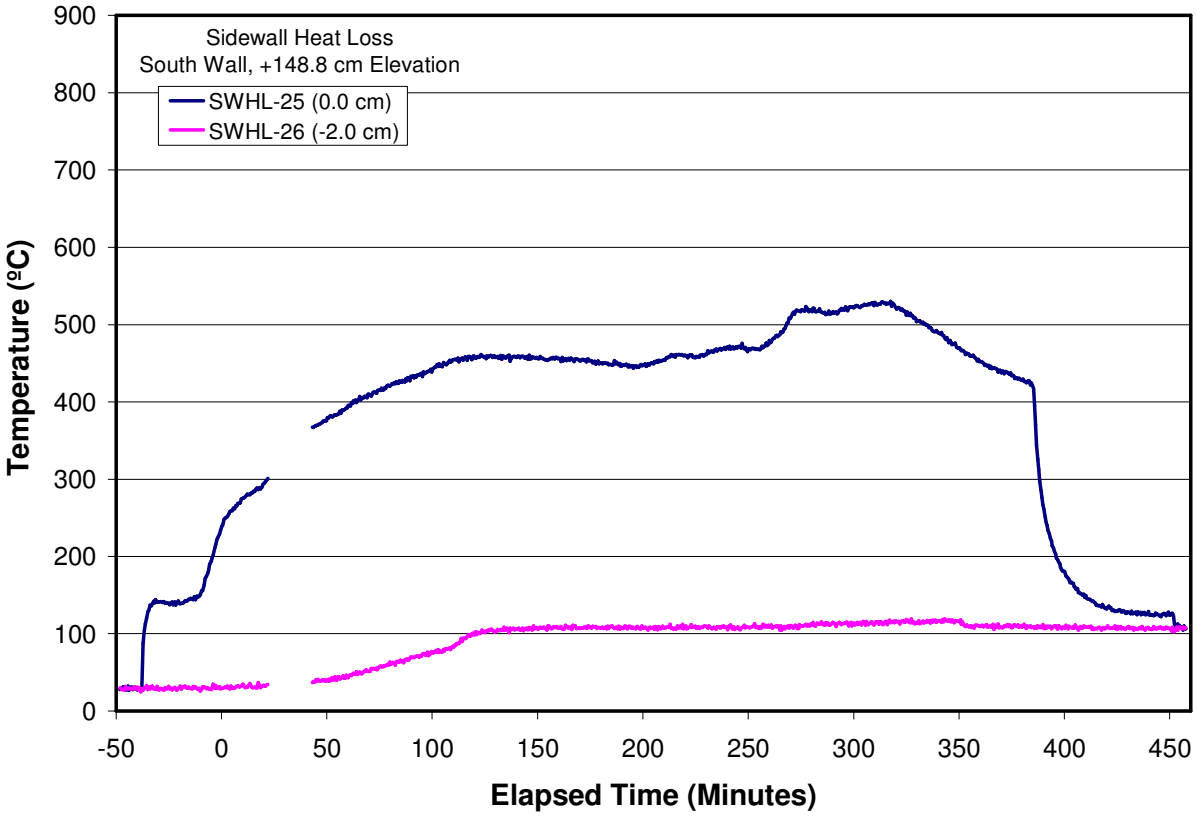

Figure B-37. Test Section Sidewall Heat Loss Data at the + 148.8 cm Elevation.

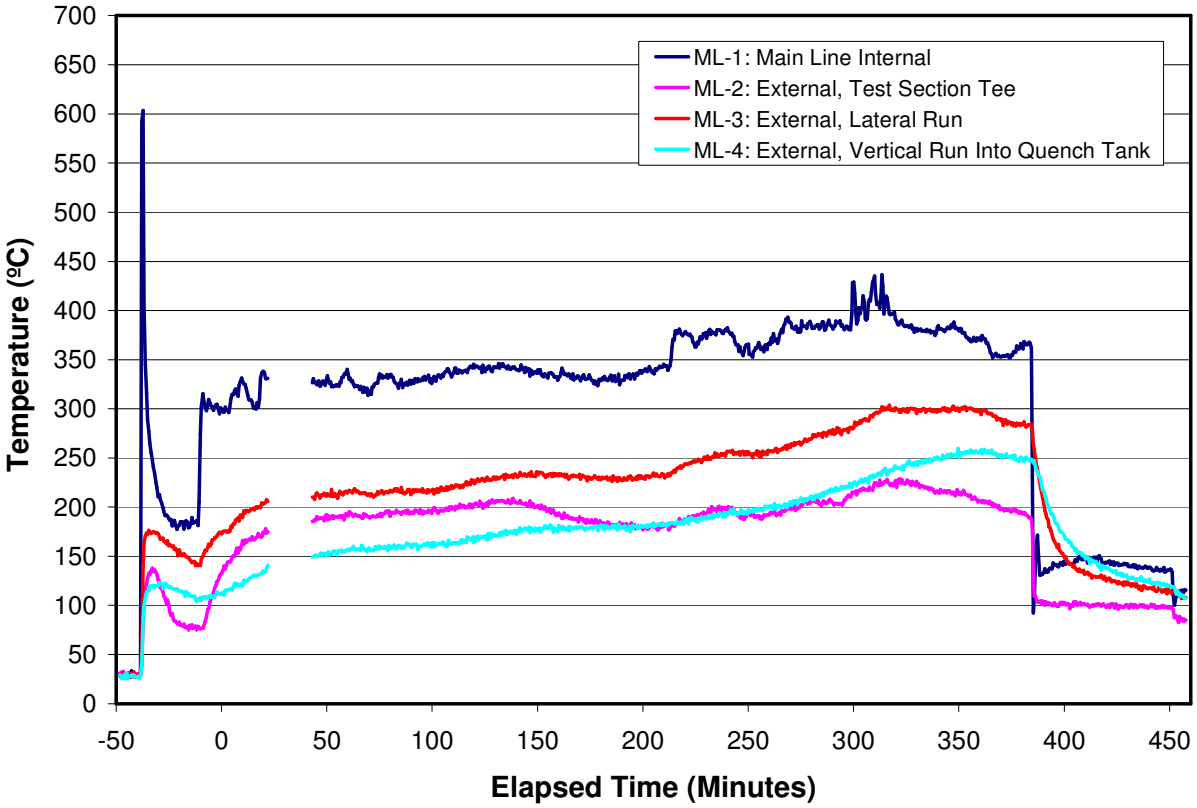

Figure B-38. Test Section Mainline Thermocouple Data.

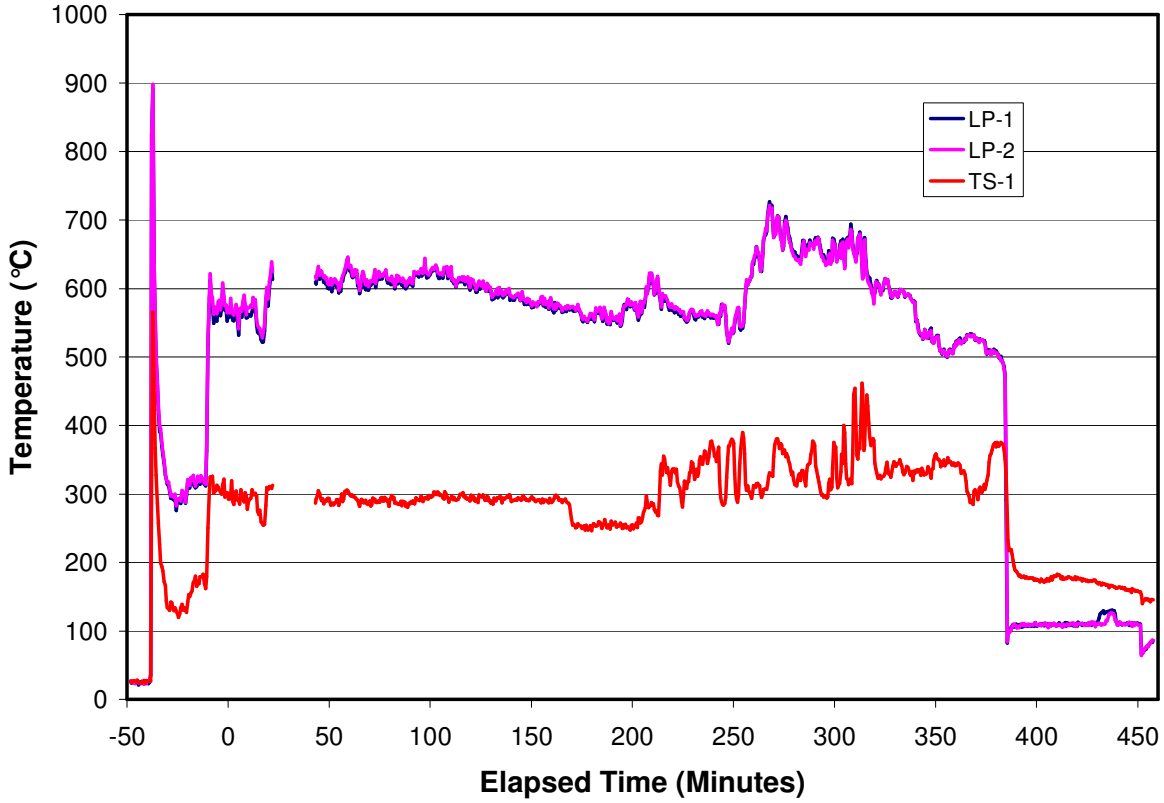

Figure B-39. Test Section Plenum and Insertable Water Level Probe Thermocouple Data.

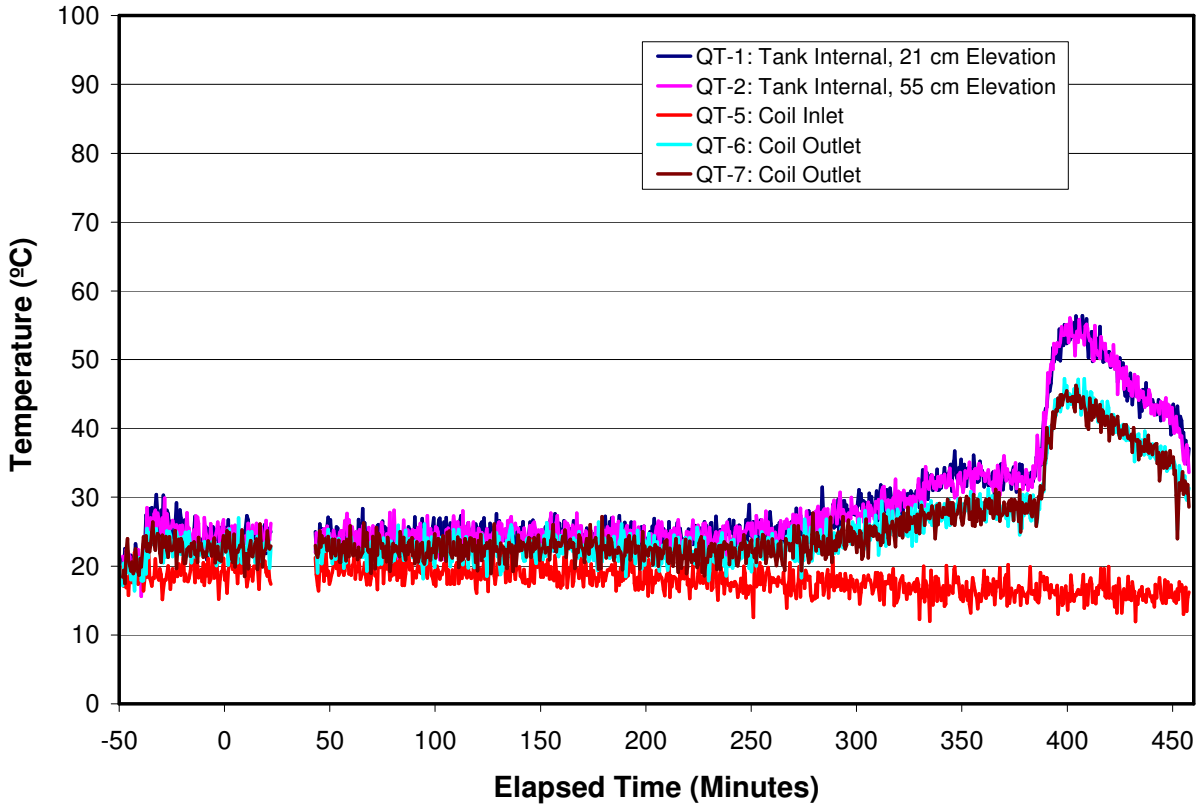

Figure B-40. Quench Tank Water Volume, Coil Inlet, and Coil Outlet Temperature Data.

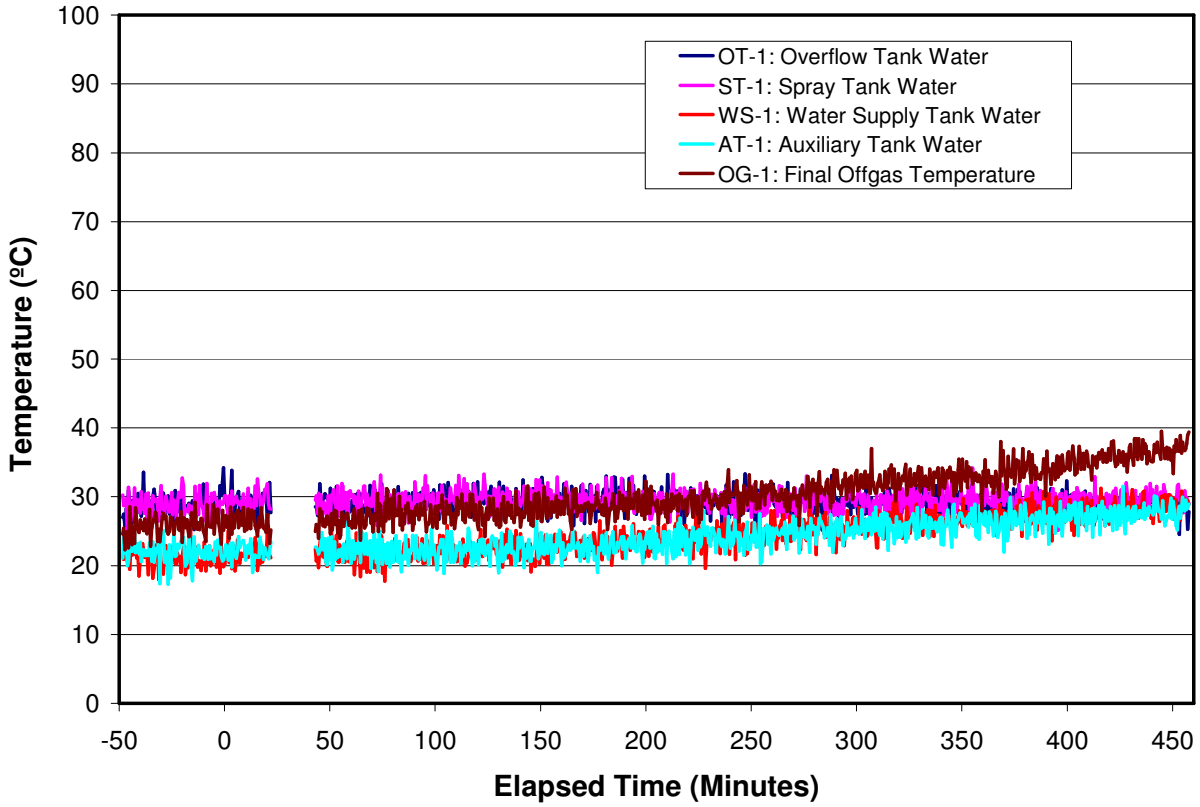

Figure B-41. Miscellaneous Temperatures in Water Supply, Quench, and Off Gas Systems.

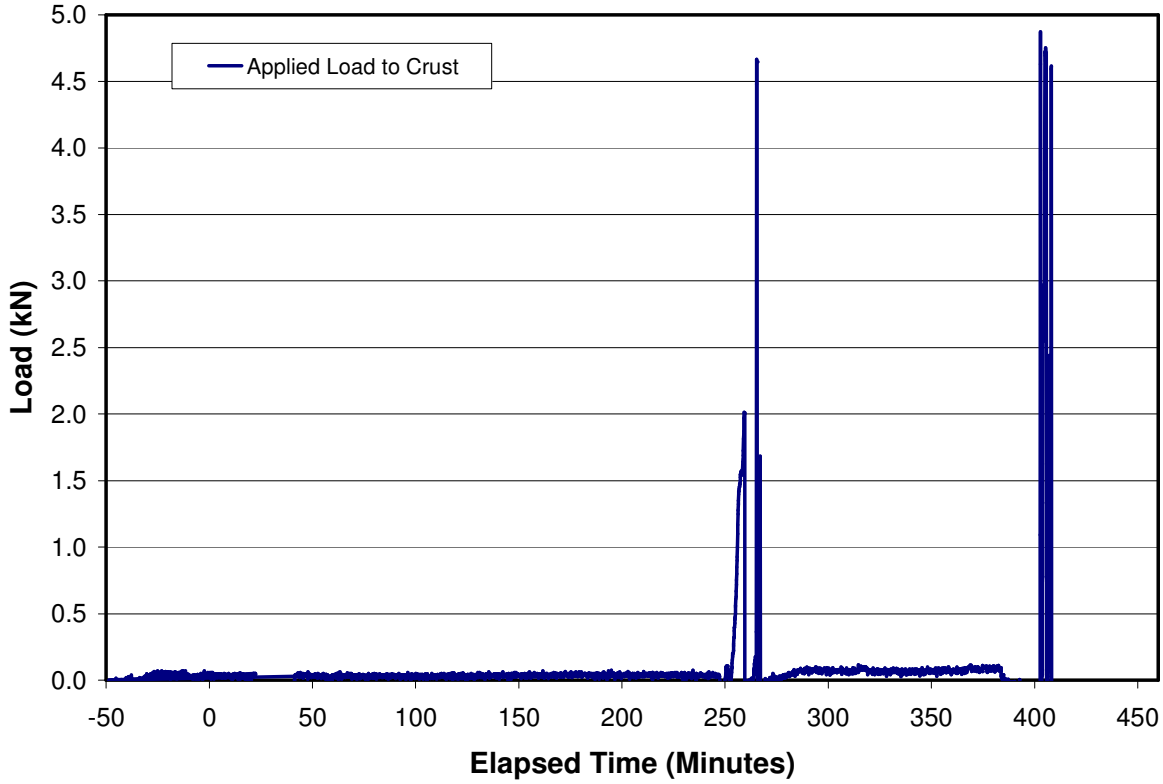

Figure B-42. Crust Lance Load Cell Data.

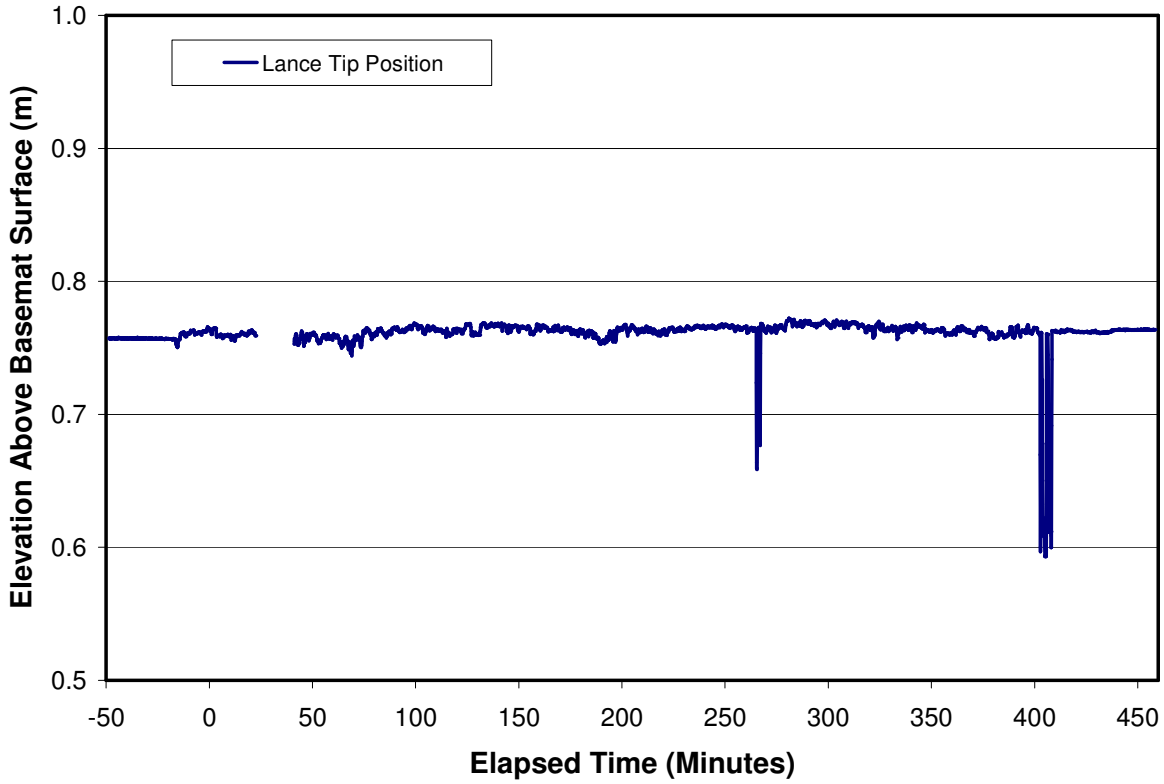

Figure B-43. Lance Position Indicator Data.

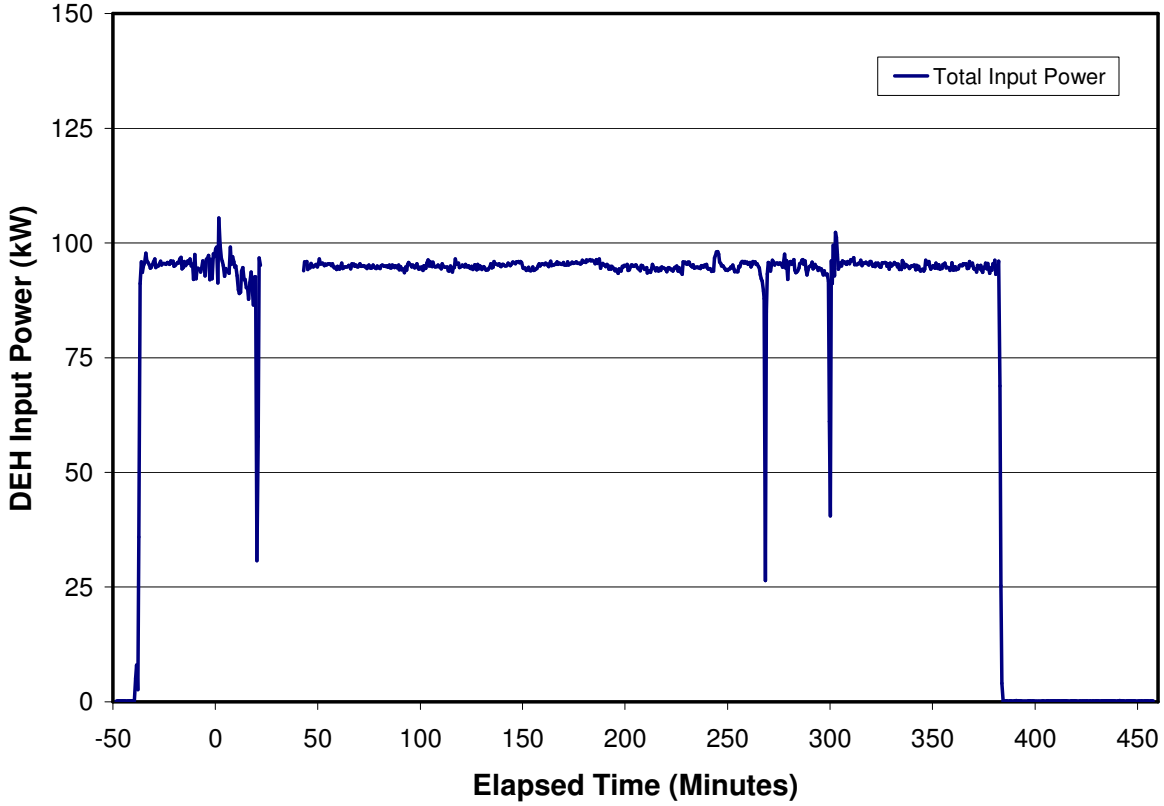

Figure B-44. Total Power Supply Power.

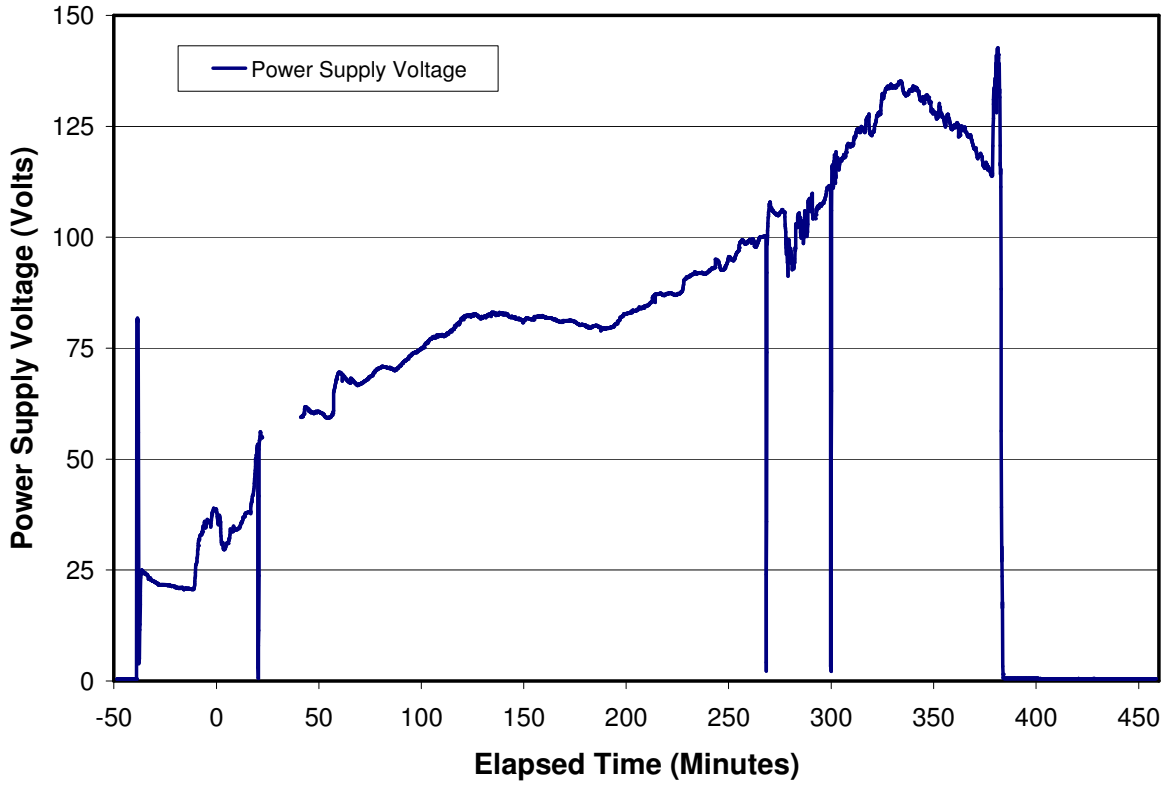

Figure B-45. Power Supply Voltage Data.

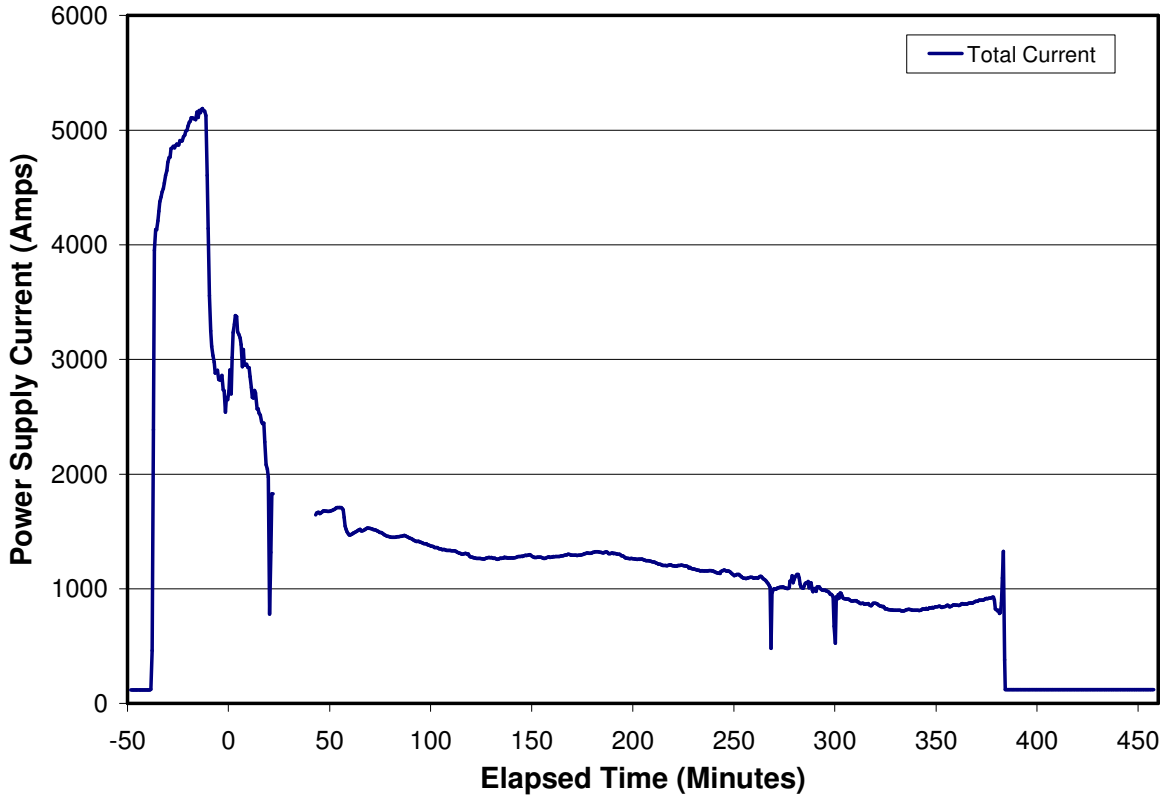

Figure B-46. Total Power Supply Current Data.

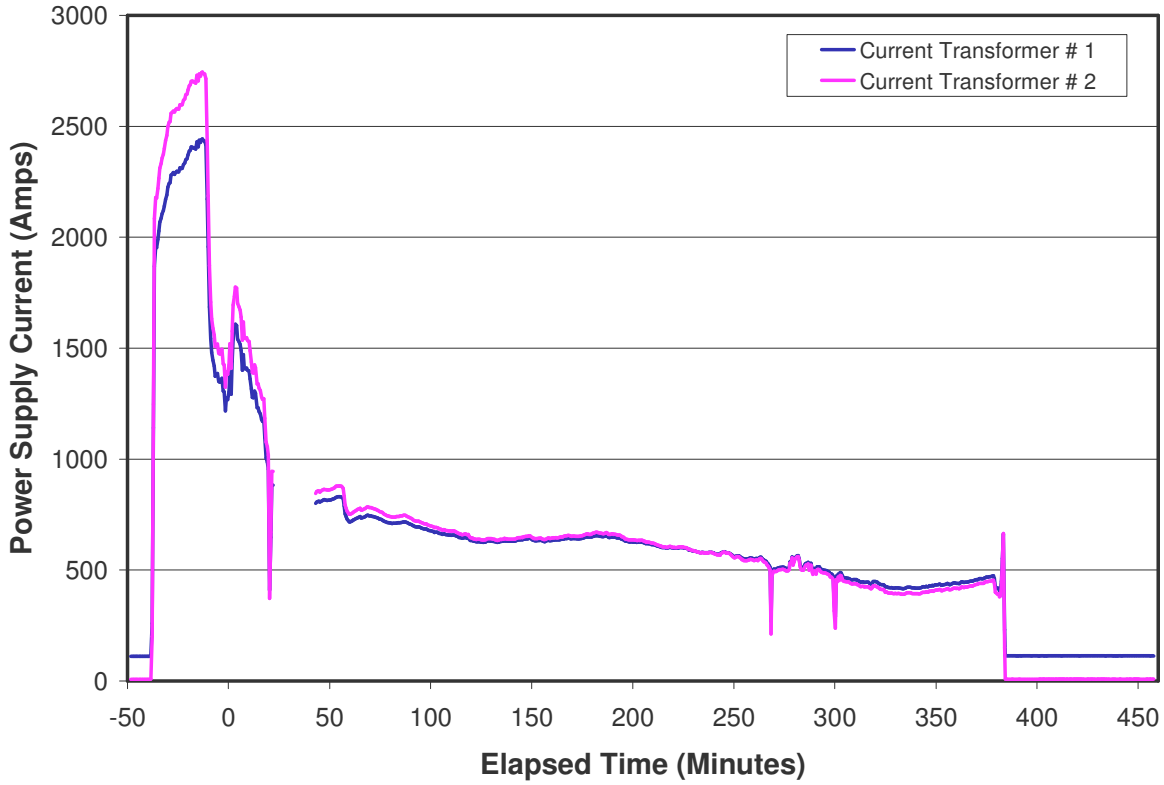

Figure B-47. Power Supply Current Transformer Data.

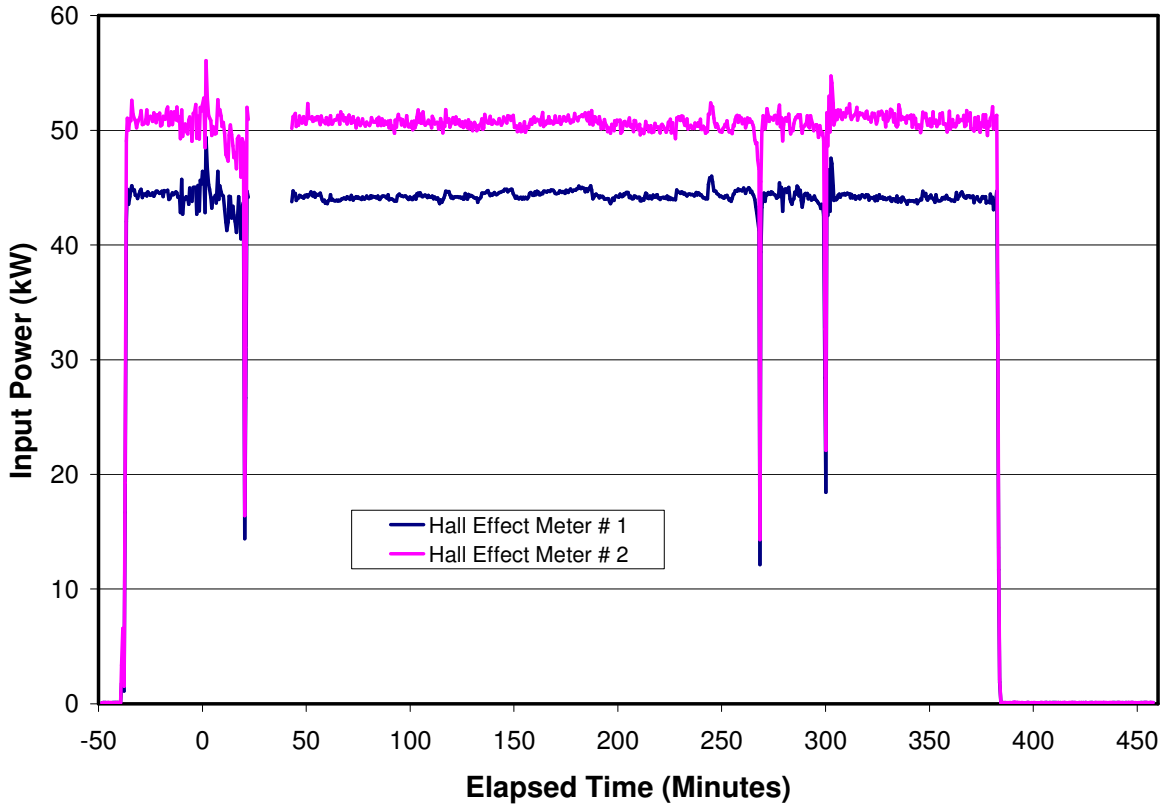

Figure B-48. Hall Effect Meter Data.

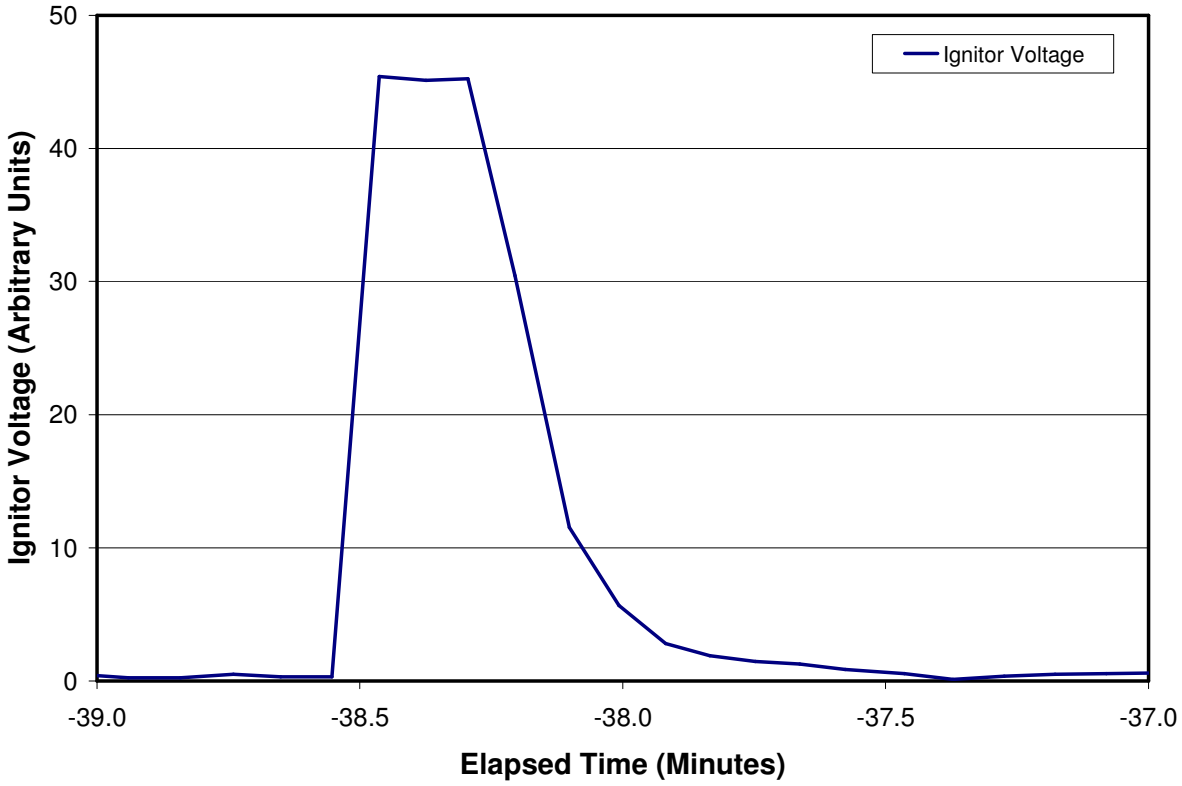

Figure B-49. Voltage across Igniter Shunt.

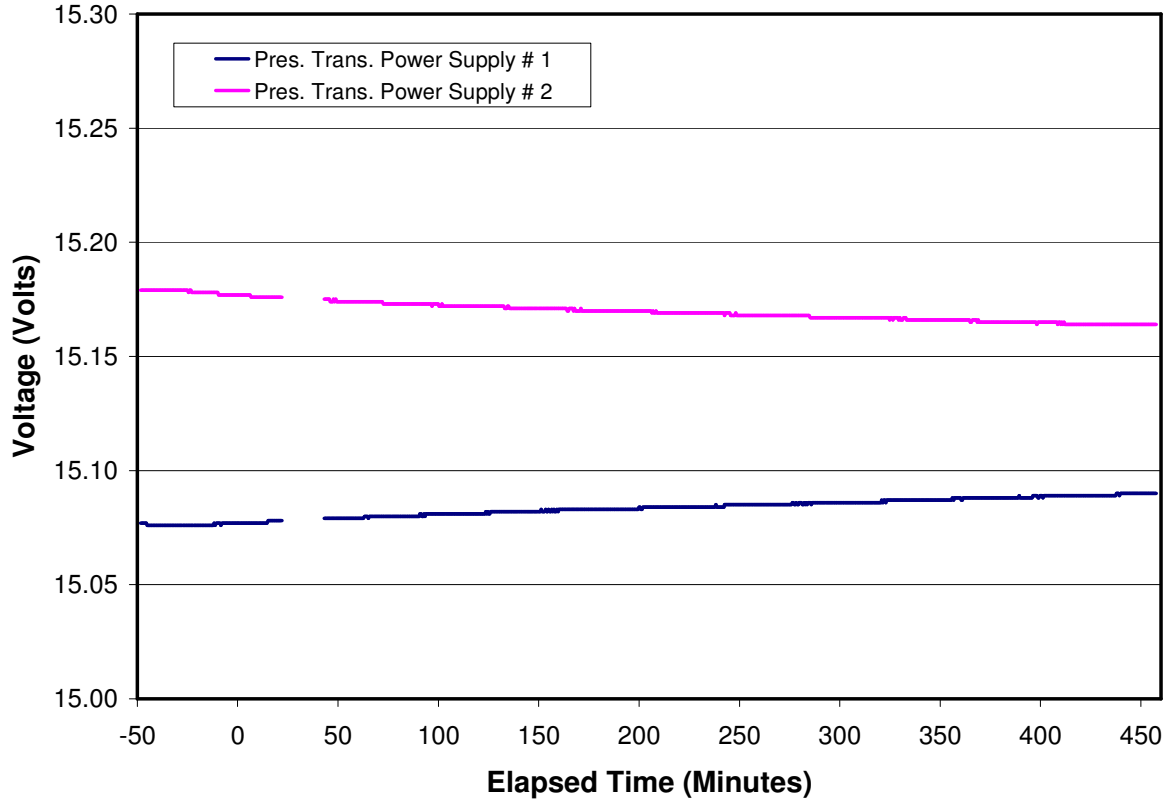

Figure B-50. Pressure Transducer Power Supply Voltages.

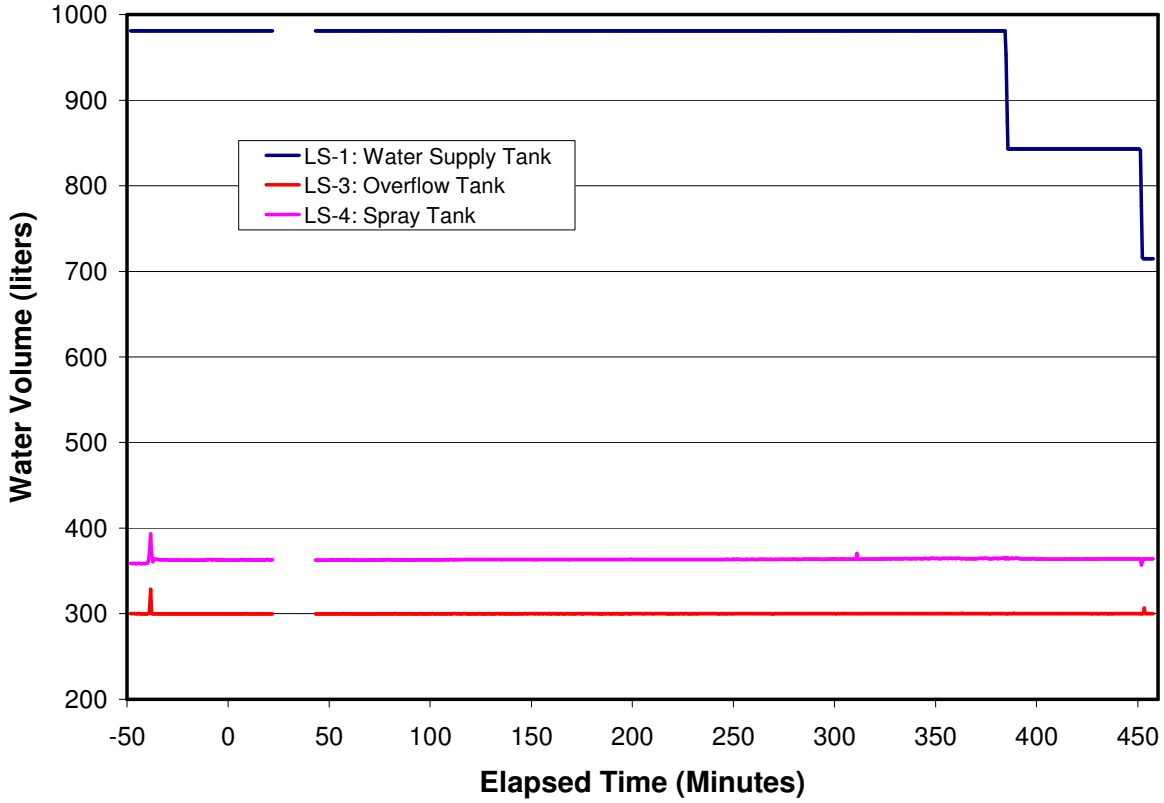

Figure B-51. Water Supply, Overflow, and Spray Tank Water Volume Data.

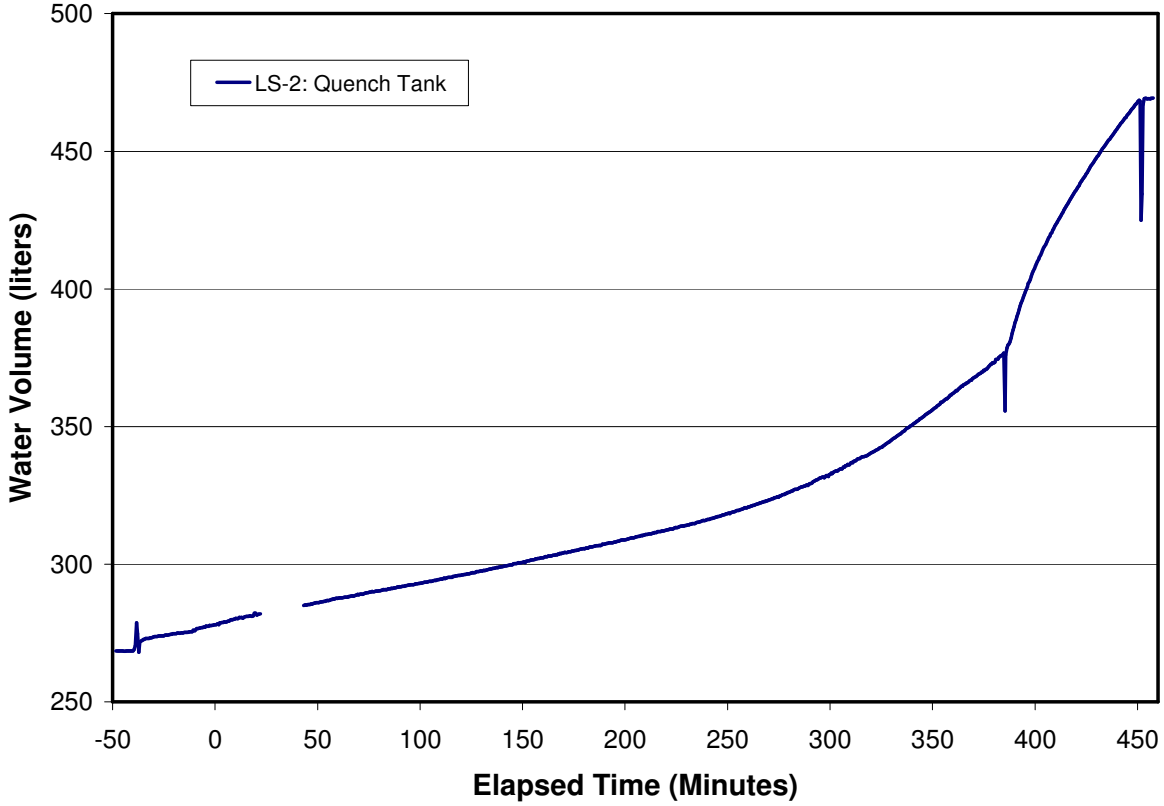

Figure B-52. Quench Tank Water Volume Data.

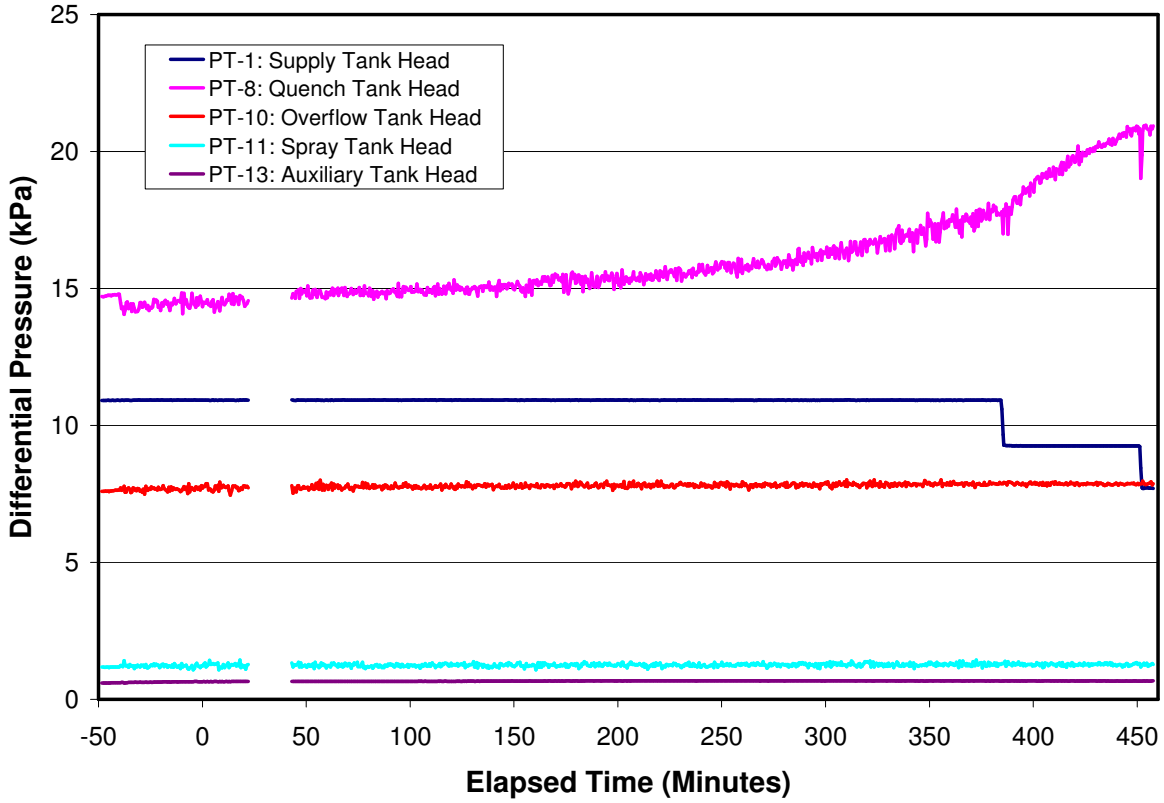

Figure B-53. Supply and Quench System Tank Head Data (Backup).

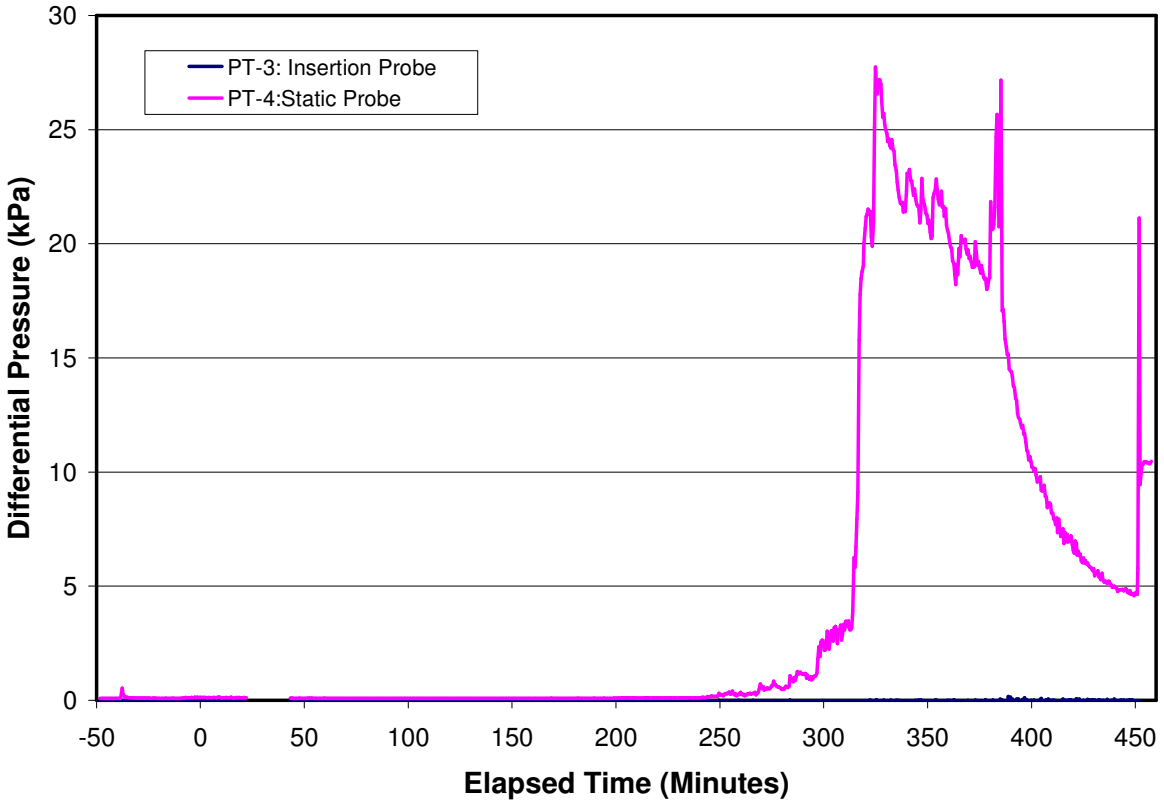

Figure B-54. Test Section Water Head Transducer Data.

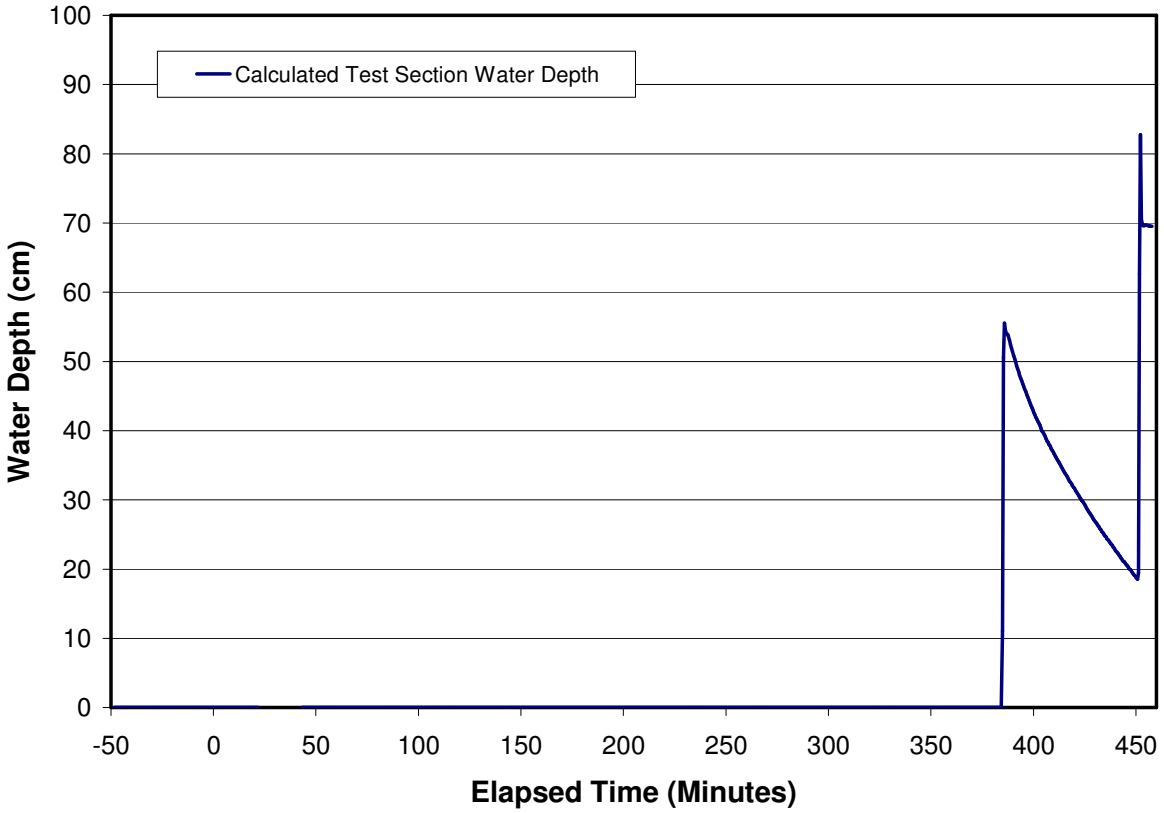

Figure B-55. Calculated Water Depth in Test Section.

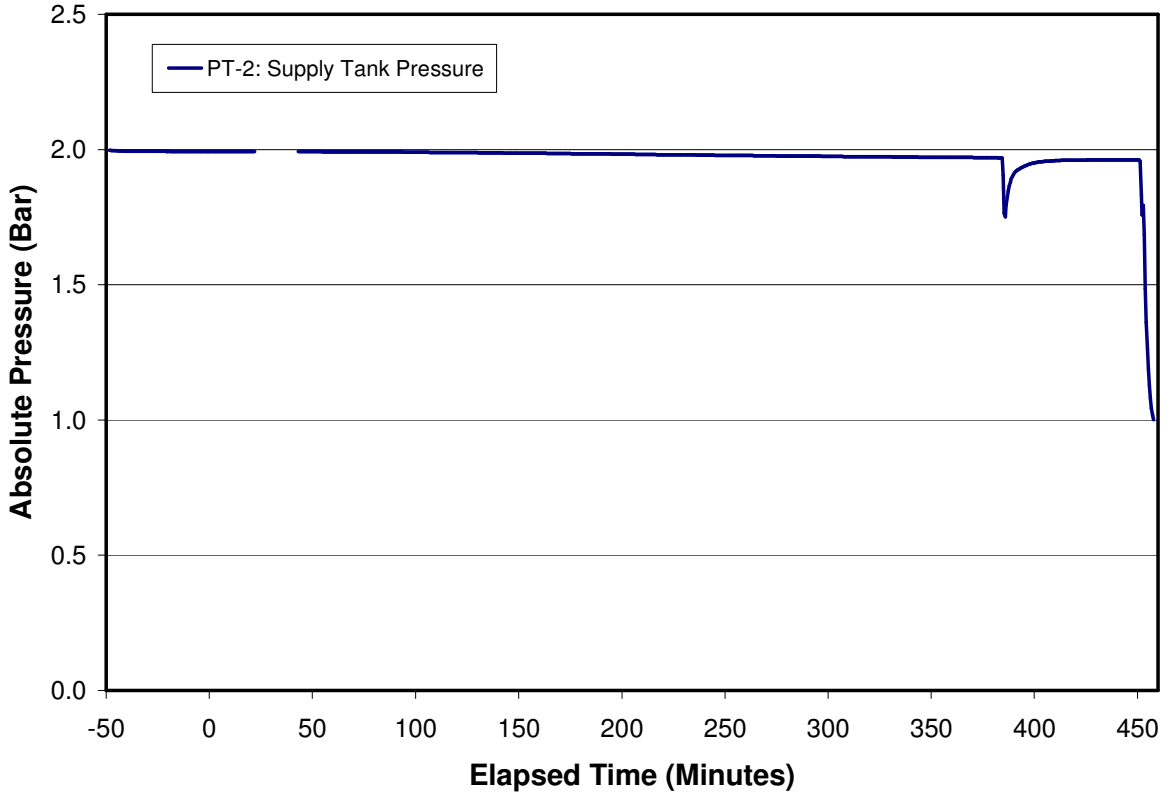

Figure B-56. Water Supply Tank Pressure.

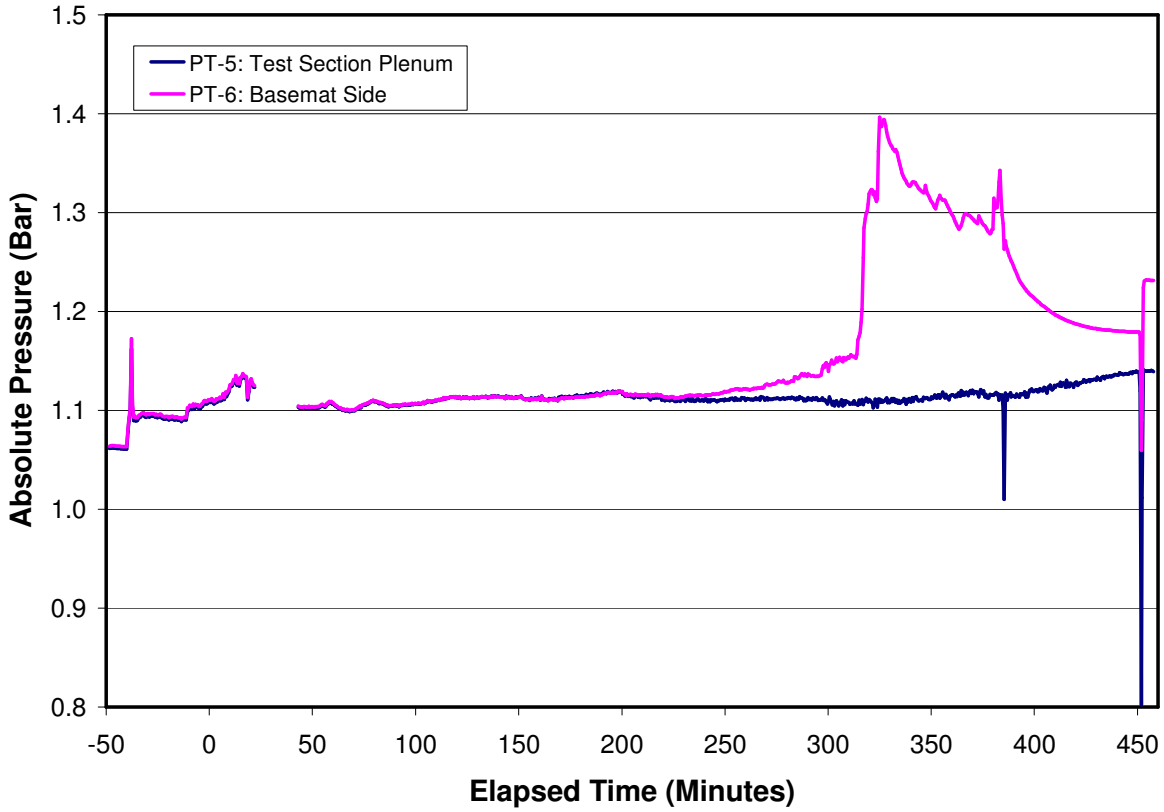

Figure B-57. Test Section Pressure.

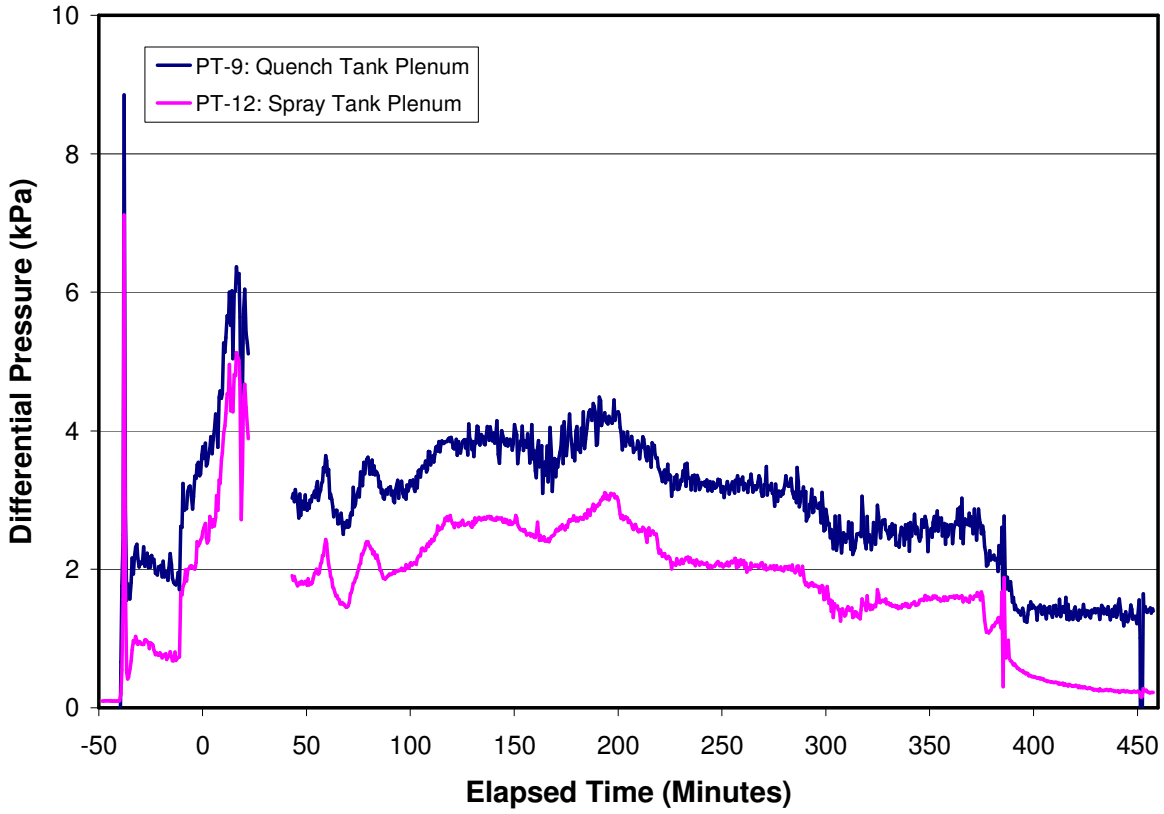

Figure B-58. Quench/Overflow and Spray Tank Plenum Differential Pressures.

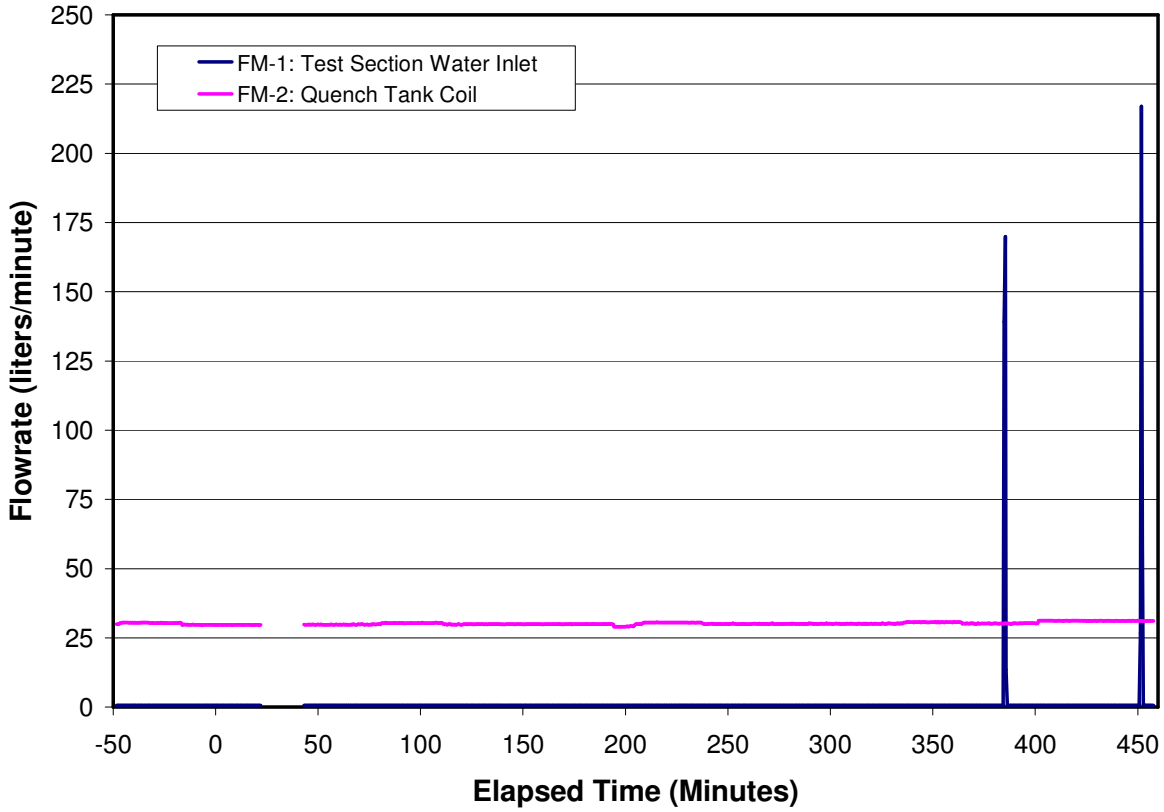

Figure B-59. Water Flow Rates.

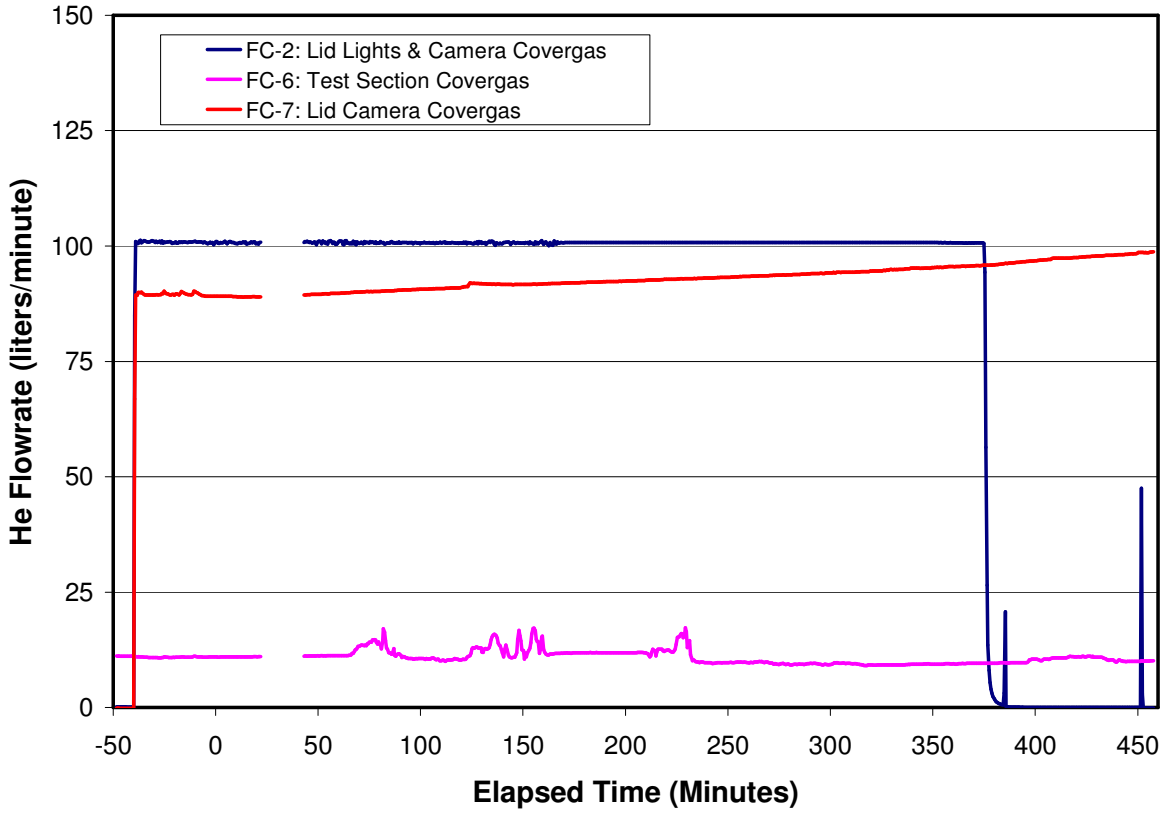

Figure B-60. Test Section Helium Cover Gas Flow Rates.

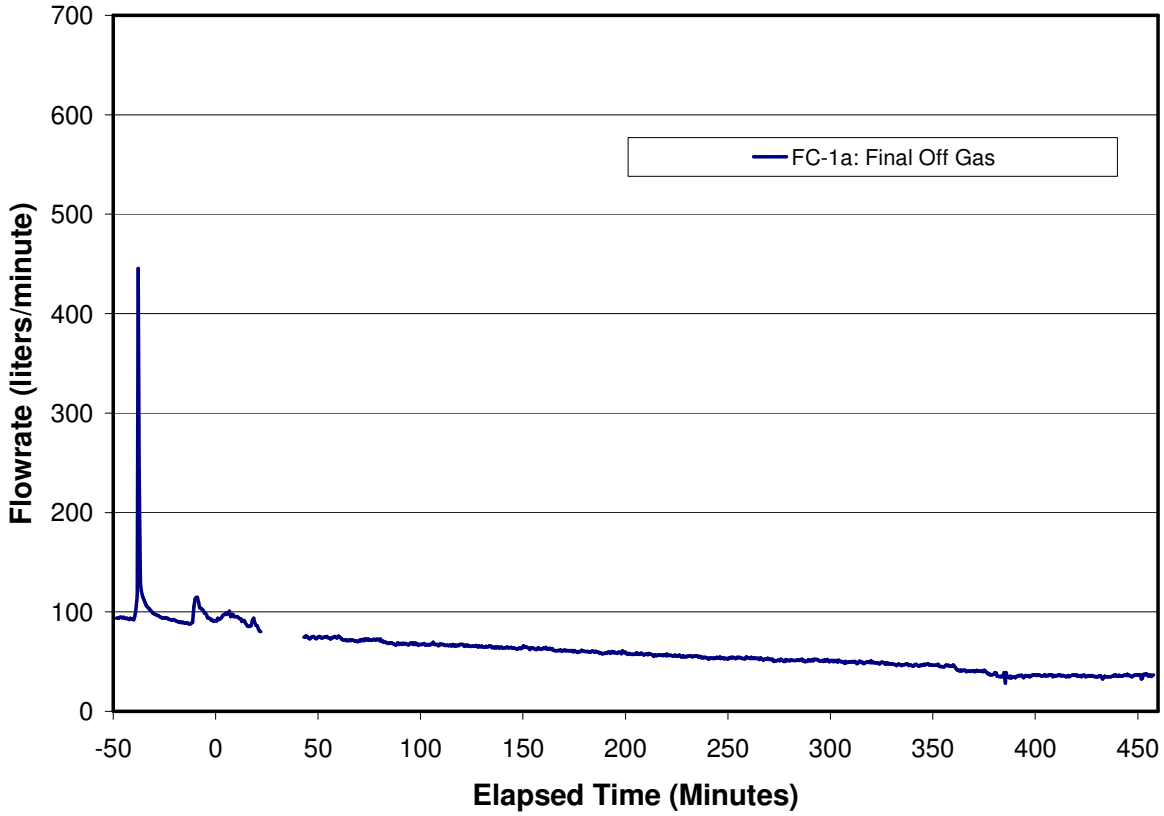

Figure B-61. Final Off Gas Flow Rate.

APPENDIX C
Chemical Analysis Results

This Appendix provides the raw data from the chemical analysis of the seven corium samples that were collected as part of the posttest examinations for CCI-4. Sample locations are described in Section 4.7 of the main body of the report.

All samples were analyzed using Inductively Coupled Plasma Atomic Emission Spectroscopy (ICP/AES). The analysis was carried out by the Analytical Chemistry Laboratory (ACL) at Argonne National Laboratory. Results are provided in Table C-1. The ICP/AES analysis provides elemental concentrations of selected elements; the elements have been converted to assumed oxide forms in the table. The resultant mass balance should sum to within the measurement error (reported as ± 10 % of the reported elemental concentration for each constituent) if the assumed oxide forms are reasonable and all key sample constituents have been included in the element scan list. As shown in Table C-1, all oxide mass balances fall well within the range of 100± 10%, which confirms that key elements are accounted for and that the assumed oxide forms are reasonable.

Table C-1. Raw Data from CCI-4 Sample Analyses. (All constituents with elemental concentrations of > 0.1 wt% are shown)

Elem.	Oxide Form	Sample Number															
		1		4		5		7		8		9		10		10 Duplicate	
		Wt% Elem.	Wt% Oxide	Wt% Elem.	Wt% Oxide	Wt% Elem.	Wt% Oxide	Wt% Elem.	Wt% Oxide	Wt% Elem.	Wt% Oxide	Wt% Elem.	Wt% Oxide	Wt% Elem.	Wt% Oxide	Wt% Elem.	Wt% Oxide
Al	Al_2O_3	1.26	2.38	0.30	0.57	1.13	2.14	1.74	3.29	1.70	3.22	1.53	2.89	0.86	1.62	0.76	1.43
Ca	CaO	20.75	29.04	3.18	4.45	20.15	28.20	22.25	31.13	22.28	31.17	21.98	30.75	16.22	22.69	16.13	22.56
Cr	Cr_2O_3	0.25	0.36	0.24	0.35	0.29	0.42	0.20	0.30	0.22	0.32	0.26	0.38	0.29	0.43	0.27	0.40
Fe	Fe_2O_3	2.37	3.39	0.03	0.05	1.91	2.73	2.48	3.54	2.35	3.36	2.18	3.11	1.19	1.70	1.16	1.66
Mg	MgO	6.19	10.26	0.28	0.47	5.84	9.68	6.86	11.37	6.80	11.28	6.61	10.96	5.18	8.59	5.14	8.52
K	K_20	0.27	0.32	0.00	0.00	0.29	0.35	0.44	0.54	0.39	0.47	0.37	0.45	0.18	0.22	0.17	0.21
Si	SiO_2	11.25	24.06	2.39	5.12	10.69	22.88	11.83	25.31	12.00	25.67	11.54	24.70	10.68	22.85	7.13	15.24
Na	Na_2O	0.25	0.33	0.03	0.05	0.24	0.32	0.35	0.48	0.34	0.46	0.30	0.41	0.17	0.23	0.16	0.22
U	UO_2	14.21	16.12	58.91	66.83	16.66	18.90	10.72	12.16	10.89	12.35	11.65	13.21	33.45	37.94	33.26	37.73
W	WO_3	1.12	1.42	1.20	1.52	1.33	1.67	1.64	2.07	1.60	2.02	1.36	1.71	0.82	1.03	0.81	1.02
Zr	ZrO_2	7.67	10.36	14.16	19.13	8.96	12.10	5.40	7.29	5.64	7.61	5.76	7.78	6.37	8.60	6.28	8.48
Total			98.03		98.53		99.39		97.46		97.94		96.37		105.89		97.46